



University
of Glasgow

Egan, Jacquelyn Grace (2023) *Modifying the self-assembled nanostructures of perylene bisimides in water and their applications*. PhD thesis.

<https://theses.gla.ac.uk/83830/>

Copyright and moral rights for this work are retained by the author

A copy can be downloaded for personal non-commercial research or study, without prior permission or charge

This work cannot be reproduced or quoted extensively from without first obtaining permission from the author

The content must not be changed in any way or sold commercially in any format or medium without the formal permission of the author

When referring to this work, full bibliographic details including the author, title, awarding institution and date of the thesis must be given

Enlighten: Theses

<https://theses.gla.ac.uk/>
research-enlighten@glasgow.ac.uk



Modifying the self-assembled nanostructures of perylene bisimides in water and their applications

PhD Thesis submitted by:

Jacquelyn Grace Egan

May 2023

Submitted in fulfilment of the requirements for the
Degree of Doctor of Philosophy

College of Science and Engineering
School of Chemistry
University of Glasgow

Abstract

Perylene bisimide (PBI) performance in photovoltaic applications is highly dependent on their ability to form photogenerated radicals. Their aggregation and self-assembled nanostructures can have a large impact on their ability to form the photoconductive radical. Currently, the literature has been primarily focused on changing their aggregation and self-assembled nanostructures in organic solvents. However, there is a desire to move away from organic solvents and towards water as it is more environmentally friendly. The addition of pH-sensitive groups onto the PBI chemical structure allows for them to be solubilised in water. This also allows for their aggregation and self-assembled nanostructures to be tailored through pH change.

First, this work looked at how the counterion used to make the basic solution which solubilises the PBI could be used to change the aggregates and molecular packing in solution. This is a simple method and less time consuming compared to changing the PBI chemical structure to form new structures. The different metal ions used to form the PBI aggregates had different pH sensitivities and showed different nanostructures forming over a range of pHs. This also led to a change in the gelation kinetics for pH-triggered hydrogels and a difference in the bulk rheological properties. The solutions of PBI solubilised with different counterions at pH 6 were used to fabricate multilayer photovoltaic devices which showed varying degrees of power conversion efficiency depending on counterion choice.

Next, the chemical structure was changed in the imide position with three similar amino acids. These PBIs were then characterised across various length scales to see how their self-assembled structures influenced their ability to form photoconductive radical at different pHs. This difference in molecular packing led to a difference in radical anion formation over a range of pHs. The difference in pH sensitivity led to a difference in the gelation kinetics when a pH trigger was used. It was also observed that the different pH sensitivities led to an increase in gel stiffness for one of the PBIs.

Lastly the synthesis of three PBIs with different amino acid side chains that have been core-substituted with pyrrolidine groups were examined. The change in the functional group on the core is expected to change the π - π stacking. The addition of the electron density to the core leads to a dramatic change in the optical and redox properties. The PBIs were able to form radical cation instead of radical anion when irradiated. Their ability to self-assemble as pH was lowered showed that amino acid choice has a major impact on the nanostructures formed. They could be used to make pH-triggered hydrogels when the initial solution concentration was increased, however, these hydrogels could no longer form radical cation.

Table of contents	
Abstract	i
List of publications	v
Acknowledgements	vi
Author’s declaration	viii
List of abbreviations	ix
Chapter 1: Introduction	1
1.1 Low molecular weight gelators	2
1.1.1 Fundamentals of self-assembled structures across multiple length scales	3
1.1.2 Factors impacting the gelation process	4
1.2 Stimulus-responsive LMWGs	6
1.2.1 pH-responsive supramolecular gels.....	6
1.2.2 Redox-responsive supramolecular gels	8
1.2.3 Photoresponsive supramolecular gels.....	9
1.3 Perylene bisimides as LMWGs	13
1.3.1 Modification of the chemical structure of PBIs.....	15
1.3.2 Modification of the bay position of PBIs.....	16
1.3.3. Modification of the imide position of PBIs	18
1.4 Self-assembled structures of PBIs impacted by external chemical stimuli	19
1.4.1 Self-assembled structures impacted by metals.....	19
1.4.2 Self-assembled structures impacted by ionic additives.....	21
1.4.3 Self-assembled structures impacted by solvent.....	22
1.4.4 Self-assembled structures impacted by pH.....	23
1.5 Applications of PBIs	25
1.5.1 Optoelectronics performance of PBIs tuned by chemical structure changes	26
1.5.2 Optoelectronics performance of PBIs tuned by external chemical stimuli	28
1.6 Aims of this work	30
1.7 References	32
Chapter 2: Improving the performance of PBI-L in interlayer photovoltaic devices using counter ions	39
2.1. Introduction	40
2.2. Results and discussion	45
2.2.1 Investigation of self-assembled micellar aggregates in solution at different pHs....	45
2.2.2 Investigation of hydrogels of PBI-L with different cations made using a pH trigger	59
2.2.3 Use of PBI-L solutions with different cations for photovoltaic applications.....	69

2.3. Conclusions	76
2.4. Experimental	77
2.4.1. Preparation of PBI-L solutions.....	77
2.4.2. Preparation of hydrogels.....	78
2.4.3. Rheological measurements.....	78
2.4.4. UV-vis absorption spectroscopy.....	79
2.4.5. Small-angle X-ray scattering (SAXS).....	80
2.4.6. pH measurements.....	81
2.4.7. Apparent pK_a titrations.....	82
2.4.8. Cyclic voltammetry (CV).....	82
2.4.9. Fabrication of PBI-L interlayer photovoltaic devices.....	83
2.4.10. Transmittance of PBI-L interlayer photovoltaic devices.....	84
2.4.11 Nanoindentation of PBI-L interlayer photovoltaic devices.....	84
2.4.12 Current–voltage characterisation of PBI-L interlayer photovoltaic devices.....	85
2.5. References	85
Chapter 3: Impact of subtle change in branched amino acid on the assembly and properties of perylene bisimides	88
3.1. Introduction	90
3.2. Results and discussion	95
3.2.1 Investigation into the branched side chain structure on self assembled micellar aggregates in solution at different pHs.....	95
3.2.2 Probe into the impact of amino acid choice on the hydrogel properties and gelation process.....	110
3.3. Conclusions	118
3.4. Experimental	119
3.4.1 Materials and Synthetic procedures.....	119
3.4.2 Methods.....	128
3.4.2.1 Characterisation of PBIs.....	128
3.4.2.2 Preparation of PBI solutions.....	128
3.4.2.3 Preparation of hydrogels.....	128
3.4.2.4 Small-angle X-ray scattering (SAXS) data.....	128
3.4.2.5 Rheological measurements.....	130
3.4.2.6 UV-vis absorption spectroscopy.....	131
3.4.2.7 pH measurements.....	132
3.4.2.8 Apparent pK_a titrations.....	132
3.4.2.9 Cyclic voltammetry (CV).....	132

3.4.2.10 ¹ H-NMR spectroscopy kinetics	132
3.5 References	133
Chapter 4: Photogenerating behaviour of a pyrrolidine bay-substituted perylene bisimide at different pH values	136
4.1. Introduction	137
4.2. Results and discussion	143
4.2.1 Synthesis, Optical and Electronic properties of novel core substituted PBIs	143
4.2.2 Investigation to the photoexcitation properties of the core substituted PBIs	148
4.2.3 Probe into the impact of pH on the packing and self assembled aggregates of the core substituted PBIs.....	158
4.2.4 Development of pH triggered hydrogel materials using core substituted PBIs	167
4.3. Conclusions.....	175
4.4. Experimental.....	176
4.4.1 Materials and synthetic procedures.....	176
4.4.2. Methods	185
4.4.2.1 Characterisation of PBIs	185
4.4.2.2 Preparation of PBI solutions.....	185
4.4.2.3 Preparation of PBI hydrogels	186
4.4.2.4 UV-vis absorption spectroscopy measurements.....	186
4.4.2.5 Rheological measurements of the irradiated samples	187
4.4.2.6 Square wave voltammetry measurements (SWV).....	189
4.4.2.8 pH measurements	190
4.4.2.9 Apparent pK _a titrations	191
4.4.2.10 Rheological measurements of the solutions at different pHs and as pH-triggered hydrogels	191
4.4.2.11 Small-angle X-ray scattering (SAXS)	192
4.4.2.12 Electron resonance spectroscopy (EPR).....	193
4.5 References	193
Chapter 5: Summary, conclusions and future work.....	196
5.1 Conclusions.....	197
Chapter 6: Appendix	201

List of publications

“Impact of subtle change in branched amino acid on the assembly and properties of perylene bisimides hydrogels” J. G. Egan, G. Brodie, D. McDowall, A. J. Smith, C. J. C. Edwards-Gayle and E. R. Draper, *Mater. Adv.*, 2021, **2**, 5248-5253

“Tuning reduction potential whilst maintaining mechanical properties in perylene bisimide hydrogels at physiological pH” J. A. Mena Jimenez, J. G. Egan, R. Randle, R. Schweins and E. R. Draper, 2023, In preparation.

“The Effects of Amino Acid Functionalisation on the Optoelectronic and Self-Assembly of Perylene Bisimides.” T. A. Welsh, J. G. Egan, B. Dietrich, N. Rafferty, R. E. Ginesi, J. Douth, R. Schweins and E. R. Draper, 2023, submitted.

Acknowledgements

This thesis is dedicated to Donna Josephine Oliver-Egan, October 8th, 1966, to January 7th, 1998. 25 years gone, but never forgotten, love you mom.

I would first like to thank my supervisor Dr. Emily Draper, first for welcoming back into the lab as a PhD student after my research placement in the winter of 2019. You took a chance on a small Canadian when no one else would. Thank you as well for all the support and guidance over the course of my PhD studies especially since it wasn't the PhD either of us were expecting. Thank you to everyone who collaborated and contributed to this thesis, your names are listed throughout where your contributions were made. Your collaborations really helped elevate the research shown in this thesis.

A big thank you goes out to the many people in the Raphael lab who have made my time in Glasgow so special over these past 3 years. Thank you to the Draper group past and present, to Rebecca Ginesi, and Nick Murray, I am so excited to see what the future holds for you two and I will always be rooting you on. Please send me updates throughout the degrees so I can continue to celebrate your wins with you. Best of luck to my office buddies, Ziyao Xu and Connor MacDonald with the rest of your research. A big thank you, past and present Adams Group as well. Thank you Ana Mari Fuentes Caparrós for reminding me I deserve good things and always reaching out. To my cohort Libby Marshall and Courtenay Patterson, this pandemic PhD was tough, but I am so happy to have had your support and friendship to brighten up my day. No one will ever understand what this was like better than you two. To the rest, Mari Laura Vieri, Max Hill, Chloe Wallace, Simona Bianco, and Emma Bowley, I wish you all the best with the rest of your degree!

A special thank you to my UK + Scot family, Becky Randle, Lisa Thomson, Beth and Dan McDowall. You guys made sure I was always taken care of, and I don't know how I would have managed the last couple years without you. You showed me all the things that make the UK wonderful, such as top only meat pies, jam vs. cream scone debate, hiking, Great British Menu, gin AND lemonade, and so many more jokes that are probably documented on a dirty lab coat somewhere! I will always treasure our friendships and cannot wait to continue Friendsgiving traditions until you're all sick of

me. Even when you are sick of me I'll still keep bothering you cause you cannot get rid of me!

Thank you, to the classic UOIT crew, Holly Freuhwald, Nadia Laschuk and Richard Bartholomew. You all provided so much support and insight from thousands of kilometres away both in my research and as friends. In particular, Nadia, you are truly one of the most supportive and inspiration women in science I have ever met. I couldn't imagine my research journey without your support and even now as I leave research, I know you'll always be proud of how far I have come. Just like how I am so proud of all the things you have accomplished!

Finally, thank you to my family, Rebecca, Caroline, Rosie, and Brian Egan. Lord knows I was really all over the place towards the end of this but all of you did nothing but support my craziness. Thank you, Caro, for all the photos of Rosie sleeping and chasing squirrels in the family group chat. Apologies to Rebecca, when you were upset that I was leaving for the UK and not coming back. I brushed it off because I wasn't expecting a global pandemic to impact my holidays. Thank you to my dad, who gave me the blinding confidence to always strive for more and never once think I couldn't have it all. As well thank you to my cousin Mairead Weir, having you in the UK during all the craziness the last couple years has made a huge difference.

This thesis was submitted on May 15th, 2023, Happy 60th Birthday Daddy!

Author's declaration

This Thesis has been written and compiled by the author, Jacquelyn G. Egan, who carried out the research at the University of Glasgow between 2019 and 2023 under the supervision of Dr. Emily Draper. I declare that, except where explicit reference is made to the contribution of others, that this thesis is the result of my own work and has not been submitted for any other degree at the University of Glasgow or any other institution.

Jacquelyn G. Egan

List of abbreviations

δ - chemical shift

λ - wavelength

θ - scattering angle

1D - one dimension

2D - two dimensions

3D - three dimensions

°C - degrees Celsius

^1H - proton

^{13}C - carbon

Ag/AgCl - silver / silver chloride

CsOH - caesium hydroxide

CP - cone plate

CV - cyclic voltammetry

DMSO - dimethyl sulfoxide

DMSO- d_6 - deuterated dimethyl sulfoxide

EPR - electron paramagnetic resonance

HR-ESI-TOF MS - high resolution electrospray ionization time of flight mass spectrometry

FTIR - Fourier transform infrared

G' - storage modulus

G'' - loss modulus

G δ L - glucono- δ -lactone

HCl - hydrochloric acid

HOMO - highest-energy occupied molecular orbital

KOH - potassium hydroxide

LED - light-emitting diode

LMWG - low molecular weight gelator

LiOH - lithium hydroxide
LUMO - lowest-energy unoccupied molecular orbital
mW - milliwatt
mgc - minimum gel concentration
NaOH - sodium hydroxide
NaCl - sodium chloride
nm - nanometre
NMR - nuclear magnetic resonance spectroscopy
OPVs - organic photovoltaics
PP - parallel plate
PBI - perylene bisimide
PTCDA - 3,4:9,10-perylenetetracarboxyldianhydride
pH - power of hydrogen
Q - scattering vector
SPP - sand-blasted parallel plate
SANS - small-angle neutron scattering
SAXS - small-angle X-ray scattering
SEC - spectroelectrochemistry
SEM - scanning electron microscopy
SLD - scattering length density
SWV - square wave voltammetry
 $\tan\delta$ - damping factor
TEM - transmission electron microscopy
TFA - trifluoroacetic acid
USANS - ultra small-angle neutron scattering
UV-vis - ultra-violet – visible

Chapter 1: Introduction

1.1 Low molecular weight gelators

Low molecular weight gelators (LMWGs) are small molecules that can self-assemble into supramolecular structures via noncovalent bonds such as π - π stacking, hydrogen bonding, and van der Waals interactions. Examples of effective LMWGs include functionalised sugars,¹⁻³ surfactants,⁴⁻⁶ and peptides.⁷⁻⁹ Using an appropriate gelation trigger, these supramolecular structures can entangle and cross-link to form a 3D gel network which entraps solvent. When the entrapped solvent is water, the materials are labelled hydrogels and if the solvent is an organic solvent, the materials are labelled organogels. Water is a particularly desirable solvent to use as it is abundant and considered a greener solvent compared to other commonly used solvents such as chloroform or toluene. Therefore, LMWG-based hydrogels have been a popular material for use in applications such as drug delivery,¹⁰ optoelectronics,¹¹ and catalysis.¹²

The use of LMWGs for the design and development of hydrogels is desirable as they offer a great alternative to other molecules that are covalently bonded together, such as polymers, as LMWG self-assembled structures can revert to the original structures. The chemical structure of LMWG can also be easily modified using easily synthetic routes compared to polymers. Due to the weaker nature of the non-covalent interactions, the self-assembled structures of LMWGs are massively process-dependent: their properties can be influenced by several factors such as temperature, concentration, and chemical structure changes. This sensitivity can provide researchers with the opportunity to change minor variables to modify supramolecular structures.

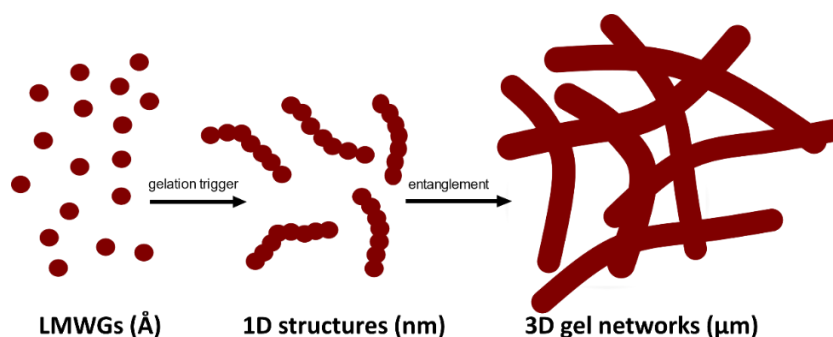


Figure 1.1. Cartoon depiction of LMWGs assembling into 1D structures and further assembling into a 3D network upon gelation, with different length scales listed.

1.1.1 Fundamentals of self-assembled structures across multiple length scales

The process of gelation relies on the kinetically and thermodynamically favourable assembly of molecular units into 1D structures. These structures then entangle and cross-link through the formation of different intermolecular forces to form a network which entraps solvent, resulting in a 3D gel network. These 1D structures are typically nanofibers, nanorods, nanotubes, or nanotapes.¹³⁻¹⁵ As the self-assembly is happening across different length scales it is important to study them using different techniques to probe the system in order to link the different gel properties back to chemical structure, as illustrated in Figure 1.2.

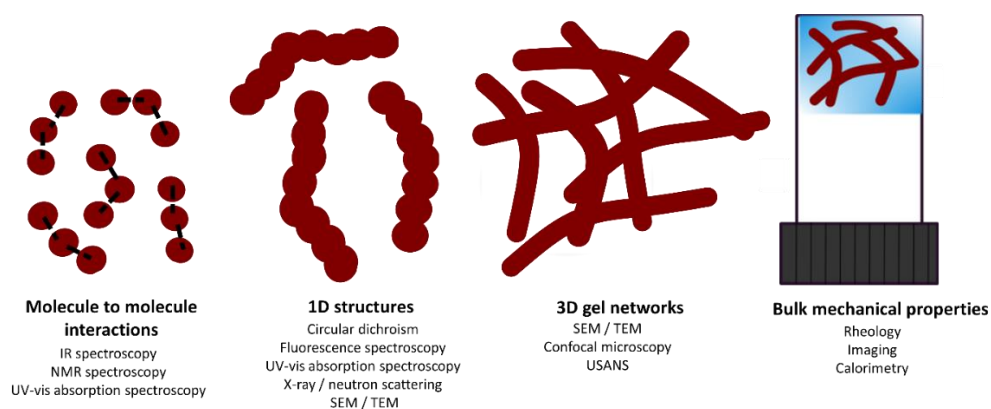


Figure 1.2. Appropriate characterisation methods across different length scales for self-assembled structures of LMWGs. Adapted from original article.¹⁶

The self-assembly and molecular packing of the LMWG molecular units can be probed using spectroscopic techniques such as UV-vis absorption spectroscopy, infrared spectroscopy, circular dichroism, and nuclear magnetic resonance spectroscopy.^{17, 18} The morphology and size of 1D structures is typically investigated using a scanning electron microscope / transmission electron microscope (SEM/TEM) or confocal microscope.¹⁹⁻²¹ Confocal microscopy requires the molecule to be fluorescent and this fluorescence cannot become quenched upon self-assembling into aggregates. Otherwise, a fluorescent stain must be added to the system which may affect the self-assembly behaviour. SEM or TEM requires the solutions or hydrogels to be dried and structures are imaged under high vacuum. This processing can lead to changes in the lengths and morphology, resulting in an inaccurate depiction of the 1D structures.²² Cryo-TEM can be used, however, it requires the

samples to be frozen and temperature can have a major impact on the self-assembled fibres and gel network.^{23, 24} Small-angle neutron scattering (SANS) or small-angle X-ray scattering (SAXS) can be used to characterise the length and morphology of nanostructures *in situ*, there is no need to dry solutions or hydrogels or add a stain. Once the data are collected, they can be fitted to a mathematical model to deduce information about the fibres and network type over a wide length scale. This technique is thus a preferable method for understanding the fibre network of solutions and gels.^{25, 26} Rheology can be used to study the gel formation kinetics and bulk mechanical properties of a gel, and network type can be inferred.²⁷ However, it is important to support the inferred network type with more than one method of characterisation as the rheological data can often show different behaviours which implies there are different underlying networks. Significant work is needed to understand this better.

1.1.2 Factors impacting the gelation process

The gelation process can be triggered using a pH change,^{28, 29} addition of a metal cation,^{13, 30} solvent switch,³¹ addition of an enzyme,³² or temperature change.³³ Regardless of the differences between the different gelation triggers, they all operate in a similar way. The gelator needs to start off solubilised in some way then a trigger is added which decreases the solubility of the molecules which begin to pack together and self-assemble into fibres. These fibres can either physically entangle or chemically crosslink into a 3D network entrapping the solvent. It should be noted that many LMWGs often exist in an assembled state in the pre-gel solution. How the pre-gelation assembled structures affect the gelation process and final gel mechanical properties is not often discussed. Understanding these aggregated structures can allow for fine-tuning of the hydrogels' bulk mechanical properties.

Cardoso *et al.* investigated a dipeptide LMWG which was able to undergo aggregated structural transformations as the concentration was increased.¹³ Initially, in solution this LMWG formed spherical micelles then, as the concentration was increased, it formed worm-like micelles, followed by association of these worm-like micelles. The workers were able to track the different micellar structures as concentration increased using confocal microscopy and SANS. The work showed that the salt-trigger gelation

of this dipeptide relies on the initial solution having worm-like micellar structures present for chemical crosslinks to sufficiently entrap the solvent. At low concentrations when spherical micelles were present, the solutions could not pass an inversion test and therefore were not considered hydrogels. However, when the concentration increased past the first critical micelle concentration (cmc), there was a phase transition from spherical micelles to worm-like micelles. The final gels of these worm-like micelles could pass the inversion test although this phenomenon happened at a lower concentration than predicted. In this phase, samples showed typical behaviour for weak LMWGs in terms of rheological properties. When the concentration was higher than the second cmc, elongated worm-like micellar structures had formed and the samples all passed the inversion test. This study highlighted the concentration dependency of assembled structures on the formation of hydrogels.

There are many other factors besides concentration that can impact the assembly leading to changes in the rheological properties of hydrogels. Some factors can be external, such as the initial pH when using a pH trigger, or the addition of salt additives to help solubilise the LMWG.³⁴ Internal factors can be minor changes in chemical structure of the LMWGs themselves. Design of LMWGs is difficult as the structural requirements that influence self-aggregation are often not well understood and hard to predict. Prediction of final gel properties based on the chemical structure is also difficult because of the pathway dependency of gelation.³⁵⁻³⁷

There have been advances in linking chemical structure to gelation using libraries and computational approaches. Work by Frederix *et al.* was able to effectively predict tripeptide-based gelators using computational tools which screened 8,000 possible tripeptides and evaluated them by comparison with known examples.³⁸ Work by Gupta *et al.* also developed a computational method that screened 2025 dipeptide candidates and correctly identified 9 which were synthesised and tested to support the computational findings of their gelation properties.³⁹ The use of libraries is more time- and labour-intensive but often the most successful way to find gelators. Computational models require the initial work done by screening libraries of structures to define model parameters and improve their predictions as well. Therefore, it is important to continue to contribute new gelators to these libraries.

1.2 Stimulus-responsive LMWGs

Supramolecular gels are kinetically trapped and typically do not show changes in materials properties after formation. However, through thoughtful design of the LMWG chemical structure, functional groups can be incorporated which allow them to become stimulus-responsive. These functional groups can be incorporated through simple synthetic routes making LMWGs more favourable compared to their polymer competitors. Upon the stimulus being applied, changes in the molecular aggregation of LMWGs can allow for gel-to-gel and gel-to-sol transitions which result in changes in the physical properties of the gels.⁴⁰⁻⁴² This property allows for possible application as smart materials (electrochromic devices, photothermal devices and drug delivery). Some of the possible external stimuli that can be used to change the gels' physical properties include electrical, optical, or pH change.⁴³⁻⁴⁵ All of these are dependent on the chemical structure of the LMWG itself. Regardless of the functional group chosen, a common feature in many of these structures is sterically large groups such as benzene rings. Aromatic groups aid in gelation due their ability to self-assemble into aggregates through π - π stacking and lack of solubility.⁴⁶⁻⁴⁸ The ability to modify the gel properties post gelation expands the possible applications for these hydrogel systems greatly. This section aims to give an overview of the diversity in chemical structure for stimulus-responsive LMWGs and discuss how chemical structure design is important to their responsive properties.

1.2.1 pH-responsive supramolecular gels

As mentioned earlier, gelation can be triggered by changing the pH because LMWGs form gels based on noncovalent bonds where self-assembly can be reversed. As many biological applications for hydrogels require a specific pH value, pH-responsive hydrogels whose network can degrade at a different pH to the gelation pH are ideal candidates for use as drug-releasing materials. The pH-responsive behaviour relies on a pH-sensitive group being incorporated into the chemical structure. These functional groups are commonly ionisable groups such as amines or carboxylic acid groups incorporated into the gelator backbone.^{9, 49-51} For ionisable groups, the solubility is controlled by the degree of protonation of the groups. Some examples of chemical structures with ionisable groups are shown in Figure 1.3.

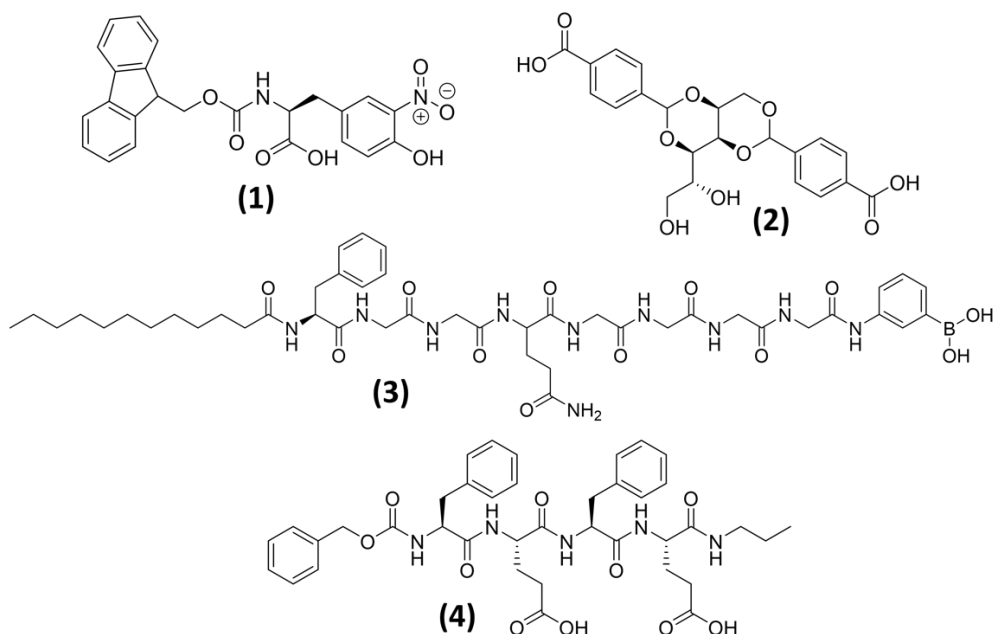


Figure 1.3. A small example set of pH-responsive LMWGs showcasing the diversity in chemical structure: (1) fluorenylmethyleneoxycarbonyl (Fmoc) based gelator;⁴¹ (2) 1,3:2,4-dibenzylidene-D-sorbitol;⁵² and (3) terminal phenylboronic acid oligopeptide.⁵³

Most commonly, pH changes will lead to morphological transformations or change in molecular conformation. This phenomenon is what makes them such good candidates for commercial applications for drug delivery.⁵³⁻⁵⁵ Tao *et al.* synthesised an oligopeptide with a phenylboronic acid functional group at the *N*-terminal which could form hydrogels using a temperature change, Figure 1.3 LMWG (3).⁵³ They initially heated the mixture of gelator and drug to improve solubility then allowed the mixture to cool, and used ¹H-NMR spectroscopy to track the aggregation mode of the gelators. They observed a downfield shift for a signal assigned to a benzene ring proton and the signal corresponding to the N-H proton as the temperature decreased. The researchers believed this shift was due to changes in hydrogen bonding upon gelation. The gelator had phenylboronic acid and amide functional groups. In acidic or alkaline solutions these groups can become charged and lead to the breaking of the gel network. UV-vis absorption spectroscopy was used to investigate the pH-sensitive controlled release of a model drug molecule. To evaluate the pH-sensitive controlled release, both blank hydrogels and drug-loaded hydrogels were submerged in

solutions at different pH and the breakdown of the gel network was monitored with time. The blank hydrogels showed the breaking of the gel network was the most efficient at pH 5 while the drug-loaded hydrogels showed more efficient breaking of the network at pH 4.4. This difference in activity is believed to be due to a difference in the gel networks for the systems, which was supported by TEM imaging. For the drug-loaded hydrogel they even observed a significant difference in drug release speed between pH 7.4 and 6.8, the pH of tumour extracellular matrices.

1.2.2 Redox-responsive supramolecular gels

Redox-responsive gels based on LMWGs have been seen to be promising molecules for use in the biomedical field due to their biocompatibility and versatility.⁵⁶ The sensitivity to an electric field could be accomplished through the addition of a redox-responsive filler or directly incorporated into the chemical structure of the LMWG. The filler is typically a redox-active metal ion that has been accumulated into the gel fibres. These types will not be discussed here, instead we focus on redox-active LMWGs themselves. Functional groups commonly incorporated into the chemical structure that have redox-responsive properties include tetrathiafulvalenes (TTF),⁵⁷⁻⁵⁹ catechols,^{11, 60} thiophenes,^{59, 61} or disulfides.^{62, 63} While TTF is the most widely used functional group incorporated in LMWGs, they are more often used to make organogels than hydrogels.^{57, 59, 64, 65}

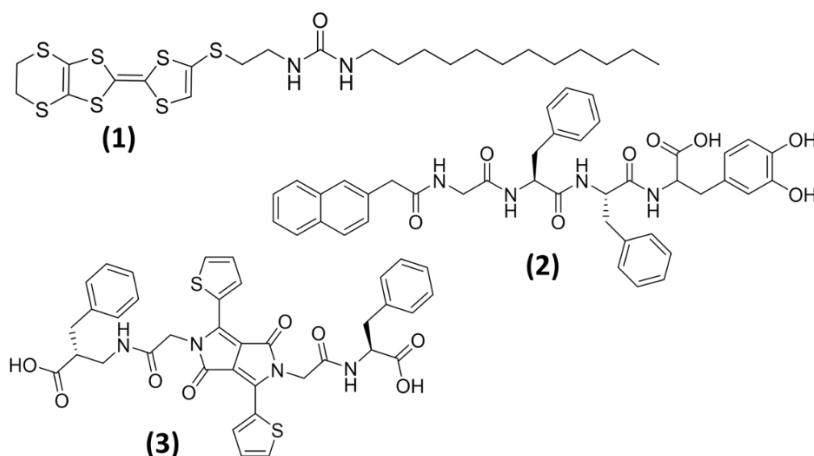


Figure 1.4. A small example set of redox-responsive LMWGs showcasing the diversity in chemical structure: (a) tetrathiafulvalene-based gelator;⁵⁷ (2) catechol-based tripeptide;⁶⁰ and (3) a diketopyrrolopyrrole (DPP).⁶¹

Recently, Xue *et al.* reported a stimulus-responsive gelator with the addition of a catechol functional group, Figure 1.4 LMWG (2).⁶⁰ They showed how the gelator could be used to develop an artificial actuator. The 3,4-dihydroxybenzyl residue on 3,4-dihydroxyphenylalanine (DOPA) gives the gelator its electrochemical-responsive properties as the DOPA is converted to dopaquinone upon oxidation. This change in the redox states led to a dramatic change in the hydrogel's volume and mechanical properties. The workers used atomic force microscopy (AFM) to study the fibre structures before and after oxidation and saw an increase in fibre size from 0.8 nm to 2.5 nm. Since they observed a dramatic volume change in the hydrogel size after oxidation, they used rheology to study the mechanical properties before and after. The storage modulus was 200 Pa for the initial hydrogel and approximately 2.5 kPa for the hydrogel post oxidation. They believe this change is due to the change in hydrophobicity after oxidation causing a bundling of the fibres and leading to an increase in inter-fibre cross-linking. However, the hydrogel was limited in terms of its reversibility. After the first cycle the hydrogel released unbound water. After releasing the water, the hydrogel volume could not be fully recovered. There were also concerns that after multiple cycles the DOPA functional group might polymerise. Redox-responsive LMWGs can be limited in their reversibility and by the need for a uniform electric field across the system.

1.2.3 Photoresponsive supramolecular gels

Light is a non-invasive stimulus so the gel network does not have to be disrupted by the incorporation of electrodes as for redox-responsive systems, and total volume changes through addition of acid or base for pH-responsive systems. These benefits make it one of the most popular external stimulus methods used extensively in cell culture and optoelectronics applications.^{45, 66} There is also a great variety in chemical structure design which can lead to different photoresponses. Chemical structure is very important to these systems as they need to still be able to self-assemble *via* noncovalent bonds and the various functional groups will dictate the reactivity. Some moieties capable of being used in photoresponsive LMWGs include dithienylethene,^{67, 68} spiropyran,^{69, 70} azobenzene,^{9, 71, 72} stilbene,^{73, 74} coumarin,^{75, 76} naphthalene diimides (NDIs),^{77, 78} and perylene bisimides (PBIs).^{73, 79} Their chemical structures are shown below in Figure 1.5. The reactivities of the LMWGs shown

include electrolytic reactions, photoisomerisation, photodimerisation, and photoredox reactions, as determined by the moiety used.

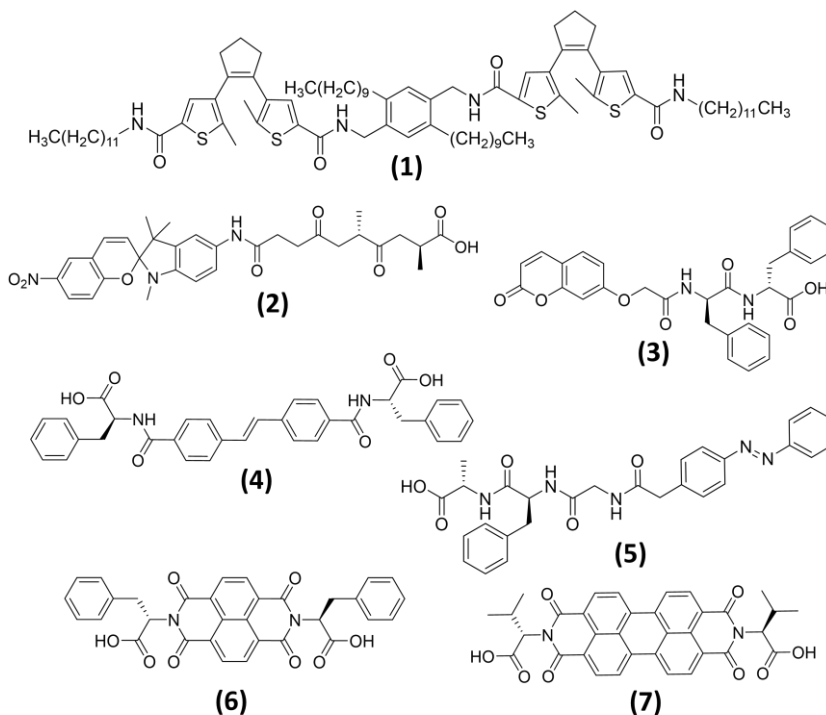


Figure 1.5. A small example set of photoresponsive LMWGs showcasing the diversity in chemical structure: (1) dithienylethene-based tetrapeptide;⁶⁸ (2) spiropyran-based dipetide;⁷⁰ (3) coumarin-based dipetide;⁷⁶ (4) stilbene-based dipetide;⁷³ (5) azobenzene functional group at the N-terminal;⁹ amino acid-functionalised (6) NDI;⁷⁷ and (7) PBI.⁷⁹

Electrocyclic reactions involve the forming or breaking of covalent bonds. For photoresponsive gelators this is often a ring-closing or ring-opening reaction. LMWGs that include dithienylethene or spiropyran functional groups can undergo these electrocyclic reactions. The ring-opening or ring-closing can change the colour,^{80, 81} or electronic properties,⁸² or cause a gel-sol transition.⁷⁰ When dithienylethene functional groups are irradiated with UV light they undergo an electrocyclic ring closure leading to an increase in the number of sp³ centres and the molecules become more rigid compared to the original conformation. LMWGs with spiropyran functional groups undergo electrocyclic ring opening when irradiated with UV light. The gel transformation is driven by the changes in planarity due to an increase in the number of sp²-hybridised centres. Making the chemical structure of these LMWGs

more or less flexible leads to a change in the stacking interactions between gelators which can lead to changes in the hydrogel network.

Photodimerisation involves the formation of highly stressed cyclobutane rings upon irradiation. The increase in the chemical structure size causes the gelator to be less soluble and this can increase the hydrophobicity and disrupt the gel network. Draper *et al.* reported the formation of bulk hydrogels or thin gels via an electrochemical pH drop using a coumarin-based gelator.⁷⁶ The bulk gels in Sterilin vials became turbid after being exposed to UV light, with the turbidity being most pronounced where the gel had been directly exposed. This observation indicates the changes in the bulk gels after irradiation were not homogenous. To obtain a homogenous system, the thin gel films were then grown on an electrode using an electrochemical pH drop method. The rheological strain sweeps of these electrochemically grown gels showed that the stiffness increased after irradiation with UV light for 15 minutes. This observation was due to the coumarin's ability to photodimerise. Further irradiation resulted in a decrease in the rheological properties, but the gels were still stiffer than before irradiation. SEM showed the electrochemically grown gels formed a random fibrous network like the bulk gels. After irradiation, the network had changed and showed less defined structures. The workers believe the change in the gel network was caused by the dimerisation of coumarins leading to stiffer fibres, as opposed to an increase in the number of cross-links between fibres.

In photoisomerisation a reaction occurs where the atomic connectivity of the molecule stays intact upon irradiation, however, the photoresponsive group switches between two configurations. A typical example is a change from a *trans* isomer to a *cis* isomer or *vice versa*. LMWGs that include stilbene and diazo functional groups can undergo these switches. Generally, the *trans*-isomer is more stable than the *cis*-isomer.^{44, 83, 84} Huang *et al.* screened several dipeptide and tripeptide LMWGs with an azobenzene group at the *N*-terminus, and investigated the hydrogelation properties.⁹ Aromatic amino acids including *D*-phenylalanine and *D*-tyrosine promoted hydrogelation of the azo-dipeptides while cationic amino acids such as *D*-arginine and *D*-lysine were found to be unfavourable for hydrogelation. They predicted that upon irradiation there would be a partial *trans-cis* isomerisation of the azobenzene, which would disturb the balance of the intermolecular interactions and would lead to a gel-sol transformation.

They studied the changes in the molecular packing before and after irradiation using UV-vis absorption spectroscopy, which showed a decrease in the absorbance upon irradiation at the *trans*-azobenzene peak around 330 nm. They also used rheology to measure the bulk mechanical properties before and after irradiation and found that after irradiation there was a sharp drop in the stiffness of the hydrogels. Since the hydrogel network could degrade upon irradiation with UV light, which penetrates through the epidermis layer of skin, these materials demonstrated promising photoresponsive behaviour for controlled release of drug molecules within that layer of skin tissue.

Lastly, photoredox reactions are similar to redox-responsive LMWGs in that an electron is either lost or gained causing a change in the electronic state. However, the reaction is accomplished through irradiation as opposed to applying an electric field. Due to this similarity in the reaction mechanism, some redox-responsive gelators can also be used as photoresponsive gelators. LMWGs capable of this typically have chemical structures that are highly π -conjugated such as NDIs or PBIs and are far less explored compared to the photoresponsive gelators already discussed.

The addition of amino acid or dipeptide groups onto the imide positions of these LMWGs has been reported to increase their solubility in water.^{85, 86} Hydrogelation was accomplished using an NDI functionalised with a glycine-phenylalanine dipeptide (**NDI-GF**) and this hydrogel could be irradiated using UV light in order to form radical anion.⁷⁷ The bulk rheology showed that the hydrogel was stronger when the radical anion was formed and the strength decreased when the radical anion was oxidised back to the natural state. It is believed this could be due to the introduction of charge into the self-assembled structures and radical- π interactions.⁸⁷ It was reported that the choice of functional group at the imide had a large impact on the gelation properties of these NDIs. Gelation could not be accomplished when functionalised with *L*-phenylalanine amino acids (**NDI-F**) even though it contained a similar bulky aromatic amino acid chemical structure.⁸⁸

Several PBIs with various amino acid functional groups have been reported to form hydrogels using a pH trigger regardless of the difference in chemical structure of the amino acid side chain.^{14, 89, 90} This is possibly due to the increase in the π -surface for

PBIs compared to NDIs, and also makes them more reliable photogenerator gelators. Similar to the NDI discussed above, it has been reported for a *L*-valine-functionalised PBI hydrogel (**PBI-V**) that the formation of radical anion upon irradiation with UV light resulted in an alteration of the stacking upon the change in charge and radical- π stacking. This phenomenon led to improved rheological properties and these changes in the rheological properties were reversible upon oxidation of the radical anion.⁷⁹ The different amino acids on the PBIs did have an impact on the radical anion formation in solution at pH 8 due to the impact of the chemical structure on their self-assembled structures.⁹¹ The use of pH in solution to tailor the self-assembled structures of these PBIs to improve the radical formation behaviour has been investigated, albeit for photocatalyst applications.⁹²⁻¹²

1.3 Perylene bisimides as LMWGs

PBIs are organic materials which were first discovered in 1913 and initially used as red dyes and pigments.⁹³ Their photostability, high quantum yields, and *n*-type semiconducting properties have made them ideal candidates for organic optoelectronic applications.⁹⁴ For PBI systems, the highest occupied molecular orbital (HOMO) is determined by the π bonding orbitals and the lowest unoccupied molecular orbital (LUMO) is determined by the π antibonding orbitals which are localised on the PBI core. The semiconductor bandgap for these materials is therefore determined by the HOMO/LUMO energy gap. Upon irradiation with photons possessing energy greater than or equal to the band gap, electrons are promoted to the conduction band, leading to the formation of excitons. The mechanism for the formation radicals under photoexcitation is described below in Figure 1.6.

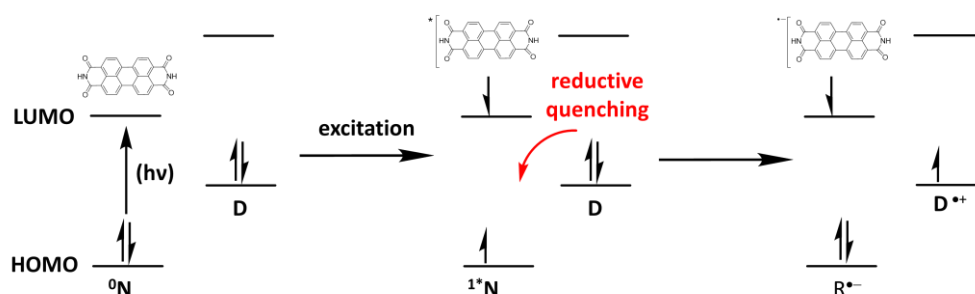


Figure 1.6. Energy level diagrams for the formation of radical anion on PBI in the presence of an electron donor through photoexcitation. Adapted from the following publications.⁹⁵⁻⁹⁷

The PBI is initially irradiated with a light source of a certain energy ($h\nu$) this leads to the transformation from the ground state (0N) to an excited singlet state (1N). Typically, the 1N quickly relaxes back to the 0N , however, in the presence of an electron donor (D) the 1N can undergo reductive quenching to form the radical anion species ($R^{\bullet-}$). The charge is further stabilised by self-doping in the chemical structure or the Coulombic repulsion effects of the solvent choice. For systems in water, the water molecules will help stabilise the charge based on pH as well as act as an electron donor.

Their large aromatic core allows for them to self-assemble into aggregates through π - π stacking. These aggregates can self-assemble further into nano- and micro-structures under the correct conditions. The π - π stacking of PBIs is typically described as either *J*-types or *H*-type, where *H*-type aggregates are described as face-to-face stacked and *J*-type aggregates are slip-stacked structure, Figure 1.7. *H*-types get their name from “hypochromic” as this aggregation results in a hypochromic (blue) shift of the absorption spectrum compared to the monomeric solution due to a strong excitonic coupling between the closely packed molecules. *J*-type aggregation results in a bathochromic (red) shift of the absorbance bands.

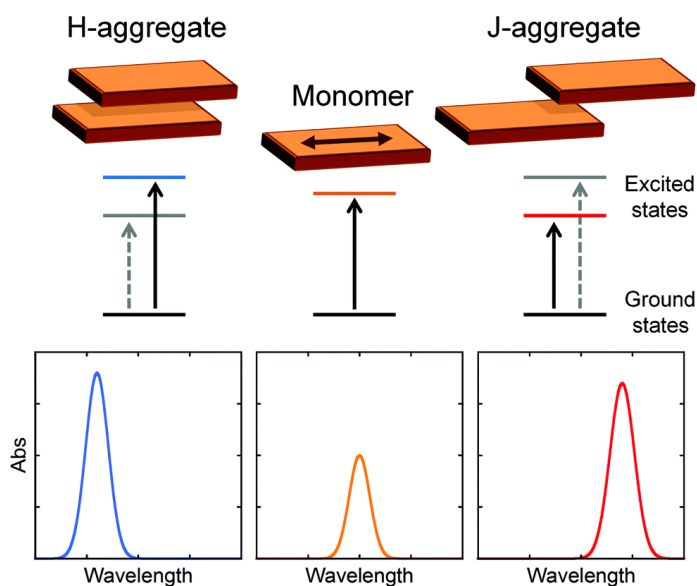


Figure 1.7. Schematic illustrating the stacking of PBI monomers (centre) to produce *H*-type (left) and *J*-type aggregates (right), and below the corresponding UV-Vis

*absorption spectra showing the blue and red shifts in spectra with respect to the monomer. Taken from following publication.*⁹⁸

Supramolecular studies of PBIs have mostly been restricted to investigations in organic solvents due to their poor solubility in water.^{96, 99, 100} More recently there have been reports of self-assembled structures of PBIs which can be solubilised in water.^{101, 102} However, understanding the self-assembled nano- and micro-structures of these PBIs in water can be challenging due to poor understanding of how water can influence the aggregates' structure and stability.¹⁰¹

It has been reported that the morphology of these nano- and micro-structures has a major impact upon their performance in organic optoelectronics.¹⁰² This means there is a need to investigate the morphology of the nano- and micro-structures for water-soluble PBIs further as water is an environmentally friendly and abundant solvent. A popular method for tailoring the self-assembled structures and their photoredox properties is through the modification of the chemical structure of the PBI.^{96, 103, 104} The self-assembled structures and their photo-redox properties can also be tuned through external chemical stimuli.^{105, 106} Both methods offer advantages and disadvantages. Changes in the chemical structure will have a greater influence on these properties. However, tuning these properties using an external chemical stimulus can be less time-consuming.

1.3.1 Modification of the chemical structure of PBIs

As mentioned, LMWGs have the advantage that their chemical structures can be modified through simple synthetic methods compared to polymer competitors. This is true for PBIs as well, there are three main positions on PBIs that can be chemically modified to change their properties: the bay and ortho positions, which are on the aromatic core, and the imide positions at either end of the core (highlighted below in Figure 1.6).

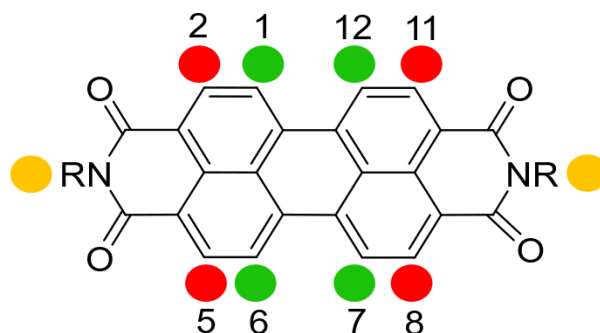


Figure 1.8. Chemical structure of a PBI with the imide (yellow), bay (green), and ortho (red) positions highlighted. Adapted from following publications.^{85, 103}

Changing the chemical structure at the various positions of the PBI will impact their properties in different ways. The choice of functional group for the imide position will greatly impact the solubility and therefore the self-assembled molecular packing and nanostructures.^{96, 101} However, different imide functional groups have a negligible influence on the redox potentials and absorption properties compared to core substitution.^{95, 103, 104, 107} Substitution at the bay position with electron-donating or electron-withdrawing substituents is an effective way of tailoring the redox potentials and absorption properties although it should be noted that bay substituents lead to a distortion of the core and affect π - π stacking.^{108, 109} The redox potentials and absorption properties of the PBI can also be changed by substituting at the ortho position.^{110, 111} Unlike substituting at the bay position, this does not lead to a twisting of the planar field of the core and π - π stacking is not affected.^{112, 113} However, it does typically require harsher reaction conditions and a precious metal catalyst.¹¹³⁻¹¹⁵ This thesis focuses on changing the chemical structure at the imide position or the bay position due to their easier synthetic accessibility and ability to impact molecular packing and nanostructures.

1.3.2 Modification of the bay position of PBIs

There are numerous ways of performing bay substitution and it is possible to have mono-, di-, tri-, and tetra-substituted materials. Many of these synthetic procedures involve an initial substitution with halogens, particularly bromine.¹⁰⁴ The bromination of PBI is usually done in concentrated H_2SO_4 with heating. Other functional groups can be substituted for the bromine through subsequent nucleophilic substitution or

transition metal-catalysed cross-coupling reactions.¹¹⁶⁻¹¹⁹ The other functional groups can be chosen based on desired optical and redox properties.^{103, 120-122}

The harsh conditions required for bay substitution have pushed researchers to seek milder ways to substitute the core. Early work by Rajasingh *et al.* substituted bromine onto a PBI with a bulky side group on the imide position by adding the PBI to a solution of Br₂ in chloroform and letting it stir at room temperature for four days. After purification by column chromatography they obtained the 1,6- and 1,7-dibrominated PBI with a yield of 89%. Then they used this product as a starting material and exchanged the bromines for piperidinyl groups.¹²¹ This method has the advantage that it does not require strong acids or high temperatures and can be used to substitute Br onto PBIs that are already substituted at the imide position. However, due to the large excess of bromine required for this synthesis, others have proposed nitration of PBIs as an alternative to bromination.¹⁰³ It is believed to be the better option as the electron-withdrawing inductive and mesomeric effects of the nitro group sufficiently deactivate the PBI core towards the second electrophilic substitution. Tsai *et al.* were able to substitute nitro groups at the 1,6- or 1,7-positions of a cyclohexylamine-functionalised PBI using cerium(IV) ammonium nitrate (CAN) as a catalyst and HNO₃ as a solvent under ambient conditions for 48 hours with an 80% yield.¹²³ The regioisomeric mixture was separated using high-performance liquid chromatography (HPLC). The nitro groups could be reduced to amino groups using tin(II) chloride catalysis in refluxing tetrahydrofuran (THF) for six hours with a yield of 82% each. In both cases the researchers were faced with the challenge of purifying a regioisomeric mixture.

Purification of bay-substituted PBIs is difficult. Usually, the initial reaction can result in a mixture of di-, tri-, and tetra-substituted PBIs. Chromatography can be used to separate the mixture of di-, tri-, and tetra-substituted PBIs but this can be time consuming and reduce product yield. The separation of the 1,7 (major) and 1,6 (minor) di-substituted PBI regioisomers is not very effective using column chromatography due to their similar sizes and polarities. Purification of the 1,7- and 1,6-regioisomers by repetitive recrystallization has been reported by Würthner *et al.*¹²⁴ Recrystallization is a more attractive purification method as it is simpler than chromatography. The major challenge of recrystallization is the identification of a

suitable solvent to use with a new product. Easier synthesis and purification methods are an important consideration for LMWGs. Since studies on gelators often require solution with concentrations of 0.5 mg/mL - 15 mg/mL, the materials need to be synthesised on a multigram scale. If these studies are then to be used in commercial applications, being able to synthesise materials at a commercial scale with high yields becomes increasingly important.

1.3.3. Modification of the imide position of PBIs

Substitution of PBIs at the imide position is one of the most common methods as it is the easiest and typically can be done using a 'one-pot' procedure. The starting material 3,4:9,10-perylenetetracarboxylic acid dianhydride (PTCDA) has poor solubility in numerous solvents but a change from the anhydride to an imide dramatically increases solubility. The anhydride can be changed to an imide directly through an imidisation reaction or through a stepwise process in which the anhydride is converted to a perylene tetracarboxylic acid tetraester (PTE), which is then further converted to the desired diimide. The imidisation reaction is used extensively as it is typically a one-pot synthesis and has high yields.^{125, 126} A more elaborate pathway involves PTEs, which have better solubility and are more reactive in electrophilic aromatic substitution which can be advantageous if the desired end product is substituted at the bay position.¹²⁷⁻¹²⁹

Typically, due to their large aromatic core, PBIs tend to have poor solubility in water.^{101, 130} Through careful design, ionic, non-ionic, and polar groups can be added to the imide position of PBIs to improve their solubility in water. Ionisable groups such as amines,^{131, 132} carboxylic acids,^{90, 133-136} and phosphonic acids^{97, 137} have been added to improve the solubility of PBIs in water, (Figure 1.7). By chemically modifying the imide position with these ionisable groups, the PBIs may become pH sensitive. The resulting morphology of PBI nanomaterials can then be tuned by changing the pH. PBIs with ionisable groups such as amines at the imide position may also be used in self-doping materials.⁹⁵

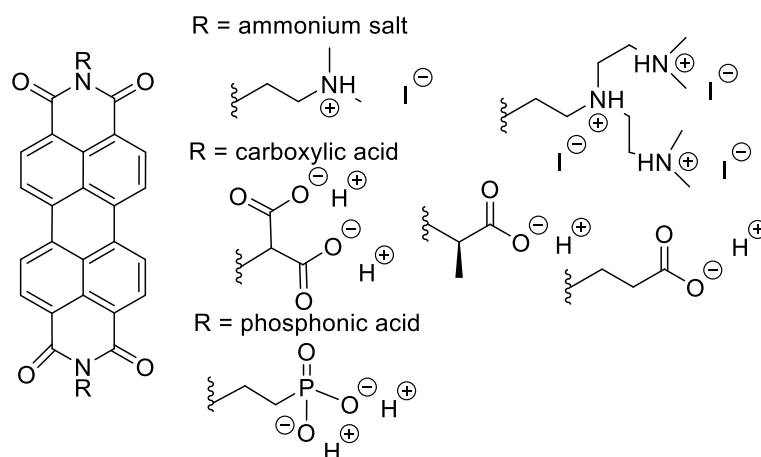


Figure 1.9. Chemical structures of different PBIs with ionisable groups at the imide position.¹⁰¹

1.4 Self-assembled structures of PBIs impacted by external chemical stimuli

It is known that self-assembled nanostructures can have a great impact on the performance of PBIs for optoelectronics.^{39, 91, 138} Generally, the choice of functional groups and core substitution will dictate to which chemical stimuli the PBI will respond. Linking the LMWG's chemical structure to get the desired gel properties is critical. However, understanding how changes in the chemical structure and application of external stimuli can be used to tailor the self-assembled structures of PBI assemblies is still a challenge. We have already discussed how external physical and chemical stimuli can be used to change a hydrogel network post gelation for various LMWGs. This section focuses on the use of chemical stimuli to improve the pre-gel assemblies in solution for PBIs specifically. The use of chemical stimuli to tailor PBI self-assembled nanostructures from spherical micelles to fibres or tubes is also a great method as it is a much simpler method, requiring no synthetic skill and can be much less time consuming. Some examples of chemical stimuli that can be used to change the self-assembled nanostructures of PBIs include pH change,^{12, 133} addition of enzymes,^{139, 140} solvent,^{141 142, 143} ionic additives,^{105, 106, 144} or metals.^{105, 106}

1.4.1 Self-assembled structures impacted by metals

Chemical structure determines which metals can influence self-assembled structures and how they are incorporated into them.¹⁴⁵⁻¹⁴⁷ Chelating functional groups can be added at the imide or bay positions which can coordinate to transition metals.^{148, 149}

Ligand coordination to metal ions can easily surpass the inherent strength of π - π interactions in PBIs.⁹⁶ The choice of metal used to coordinate to the chelating group is derived from established organometallic principles. Metal-ligand interactions have been applied to produce well-defined PBI-based metallosupramolecular systems. These systems include metallosupramolecular polymers, macrocycles, polyhedrons, and co-assemblies.⁹⁶ Several reported polymer examples involve the addition of a chelating terpyridine group to a PBI backbone, which is able to coordinate to transition metals such as zinc or iron.^{150, 151} Similarly to the polymers, macrocycles involve the 2D archetypes based on chelating groups but self-assembled into more organized structures. This aim is accomplished by the thermodynamically controlled self-assembly between linear ditopic bridging functional groups and *cis*-coordinating transition metal centers.^{152, 153} Polyhedrons are 3D self-assembled structures with porous cavities which offer promise in applications in catalysis, sensing, or transport processes.¹⁵⁴

Golubkov *et al.* reported a PBI with terpyridine substituted on the core (**PBI-PEG-terpy**) which could coordinate to soft transition metals in a water/THF mixture to form various nanostructures, as illustrated in Figure 1.8.¹⁵⁵ In solution this PBI formed long ribbon-like structures according to cryo-TEM. Upon coordination to Pd^{2+} the PBI formed vesicular aggregates and long tubular fibre structures. Alternatively, when coordinated to Ag^+ the PBI preferred 2D aggregates and nanosheets.

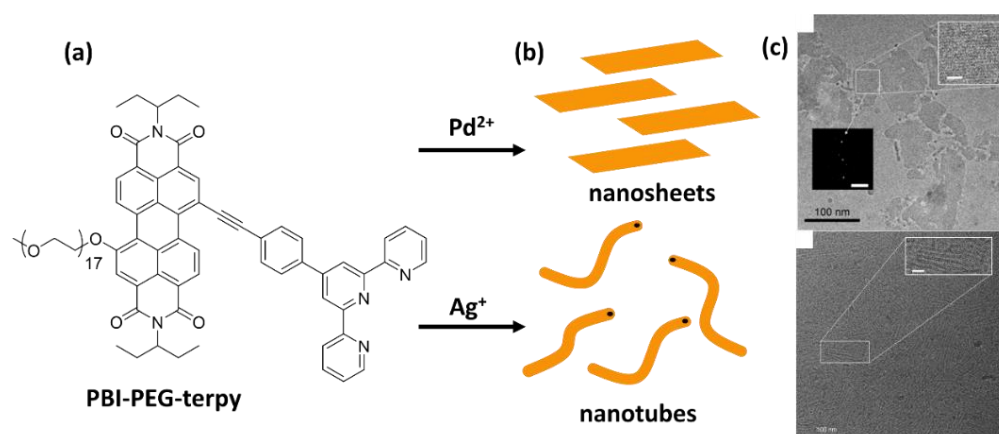


Figure 1.10. (a) Chemical structure of **PBI-PEG-terpy**, (b) cartoon illustration of different nanostructures formed upon coordination with soft transition metals, and (c)

*Cryo-TEM images of solutions of **PBI-PEG-terpy** with different metals in water:THF (9:1 v/v). Adapted from original publication.¹⁵⁵*

UV-vis absorption spectroscopy showed that after binding to either metal there is a broadening of the strong S_0-S_1 transitions between 500 nm and 650 nm. There is also a change in the S_0-S_1 ratios for the **PBI-PEG-terpy** after coordinating to either metal indicating a change in the molecular packing. For **PBI-PEG-terpy** alone, the S_0-S_1 ratio is close to one. When coordinated to Pd^{2+} , the 0-1 vibronic transition at 525 nm is larger compared to the 0-0 vibronic transition at 600 nm. The opposite trend in the S_0-S_1 ratios is observed for **PBI-PEG-terpy** coordinated to Ag^+ , thus showing the variability in molecular packing with the different metals present.

Not only can the addition of different metals be used to tailor the self-assembly of 2D to 3D structures, but it can also allow for a change in the redox properties of the materials.^{148, 156} On top of the redox properties of the PBI, the addition of a redox-active metal will increase the redox-responsive properties. These properties offer the potential to modify the self-assembled structures through applying an electric field, which has been explored for other gelator complexes.^{157, 158}

1.4.2 Self-assembled structures impacted by ionic additives

By including ionic groups in the design of PBI molecules, the aggregates can become slightly charged. The charge can be stabilised using different anions and cations.^{105, 106, 159} Positively charged ammonium salts have been incorporated into either the imide or bay positions of the PBI and are stabilised using organic anions. The use of anions to change the self-assembled nanostructures of LMWGs has been reported by others.^{14, 32}

Marullo *et al.* studied the effect of anion on the self-assembly of PBIs with diimidazolium salts at the imide position (**PBI-DAZ**) by comparing tetrafluoroborate (BF_4^-) and bistriflimide (NTf_2^-).¹⁶⁰ The SEM images of **PBI-DAZ** with BF_4^- showed that elongated structures with a length of approximately 100 μm and a diameter of approximately 20 μm had formed. In contrast, the SEM images of **PBI-DAZ** with NTf_2^- showed they had formed smaller nanostructures with more irregular morphologies with an average size of 20 μm . The sizes determined by TEM imaging yield a trend in agreement with that observed in SEM images. The workers believed that the distinct

morphologies observed could arise from the different charge densities of the two anions. This study did not extend to hydrogel materials and how the anion could be used to tailor their gel network or bulk mechanical properties.

For ionic groups the choice of metal cation is often overlooked as they have less of an impact compared to the choice of organic anion groups.^{95, 144, 161} PBIs functionalised with negatively charged groups such as carboxylic or phosphonic acid groups are stabilised through a cation and the impact of the cation has only been explored on a few occasions.^{105, 106, 162} The impact of cation choice on the bulk hydrogel properties and self-assembled nanostructures for PBIs has not been reported. However, others have shown for different gelators that these cations do have an impact on the self-assembled fibre structures in solution and as hydrogels.³⁴

1.4.3 Self-assembled structures impacted by solvent

Initially, the impact of solvent choice on PBI aggregates or nanostructures in solution was investigated using various organic solvents as PBIs had better solubility in these solvents.^{95, 163-165} Now there is a push to make the processing of materials like PBIs more environmentally friendly by including functional groups in the chemical structure to improve solubility in water.¹⁶⁶ A way to change the aggregation and nanostructures in water is the addition of an anti-solvent.^{97, 167} Typically, the anti-solvent is another polar solvent such as methanol, ethanol, or acetone that is miscible with water. Roy *et al.* reported the synthesis of a PBI disodium salt with benzenesulfonic acid (**PBI-SA**) which is soluble in water due to the sulfonate groups (Figure 1.9). The **PBI-SA** also has reasonable solubility in polar solvents like methanol, ethanol, *N,N*-dimethylformamide (DMF), and dimethyl sulfoxide (DMSO). However, they reported that **PBI-SA** had very limited solubility in other polar solvents like tetrahydrofuran (THF) or acetonitrile. **PBI-SA** underwent a transformation of nanostructures when varying amounts of ethanol were introduced to the solution.¹⁶⁸

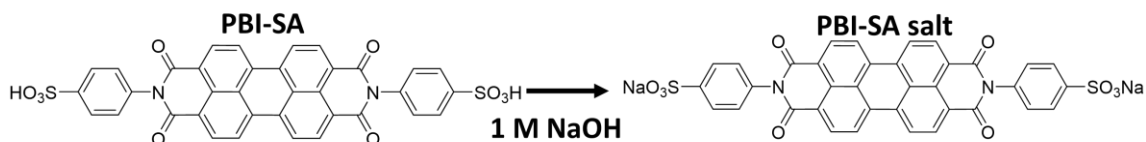


Figure 1.11. Chemical structure and final synthesis step for **PBI-SA** disodium salt. Adapted from the original publication.¹⁶⁸

The workers used UV-vis absorption spectroscopy to characterise changes in packing as the percentage of ethanol in water increased. They saw a decrease in the absorbance for the peaks at 473 nm and 501 nm accredited to the 0-2 and 0-1 vibrational transitions as the percentage of ethanol increased. However, they observed an increase and slight shift in the absorbance at 546 nm for the 0-0 vibronic transition. Fluorescence spectroscopy showed that as the percentage of ethanol increased the fluorescence intensity increased. These trends were observed for the dried films of **PBI-SA** in water and in a 40% ethanol-water mixture. The SEM images of the films showed that **PBI-SA** in water had formed microrods of varying lengths while **PBI-SA** in the ethanol mixture had formed uniform nanospheres. Dynamic light scattering (DLS) measurements agreed with the difference in uniformity of the size of micro- and nano-structures for the different solvent conditions. The current-voltage curves of these films showed that the microrods had a higher current compared to the nanosphere films. The higher currents for microrods were attributed to the long range of π -stacking between the **PBI-SA** which provided a more efficient pathway for electron transfer.¹⁶⁹ This work highlights the role solvents can play in the self-assembly mechanism of PBIs and their morphological tunability along with the semiconducting properties in solvent-tuneable aggregates.

1.4.4 Self-assembled structures impacted by pH

Adding ionisable groups to the PBI chemical structure allows for the self-assembled structures to be tuned with the pH as long as protonation of the PBI decreases its solubility in water. This method is preferable to the others as it allows for adjustment of the rate of trigger action: the addition of HCl/NaOH will change the pH quickly, while the addition of glucono- δ -lactone (GdL) will lower the pH at a much slower rate.²⁸ The difference in rate of the pH change is critical and has a major impact on the uniformity of the nanostructures.

The PBIs have different solubilities over a range of pHs depending on the structures of their ionisable groups as the ionisable groups have different acid strengths. These different acid strengths are described by apparent pK_a values, of which there are

usually as many as there are individual ionisable groups. There have been several reports of PBI systems functionalised with amino acids at the imide position with two apparent pK_a values. These are apparent pK_a values as they are describing the acid strength for the aggregates and not the single molecule.^{14, 89-91, 170} Such molecules are soluble in water at high pH when the terminal carboxylic groups are deprotonated, and form hydrogels upon lowering the pH due to the gradual protonation of those groups. When the pH is lowered there are typically transitional aggregate structures around the apparent pK_a values.¹⁷¹ The self-assembly and resulting morphology in the PBI aggregates with pH-sensitive groups is illustrated below in Figure 1.10.

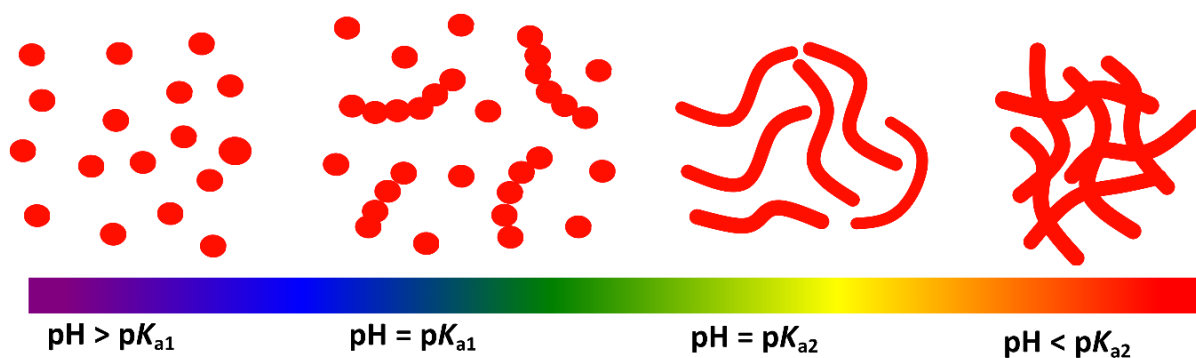


Figure 1.12. Cartoon depicting the self-assembly of pH-sensitive PBI molecules into aggregates and nanostructures as the pH is lowered below the apparent pK_{a1} and pK_{a2} values. Adapted from original publication.⁷³

There are a number of reports where ionisable groups are added to the PBIs to give them pH-sensitive properties.^{14, 133, 134} However, their photogenerator behaviour at different pHs has not been investigated in great detail. *Draper et al.* showed it was possible to control the packing of a single PBI functionalised with *L*-DOPA (**PBI-DOPA**) by changing the pH of the solution which impacted gelation and photoconductivity.⁸⁹ When the initial pH of the solution was 6.7, the PBI could not form a hydrogel when the pH was decreased further with a pH trigger (**A1**). However, when the initial pH of the solution was 8.2, the PBI formed a hydrogel when the pH was lowered using the same trigger (**A2**), Figure 1.11.

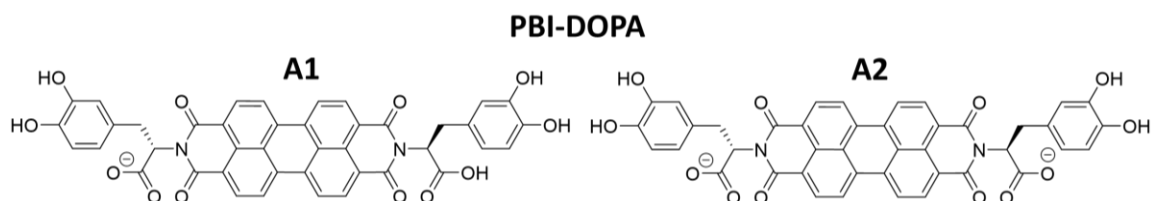


Figure 1.13. Chemical structure of **PBI-DOPA** under different conditions. Adapted from original publication.⁸⁹

The UV-vis absorption and fluorescence spectroscopy of **PBI-DOPA** under the different conditions revealed a difference in the molecular packing. The UV-vis absorption spectrum for **A1** had an additional low-intensity peak at 620 nm which has been assigned to the *J*-type aggregate. However, the smaller fluorescence intensity for **A1** suggest that *H*-type aggregates are formed. Improving exciton charge carrier mobility is expected to increase photoconductivity and can be accomplished through changing the aggregation choice. Density functional theory (DFT) calculations were carried out to link the aggregates to the molecular packing differences. It was revealed that aggregates with larger twist angles explained the presence of the *J*-type red shifted shoulder seen in the UV-vis absorption spectra.¹⁷²⁻¹⁷⁴ The current-voltage curve showed that **A1** films were better photogenerators compared to the **A2** films of **PBI-DOPA**, thus illustrating how it is possible to change macroscopic photoconductive properties through adjusting the molecular-level packing using pH change.

1.5 Applications of PBIs

The ability to tune self-assembled PBI nanostructures is important as it can have a large impact on their optoelectronic properties, as shown in the examples above.^{142, 175} There is an expected increase in the photoconductivity of the PBIs when the exciton and charge carrier mobility is improved. Controlling the assembled structures formed is an excellent strategy for improving these parameters. Throughout this introduction it has been highlighted how either chemical structure design or use of external chemical stimuli can be used to alter the assembly of nanostructures. This final section will dive into how these two methods have been used in optoelectronic applications to improve performance, particularly of photoconductive/photovoltaic devices.

1.5.1 Optoelectronics performance of PBIs tuned by chemical structure changes

There are numerous examples where researchers modified the PBI chemical structures to improve performance as photovoltaic devices.^{11, 94, 176} This interest is due to the large impact that changing the chemical structure can have as regards solubility, and optical and electronic properties of the molecule. However, the π - π stacking of the aggregates formed in solution is disrupted due to twisting of the core when the core is changed.¹⁷⁷ The π - π stacking of the aggregates enables exciton and charge transport through the structure due to the overlap of the HOMO and LUMO orbital wavefunctions, which is important for performance of photovoltaic devices. The π - π stacking also allows the PBIs to self-assemble into organised nanostructures. This phenomenon makes it important to find a balance between improving solubility, and optical and electronic properties without major disruption to the π - π stacking.

Sun *et al.* demonstrated that subtle changes in branched alkyl chains functionalised at the imide position led to significant changes in the solubility, thin-film self-assembly, and optical properties.¹⁷⁸ The PBIs were functionalised with 1-ethylpropyl (**PBI-EP**), 1-propylbutyl (**PBI-PB**), 2-ethylhexyl (**PBI-EH**), and 1-heptyloctyl (**PBI-HO**) structures as shown in Figure 1.12. **PBI-EH** had the lowest solubility in chloroform and chlorobenzene compared to the other PBIs.

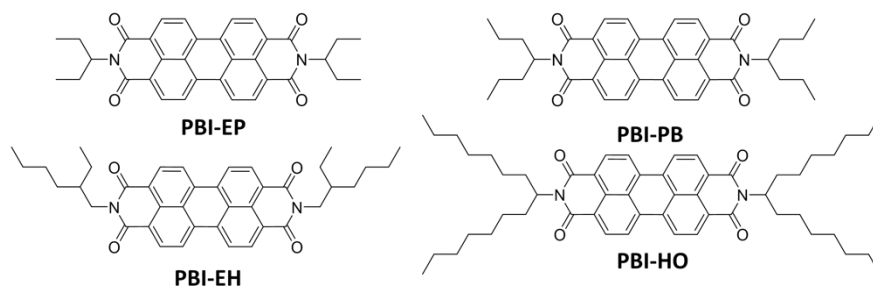


Figure 1.14. Chemical structures of different PBIs used in active layer of bulk heterojunction (BHJ) photovoltaic devices. Adapted from original publication.¹⁷⁸

UV-vis absorption spectroscopy of the thin films made from filtered solutions at 10 mg/mL in chloroform showed that **PBI-EH** had a largest absorbance at the 0-2 vibronic transition at 470 nm. The branched PBIs were blended with a small molecule donor (F-DTS) and spin-coated to make the active layer of the bulk heterojunction

(BHJ) photovoltaic devices. **PBI-EH** and **PBI-HO** devices showed poor performance over 18 devices which the authors attribute to the irregular film morphology making charge transport less uniform. **PBI-PB** showed the most consistent performance, but **PBI-EP** showed the highest power conversion efficiency (PCE) of 3.2%. Both **PBI-PB** and **PBI-EP** also showed phase separation compared to the longer alkyl chain-functionalised PBIs.

Nazari *et al.* reported a direct comparison of optoelectronic properties and photovoltaic device performance for 4 different PBIs with a larger variation in chemical structures, Figure 1.13.¹⁷⁹ The impacts of *N*-annulation at the bay position of the PBI and dimerisation of the PBIs were evaluated. This work looks to make a direct comparison between increase chemical structure size to photovoltaic device performance to link aggregation to performance, which had not been previously looked at. The bay substitution of the monomer is expected to change the π - π stacking and the electronic and optical properties. The dimerization will have an even greater impact on the π - π stacking and the aggregates formed. This study helps provide design parameters for chemical structure of the PBIs for future work in the photovoltaic field. Films of the 4 PBIs were spin-coated from 10 mg/mL solutions in chlorobenzene onto cleaned glass substrates under identical conditions.

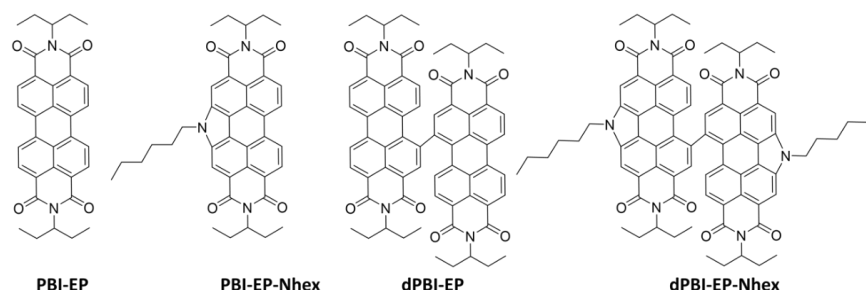


Figure 1.15. Chemical structures of different PBIs directly compared in the study. Adapted from original publication.¹⁷⁹

The thin film morphology of the 4 PBIs was studied using polarized optical microscopy (POM) and atomic force microscopy (AFM). The non-annulated PBI monomer (**PBI-EP**) formed highly unorganised aggregated nanostructures with a width of up to 1000 nm. The *N*-annulated PBI (**PBI-EP-Nhex**) formed smaller, more fibril-like structures with a width ranging from 300 nm to 500 nm. The dimerised PBIs

(**dPBI-EP** and **dPBI-EP-Nhex**) showed a tendency to form smoother and well-organised films. Photovoltaic device performance can be affected by process conditions and therefore identical conditions were implemented in this study to only focus on chemical structure impact. The addition of the *N*-annulated group for **PBI-EP-Nhex** and **dPBI-EP-Nhex** at the bay position decreased the electron affinity of the PBI which led to an increase in the open circuit voltages by 200 mV. Furthermore, **dPBI-EP** and **dPBI-EP-Nhex** had slightly better performance compared to their monomer counterparts which was attributed to them being more uniform films. **dPBI-EP-Nhex** showed the best PCE of 5.5%, demonstrating the importance of balance between the π - π stacking and changing the redox and optical properties.

The above examples only look at changes in chemical structure of PBIs which are soluble in organic solvents. Similar investigations of water-soluble PBIs are not often reported.^{138, 180} Aggregation of PBIs with different chemical structures in water for photovoltaic devices needs further investigation as water is a non-toxic solvent and there are additional intermolecular interactions such as hydrogen bonding at play.

1.5.2 Optoelectronics performance of PBIs tuned by external chemical stimuli

Designing PBIs with functional groups that allow for the tuning of the self-assembled aggregates and nanostructures through chemical stimuli is more advantageous compared to chemical structure changes as there is the potential for improved performance through environmental factors. Such factors are easier to modify than a chemical synthesis. Here we will discuss how chemical stimuli are used to tailor the self-assembly of PBIs to improve their performance in photovoltaic/photoconductive devices. There will be a focus on chemical structures with ionic groups as these can be impacted by ionic additives, pH change, and solvent choice. Additionally, these ionic PBIs have improved solubility in water, which is the preferred solvent for industrial-scale optoelectronics manufacture.

PBIs functionalised with amine/ammonium-containing groups at the imide position have been shown to be useful self-*n*-doping-type materials. In this case the amine or ammonium groups act as an electron source. Self-doping is a promising method of tuning carrier concentrations because it mitigates dopant phase segregation and aggregation. Powell *et al.* studied a series of amine-functionalised PBIs to investigate

the effects of anion selection, tether length, and steric encumbrance on doping, stability, morphology, and carrier mobility.¹⁴⁴ They found counterion choice to be the most important parameter which could increase doping, alter solubility for improved processing, influence carrier mobility, and even direct morphological orientation in structurally diverse systems. However, with all of this known about anion impact on the performance of PBIs, the use of different anions to improve the photovoltaic performance of PBI systems has only been reported for a polymer.¹⁸¹ Cation choice has not been explored before in terms of impact on photovoltaic device performance. It is expected to have less of an impact on the self-assembled structures compared to anions but is still an important parameter to explore.

Tailoring the photovoltaic properties of PBIs through pH change to improve photovoltaic performance is not often investigated. However, this is important since there is a push to develop water soluble PBIs as water is nontoxic and abundant. Understand the impact of pH on the self-assembly of these new water soluble PBIs can help provide design parameters (optimal pH for performance and aggregation) which allow researchers to make smarter design choices in the future. Harding *et al.* reported an amine-substituted PBI (**PBI-EP-NH**) which could be deprotonated with the addition of NaOH to allow the material to be more soluble in alcohol or water, Figure 1.14.¹⁸⁰ As the amount of NaOH was varied, there was a colour change from orange/red to purple. As the proportion of NaOH in a propanol solution of **PBI-EP-NH** was increased from 0.5 to 10 equivalents, there was a gradual decrease in the dominant absorption peaks at 459, 490, and 525 nm in the UV-vis absorption spectra in addition to the gradual increase in absorption of a peak at 601 nm which is attributed to the formation of radical anion. When spin-coated, **PBI-EP-NH** was no longer deprotonated and dried back to the original red colour. Proof-of-concept photovoltaic devices fabricated from **PBI-EP-NH** and 1 equivalent of NaOH showed that this system could be used as an electron transport layer. With the push to make use of more environmentally friendly solvents for the processing of photovoltaics, pH-tailored nano- and micro-structures are another tool in the designer's toolbox.



Figure 1.16. (a) Chemical structure of **PBI-EP-NH**, with a photograph of its resulting red slurry at 10 mg/mL in 1-propanol. (b) Chemical structure of **PBI-EP-N-Na⁺**, with a photograph of the resulting purple solution after being treated with 1 equivalent NaOH. (c) Spin-coating the deprotonated **PBI-EP-NH** solution onto a substrate yields a red coloured organic film owing to the spontaneous protonation of the **PBI-EP-NH** anion. Adapted from original publication.¹⁸⁰

1.6 Aims of this work

It has been shown throughout the literature that PBIs are great candidates for photogenerating applications due to their strong absorbances and high quantum yields. Like many LMWGs they also offer the advantage that their chemical structure can be easily changed to tailor their optical and electronic properties unlike their polymer competitors. There are numerous studies about tuning the formation of radical anion properties of PBIs by tuning their aggregation in organic solvents.^{96, 99} These studies investigate how the aggregation and nanostructures can be changed through the addition of metal ions, solvents switches, or chemical structure changes. However, with the push to develop more environmentally friendly processing methods it is important to focus on water-soluble PBIs. The use of water-soluble PBIs is favourable not only because water is a green solvent but it also offers the opportunity to change aggregation or nanostructures through pH change, in addition to the more common chemical structure changes or metal ion additions. The number of water-soluble PBIs is increasing, however, the use of pH change to tailor aggregation for photovoltaic devices has not been investigated greatly. This is a missed opportunity

as pH change is an easy parameter to control and other the potential for reversible self-assembly, a major advantage for LMWGs.

The aim of this study is to investigate how radical formation is impacted in self-assembled nanostructures of pH-responsive PBIs with different chemical structures. To provide better understandings of the to parameters and offer design criteria for future water soluble PBIs. The impact of the counterion in the basic solution used to solubilise the PBIs on the radical formation is also investigated. This study is presented across multiple length scales to get a more complete picture of the different self-assembled structures. Understanding the impact of chemical structure, self-assembly, and gelation on the formation of radical anion will help to improve PBI design for their desired photovoltaic applications.

Chapter 2 focuses on an amino acid-functionalised PBI that had previously been used in the interlayer of a multilayer photovoltaic device. Here we examine the possibility of improving the performance of the PBI in photovoltaic devices by simply changing the solubility and aggregate morphology through variation of the pH of the basic solutions containing different counterions. The impact of the different aggregate morphologies on radical anion formation in solution at various pHs and as hydrogels at low pH is also investigated.

Chapter 3 investigates three amino acid-functionalised PBIs with hydrophobic side chains with slightly different chemical structures. The slight differences in the side chain structure led to differences in the formation of radical anion upon irradiation with UV light. We show how these slight differences lead to differences in the self-assembly at various pHs. The PBIs are used to make hydrogels using a pH trigger. The differences in the bulk rheological properties show the possibility for the tuning of hydrogel mechanical properties based on side chain choice.

Chapter 4 investigates three amino acid-functionalised PBIs with hydrophobic side chains with slightly different chemical structures that have been core-substituted with pyrrolidine groups at the 1,6-bay positions. This core substitution has led to a more dramatic change in both the optical and electronic properties, while still allowing them to be solubilised in aqueous solution. The PBIs were obtained in a high-yielding one-step synthesis with no requirement for chromatographic purification. To the best of

our knowledge this is the first time these materials have been reported. Upon irradiation with UV light the PBIs form radical cation instead of radical anion. Upon the formation of the radical cation there is a change in the self-assembled nanostructures and microstructures. The impact of pH on the self-assembled nanostructures and their radical cation formation properties is also investigated.

1.7 References

1. J. H. Jung, G. John, M. Masuda, K. Yoshida, S. Shinkai and T. Shimizu, *Langmuir*, 2001, **17**, 7229-7232.
2. K. Yoza, N. Amanokura, Y. Ono, T. Akao, H. Shinmori, M. Takeuchi, S. Shinkai and D. N. Reinhoudt, *Chemistry – A European Journal*, 1999, **5**, 2722-2729.
3. O. Gronwald and S. Shinkai, *Chemistry – A European Journal*, 2001, **7**, 4328-4334.
4. F. M. Menger and J. S. Keiper, *Angewandte Chemie International Edition*, 2000, **39**, 1906-1920.
5. F. M. Menger, V. A. Seredyuk, R. P. Apkarian and E. R. Wright, *Journal of the American Chemical Society*, 2002, **124**, 12408-12409.
6. F. M. Menger, H. Zhang, K. L. Caran, V. A. Seredyuk and R. P. Apkarian, *Journal of the American Chemical Society*, 2002, **124**, 1140-1141.
7. A. M. Castilla, M. Wallace, L. L. Mears, E. R. Draper, J. Douth, S. Rogers and D. J. Adams, *Soft Matter*, 2016, **12**, 7848-7854.
8. A. M. Castilla, E. R. Draper, M. C. Nolan, C. Brasnett, A. Seddon, L. L. E. Mears, N. Cowieson and D. J. Adams, *Scientific Reports*, 2017, **7**, 8380.
9. Y. Huang, Z. Qiu, Y. Xu, J. Shi, H. Lin and Y. Zhang, *Organic & Biomolecular Chemistry*, 2011, **9**, 2149-2155.
10. K. J. Skilling, F. Citossi, T. D. Bradshaw, M. Ashford, B. Kellam and M. Marlow, *Soft Matter*, 2014, **10**, 237-256.
11. S. S. Babu, V. K. Praveen and A. Ajayaghosh, *Chemical Reviews*, 2014, **114**, 1973-2129.
12. M. C. Nolan, J. J. Walsh, L. L. E. Mears, E. R. Draper, M. Wallace, M. Barrow, B. Dietrich, S. M. King, A. J. Cowan and D. J. Adams, *Journal of Materials Chemistry A*, 2017, **5**, 7555-7563.
13. A. Z. Cardoso, L. L. E. Mears, B. N. Cattoz, P. C. Griffiths, R. Schweins and D. J. Adams, *Soft Matter*, 2016, **12**, 3612-3621.
14. S. Roy, D. Kumar Maiti, S. Panigrahi, D. Basak and A. Banerjee, *RSC Advances*, 2012, **2**.
15. G. Godeau, J. Bernard, C. Staedel and P. Barthélémy, *Chemical Communications*, 2009, 5127-5129.
16. E. R. Draper and D. J. Adams, *Chem*, 2017, **3**, 390-410.
17. G. Yu, X. Yan, C. Han and F. Huang, *Chemical Society Reviews*, 2013, **42**, 6697-6722.
18. V. J. Nebot and D. K. Smith, *Functional Molecular Gels; Escuder, B.; Miravet, JF, Eds*, 2013, 30-66.
19. P. Rajamalli and E. Prasad, *Organic Letters*, 2011, **13**, 3714-3717.
20. M. C. Mañas-Torres, G. B. Ramírez-Rodríguez, J. I. García-Peiro, B. Parra-Torrejón, J. M. Cuerva, M. T. Lopez-Lopez, L. Álvarez de Cienfuegos and J. M. Delgado-López, *Inorganic Chemistry Frontiers*, 2022, **9**, 743-752.
21. A. M. Fuentes-Caparrós, Z. Canales-Galarza, M. Barrow, B. Dietrich, J. Läger, M. Nemeth, E. R. Draper and D. J. Adams, *Biomacromolecules*, 2021, **22**, 1625-1638.

22. L. L. E. Mears, E. R. Draper, A. M. Castilla, H. Su, Zhuola, B. Dietrich, M. C. Nolan, G. N. Smith, J. Douth, S. Rogers, R. Akhtar, H. Cui and D. J. Adams, *Biomacromolecules*, 2017, **18**, 3531-3540.
23. E. R. Draper, H. Su, C. Brasnett, R. J. Poole, S. Rogers, H. Cui, A. Seddon and D. J. Adams, *Angewandte Chemie*, 2017, **129**, 10603-10606.
24. V. Grande, B. Soberats, S. Herbst, V. Stepanenko and F. Würthner, *Chemical Science*, 2018, **9**, 6904-6911.
25. D. McDowall, D. J. Adams and A. M. Seddon, *Soft Matter*, 2022, **18**, 1577-1590.
26. R. I. Randle, A. M. Fuentes-Caparrós, L. P. Cavalcanti, R. Schweins, D. J. Adams and E. R. Draper, *The Journal of Physical Chemistry C*, 2022, **126**, 13427-13432.
27. T. Xia, W. Liu and L. Yang, *Journal of Biomedical Materials Research Part A*, 2017, **105**, 1799-1812.
28. D. J. Adams, M. F. Butler, W. J. Frith, M. Kirkland, L. Mullen and P. Sanderson, *Soft Matter*, 2009, **5**, 1856-1862.
29. L. Thomson, R. Schweins, E. R. Draper and D. J. Adams, *Macromolecular Rapid Communications*, 2020, **41**, 2000093.
30. L. Chen, G. Pont, K. Morris, G. Lotze, A. Squires, L. C. Serpell and D. J. Adams, *Chemical Communications*, 2011, **47**, 12071-12073.
31. S. Bianco, S. Panja and D. J. Adams, *Gels*, 2022, **8**, 132.
32. S. Roy, N. Javid, J. Sefcik, P. J. Halling and R. V. Ulijn, *Langmuir*, 2012, **28**, 16664-16670.
33. R. Vegners, I. Shestakova, I. Kalvinsh, R. M. Ezzell and P. A. Janmey, *Journal of Peptide Science*, 1995, **1**, 371-378.
34. K. McAulay, P. A. Ucha, H. Wang, A. M. Fuentes-Caparrós, L. Thomson, O. Maklad, N. Khunti, N. Cowieson, M. Wallace, H. Cui, R. J. Poole, A. Seddon and D. J. Adams, *Chemical Communications*, 2020, **56**, 4094-4097.
35. J. Raeburn, A. Zamith Cardoso and D. J. Adams, *Chemical Society Reviews*, 2013, **42**, 5143-5156.
36. J. Wang, K. Liu, R. Xing and X. Yan, *Chemical Society Reviews*, 2016, **45**, 5589-5604.
37. P. A. Korevaar, C. J. Newcomb, E. Meijer and S. I. Stupp, *Journal of the American Chemical Society*, 2014, **136**, 8540-8543.
38. P. W. J. M. Frederix, G. G. Scott, Y. M. Abul-Haija, D. Kalafatovic, C. G. Pappas, N. Javid, N. T. Hunt, R. V. Ulijn and T. Tuttle, *Nature Chemistry*, 2015, **7**, 30-37.
39. J. K. Gupta, D. J. Adams and N. G. Berry, *Chemical Science*, 2016, **7**, 4713-4719.
40. Y. Wang, X. Yu, Y. Li, Y. Zhang, L. Geng, F. Shen and J. Ren, *ACS Applied Materials & Interfaces*, 2019, **11**, 19605-19612.
41. P. Singh, S. Misra, A. Das, S. Roy, P. Datta, G. Bhattacharjee, B. Satpati and J. Nanda, *ACS Applied Bio Materials*, 2019, **2**, 4881-4891.
42. M. Mauro, *Journal of Materials Chemistry B*, 2019, **7**, 4234-4242.
43. S. Panja and D. J. Adams, *Chemical Society Reviews*, 2021, **50**, 5165-5200.
44. E. R. Draper and D. J. Adams, *Chemical Communications*, 2016, **52**, 8196-8206.
45. E. R. Draper and D. J. Adams, *Responsive Materials by the Self-assembly of Low Molecular Weight Gelators*, Royal Society of Chemistry, 2015.
46. S. Awhida, E. R. Draper, T. O. McDonald and D. J. Adams, *Journal of Colloid and Interface Science*, 2015, **455**, 24-31.
47. D. J. Adams, L. M. Mullen, M. Berta, L. Chen and W. J. Frith, *Soft Matter*, 2010, **6**, 1971-1980.
48. S. Ghosh, V. K. Praveen and A. Ajayaghosh, *Annual Review of Materials Research*, 2016, **46**, 235-262.
49. C. Tang, A. M. Smith, R. F. Collins, R. V. Ulijn and A. Saiani, *Langmuir*, 2009, **25**, 9447-9453.
50. L. Ma, H. Kang, R. Liu and Y. Huang, *Langmuir*, 2010, **26**, 18519-18525.
51. S. Panja and D. J. Adams, *Chemical Communications*, 2019, **55**, 47-50.

52. D. J. Cornwell, O. J. Daubney and D. K. Smith, *Journal of the American Chemical Society*, 2015, **137**, 15486-15492.
53. N. Tao, G. Li, M. Liu, W. Gao and H. Wu, *Tetrahedron*, 2017, **73**, 3173-3180.
54. A. Valls, M. Isabel Burguete, L. Kuret, B. Altava and S. V. Luis, *Journal of Molecular Liquids*, 2022, **348**, 118051.
55. W. Gao, Y. Hu, L. Xu, M. Liu, H. Wu and B. He, *Chinese Chemical Letters*, 2018, **29**, 1795-1798.
56. I. Carayon, A. Gaubert, Y. Mousli and B. Philippe, *Biomaterials Science*, 2020, **8**, 5589-5600.
57. C. Wang, D. Zhang and D. Zhu, *Journal of the American Chemical Society*, 2005, **127**, 16372-16373.
58. X. Yang, G. Zhang and D. Zhang, *Journal of Materials Chemistry*, 2012, **22**, 38-50.
59. E. R. Draper, B. Dietrich, C. Brasnett, S. Sproules, T. O. McDonald, A. M. Seddon and D. J. Adams, *Macromolecular Rapid Communications*, 2018, **39**, 1700746.
60. B. Xue, M. Qin, T. Wang, J. Wu, D. Luo, Q. Jiang, Y. Li, Y. Cao and W. Wang, *Advanced Functional Materials*, 2016, **26**, 9053-9062.
61. E. R. Draper, B. Dietrich and D. J. Adams, *Chemical Communications*, 2017, **53**, 1864-1867.
62. X. Sui, X. Feng, M. A. Hempenius and G. J. Vancso, *Journal of Materials Chemistry B*, 2013, **1**, 1658-1672.
63. D. Roy, J. N. Cambre and B. S. Sumerlin, *Progress in Polymer Science*, 2010, **35**, 278-301.
64. S. K. M. Nalluri, N. Shivarova, A. L. Kanibolotsky, M. Zelzer, S. Gupta, P. W. J. M. Frederix, P. J. Skabara, H. Gleskova and R. V. Uljin, *Langmuir*, 2014, **30**, 12429-12437.
65. D. A. Stone, A. S. Tayi, J. E. Goldberger, L. C. Palmer and S. I. Stupp, *Chemical Communications*, 2011, **47**, 5702-5704.
66. S. Khetan and J. A. Burdick, *Soft Matter*, 2011, **7**, 830-838.
67. H. Tian and S. Yang, *Chemical Society Reviews*, 2004, **33**, 85-97.
68. K. Zheng, H. Wang and H.-F. Chow, *Organic & Biomolecular Chemistry*, 2019, **17**, 3285-3291.
69. Q. Chen, Y. Feng, D. Zhang, G. Zhang, Q. Fan, S. Sun and D. Zhu, *Advanced Functional Materials*, 2010, **20**, 36-42.
70. Z. Qiu, H. Yu, J. Li, Y. Wang and Y. Zhang, *Chemical Communications*, 2009, DOI: 10.1039/B822840J, 3342-3344.
71. M. S. de Luna, V. Marturano, M. Manganelli, C. Santillo, V. Ambrogi, G. Filippone and P. Cerruti, *Journal of colloid and interface science*, 2020, **568**, 16-24.
72. Z. Chen, Z. Lv, G. Qing and T. Sun, *Journal of Materials Chemistry B*, 2017, **5**, 3163-3171.
73. E. R. Draper, J. R. Lee, M. Wallace, F. Jäckel, A. J. Cowan and D. J. Adams, *Chemical Science*, 2016, **7**, 6499-6505.
74. E. R. Draper, E. G. Eden, T. O. McDonald and D. J. Adams, *Nature Chemistry*, 2015, **7**, 848-852.
75. S. H. Kim, Y. Sun, J. A. Kaplan, M. W. Grinstaff and J. R. Parquette, *New Journal of Chemistry*, 2015, **39**, 3225-3228.
76. E. R. Draper, T. O. McDonald and D. J. Adams, *Chemical Communications*, 2015, **51**, 12827-12830.
77. L. Gonzalez, C. Liu, B. Dietrich, H. Su, S. Sproules, H. Cui, D. Honecker, D. J. Adams and E. R. Draper, *Communications Chemistry*, 2018, **1**, 77.
78. R. I. Randle, L. Cavalcanti, S. Sproules and E. R. Draper, *Materials Advances*, 2022, **3**, 3326-3331.
79. E. R. Draper, R. Schweins, R. Akhtar, P. Groves, V. Chechik, M. A. Zwijnenburg and D. J. Adams, *Chemistry of Materials*, 2016, **28**, 6336-6341.
80. S. Wang, W. Shen, Y. Feng and H. Tian, *Chem Commun*, 2006, 1497-1499.
81. D. Chang, W. Yan, Y. Yang, Q. Wang and L. Zou, *Dyes and Pigments*, 2016, **134**, 186-189.
82. S. Xiao, T. Yi, F. Li and C. Huang, *Tetrahedron Letters*, 2005, **46**, 9009-9012.
83. H. M. D. Bandara and S. C. Burdette, *Chemical Society Reviews*, 2012, **41**, 1809-1825.
84. C. Dugave and L. Demange, *Chemical Reviews*, 2003, **103**, 2475-2532.

85. Z. Guo, X. Zhang, Y. Wang and Z. Li, *Langmuir*, 2019, **35**, 342-358.
86. A. Weißenstein, V. Grande, C. R. Saha-Möller and F. Würthner, *Organic Chemistry Frontiers*, 2018, **5**, 2641-2651.
87. C. R. Martinez and B. L. Iverson, *Chemical Science*, 2012, **3**, 2191-2201.
88. R. I. Randle, R. E. Ginesi, O. Matsarskaia, R. Schweins and E. R. Draper, *Macromolecular Rapid Communications*, 2022, **44**, 2200709.
89. E. R. Draper, B. J. Greeves, M. Barrow, R. Schweins, M. A. Zwijnenburg and D. J. Adams, *Chem*, 2017, **2**, 716-731.
90. E. R. Draper, J. J. Walsh, T. O. McDonald, M. A. Zwijnenburg, P. J. Cameron, A. J. Cowan and D. J. Adams, *Journal of Materials Chemistry C*, 2014, **2**, 5570-5575.
91. E. R. Draper, L. J. Archibald, M. C. Nolan, R. Schweins, M. A. Zwijnenburg, S. Sproules and D. J. Adams, *Chemistry*, 2018, **24**, 4006-4010.
92. D. McDowall, B. J. Greeves, R. Clowes, K. McAulay, A. M. Fuentes-Caparrós, L. Thomson, N. Khunti, N. Cowieson, M. C. Nolan, M. Wallace, A. I. Cooper, E. R. Draper, A. J. Cowan and D. J. Adams, *Advanced Energy Materials*, 2020, **10**.
93. M. Kardos, *German Patent, DE*, 1913, **276357**.
94. R. K. Gupta and A. A. Sudhakar, *Langmuir*, 2019, **35**, 2455-2479.
95. D. Powell and L. Whittaker-Brooks, *Materials Horizons*, 2022, **9**, 2026-2052.
96. F. Würthner, C. R. Saha-Möller, B. Fimmel, S. Ogi, P. Leowanawat and D. Schmidt, *Chemical Reviews*, 2016, **116**, 962-1052.
97. R. O. Marcon and S. Brochsztain, *Langmuir*, 2007, **23**, 11972-11976.
98. G. Pescitelli, L. Di Bari and N. Berova, *Chemical Society Reviews*, 2014, **43**, 5211-5233.
99. F. Würthner, *Chemical Communications*, 2004, 1564-1579.
100. Z. Chen, A. Lohr, C. R. Saha-Möller and F. Würthner, *Chemical Society Reviews*, 2009, **38**, 564-584.
101. D. Görl, X. Zhang and F. Würthner, *Angewandte Chemie International Edition*, 2012, **51**, 6328-6348.
102. S. Chen, P. Slattum, C. Wang and L. Zang, *Chemical Reviews*, 2015, **115**, 11967-11998.
103. L. Rocard, A. Goujon and P. Hudhomme, *Molecules*, 2020, **25**.
104. A. Nowak-Król and F. Würthner, *Organic Chemistry Frontiers*, 2019, **6**, 1272-1318.
105. C. Backes, F. Hauke and A. Hirsch, *Physica Status Solidi (b)*, 2013, **250**, 2592-2598.
106. C. Backes, T. Schunk, F. Hauke and A. Hirsch, *Journal of Materials Chemistry*, 2011, **21**, 3554-3557.
107. C. Huang, S. Barlow and S. R. Marder, *The Journal of Organic Chemistry*, 2011, **76**, 2386-2407.
108. P. Osswald and F. Würthner, *Journal of the American Chemical Society*, 2007, **129**, 14319-14326.
109. Á. J. Jiménez, M.-J. Lin, C. Burschka, J. Becker, V. Settels, B. Engels and F. Würthner, *Chemical Science*, 2014, **5**, 608-619.
110. G. Battagliarin, Y. Zhao, C. Li and K. Müllen, *Organic Letters*, 2011, **13**, 3399-3401.
111. G. Battagliarin, M. Davies, S. Mackowiak, C. Li and K. Müllen, *ChemPhysChem*, 2012, **13**, 923-926.
112. S. Nakazono, S. Easwaramoorthi, D. Kim, H. Shinokubo and A. Osuka, *Organic letters*, 2009, **11**, 5426-5429.
113. T. Teraoka, S. Hiroto and H. Shinokubo, *Organic letters*, 2011, **13**, 2532-2535.
114. S. Nakazono, Y. Imazaki, H. Yoo, J. Yang, T. Sasamori, N. Tokitoh, T. Cédric, H. Kageyama, D. Kim and H. Shinokubo, *Chemistry—A European Journal*, 2009, **15**, 7530-7533.
115. G. Battagliarin, C. Li, V. Enkelmann and K. Müllen, *Organic letters*, 2011, **13**, 3012-3015.
116. A. Boehm, H. Arms, G. Henning and P. Blaschka, *Ger. Offen. DE*, 1997, **19547209**.
117. A. de Craats, *Journal of Materials Chemistry*, 2001, **11**, 1789-1799.
118. Y. Zhao and M. R. Wasielewski, *Tetrahedron Letters*, 1999, **40**, 7047-7050.

119. M. J. Ahrens, M. J. Fuller and M. R. Wasielewski, *Chemistry of Materials*, 2003, **15**, 2684-2686.
120. G. Rauch and S. Hoger, *Chem Commun (Camb)*, 2014, **50**, 5659-5661.
121. P. Rajasingh, R. Cohen, E. Shirman, L. J. W. Shimon and B. Rybtchinski, *The Journal of Organic Chemistry*, 2007, **72**, 5973-5979.
122. M. Kremer, M. Kersten and S. Höger, *Organic Chemistry Frontiers*, 2018, **5**, 1825-1829.
123. H.-Y. Tsai, C.-W. Chang and K.-Y. Chen, *Tetrahedron Letters*, 2014, **55**, 884-888.
124. F. Würthner, V. Stepanenko, Z. Chen, C. R. Saha-Möllner, N. Kocher and D. Stalke, *The Journal of Organic Chemistry*, 2004, **69**, 7933-7939.
125. C. Xue, M. Chen and S. Jin, *Polymer*, 2008, **49**, 5314-5321.
126. X. Lv, L. Zha, L. Qian, X. Xu, Q. Bi, Z. Xu, D. S. Wright and C. Zhang, *Chemical Engineering Journal*, 2020, **386**, 123939.
127. R. Wang, Z. Shi, C. Zhang, A. Zhang, J. Chen, W. Guo and Z. Sun, *Dyes and Pigments*, 2013, **98**, 450-458.
128. M. Takahashi, K. Asaba, T. T. Lua, T. Inuzuka, N. Uemura, M. Sakamoto, T. Sengoku and H. Yoda, *The Journal of Organic Chemistry*, 2018, **83**, 624-631.
129. S. Sengupta, R. K. Dubey, R. W. M. Hoek, S. P. P. van Eeden, D. D. Gunbaş, F. C. Grozema, E. J. R. Sudhölter and W. F. Jager, *The Journal of Organic Chemistry*, 2014, **79**, 6655-6662.
130. H. Langhals, *Advanced Materials* 1998, **10**, 1022-1024.
131. Z. Xu, K. Guo, J. Yu, H. Sun, J. Tang, J. Shen, K. Müllen, W. Yang and M. Yin, *Small*, 2014, **10**, 4087-4092.
132. Z. Xu, W. Cheng, K. Guo, J. Yu, J. Shen, J. Tang, W. Yang and M. Yin, *ACS Applied Materials & Interfaces*, 2015, **7**, 9784-9791.
133. L. Zhong, F. Xing, W. Shi, L. Yan, L. Xie and S. Zhu, *ACS Applied Materials & Interfaces*, 2013, **5**, 3401-3407.
134. A. Datar, K. Balakrishnan and L. Zang, *Chemical Communications*, 2013, **49**, 6894-6896.
135. P. K. Sukul, P. K. Singh, S. K. Maji and S. Malik, *Journal of Materials Chemistry B*, 2013, **1**, 153-156.
136. S. Roy, D. Kumar Maiti, S. Panigrahi, D. Basak and A. Banerjee, *RSC Advances*, 2012, **2**, 11053-11060.
137. R. O. Marcon, J. G. dos Santos, K. M. Figueiredo and S. Brochsztain, *Langmuir*, 2006, **22**, 1680-1687.
138. J. Cameron, D. J. Adams, P. J. Skabara and E. R. Draper, *Journal of Materials Chemistry C*, 2022, **10**, 3944-3950.
139. J. T. Kern, P. W. Thomas and S. M. Kerwin, *Biochemistry*, 2002, **41**, 11379-11389.
140. Y. Lin, R. Chapman and M. M. Stevens, *Analytical Chemistry*, 2014, **86**, 6410-6417.
141. S. Bai, S. Debnath, N. Javid, P. W. J. M. Frederix, S. Fleming, C. Pappas and R. V. Ulijn, *Langmuir*, 2014, **30**, 7576-7584.
142. Y. Chen, Y. Feng, J. Gao and M. Bouvet, *Journal of Colloid and Interface Science*, 2012, **368**, 387-394.
143. S. Seifert, D. Schmidt and F. Würthner, *Chemical Science*, 2015, **6**, 1663-1667.
144. D. Powell, X. Zhang, C. I. Nwachukwu, E. J. Miller, K. R. Hansen, L. Flannery, J. Ogle, A. Berzansky, J. G. Labram, A. G. Roberts and L. Whittaker-Brooks, *Advanced Materials*, 2022, **34**, 2204656.
145. Y. Che, X. Yang and L. Zang, *Chemical Communications*, 2008, 1413-1415.
146. Y.-B. Ruan, A.-F. Li, J.-S. Zhao, J.-S. Shen and Y.-B. Jiang, *Chemical Communications*, 2010, **46**, 4938-4940.
147. Y. Wang, L. Zhang, G. Zhang, Y. Wu, S. Wu, J. Yu and L. Wang, *Tetrahedron Letters*, 2014, **55**, 3218-3222.
148. M. Schulze, A. Steffen and F. Würthner, *Angewandte Chemie International Edition*, 2015, **54**, 1570-1573.

149. N. Tuccitto, I. Delfanti, V. Torrisi, F. Scandola, C. Chiorboli, V. Stepanenko, F. Würthner and A. Licciardello, *Physical Chemistry Chemical Physics*, 2009, **11**, 4033-4038.
150. R. Dobrawa, M. Lysetska, P. Ballester, M. Grüne and F. Würthner, *Macromolecules*, 2005, **38**, 1315-1325.
151. R. Dobrawa and F. Würthner, *Chemical Communications*, 2002, 1878-1879.
152. M. Fujita, *Chemical Society Reviews*, 1998, **27**, 417-425.
153. R. Chakrabarty, P. S. Mukherjee and P. J. Stang, *Chemical reviews*, 2011, **111**, 6810-6918.
154. J.-M. Lehn and J. Sanders, *Angewandte Chemie-English Edition*, 1995, **34**, 2563.
155. G. Golubkov, H. Weissman, E. Shirman, S. G. Wolf, I. Pinkas and B. Rybtchinski, *Angewandte Chemie International Edition*, 2009, **48**, 926-930.
156. F. Würthner, A. Sautter, D. Schmid and P. J. A. Weber, *Chemistry – A European Journal*, 2001, **7**, 894-902.
157. Q. Zhou, X. Dong, J. Yuan, B. Zhang, S. Lu, Q. Wang, Y. Liao, Y. Yang and H. Wang, *Langmuir*, 2019, **35**, 15344-15351.
158. A. Panja and K. Ghosh, *Materials Chemistry Frontiers*, 2018, **2**, 1866-1875.
159. D. Powell, Z. Rhodes, X. Zhang, E. J. Miller, M. Jonely, K. R. Hansen, C. I. Nwachukwu, A. G. Roberts, H. Wang, R. Noriega, S. D. Minter and L. Whittaker-Brooks, *ACS Materials Au*, 2022, **2**, 482-488.
160. S. Marullo, M. Feroci, R. Noto and F. D'Anna, *Dyes and Pigments*, 2017, **146**, 54-65.
161. A. Perez-Velasco, V. Gorteau and S. Matile, *Angewandte Chemie International Edition*, 2008, **47**, 921-923.
162. W. Ma, Y. Luo, L. Nian, J. Wang, X. Wen, L. Liu, M. Hanif, Z. Xie and Y. Ma, *ACS Applied Materials & Interfaces*, 2018, **10**, 10513-10519.
163. X. Yang, X. Xu and H.-F. Ji, *The Journal of Physical Chemistry B*, 2008, **112**, 7196-7202.
164. B. Rybtchinski, L. E. Sinks and M. R. Wasielewski, *Journal of the American Chemical Society*, 2004, **126**, 12268-12269.
165. Y. Huang, Y. Yan, B. M. Smarsly, Z. Wei and C. F. J. Faul, *Journal of Materials Chemistry*, 2009, **19**, 2356-2362.
166. M. Sun, K. Müllen and M. Yin, *Chemical Society Reviews*, 2016, **45**, 1513-1528.
167. D. Ambrosek, H. Marciniak, S. Lochbrunner, J. Tatchen, X.-Q. Li, F. Würthner and O. Kühn, *Physical Chemistry Chemical Physics*, 2011, **13**, 17649-17657.
168. S. Roy, N. Sinha, S. Pakhira and C. Chakraborty, *Dyes and Pigments*, 2021, **192**, 109461.
169. M. Burian, F. Rigodanza, N. Demitri, L. Dörđević, S. Marchesan, T. Steinhartova, I. Letofsky-Papst, I. Khalakhan, E. Mourad, S. A. Freunberger, H. Amenitsch, M. Prato and Z. Syrgiannis, *ACS Nano*, 2018, **12**, 5800-5806.
170. J. J. Walsh, J. R. Lee, E. R. Draper, S. M. King, F. Jäckel, M. A. Zwijnenburg, D. J. Adams and A. J. Cowan, *The Journal of Physical Chemistry C*, 2016, **120**, 18479-18486.
171. E. R. Draper, L. Wilbraham, D. J. Adams, M. Wallace, R. Schweins and M. A. Zwijnenburg, *Nanoscale*, 2019, **11**, 15917-15928.
172. N. J. Hestand and F. C. Spano, *The Journal of Chemical Physics*, 2015, **143**, 244707.
173. D. M. Stoltzfus, J. E. Donaghey, A. Armin, P. E. Shaw, P. L. Burn and P. Meredith, *Chemical Reviews*, 2016, **116**, 12920-12955.
174. N. Sikdar, D. Dutta, R. Haldar, T. Ray, A. Hazra, A. J. Bhattacharyya and T. K. Maji, *The Journal of Physical Chemistry C*, 2016, **120**, 13622-13629.
175. M. Guide, S. Pla, A. Sharenko, P. Zalar, F. Fernández-Lázaro, Á. Sastre-Santos and T.-Q. Nguyen, *Physical Chemistry Chemical Physics*, 2013, **15**, 18894-18899.
176. N. Zink-Lorre, E. Font-Sanchis, Á. Sastre-Santos and F. Fernández-Lázaro, *Chemical Communications*, 2020, **56**, 3824-3838.
177. F. Zhang, Y. Ma, Y. Chi, H. Yu, Y. Li, T. Jiang, X. Wei and J. Shi, *Scientific Reports*, 2018, **8**, 1-11.

178. J.-P. Sun, A. D. Hendsbee, A. J. Dobson, G. C. Welch and I. G. Hill, *Organic Electronics*, 2016, **35**, 151-157.
179. M. Nazari, E. Cieplechowicz, T. A. Welsh and G. C. Welch, *New Journal of Chemistry*, 2019, **43**, 5187-5195.
180. C. R. Harding, J. Cann, A. Laventure, M. Sadeghianlemraski, M. Abd-Ellah, K. R. Rao, B. S. Gelfand, H. Aziz, L. Kaake and C. Risko, *Materials Horizons*, 2020, **7**, 2959-2969.
181. Z. Hu, R. Xu, S. Dong, K. Lin, J. Liu, F. Huang and Y. Cao, *Materials Horizons*, 2017, **4**, 88-97.

Chapter 2: Improving the performance of PBI-L in interlayer photovoltaic devices using counter ions

2.1. Introduction

As mentioned in Chapter 1, perylene bisimides (PBIs) can be used in organic photovoltaic devices (OPVs) because they are *n*-type semiconducting materials and strongly light absorbant.^{1, 2} Their highly conjugated π -system allows them to stack into 1D aggregates. The type of aggregate that is formed plays a critical role in their performance in OPVs.³ It was also discussed how the aggregation could be changed by changing the chemical structure of the PBIs for improved performance in OPVs.^{1, 4-6} Work by Cameron *et al.* investigated a series of eight amino acid-functionalised PBIs, Figure 2.1, for use as interlayers between zinc oxide (ZnO) and poly(3-hexylthiophene):[6,6]-phenyl C61-butyric acid methyl ester (P3HT/PC₆₁BM) for a multilayer photovoltaic device.⁷ Currently, fabrication of multilayer photovoltaic devices beyond bulk heterojunction layers is limited due to solution processing leading to dissolution of layers. However, amino acid-functionalised PBIs can easily be solubilised in water, which the organic donor and acceptor layers are not soluble in. This difference in solubility allows for an easy solution processing method that reduces the possibility of dissolution of organic layers. It was already seen that different amino acid side chains impact the aggregation of these eight PBIs.⁸

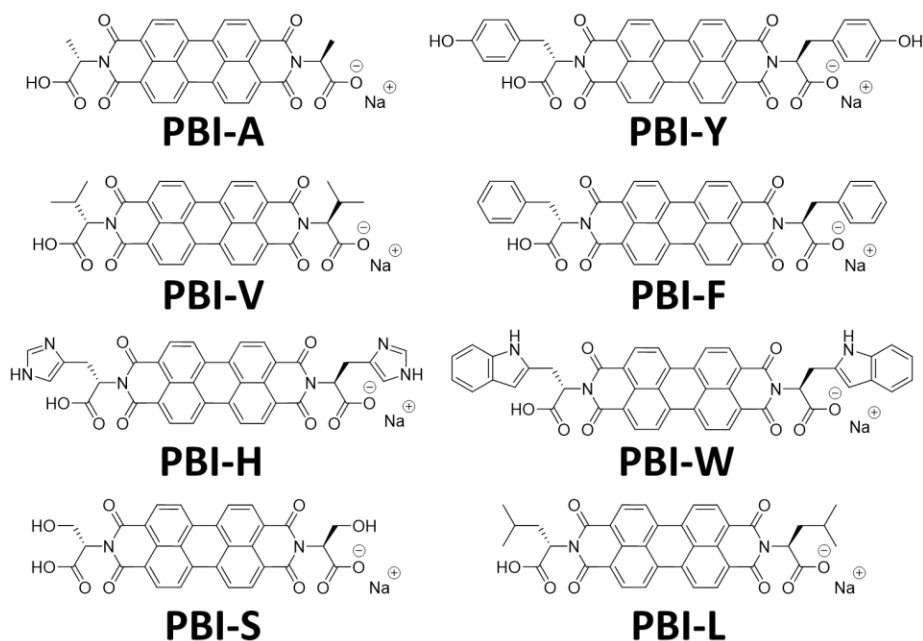


Figure 2.1. Chemical structures of the eight different amino acid-functionalised PBIs as salts with Na⁺ used for the interlayers of photovoltaic devices.⁷

The PBIs were solubilised in water using 1 equivalent of a 0.1 M NaOH solution to raise the pH to above the apparent pK_a , then the solutions were spin-coated onto an indium-doped tin oxide (ITO) glass slide with a ZnO electron transport layer (ETL). The OH^- deprotonates the carboxyl groups of amino acids, improving the solubility and leaves behind a Na^+ which means the PBI and Na^+ exist as an anion-cation pair. P3HT/PC₆₁BM was spin-coated on top of the PBI interlayer and annealed then molybdenum trioxide (MoO_3) and silver electrodes were deposited using thermal evaporation. A diagram of the device is shown in Figure 2.2. The best-performing PBIs were those functionalised with *L*-phenylalanine (**PBI-F**), *L*-tryptophan (**PBI-W**), and *L*-tyrosine (**PBI-Y**). The poorest performance was seen for PBI functionalised with *L*-leucine (**PBI-L**), which was explained by parasitic absorption which caused a reduction in the transmittance at the λ_{max} .

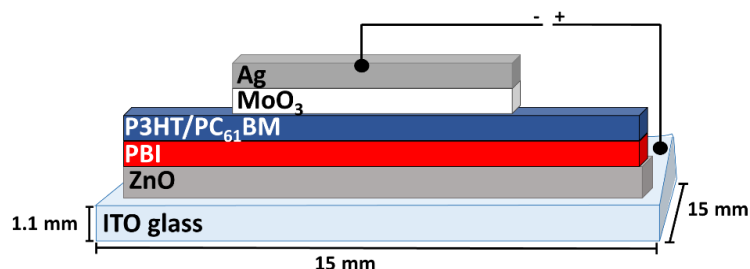


Figure 2.2. Cartoon depiction of the photovoltaic devices used in the reported study.⁷

A route for changing the aggregation and self-assembly of PBIs without changing the chemical structure is by the use of additives.^{9, 10} This chapter examines the possibility of improving the performance of **PBI-L** in photovoltaic devices by changing the solubility and aggregate morphology through variation of the pH of the basic solutions containing different cations instead of changing the chemical structure. **PBI-L** was chosen over **PBI-Y** or **PBI-F** was chosen because it has a very great synthetic yield, and for commercialisation it would be more favourable to improve its performance through a simpler method. Previous reports indicate that the morphology is greatly impacted by the pH.¹¹⁻¹⁴ However, the role of cations other than Na^+ on the self-assembly and aggregation of these PBIs has not been investigated. When the pH is lowered, the deprotonated carboxylic acid groups responsible for the solubility in water become protonated and the PBI no longer exists as a salt with Na^+ . Instead, there is now a presence of additives such as sodium gluconate or sodium chloride,

depending on how the pH is lowered.¹⁵ These have been shown to have little interaction with or effect on the low-pH structure. However, the impact of the choice of cation in these salt additives on the ability of PBI to aggregate and self-assemble into fibrous structures has not been investigated.

The role that salt additives have on the fibre-solution interface is an important parameter to understand in order to modify the final hydrogel properties and the process by which they form, however, it can be challenging to understand. Typically, the ability of self-assembled materials to salt in and salt out has been recognized and explained by the Hofmeister series (HS).¹⁶⁻¹⁸ The HS has varied effects on the stability of secondary and tertiary structures of large self-assembled materials with anions having a greater effect than cations.^{17, 19, 20} The HS for cations is shown in Figure 2.3. Weakly hydrated cations, which are more likely to salt out, are on the left-hand side, whereas divalent cations, which are more likely to salt in, are on the right-hand side. This has been linked to their differences in the charge densities of the ion's which interact with the charged surfactants in solution.

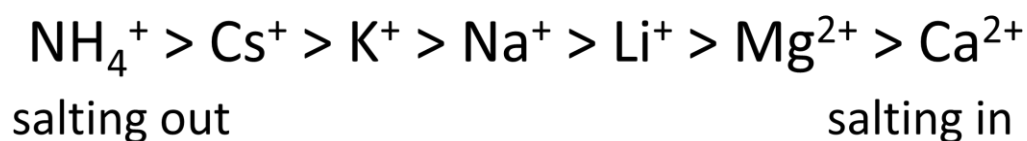


Figure 2.3. Partial listing of cations studied for the HS.^{17, 18}

Salting out describes an increase in surface tension at the fibre-solution interface. This in turn leads to an increase in the stability of the aggregate due to a strengthening of the hydrophobic effect. As we discussed earlier, the hydrophobic effect drives the surfactant-like gelators to form aggregates at high pHs.²¹⁻²³ On the other hand, salting in describes a decrease in surface tension at the fibre-solution interface. The hydrophobic effect is weakened and the gelators become more soluble in aqueous media. With the increased solubility the gelator can interact with water easier and the stability of the aggregates formed is decreased. As described below in Figure 2.4.

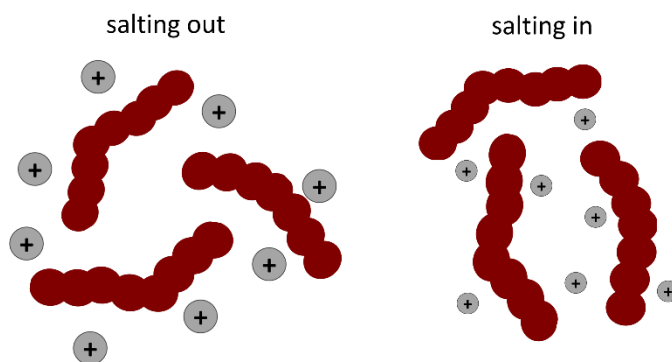


Figure 2.4. Cartoon depicting the affect of salting out vs salting in on PBI aggregates.

Others have explored how the choice of cation can impact the solubility and aggregation of LMWGs. McAulay *et al.* reported that, in a naphthalene-dipeptide system (**2NapFF**), changing the size of the cation (Li^+ , Na^+ , K^+ , Rb^+ , Cs^+ , tetrabutylammonium hydroxide) resulted in a change in the structure of micellar aggregates.²⁴ The different aggregates had different behaviours on heating and cooling and had different apparent pK_a values. The differences in their apparent pK_a values meant **2NapFF** formed hydrogels using a pH trigger at different rates as the pH was lowered. For the larger cations (Rb^+ , Cs^+ , tetrabutylammonium hydroxide) the gelation process became more of a gradual transition compared to **2NapFF** with smaller cations (Li^+ , Na^+ , and K^+). The resulting gels all had the same final pH of 3.6 but there were differences in turbidity and stiffness.

Mañas-Torres *et al.* investigated the gelation kinetics for *N*-fluorenyl methyleneoxycarbonyl-diphenylalanine (**Fmoc-FF**) with Cs^+ and Ca^{2+} using *in-situ* fluorescence lifetime imaging microscopy (FLIM) and found differences in the self-assembly mechanism with different cations.²⁵ It was expected that Ca^{2+} should decrease the solubility and increase the stability of the aggregates while Cs^+ should have the opposite result. With the addition of Ca^{2+} , they were able to prompt self-assembly and form hydrogels more quickly than with Cs^+ ions. The difference in self-assembly mechanism was explained by **Fmoc-FF** with Cs^+ undergoing a multistep assembly of the monomers into nanospheres then into a mixture of nanospheres and amorphous fibres. By contrast, **Fmoc-FF** with Ca^{2+} just assembles into nanofibres. This mixture of fibres and nanospheres for **Fmoc-FF** with Cs^+ was observed both by FLIM and transmission electron microscopy (TEM). Rheological measurements

showed that hydrogels formed using Ca^{2+} were frequency-independent and stiffer than those made with Cs^+ .

Backes *et al.* studied how cations (Li^+ , Na^+ , and K^+) affect the aggregation of an anionic PBI for use as a surfactant for the dispersion of carbon nanotubes.²⁶ They measured the UV-vis absorption over a series of dilutions with the different cations at pH 7 and pH 11 to determine the decay constants which represented the change in the PBI from monomeric form to aggregate. These two pHs were chosen because of the differences in ionic strength and concentration of cations at those values. The dilution series showed that at both pH 7 and pH 11 the anionic PBI had the highest affinity for Na^+ , followed by Li^+ , and then K^+ . Although the trends of the cation affinities at the two pHs were the same, the overall decay constants for pH 11 had decreased by a factor of 1.65 compared to pH 7. This is explained in terms of an increased concentration of the respective cations resulting in a stronger tendency of monomer to self-assemble into aggregates.

Due to the literature precedents of the cations having such an impact on the assembly, this chapter looks at how the choice of cation of XOH ($\text{X} = \text{Li}^+$, Na^+ , K^+ , or Cs^+) used to solubilise **PBI-L** can improve the solubility and stability of aggregates and fibrous structures formed in solution for use in hydrogels and photovoltaic devices. Electron paramagnetic resonance (EPR) has shown that **PBI-L** in solution has a comparable amount of radical anion to **PBI-Y** and **PBI-W** which did perform well as electron transporting layers in multilayer photovoltaic devices.^{7, 8} The aggregates of **PBI-L** formed in solutions with different cations at different pHs were studied using UV-vis absorption spectroscopy to determine if the different cations affect the molecular packing, and to investigate their ability to form photoconductive radical anions. Small-angle X-ray scattering (SAXS) data were collected, and dynamic viscosity was measured to evaluate differences in the secondary fibre structures. Differences in bulk rheological properties and the kinetics of gel formation were monitored using rheology and compared to the change in pH over time.

Lastly, **PBI-L** solutions with different cations at pH 6 were used as the electron transporting layer in a multilayer photovoltaic device. Cyclic voltammograms (CVs) of **PBI-L** at pH 6 were measured to see if the different aggregates had resulted in a

change in the reduction potential for the radical anion. The devices were constructed similarly to the previously published method with two separate donor materials, poly(3-hexylthiophene) (P3HT) and poly[(ethylhexyl-thiophenyl)-benzodithiophene-(ethylhexyl)-thienothiophene] (PCE10).⁷ Transmittance measurements were carried out on the ZnO/**PBI-L** bilayer films to compare the effect of different cations on the absorbance. Nanoindentation was measured to determine the Young's modulus before and after irradiation for OPV devices of **PBI-L** with Li⁺, Na⁺, K⁺, and Cs⁺.

2.2. Results and discussion

2.2.1 Investigation of self-assembled micellar aggregates in solution at different pHs

The dynamic viscosity of the solutions of **PBI-L** with different cations at pH 6 was used to probe for possible differences in micellular aggregates caused by the cation choice. Differences in the 1D structure's morphology, length, or ambulations will result in a difference in their viscosity values at low shear rates. This is the same pH used in the initial PBI study by Cameron *et al.*⁷ Figure 2.5 (a) shows the viscosity for **PBI-L** with different cations. Henceforth, solutions of 10 mg/mL of **PBI-L** with the different cations will just be referred to in terms of the cation present in solution. Typically, Na⁺ at pH 6 and above has a viscosity close to that of water which could indicate that few or no structures are present.⁸ Li⁺, K⁺, or Cs⁺ exhibit shear thinning, an indication of the presence of worm-like micelles, or fibrous-type structures.^{13, 22, 27} It should be noted that the viscosity did change with the different cations. Li⁺ and K⁺ had higher viscosity initially than Na⁺, and Cs⁺ had the highest viscosity. These differences in viscosity could be indicative of differences in a number of aggregate properties such as shape, length, size, or amount. Figure 2.5 (b) shows the viscosity of the solutions at a shear rate of 10 s⁻¹. Here, the difference in viscosity between Cs⁺ and the other cations is clearer, the high error bars can be due to viscosity can be impacted greatly by other environmental factor like humidity, sample aging or solution quality. However, Cs⁺ still has a higher viscosity than the other solutions including the error bars.

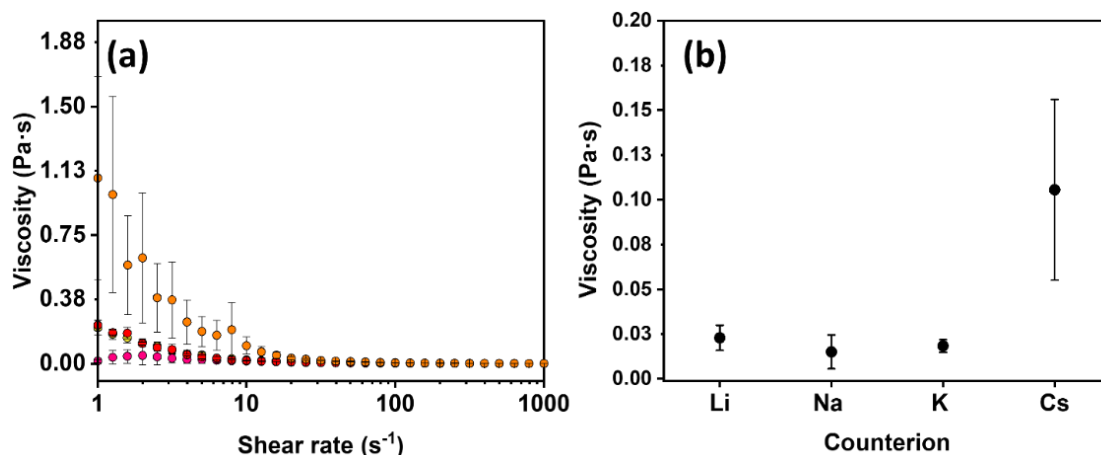


Figure 2.5. (a) Dynamic viscosity measurements of Li⁺ (yellow), Na⁺ (pink), K⁺ (red) and Cs⁺ (orange) at pH 6. (b) Summarized dynamic viscosity at a shear rate of 10 s⁻¹ for solutions with different cations. Measurements were performed in triplicate and errors were calculated from the standard deviation.

Next the effect of pH on the aggregate's morphology, abundance and length was scanned for again using dynamic viscosity. Figure 2.6 (a) to (d) shows the viscosity data for the different cations at pH 5, 6, 7, 8, and 9. For Li⁺ or K⁺, shear thinning was observed at all pHs. The viscosities of Li⁺ or K⁺ at pH 8, and 9 at a low shear rate did appear to be higher than Na⁺, but they were all within error. At pH 5 there was a more obvious increase in viscosity, which indicates changes in micelle self-assembly properties. Li⁺ had a higher viscosity than K⁺ which may be result of differences in micelle morphology, amount of structures present, or length of structures due to Li⁺ being better at salting out than K⁺. Na⁺ saw the largest viscosity value at a low shear rate for pH 5 when the pH was well below its apparent p*K*_a. At pH values above 5 the viscosity was similar to that of water. The viscosity for Na⁺ at pH 5 was like that of Li⁺ at the same pH which is expected as they are similar on the HS and impact the aggregates stability similarly. For Cs⁺ the viscosity was larger at low shear. Due to the large variability in the viscosity measured between the repeats it is difficult to draw any conclusions from these low-shear data.

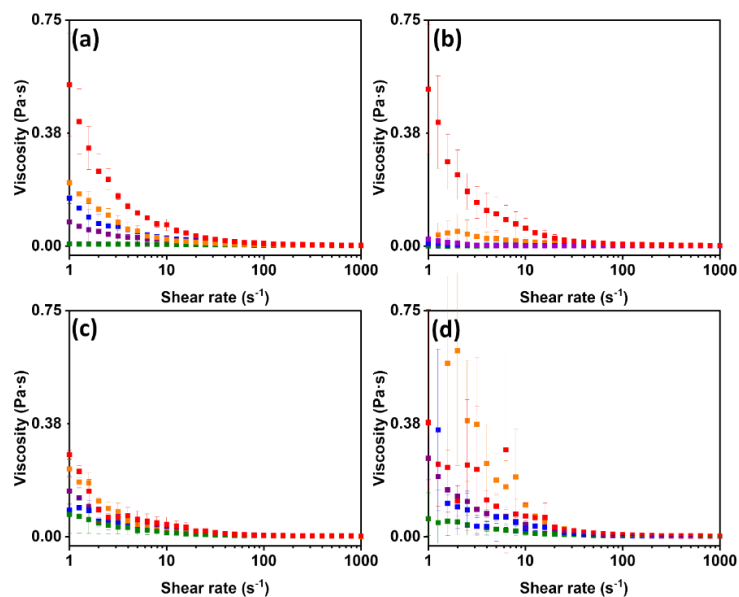


Figure 2.6. Dynamic viscosity measurements of (a) Li^+ , (b) Na^+ , (c) K^+ , and (d) Cs^+ at pH 5 (red), 6 (orange), 7 (green), 8 (blue), and 9 (purple). Measurements were performed in triplicate and errors were calculated from the standard deviations.

As the viscosity had shown the different pH responses of the aggregates this was further investigated by determining the apparent $\text{p}K_a$ values of the systems, which describe the aggregate acid strength. The higher the apparent $\text{p}K_a$ values the weaker the acid dissociation constant. This means when the apparent $\text{p}K_a$ values are higher, the pH matching the $\text{p}K_a$ value can be reached more quickly. This can change the kinetics of the self-assembly of the PBI and influence the final fibrous structures formed. The viscosity measurements showed cation-dependent differences in assembly which may be due to differences in the apparent $\text{p}K_a$ values. To investigate this, apparent $\text{p}K_a$ titrations were carried out, with results shown in Figure 2.7 (a) to (d). The titration data were used to determine the two apparent $\text{p}K_a$ values for each cation and are listed in Table 2.1. Interestingly, all the apparent $\text{p}K_{a2}$ values are similar in value and significant differences are only observed for the apparent $\text{p}K_{a1}$ values. This means **PBI-L** is becoming protonated and undergoing a transition of nanostructures earlier when the solutions are made with Na^+ or Cs^+ than when they are made with Li^+ or K^+ . This shows that cation size is impacting the aggregation behaviour and while it does not follow the HS series this similarly for PBIs with Li^+ and K^+ has been observed before.²⁶ It is also observed that Cs^+ has the biggest interval between the apparent $\text{p}K_a$ values while K^+ has the narrowest. This agrees with

observations from dynamic viscosity measurements at different pH values. Indicating that even though they should have similar aggregates sizes / shapes they respond to pH differently.

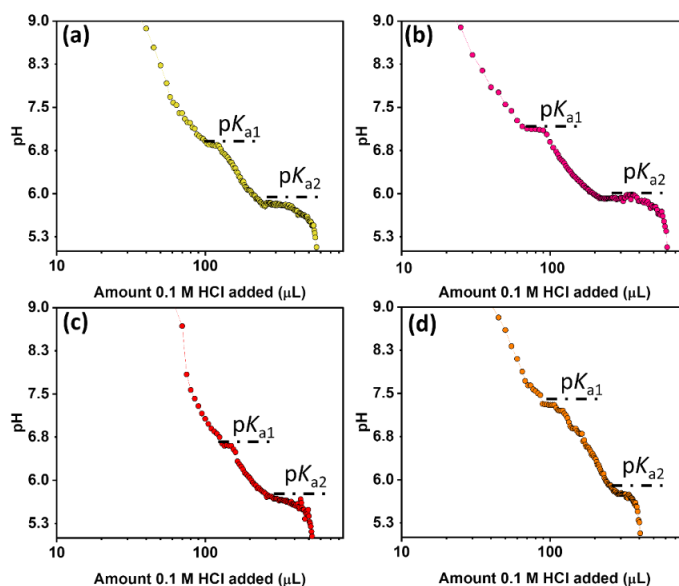


Figure 2.7. Apparent pK_a titrations of (a) Li^+ (yellow), (b) Na^+ (pink), (c) K^+ (red), and (d) Cs^+ (orange) using 0.1 M HCl solution.

Table 2.1. Apparent pK_a values with different cations.

Cation	pK_{a1}	pK_{a2}
Li^+	6.8	5.8
Na^+	7.2	5.9
K^+	6.6	5.7
Cs^+	7.3	5.8

The different pK_a values was examined using UV-vis absorption spectroscopy to see if this difference in acid strength could be used to change the molecular packing. Figure 2.8 shows the UV-vis absorption spectra with the different cations at different pHs. At pHs below the apparent pK_a values it is expected that the network of fibres begins to lose some negative charge and there is an increase in the fibre-fibre interactions. The increase in the aggregation of these fibres is represented in the UV-vis absorption spectra by a change in the absorbance of the strong S_0 - S_1 transitions at 507 and 550 nm due to the larger aggregates scattering light in the background.¹² As these pHs are close to the apparent pK_a values, changes in aggregation may be

beginning to occur. This agrees with Li^+ and K^+ having similar apparent $\text{p}K_{\text{a}1}$ and $\text{p}K_{\text{a}2}$ values. At pH 5 there is a more significant change in the absorbance of the $\text{S}_0\text{-S}_1$ absorptions. However, the spectrum of K^+ was different from that of Li^+ at pH 5, which indicates different molecular packing. This difference could be due Li^+ being better at salting in meaning the aggregates are less stable. This is also very different to what was seen with Na^+ at pH 5 which showed a significant decrease in the absorbance at this pH due to **PBI-L** forming a gel. A scaled version of the UV-vis absorption spectrum at pH 5 in the Appendix 1, it shows the high background absorption, this is likely due to the formation of very large aggregates. These aggregates are a sufficient size to scatter the light. For Cs^+ the absorbance of the $\text{S}_0\text{-S}_1$ peaks at pH 9 was smaller than at pH 8 or 7. A shoulder peak at 480 nm became more pronounced for Cs^+ at pH 8 which is a higher pH than for the other systems. This shows it has a different behaviour and possibly quite different aggregation to the rest. This follows the HS which predicts that Cs^+ should increase the surface tension at the fibre solution interface and improve aggregate stability. The different cations did not change the region in which the aggregates absorbed light but did affect how **PBI-L** would assemble at different pHs which is expected given they show impact the aggregates stability according to the HS. This is advantageous as changing the self-assembly of nanostructures with a simple change in an external stimulus is simpler than changing the underlying chemical structure.

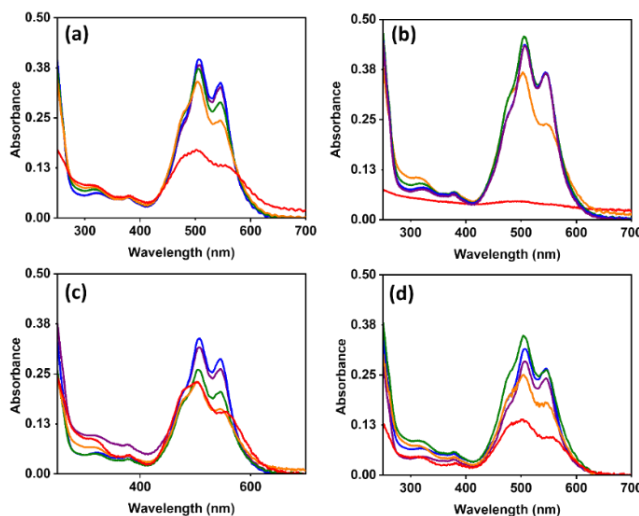


Figure 2.8. UV-vis absorption spectra with (a) Li^+ , (b) Na^+ , (c) K^+ , and (d) Cs^+ at different pHs. pH 5 (red), pH 6 (orange), pH 7 (green), pH 8 (blue), and pH 9 (purple).

To characterise the fibrous structures in solution seen by viscosity and UV-vis absorption spectroscopy at different pH values, SAXS was collected. SAXS is a non-destructive technique applicable to *in-situ* measurement of soft samples giving a better idea of self-assembled structures without interference from drying effects.^{28, 29} In this technique the systems are hit with an X-ray beam which then scattered off the sample (Figure 2.9). The scattering is elastic and coherent meaning there is no net loss of energy. Incoherent scattering arising from the solvent can be removed by background subtraction during data processing.

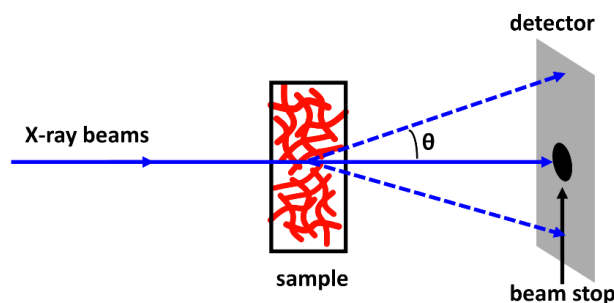


Figure 2.9. Cartoon representation of small angle X-ray scattering experiment. θ is the scattering angle of the beam from the sample. Adapted from the following publication.²⁹

When X-rays beams are scattering from the system the intensity of scattering ($I(Q)$) is measured as a function of the scattering vector, Q . Q is related to the scattering angle by Equation 1 and thus can be seen to give a size range of the scattering experiment which is agnostic to the instrument or source.

$$I(Q) = Q = \frac{4}{\lambda} \sin\left(\frac{\theta}{2}\right) \quad (\text{Equation 1})$$

The longer this length, the smaller the angle which can be probed, and thus larger structures can be measured. It can be used to assess non-crystalline aggregates of a 1 - 1000 nm size. The scattering from the non-crystalline aggregates is analysed by reducing the observed data into one-dimensional (1D) scans, Figure 2.10. Structure parameters are extrapolated from the scattering of X-rays by the system and typically analysed by using approximations (such as Guinier and Porod) that are valid over a limited angular range or fitted to theoretical models. Based on their size our systems are best fitted with the shape and interference regions.

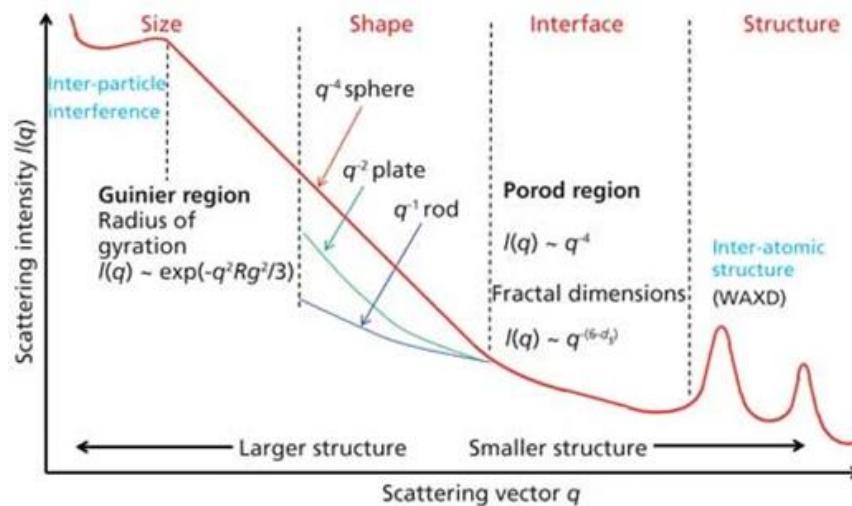


Figure 2.10. Schematic of 1D SAXS scan from a particulate system. The intensity is plotted as a function of scattering vector Q . The three commonly recognized regions of the SAXS regions are indicated.³⁰

Typically, amino acid-functionalised PBI systems have been modelled using various cylindrical-type or spherical models at different pHs.¹¹⁻¹³ A flexible cylinder model and its parameters are illustrated below in Figure 2.11 (a); these are typically used when the pH is below the apparent pK_a values and the aggregates have assembled into worm-like micelles. A spherical model and its parameters are illustrated in Figure 2.8 (b): this is used when the pH is above the apparent pK_a values. However, the systems may not always fit these two models possibly due to changes in solubility. In those cases shape-independent models can be used.

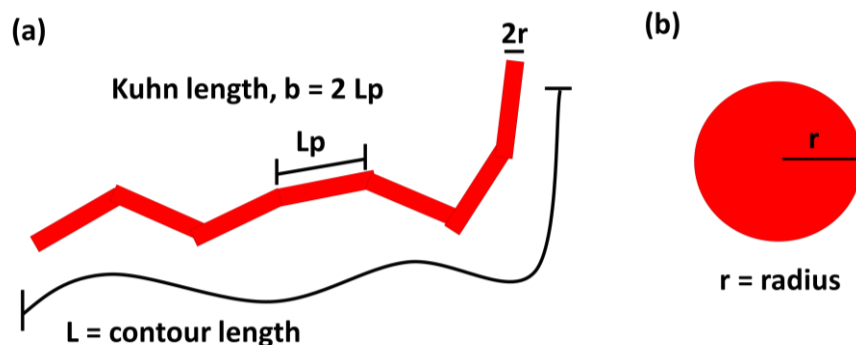


Figure 2.11. Schematic representations of (a) the flexible cylinder and (b) sphere models in SasView.

SAXS was used to characterise the suspected structures formed in solution. As the pH is increased, the number of cations available to interact with the PBI increases. This section also investigates whether it is the OH^- predominantly impacting the fibre structure or the cation as well. Figure 2.12 shows the SAXS data for solutions at pH 7 and the fits used to model the data. Model parameters used to fit the data are summarised in Table 2.2. At pH 7 all cations were fitted to a sphere model at low Q and a power law model at higher Q . The need to fit the data to a power law suggests that aggregation is beginning at this pH. The level of aggregation is expected to be different for K^+ and Cs^+ compared to Na^+ and Li^+ according to the HS. The power law value was largest for K^+ at 3.56 and smallest for Li^+ at 3.46. The larger power law indicates greater aggregation begin to form, since K^+ is better at salting it is expected to improve aggregates stability. Na^+ had the smallest spherical radius of 1.18 nm and Cs^+ had the largest spherical radius of 1.44 nm. The difference in the spherical size with the different cations is modest, it does indicate some difference in the molecular packing due to cation choice.

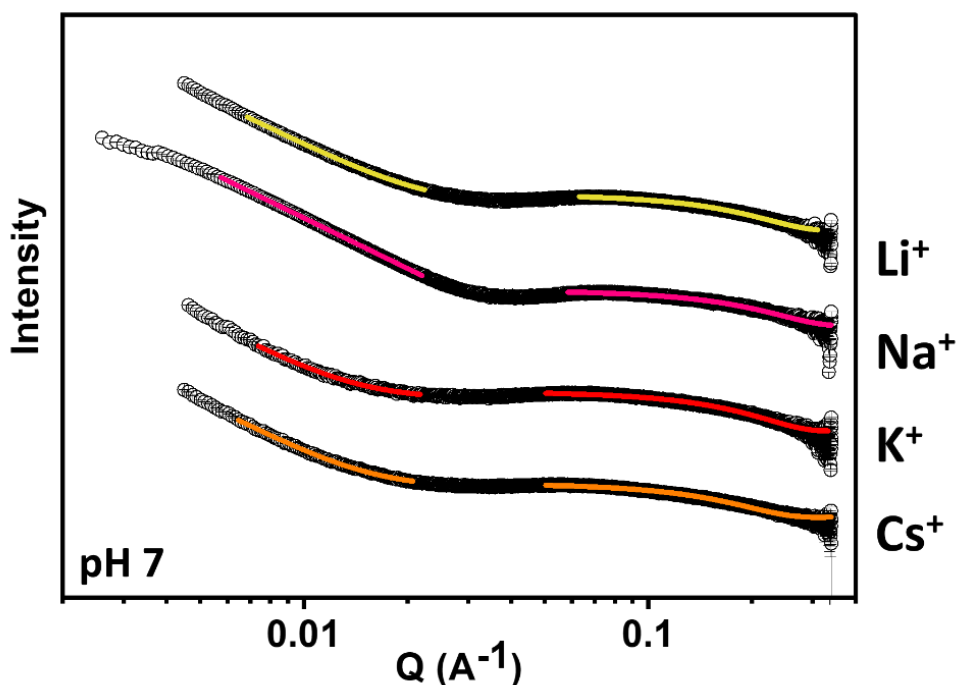


Figure 2.12. SAXS data for solutions prepared at pH 7 with Li^+ (yellow), Na^+ (pink), K^+ (red), and Cs^+ (orange) with the experimental data shown as black symbols and the fits as coloured lines. Note the data are offset on the intensity scale for clarity.

Table 2.2. SAXS fit table for solutions prepared at pH 7 with Li⁺, Na⁺, K⁺, and Cs⁺.

Cation	Li ⁺	Na ⁺	K ⁺	Cs ⁺
Model	Sphere	Sphere	Sphere	Sphere
Sphere radius (nm)	1.29 ± 0.00216	1.18 ± 0.00385	1.32 ± 0.00232	1.44 ± 0.0212
χ^2	1.9	1.6	2.4	2.2
Model	Power law	Power law	Power law	Power law
Power law	3.46 ± 0.000112	3.48 ± 0.000111	3.59 ± 0.00478	3.56 ± 0.0223
χ^2	1.9	4.4	1.6	2.9

The viscosity of these solutions with different cations at pH 6 showed shear thinning at low shear rates which is an indication that worm-like micelle structures are already present. However, due to this pH being in between the apparent pK_a values the aggregates have begun to transition and the solubility is greatly impacted. In this case, a cylinder or spherical model may not be suitable and a shape-independent model may be preferred. The data at pH 6 were fitted using a functional form model described by Equation 1 below, based on a related fibre system.³⁰⁻³²

$$I(Q) = \frac{A}{Q^n} + \frac{C}{(1+Q\xi)^m} + B \quad (\text{Equation 2})$$

The network scattering in the low-Q region is described by the first term and is qualitatively similar to Porod-like scattering.³³ The second term is a Lorentzian function that describes the morphology of the fibre structures and interactions with the solvent in the high-Q region.³⁴ In the equation, B is the background scattering, A and C correspond to multiplicative factors for the two terms. The scattering exponents Porod exponent (n) and Lorentz exponent (m) represent the fibril density at low-Q and high-Q scattering, respectively. The correlation length (ξ) describes the distance between crosslinks of the fibres as illustrated below in Figure 2.13.

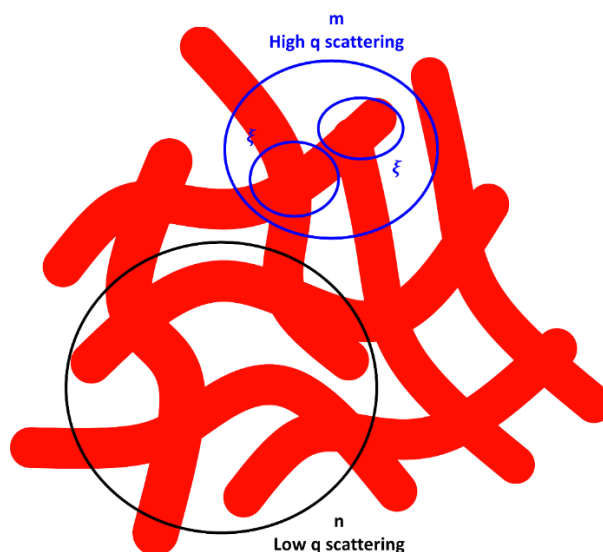


Figure 2.13. Illustration of fibre system described by the correlation length model with the scattering parameters of Porod exponent (n), Lorentz exponent (m), and correlation length (ξ) labelled. Adapted from original publication.³⁰

Visually looking at the data, Figure 2.14, Na^+ is scattering differently to the other cations at this pH and this is reflected in the fit parameters. These differences in morphology at pH 6 for Na^+ at the same pHs agree with the dynamic viscosity measurements. At pH 6 all solutions show shear thinning and very low viscosity, however, for Na^+ at pH 6 there is only a slight increase in viscosity while the other cations see a larger increase. At pH 6, all aggregates are nearly at their apparent pK_{a2} , and the gel is beginning to form. The correlation length model indicates the nanostructures are very branched which is indicative of a transition of structure between apparent pK_a values. The correlation length for Li^+ was 0.638 nm which was smaller than K^+ (0.748 nm) and Cs^+ (0.857 nm) meaning at this pH they all had differences entanglement density which followed the HS. Na^+ on the other hand had a much larger correlation length of 14 nm meaning there was a larger distance between cross links and a greater mesh size. The Porod exponents for Li^+ , 2.63, was similar to Cs^+ , 2.60, which implies that their tertiary and secondary structures are similar.³⁵ The Porod exponent for K^+ was slightly larger at 2.84 and that for Na^+ was even larger at 3.41. Differences in the low- Q scattering suggests differences between the micellar and nanostructures for these cations.²⁹ The Lorentzian exponent followed a slightly different trend: exponents for K^+ , 2.26, and Cs^+ , 2.35, were similar to one another. Li^+

had a larger exponent value of 3.19 and Na⁺ had the smallest value of 1.64. This shows that smaller cations are having a greater impact on the fibre density on the local scale which is to be expected as they have a higher charge density and show form more tightly packed aggregates according to the HS series.

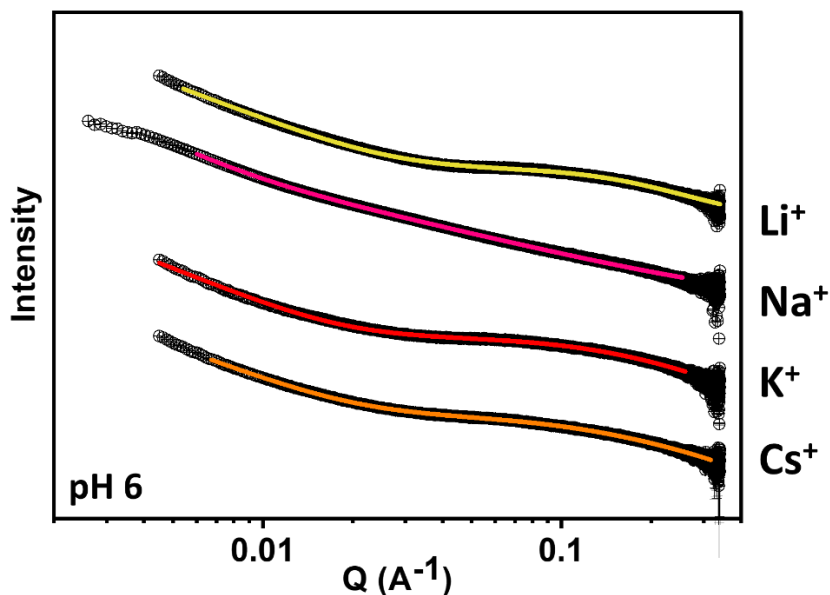


Figure 2.14. SAXS data for solutions prepared at pH 6 with Li⁺ (yellow), Na⁺ (pink), K⁺ (red), and Cs⁺ (orange) with the experimental data shown as black symbols and the fits as coloured lines. Note the data are offset on the intensity scale for clarity.

Table 2.3. SAXS fit table for solutions prepared at pH 6 with Li⁺, Na⁺, K⁺, and Cs⁺.

Cation	Li ⁺	Na ⁺	K ⁺	Cs ⁺
Model	Correlation length	Correlation length	Correlation length	Correlation length
Correlation length (nm)	0.638 ± 0.00134	14.8 ± 0.00515	0.748 ± 0.00212	0.857 ± 0.00124
Porod exponent	2.63 ± 0.00211	3.41 ± 0.000155	2.84 ± 0.00316	2.60 ± 0.00322
Lorentzian exponent	3.19 ± 0.0211	1.64 ± 0.000265	2.26 ± 0.0161	2.35 ± 0.00422
χ^2	5.0	4.8	4.5	3.0

The final pH in solution investigated using SAXS was pH 5. At this pH all the systems are below their apparent pK_a values. At pH 5, K⁺ could only be suitably fitted to the mass fractal model with the high-Q cut off. This indicates the structures of K⁺ at this

pH may be diffusion limited for this measurement and their structures are no uniform throughout. All other cations at pH 5 were fitted to a flexible elliptical cylinder combined with a power law model with, for Na⁺ and Li⁺, the high-Q cut off. This is due to there being a large tick in this region for these solutions which could be the result of a solvent peak, making it challenging to fit this region. For Na⁺, the length of cylinders was 64.4 nm and this was largest for any of the cation systems at this pH. However, Na⁺ had the smallest Kuhn length of 3.94 nm, meaning it had the greatest flexibility. This difference in self-assembled structures compared to the other cations agrees with the UV-vis absorption data which showed that Na⁺ began to precipitate out at this pH, unlike the others. Both Li⁺ and Cs⁺ also had similar Kuhn lengths of 8.65 nm and 8.57 nm meaning the fibres should have similar stiffness. However, the cylinder radius of the fibres for Li⁺ was 1.14 nm, while that for Cs⁺ was 1.31 nm meaning less PBIs were packing together for Li⁺. This agrees with the UV-vis absorption spectroscopy and dynamic viscosity which showed the Li⁺ aggregates should be smaller due to the salting in effect. This shows how the choice of cation is having an impact on the micellar structures of **PBI-L** at different pHs given the change in the cation concentration.

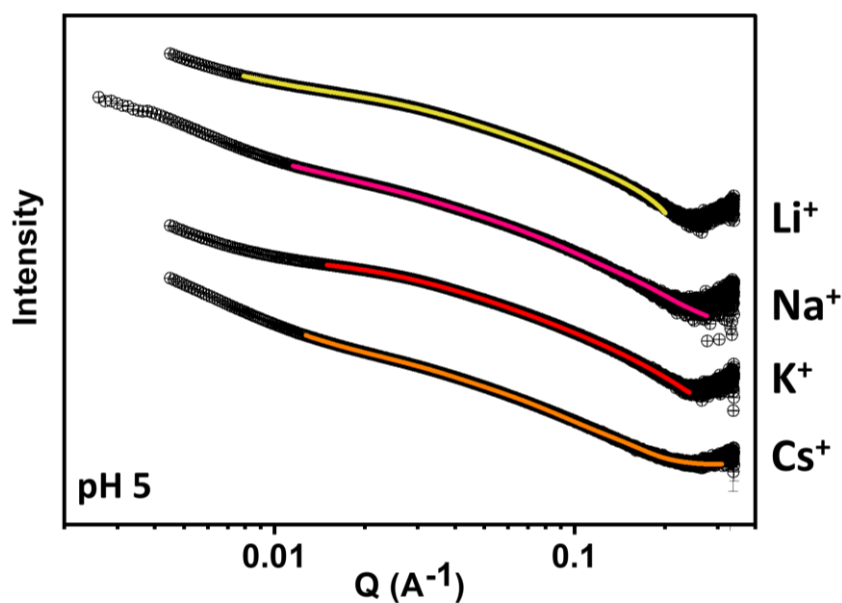


Figure 2.15. SAXS data for solutions prepared at pH 5 with Li⁺ (yellow), Na⁺ (pink), K⁺ (red), and Cs⁺ (orange) with the experimental data shown as black symbols and the fits as coloured lines. Note the data are offset on the intensity scale for clarity.

Table 2.4. SAXS fit table for solutions prepared at pH 5 with Li⁺, Na⁺, K⁺ and Cs⁺.

Cation	Li ⁺	Na ⁺	K ⁺	Cs ⁺
Model	Flexible elliptical cylinder + power law	Flexible elliptical cylinder + power law	Mass fractal	Flexible elliptical cylinder + power law
Length (nm)	34.5 ± 0.0000333	64.4 ± 0.0554	N/A	34.2 ± 0.00326
Kuhn length (nm)	8.64 ± 0.0234	3.94 ± 0.0644	N/A	8.57 ± 0.0367
Cylinder radius (nm)	1.14 ± 0.00165	1.24 ± 0.000527	N/A	1.31 ± 0.00133
Axis ratio	3.15 ± 0.00526	2.67 ± 0.00123	N/A	2.88 ± 0.00618
Power law	3.23 ± 0.00215	2.46 ± 0.00673	N/A	3.51 ± 0.00832
Radius (nm)	N/A	N/A	1.06 ± 0.004	N/A
Mass fractal dimension	N/A	N/A	2.44 ± 0.00119	N/A
Cut-off length (nm)	N/A	N/A	4.08 ± 0.00445	N/A
χ^2	7.2	6.5	9.7	4.0

It was already seen in the SAXS that the pH is impacting the fibre structures with different cations. We now wanted to investigate how those different fibre structures would form radical anion when irradiated to link nanostructure to radical anion performance and determine an optimal pH to use for photovoltaic devices. Solutions were irradiated using a 365 nm LED for 5 minutes to generate the radical anion.³⁶ Figure 2.16 (a) to (d) shows the spectra before and after irradiation. For all solutions at pH values between 5 and 9 peaks appeared at 725, 815, and 980 nm after irradiation, indicating formation of the radical anion.³⁷ There is also a change in the absorbance of the strong S₀-S₁ peaks indicating a change in molecular packing and the aggregates begin to self-assemble into larger nanostructures. However, these larger nanostructures can crash out making for less uniform solutions with varying structures in the precipitates. An increase in radical anion formation at the lower pHs is observed, meaning that the radical formation is favoured in the more aggregated or larger structures present at those pH values. Due to better stacking between the PBI core offering better electron transport between orbitals. According to the HS series K⁺ and Cs⁺ should stabilise larger aggregates and nanostructure better than the other

cations. For Li^+ and K^+ , the amount of radical formed is similar at pH 6 to 9. Only at pH 5, which is below both apparent pK_a s of Li^+ and K^+ , is there an increase in radical formed. This similarity in behaviour could be due to their similar apparent pK_a values which are closer together than the apparent pK_a values for Na^+ and Cs^+ . Cs^+ had the longest interval between apparent pK_a values and showed similar formation of radical anion at pH 6 and above. At pH 5, Cs^+ formed the most amount of radical compared to any other cation at the same pH. The SAXS at this pH showed that Cs^+ could be fitted to a flexible elliptical model with a larger power law, indicating the increased aggregation of nanostructures, possibly due to the increased stability of the larger aggregates due to Cs^+ . This improved stability of the self-assembled aggregates may be what allows them to form the most radical as well. Future work would look to quantify the different amount of radical anion at the different pHs using electron paramagnetic resonance (EPR).

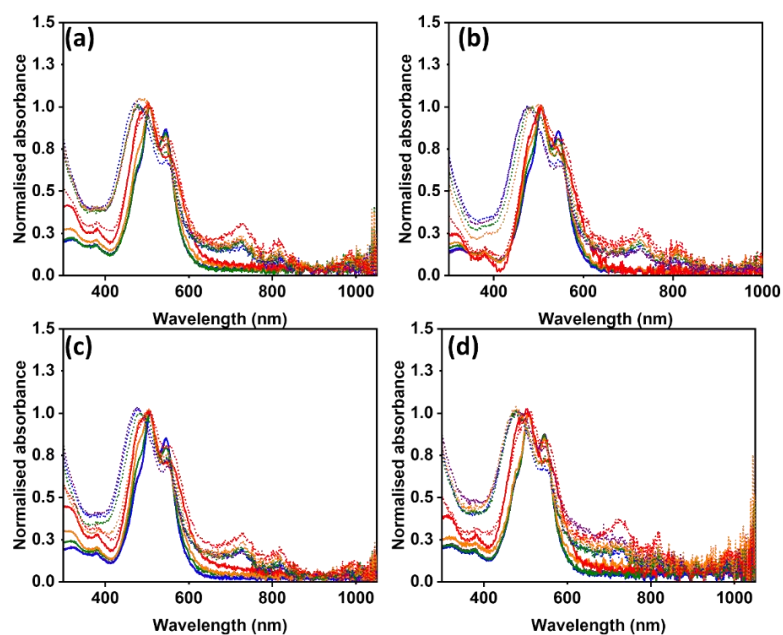


Figure 2.16. UV-vis absorption spectra of solutions with (a) Li^+ , (b) Na^+ , (c) K^+ , and (d) Cs^+ , at pH 5 before (solid red) and after irradiation (dotted red), pH 6 before (solid orange) and after irradiation (dotted orange), pH 7 before (solid green) and after irradiation (dotted green), pH 8 before (solid blue) and after irradiation (dotted blue), and pH 9 (solid purple) and after irradiation (dotted purple).

2.2.2 Investigation of hydrogels of **PBI-L** with different cations made using a pH trigger

Solutions at pH 7 were then used to prepare hydrogels using a pH trigger, as seen above the longer nanostructure materials can form more radical anion. By using a pH trigger the PBI can form even larger nanostructures and a 3D network more uniformly than when the pH was lowered using HCl. Reducing the inconsistencies of the aggregate sizes found in the precipitated solutions. The pH trigger used was GdL, as it is known to lower the pH through hydrolysis at a rate slower than the rate of its dissolution in water, giving uniform hydrogels.³⁸ Figure 2.17 shows a photo of the hydrogels with a final pH of 3.4 made using solutions containing different cations and triggered using GdL. It was observed that samples with the different cations could all be inverted after being allowed to gel overnight, which is a good initial indication that they may have formed hydrogels.

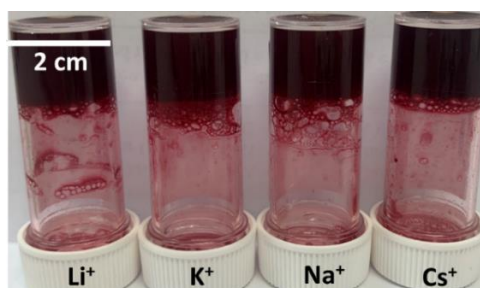


Figure 2.17. Pictures of inverted Sterilin vials showing hydrogels made with Li^+ , K^+ , Na^+ , and Cs^+ and triggered using GdL.

The differences in the bulk mechanical properties of the hydrogels were evaluated using rheology. The average strain and frequency sweeps were collected and are shown in Figure 2.18 (a) and (b) with the key bulk mechanical properties of the hydrogels summarized in Table 2.5. The linear viscoelastic region is the range over which a strain can be applied without causing any structural damage to the network of the sample. The $\tan\delta = (G''/G')$ is a measure of how elastic ($\tan\delta < 1$) or plastic ($\tan\delta > 1$) a system is. The yield point is the point when G'' and G' deviate from linearity, indicating that the network is starting to break. The flow point is the point when G'' and G' cross and the sample becomes more like a solution.

The shapes of the strain sweeps and $\tan\delta$, Figure 2.18 (a), are all very similar indicating that the 3D hydrogel matrices they are forming are similar in terms of cross-

link density or entanglement. However, both the strain and frequency sweeps indicate that stiffness changes with increasing size of cation, which agrees with what has been previously reported.²⁴ A further observation was that when the cation size was increased, the yield point of the hydrogel increased. Yield points around 10% are lower than what is seen for polymer but expected for that of low molecular weight gelators (LMWGs).¹⁰ Bulk mechanical properties such as the stiffness and strength can be impacted by a number of the gels' properties such as fibre shapes or type of cross link.¹⁰ It is difficult to pinpoint which of these factors is impacting the stiffness, however, because the stiffness does change following the cation size, we can estimate that it has to do with the ability of the cations to salt out. Due to their smaller charge density, larger cations such as K^+ and Cs^+ are better at salting out and can strengthen the hydrophobic effect of the fibre structures. The largest stiffness was seen for Li^+ and Na^+ with $G' = 1300$ Pa and $G'' = 95$ Pa, and $G' = 1100$ Pa and $G'' = 77$ Pa, respectively. The stiffness for K^+ and Cs^+ was similar with $G' = 628$ Pa and $G'' = 45$ Pa, and $G' = 680$ Pa and $G'' = 52$ Pa, respectively. Li^+ , due to its small size it can pack better between molecules leading to smaller aggregates and make the larger fibre structures less stable. Cs^+ should lead to more stable fibre structures because of its large size leading to larger aggregates. As the pH is lowered and the fibres begin to elongate and entangle, the improved solubility may allow the fibres to cross-link better. The yield point is the point at which the hydrogel network begins to break: a higher yield point means a stronger hydrogel network. Cs^+ formed the strongest hydrogel with a yield point of 16% strain, and K^+ the second strongest with a yield point of 13% strain. This was followed by Na^+ with a yield point of 10% strain and lastly Li^+ , with a yield point of 7.9% strain. These differences may have to do with the different cations' ability to stabilise the aggregates, which in turns strengthens the fibres as they bundle together and causes fibre thickening.

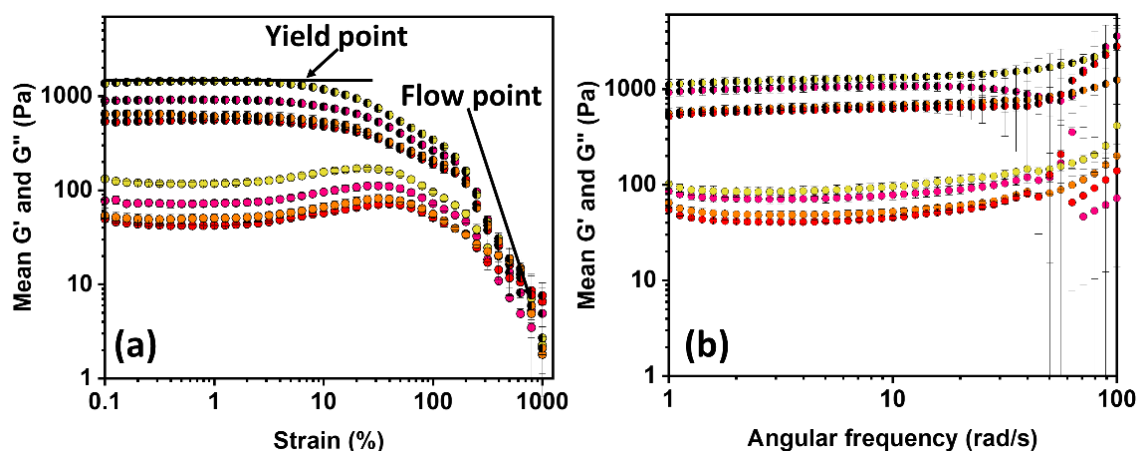


Figure 2.18. (a) Strain sweep at 10 rad/s and (b) frequency sweep at 0.5% strain. Data for Li⁺ (yellow), Na⁺ (pink), K⁺ (red), and Cs⁺ (orange). In all cases, the storage modulus (G') is represented by closed symbols and the loss modulus (G'') is represented by open symbols. Measurements were performed in triplicate and errors were calculated from the standard deviations.

Table 2.5. Key bulk mechanical properties of the hydrogels with Li⁺, Na⁺, K⁺, and Cs⁺. G' and G'' are taken at 10 rad/s frequency.

	Li ⁺	Na ⁺	K ⁺	Cs ⁺
Loss modulus G'' (Pa)	95 ± 11	77 ± 8.2	45 ± 2.1	52 ± 4.2
Storage modulus G' (Pa)	1300 ± 110	1100 ± 99	620 ± 21	680 ± 73
Yield point (%)	7.9	10	13	16
Flow point (%)	790	N/A	790	410
$\tan\delta$ (G''/G')	0.073	0.071	0.072	0.076

The bulk rheological properties of the hydrogels with different cations are different and this may be due to variation in the fibre structures. To investigate this further, SAXS of the hydrogels was collected to gain insight into the micellar and nanostructures. Figure 2.19 shows the SAXS data and suitable fits. Full fitting parameters for Li⁺, Na⁺, K⁺, and Cs⁺ are found in Table 2.6. Hydrogels for Li⁺, Na⁺, and K⁺, were fitted to a flexible elliptical cylinder model combined with a power law: we have reported this previously for similar systems.^{13, 39} However, the SAXS data of

Cs⁺ hydrogels were fitted to a mass fractal model. This indicates the network formed with Cs⁺ may be diffusion limited and branched: this shows how the choice of cation can have an impact on the gel network due to the larger aggregates formed with the large cation. Hydrogels with Na⁺ had the largest cylinder radius at 3.57 nm, while the cylinder radius for Li⁺ was 1.61 nm, and for K⁺ it was 1.41 nm. The cylinder length for Na⁺ was manually fitted to 300 nm. This length value was chosen because it is sufficiently large and is outside the range of the measurement for long cylinders. The cylinder lengths for Li⁺ is the smallest and increases with K⁺, this follows the HS which indicates the larger the cation the larger the overall aggregates and micellar structure should be. Showing how the cations salt in/out affect can be used to impact the morphology and length of the fibres which in term can lead to a change in the gel network.

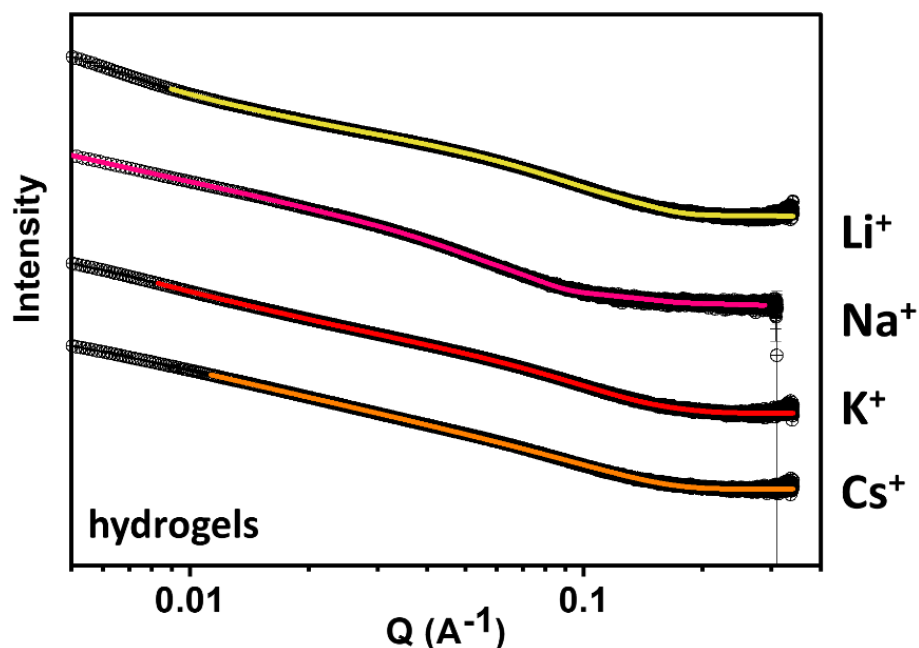


Figure 2.19. SAXS data for hydrogels with Li⁺ (yellow), Na⁺ (pink), K⁺ (red), and Cs⁺ (orange). Experimental data shown as black symbols and fits as solid-coloured lines. Note the data are offset on the intensity scale for clarity.

Table 2.6. SAXS fitting results for solutions with Li^+ , Na^+ , K^+ , and Cs^+ , counter ions as hydrogels. *No fitting error available.

Cation	Li^+	Na^+	K^+	Cs^+
Model	Flexible elliptical cylinder + power law	Flexible elliptical cylinder + power law	Flexible elliptical cylinder + power law	Mass fractal
Length (nm)	103 ± 0.000623	300*	275 ± 2.99	N/A
Kuhn length (nm)	10.3 ± 0.0537	15.2 ± 0.135	4.01 ± 0.0517	N/A
Cylinder radius (nm)	1.61 ± 0.00282	3.57 ± 0.0176	1.41 ± 0.00553	N/A
Axis ratio	2.52 ± 0.00524	2.23 ± 0.00134	2.13 ± 0.0734	N/A
Power law	4.21 ± 0.00746	2.76 ± 0.00446	3.47 ± 0.00376	N/A
Radius (nm)	N/A	N/A	N/A	1.72 ± 0.00275
Mass fractal dimension	N/A	N/A	N/A	2.25 ± 0.00165
Cut-off length (nm)	N/A	N/A	N/A	90.5 ± 10.1
χ^2	2.4	2.1	1.7	1.2

Gelation is triggered by the hydrolysis of GdL, which is slow and reproducible enough to be monitored over time using parallel techniques. The difference in apparent pK_a values will directly impact the gelation process as the pH required to undergo a transition in self-assembly will be reached at different points in time with different cations. The differences in the assembly with different cations in solution at different pHs have already been seen in the viscosity, UV-vis absorption, and SAXS data. To investigate whether the differences in the structures formed and behavior of the gels are caused by the cation directly or the influence of the cation on the gelation kinetics, the pH, rheology, and viscosity of the assembly process was monitored with time. The viscosity data are useful as they measure the development of structures in solution before they may appear in the rheology.⁴⁰ Overlaying all of the data from the different techniques this way allows for correlation of differences between the self-assembly of the aggregate structures with the differences in the bulk rheological properties as the pH is changing. This gives us an idea of the gelation kinetics.

The gelation kinetics of Li^+ are plotted in Figure 2.20 and overlaid with the changes in G' , G'' , and viscosity. There is an initial drop in pH below the apparent pK_{a1} value within the first 10 minutes of gelation. After this time, solid-like properties begin emerging as G' rises steeply. The increasing trend in G' and G'' values then stops and they both begin to decrease at around 15 minutes. At this time the pH has increased due to structures rearranging causing a buffering and then slowly decreases to pH 5.6 when G' and G'' begin to increase again.⁴¹⁻⁴³ Interestingly, there is no obvious change in the viscosity during the decrease in G' and G'' . This indicates that, while the aggregates have solid-like behaviour, the structures are not elongating or thickening, but may just be rearranging or buffering. At around 25 minutes the decrease of G' and G'' stops and the viscosity begins increasing as larger structures start to form. It is not until the pH drops below the apparent pK_{a2} that G' and G'' increase sharply and then plateau as gel formation is complete ($\tan\delta = 0.02$ and unchanging over time). The viscosity plateaus earlier and then decreases as the gelling fibres begin to align under shear. Differences in the $\tan\delta$ compared to the bulk strain data are due to the change in geometry used in this measurement.⁴⁴

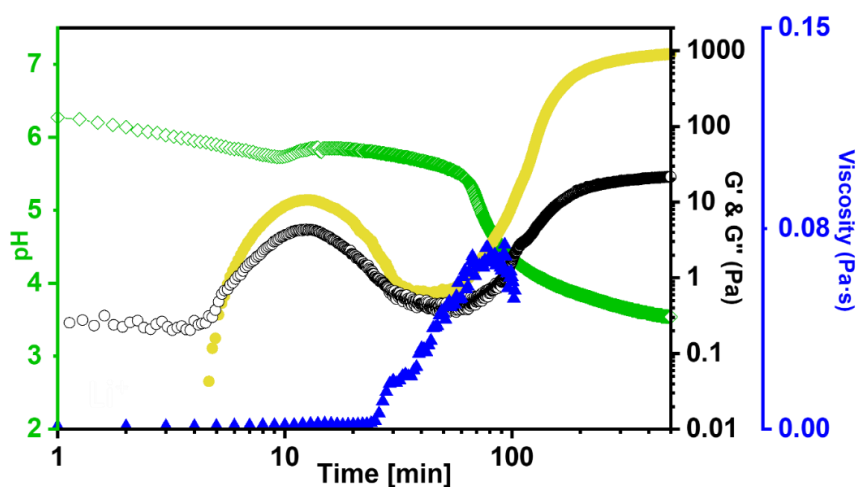


Figure 2.20. Development of G' (yellow data) and G'' (black data) over time during the gelation with Li^+ at a strain of 0.5% and a frequency of 10 rad s^{-1} , compared to the change in pH (green data) over time and the change in viscosity (blue data) at a shear rate of 10 s^{-1} .

Analogous data for Na^+ are shown in Figure 2.21. The behaviour of G' and G'' as the pH is lowered for Na^+ was more typical of what has previously been reported for other

PBI systems.⁴⁰ The viscosity increased within a couple of minutes after the measurement began. Na⁺ becomes protonated faster, and the structures begin to elongate quicker but do not exhibit solid-like behaviour yet. Once again, the viscosity plateaued after the pH had dropped below the apparent p*K*_{a2}. Then, the viscosity decreased as the gel fibres aligned under shear. Beyond 60 minutes the values of G' and G'' plateaued with a final tanδ = 0.02.

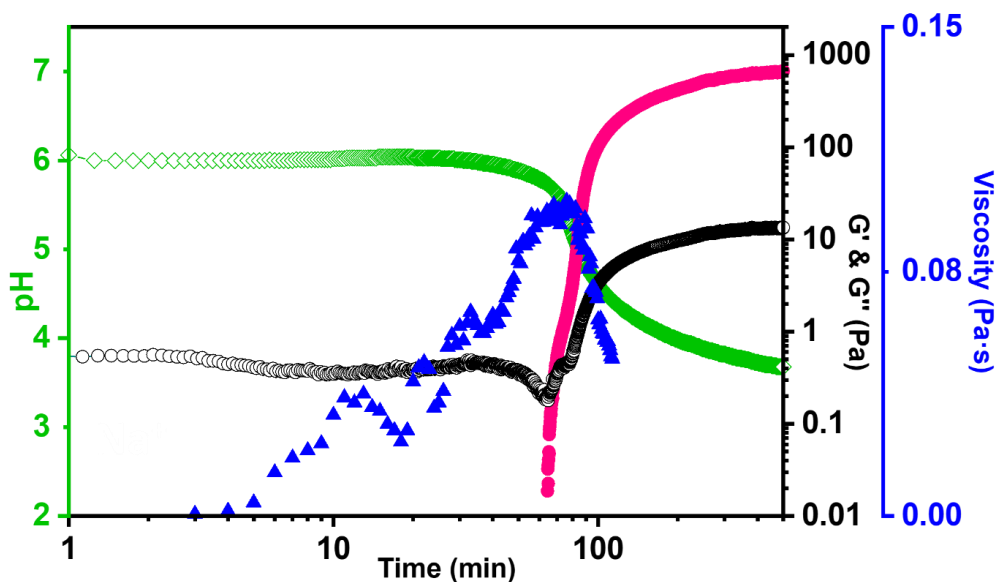


Figure 2.21. Development of G' (**pink data**) and G'' (**black data**) over time during the gelation with Na⁺ at a strain of 0.5% and a frequency of 10 rad s⁻¹, compared to the change in pH (**green data**) over time and the change in viscosity (**blue data**) at a shear rate of 10 s⁻¹.

Analogous data for K⁺ are shown in Figure 2.22. The change in G' and G'' over time shows the presence of persistent structures from the very first data point. After 10 minutes, when the pH drops below the apparent p*K*_{a1}, the G' and G'' increase further. This increase in the G' and G'' is accompanied by a sharp increase in viscosity. After 10 minutes G' and G'' increase more gradually while the pH is buffered through the apparent p*K*_{a2}. This has been observed previously for similar systems.²⁴ While G' and G'' gradually increase, the viscosity plateaus and then continues to increase as the pH begins to drop below the apparent p*K*_{a2} and the structures continue to assemble, now entangling until they have formed a gel. When the pH is lowered further, bulk

rheology shows a change in the mechanical properties which has been previously reported for hydrogels undergoing syneresis.^{15, 45} This results in a final $\tan\delta = 0.03$.

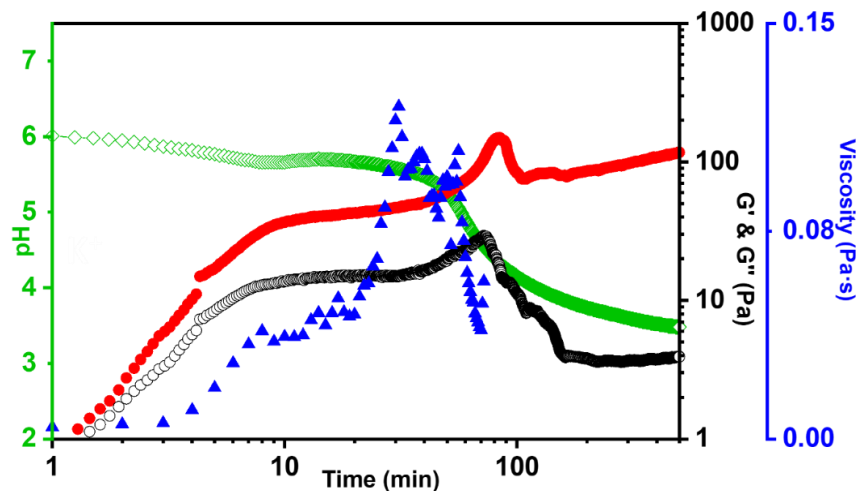


Figure 2.22. Development of G' (red data) and G'' (black data) over time during the gelation of K^+ at a strain of 0.5% and a frequency of 10 rad s^{-1} , compared to the change in pH (green data) over time and the change in viscosity (blue data) at a shear rate of 10 s^{-1} .

Lastly, analogous data for Cs^+ are shown in Figure 2.23. By the time the first measurement is taken, solid-like materials are already present in the rheology. This is accompanied by a large viscosity value for the solution, which agrees with our dynamic viscosity measurements at pH 6 which showed the viscosity to be larger for Cs^+ compared to the other systems. This can also be explained by the different apparent pK_a values. Cs^+ has the highest pK_{a1} value and longest interval between the two pK_a values. G' and G'' increase gradually while the pH is buffered through both apparent pK_a values. The viscosity data show a plateau at 10 minutes which correlates with the end of the pK_{a1} buffering phase and the beginning of the pK_{a2} buffering phase. The viscosity increases again after 15 minutes and continues increasing until the pH drops below the apparent pK_{a2} , at which point the gelled fibres are aligning with the constant shear. Below the apparent pK_{a2} there is also a change in the mechanical properties which is attributed to the hydrogels undergoing syneresis.^{15, 45} The final stiffness is like that of K^+ , which agrees with the bulk rheological measurements.

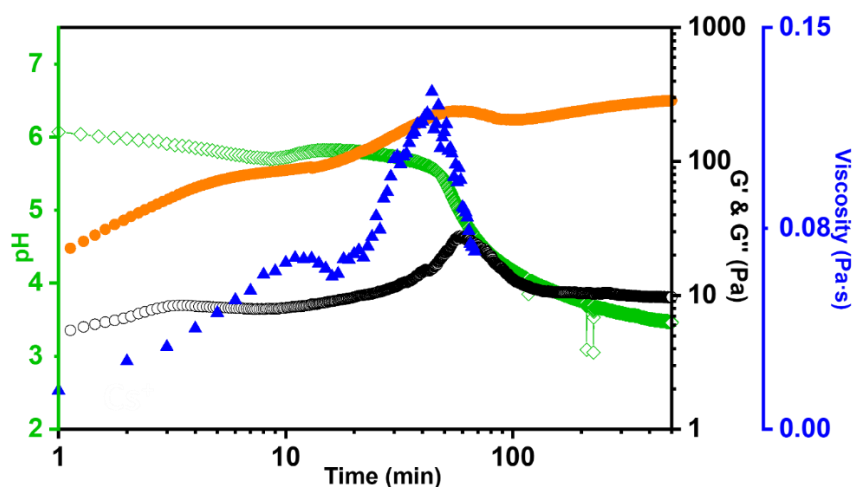


Figure 2.23. Development of G' (orange data) and G'' (black data) over time during the gelation of Cs^+ at a strain of 0.5% and a frequency of 10 rad s^{-1} , compared to the change in pH (green data) over time and the change in viscosity (blue data) at a shear rate of 10 s^{-1} .

It is apparent from kinetic studies that cation choice influences the gelation process due to its ability to change the aggregates structures. As the cation sizes increase, the viscosity starts to increase earlier as the pH is lowered. Cs^+ has the highest viscosity by the time that the first measurement is taken. This agrees with the viscosity at different pHs which showed the Cs^+ solutions to be more viscous than the others as the pH was lowered. This difference in the rate of viscosity change as the pH is lowered may be due to the larger cations' ability to stabilise the larger aggregates as it has a smaller charge density and is not able to pack into the aggregates as efficiently as larger charge density cations. This difference also agrees with the SAXS data where Cs^+ at pH 5 was the only solution that could be modelled in the high- Q region. At this pH Cs^+ was able to be fitted to a flexible elliptical cylinder model while K^+ was fitted to a mass fractal model and Na^+ and Li^+ were cut off in the high- Q region. This is possibly due to their poor solubility or ill-defined aggregation. A similar trend was also observed for the development of G' and G'' over time: as the cation size increases and the aggregates are more stable, the transition from solution to gel becomes more gradual. Li^+ and Na^+ should improve the solubility of the gelator and therefore the fibres will not have bundled together to acquire solid-like properties while K^+ and Cs^+ will reduce the solubility of the gelator and so the fibres are bundling together easier and have solid-like properties sooner.

The SAXS showed that the hydrogels with different cations had different fibre structures. To see if these different structures would impact the ability of the hydrogels to form radical anion, the UV-vis absorption spectroscopy was measured in the same way as for the solution. The spectral data are shown in Figure 2.21 (a) and (b). It is evident from Figure 2.24 (a) that the ratios of the S_0-S_1 peaks at 507 nm and 550 nm of the hydrogels with different cations have changed compared to the ratios for the solutions before irradiation. There is a higher absorbance intensity of the 0-1 vibronic transition of the S_0-S_1 transition band at 507 nm compared to the 0-0 transition band at 550 nm. This change in the ratio is expected since, as the fibres entangle and form a hydrogel network, their molecular packing will change as well.³⁶ After the hydrogels are irradiated, there is a change in the intensity ratios for the S_0-S_1 peaks: the ratio increases with Li^+ , K^+ , and Cs^+ , but decreases with Na^+ . Three new peaks at 730 nm, 815 nm, and 990 nm appear, which indicate the formation of radical anion.³⁷ Figure 2.21 (b) is an expansion of the lower frequency and near-IR region of the spectrum. It is seen that hydrogels with K^+ or Cs^+ form more radical anion than those with Li^+ or Na^+ . This shows potential for improved radical formation based on improved aggregate structure due to the salting out and salting out impact of the cation choice.

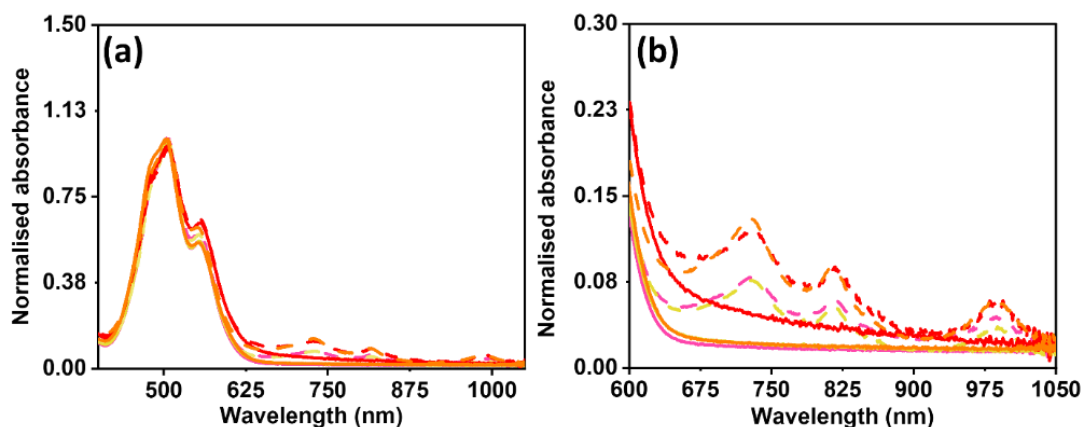


Figure 2.24. (a) UV-vis absorption spectra of hydrogels with Li^+ before (solid yellow) and after (dashed yellow) irradiation, Na^+ before (solid pink) and after (dashed pink) irradiation, K^+ before (solid red) and after (dashed red) irradiation, and Cs^+ before (solid orange) and after (dashed orange) irradiation. (b) Expansion of UV-vis absorption spectra of hydrogels with Li^+ , Na^+ , K^+ , and Cs^+ , focused on 600 nm to 1050 nm before and after irradiation.

2.2.3 Use of **PBI-L** solutions with different cations for photovoltaic applications

Solutions with different cations at pH 6 were prepared for Dr. J. Cameron to fabricate into photovoltaic devices. This pH was chosen because the SAXS showed differences in the micellar aggregated structures, and it was below the apparent pK_{a1} values. The devices were fabricated using a previously published method, except that the spin coating rate was lowered to 1000 rpm for the deposition of the **PBI-L** interlayer due to an increase in concentration used.⁷

First, we wanted to investigate the reduction potential by measuring the CVs of the solutions at pH 6, Figure 2.25. To investigate if the different micellar and nanostructures have impacted the reduction potentials of the radical anion. The reduction potentials for the radical anion are summarised in Table 2.7, there is no significant difference between the reduction potential values. The shape of the CVs did change with the different cations with, interestingly, Na^+ being different to the others. The shape of CVs changes based on how electrons are moving through the system. These systems were all set up in the same manner therefore the difference is not due to differences in experimental set-up. Instead, differences CVs shape can be linked to the in the movement of electrons due to the different micellar and nanostructures cause by the salting out/in effect from the cation choice. As the cation increases in charge density, they stabilise smaller aggregates. The different aggregate sizes lead to different micellar and nanostructures which show they affect this electron movement. The different micellar and nanostructures were confirmed by the SAXS at pH 6 which showed for all cations could be fitted to a correlation model with varying differences in the fibre density at the local scale. At pH 6, Na^+ was the one with the largest correlation length and smallest Lorentzian exponent indicating a large difference in the fibre density compared to the other cations. This explains why the shape of Na^+ was so different to the others and shows how different morphologies can cause different electron movement through the system, which leads to differences in CV shape.

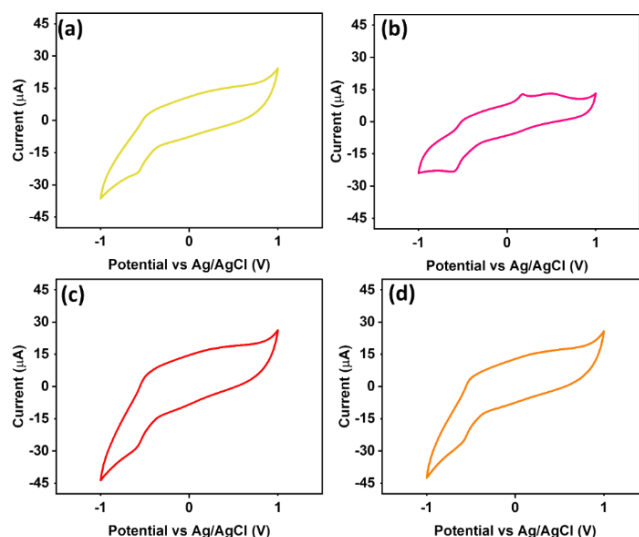


Figure 2.25. Cyclic voltammograms of Li^+ (yellow), Na^+ (pink), K^+ (red), and Cs^+ (orange) using 0.1 M NaCl electrolyte solution with a scan rate of 0.05 V/s at pH 6.

From these CVs the experimental ionization potentials (IP) were calculated. Due to limits in the solvent window for water, the electron affinity (EA) and energy band gap (E_{gap}) was determined from a Tauc Plot shown in the Appendix. The calculations for EA and IP values and Tauc Plot are described in section 2.4.8 and the values are summarised in Table 2.7. The IP can be related to the highest occupied molecular orbital (HOMO) and the EA can be related to the lowest unoccupied molecular orbital (LUMO). A lower-lying LUMO value is favourable for photovoltaics as it means there is less energy required for an electron to be further excited and form the radical anion. Altering the HOMO/LUMO energy levels of PBIs is typically done through functionalisation of the aromatic core. Here we have demonstrated adjustments in the HOMO/LUMO energy levels through simple changing of fibre structure. This is possible because of the changes in aggregation of the PBI salting in / out impact of the cation choice where Li^+ allows for them to pack more tightly than Cs^+ .

Table 2.7. Experimental ionisation potential (HOMO) and electron affinity (LUMO) values for Li^+ , Na^+ , K^+ , and Cs^+ at pH 6 using the SHE vs. vacuum = 4.28 eV.⁴⁶

Cation	-EA (eV vs vacuum)	-IP (eV vs vacuum)	ΔE_{gap}
Li^+	- 4.18	- 6.33	2.15
Na^+	- 4.20	- 6.31	2.10
K^+	- 4.15	- 6.27	2.10
Cs^+	- 4.15	- 6.29	2.15

These PBIs' ability to form radical anion after being irradiated with light has been linked to aggregation packing and self-assembled morphology.⁸ The UV-vis absorption data showed that at pH 6 the molecular packing was very similar for all cations. However, similarity in the packing does not necessarily imply similar self-assembled morphology, as was observed in the SAXS of the solutions with different cations before irradiation. After irradiation Cs⁺ formed the most amount of radical anion whereas the other cations formed larger and similar amounts.

The SAXS was collected to probe the secondary structures of the different solutions at pH 6 after forming radical anion. Figure 2.26 show the SAXS data for solutions at pH 6 after being irradiated for 5 minutes with UV light and the fits used to model the data. Model parameters used to fit the data are summarised in Table 2.8. The correlation length model was used to fit the data. There are some differences in the data compared to the initial pH 6 solutions which may be due to the different X-ray scattering instruments used.²⁹ These measurements were done using an in-house instrument and not a synchrotron and are not able to resolve larger structures as well. Therefore, the irradiated structures will only be compared to one another and not the initial structures at pH 6. The Lorentzian exponent for Li⁺ and Na⁺ after irradiation is similar and above 2 meaning reduced fibre-solvent interactions. The Lorentzian exponents for K⁺ and Cs⁺ were manually fitted to 4, implying further reduced fibre-solvent interactions compared to the other cations. This is explained by the HS which indicates that K⁺ and Cs⁺ are increasing the surface tension between the fibres and solution. The correlation lengths ranged from largest at 3.49 nm for Li⁺ to smallest at 3.02 nm for Cs⁺. This indicates the interfibrillar crosslinks for the high Q region are getting closer as the size of cation increases. This also indicates the fibre mesh is less compact compared to the other cations over a larger scale. This decrease in compactness may explain the difference in radical anion formation for Cs⁺ seen in the UV-vis absorption.

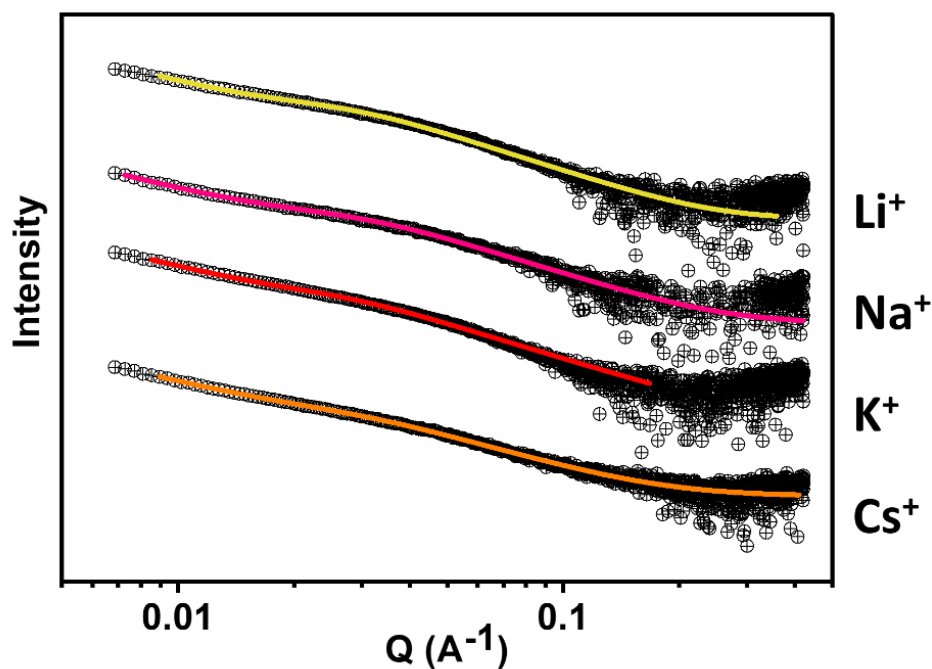


Figure 2.26. SAXS data for solutions prepared at pH 6 with Li⁺ (yellow), Na⁺ (pink), K⁺ (red), and Cs⁺ (orange) after irradiation, with the experimental data shown as black symbols and the fits as coloured lines. Note the data are offset on the intensity scale for clarity.

Table 2.8. SAXS fit table for solutions prepared at pH 6 with Li⁺, Na⁺, K⁺, and Cs⁺ after being irradiated for 5 minutes. *No fitting error available.

Cation	Li ⁺	Na ⁺	K ⁺	Cs ⁺
Model	Correlation length	Correlation length	Correlation length	Correlation length
Correlation length (nm)	3.49 ± 0.00319	3.21 ± 0.0404	3.33 ± 0.005	3.02 ± 0.0708
Porod exponent	3.08 ± 0.00142	2.79 ± 0.0402	3.21 ± 0.0005	2.62 ± 0.0547
Lorentzian exponent	3.84 ± 0.00675	3.83 ± 0.0531	4*	4*
χ^2	5.3	5.0	8.7	2.8

The transmittance of **PBI-L** layers deposited on ITO/ZnO was then investigated to compare the different aggregates' impact on absorbance of the films. Figure 2.27 (a) to (d) shows the transmittance spectra for the different cations with the transmittance values summarised in Table 2.9. These transmittance values are comparable to PBIs

with different amino acid side chains.⁷ Li⁺ and Cs⁺ had λ_{max} at a slightly shorter wavelength compared to that of Na⁺ and K⁺. Na⁺ and K⁺ had similar values for the transmittance of around 73.0% and were slightly more strongly absorbing than Li⁺ or Cs⁺. Overall, there is not a significant difference in the transmittance between the films made using different cations.

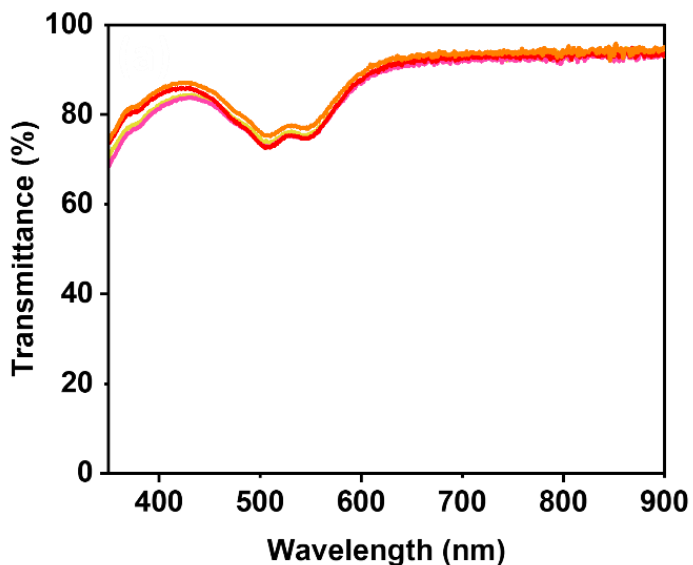


Figure 2.27. Transmittance spectra of ITO/ZnO/PBI-L films where the solution contained Li⁺ (yellow), Na⁺ (pink), K⁺ (red), and Cs⁺ (orange). Transmittance at λ_{max} is reported for the visible region.

Table 2.9. Transmittance at λ_{max} is reported for the visible region for the ZnO/PBI-L bilayer films determined.

Cation	Li ⁺	Na ⁺	K ⁺	Cs ⁺
λ_{max} (nm)	509	507	507	509
$T_{\lambda_{max}}$ (%)	73.5	72.9	72.7	75.3

The force-penetration depth curves were obtained using a nanoindenter, Figure 2.28 (a) to (b). From these curves the hardness and elastic modulus could be determined before and after being irradiated with UV light for 5 minutes. Indentation has been used to probe the PBIs in a hydrogel system before and after irradiation, it showed that the irradiation led to higher elastic moduli. We wanted to investigate if this behaviour was the same for the ZnO/PBI-L films. For the initial films it was seen that

the Na⁺ films had a lower elasticity and hardness than the others. The Li⁺ films were the hardest while Cs⁺ were the most elastic. After irradiation, there was an increase in the elasticity for all the films which is consistent with what was seen previously with hydrogels made using a similar PBI. The greatest increase was observed for Li⁺ and Na⁺. The elasticity for K⁺ and Cs⁺ before and after irradiation was within the error margins meaning there was no statistically significant change. There was also a decrease in hardness for Li⁺ after irradiation, while Na⁺ films increased in hardness. Again, there was no statistically significant change in hardness for K⁺ and Cs⁺.

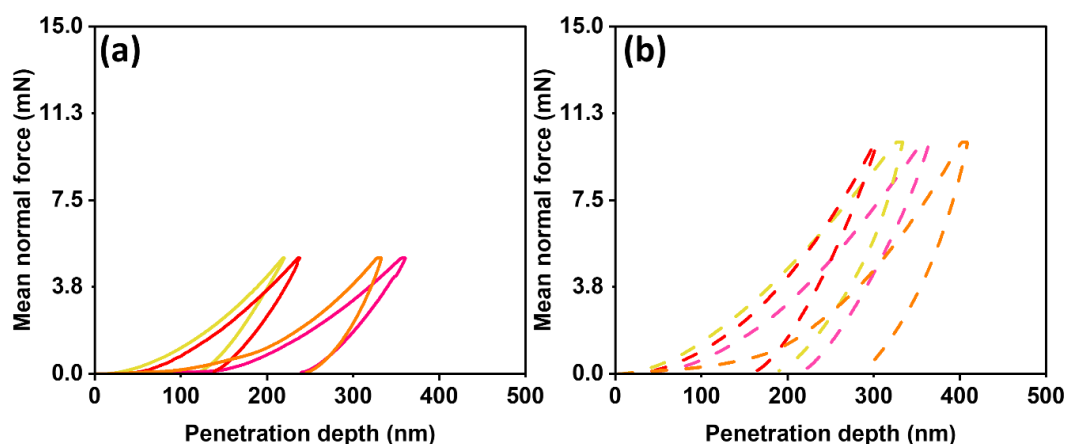


Figure 2.28. Force-penetration depth curve obtained during nanoindentation of the ZnO/PBI-L bilayer films (a) before irradiation and (b) after irradiation with UV light.

Table 2.10. Hardness and elastic moduli of the ZnO/PBI-L bilayer films determined from matrix measurements before and after irradiation with UV light using an Oliver Model.^{47, 48}

		Elastic modulus (GPa)	Indentation hardness (MPa)	Vickers hardness (Vickers)
Li ⁺	before irradiation	67.1 ± 3.11	6260 ± 393	580 ± 36.4
	after irradiation	95.7 ± 1.14	4760 ± 155	440 ± 14.7
Na ⁺	before irradiation	41.5 ± 9.28	2790 ± 830	258 ± 76.9
	after irradiation	62.4 ± 8.69	4630 ± 600	429 ± 55.5
K ⁺	before irradiation	61.2 ± 14.2	3810 ± 1690	352 ± 156
	after irradiation	70.3 ± 10.8	5100 ± 1755	472 ± 162
Cs ⁺	before irradiation	74.3 ± 6.83	4850 ± 1880	448 ± 174
	after irradiation	79.0 ± 0.533	5730 ± 2460	531 ± 227

The performance of the different aggregates of **PBI-L** with the different cations were determined by measuring their current–voltage and extrapolating their performance parameters, Table 2.11. The zinc oxide is the electron transport layer, consistent with the previous devices made with the different PBIs. As before the PBI layer is acting as an interlayer to inhibit non-geminate recombination and improve electron extraction. OPV devices were prepared using two donor materials, P3HT and PCE10. P3HT has been widely used as a donor material for OPV devices.⁴⁹⁻⁵¹ However, PCE10 has a wider absorption band and increased absorption coefficient leading to better reported efficiencies.^{52, 53} Due to **PBI-L** at 5 mg/mL being so strongly absorbing, the butyric acid methyl ester (PC₆₁BM) acceptor material that was previously combined into the donor layer was removed. Li⁺ gave the best PCEs of 0.33% when used with the donor PCE10, with the ideal PCE for similar systems being 3%. For Li⁺ compared to the other devices containing **PBI-L** tested prior the open circuit voltage (V_{oc}) was good as it was near 0.5 V, fill factor (FF) adequate as it was higher than 0.4. However, the short-circuit current density (J_{sc}) was low (below 1), albeit higher than any of the other devices tested here. One possible explanation for the better performance by Li⁺ is given by the force-penetration depth curve which showed the largest increase in elasticity of these films. Also, they were the only films to decrease in hardness showing some kind of change in the aggregated structure upon formation of the radical anion which may be more favourable. Interestingly, while K⁺ and Cs⁺ have shown the most formation of radical in solution they have performed the worse, this could be due to drying effects, however, repeats would be required to confidently conclude on this.

This may be optimised further by improving the absorption through altering layer thicknesses or improving morphology by annealing. One of the challenges of planar heterojunction device design is a low surface area for the interface between donor and acceptor and this is likely causing a low J_{sc} . The PCE is low but not far from values reported for planar heterojunctions which are not as efficient as bulk heterojunction devices. However, significant work is required to confirm the performance of these devices, ideally there would be repeat measurements with several devices to determine errors. Unfortunately, the thermal evaporation equipment was unavailable and multiple devices could not be fabricated in time. This

work instead just shows proof of concept that the different cations may be a useful way to tailor the **PBI-L** aggregation to improve its performance as an interlayer.

Table 2.11. Summary of results from P3HT and PCE10 OPV devices with different cation.

PBI layer	Donor layer	J _{sc} (mA cm ⁻²)	FF	V _{oc} (V)	PCE (%)
Li ⁺	P3HT	0.25	0.46	0.25	0.029
	PCE10	0.94	0.52	0.68	0.33
Na ⁺	P3HT	0.23	0.48	0.29	0.033
	PCE10	0.32	0.25	0.05	0.004
K ⁺	P3HT	0.044	0	0	0
Cs ⁺	P3HT	0.18	0.51	0.36	0.033
	PCE10	0.36	0.27	0.11	0.01

2.3. Conclusions

This work looked at improving the radical anion formation of **PBI-L** by changing the micellar and nanostructures in solution by changing the size of the cation of the basic solution used to solubilise the PBI. HS series says smaller more densely charged cations (Li⁺ or Na⁺) should stabilise smaller aggregates while larger less densely charge cations (K⁺ or Cs⁺) will have the opposite effect.

PBI-L with Cs⁺ was the most viscous in solution at pH 6, which indicated fibrous structures of different morphologies compared to the other cations. This was expected due to the HS predicting it would be the best at salting out. The viscosities at different pHs were then measured and showed that the changes in the aggregates structure did follow HS. Particularly at pH 5 which showed structures formed with Li⁺ and Na⁺ were noticeably different than the others. SAXS gave a deeper insight into the aggregate structures; **PBI-L** was extremely dependent on pH and cation choice as they assembled differently due to different apparent pK_a values. With the larger cations stabilising the larger aggregates packing more than the smaller cations, which resulted in the differences in the radius of the fibres formed at pH 5. UV-vis absorption spectroscopy of **PBI-L** with different cations at different pHs showed an

increase in radical formation as pH was lowered, with the amount of radical formed being best for Cs⁺ which increased the aggregates stability.

Hydrogels were made using a pH trigger because the solutions had shown the radical anion formation improved when pH was lowered. Bulk rheological measurements showed the stiffness decreased and strength increased as cation size was increased. We believe that the differences in mechanical properties were due to differences in fibre morphology. Kinetics measurements showed these aggregates were assembling into a gel network differently, with K⁺ and Cs⁺ having a more gradual increase in the solid-like properties leading to less stiff gels. UV-vis absorption spectroscopy of the hydrogels showed that K⁺ and Cs⁺ formed more radical anion. Supporting the theory that the cation choice could be used to change the micellar aggregates and improve radical formation with larger cations being favoured due to them stabilising the larger aggregates packing.

As the work had shown that the cation choice could be used to change the micellar and nanostructures in solution and in hydrogels which lead to a change in the radical anion. We wanted to see if we could improve **PBI-L** performance as an interlayer for photovoltaic devices. The solutions with different cations at pH 6 were used because the SAXS showed a difference in the nanostructure, but they had not precipitated out of solution. Nanoindentation which had only been done on hydrogels of these materials previously showed that that the irradiation led to higher elastic moduli. OPV devices with Li⁺ gave the best PCE for **PBI-L** devices that we have seen, however, these were only initial studies and multiple devices will need to be measured to confirm this.

2.4. Experimental

2.4.1. Preparation of **PBI-L** solutions

Solutions were prepared at a concentration of 10 mg/mL of **PBI-L**. For the preparation of 5 mL of solution, 50 mg of **PBI-L** was weighed into a vial. One molar equivalent of 0.1 M XOH (X = Li, Na, K, or Cs) was added to the PBI and the volume was made up to 5 mL with deionised water. The solution was stirred for at least 16 hours to allow all the PBI to dissolve. A large stock solution of each PBI was prepared to ensure that the solutions were the same for each experiment. The pH of each vial

was then adjusted as necessary using 2 M HCl or 2 M XOH (X = Li, Na, K, or Cs) to obtain the desired pH. Preparation of all samples was carried out at room temperature (around 25°C in the daytime).

2.4.2. Preparation of hydrogels

Hydrogels were formed using a pH switch from 10 mg/mL gelator solutions. 2 mL of the gelator solution was transferred to a 7 mL Sterilin vial which contained 8 mg/mL of glucono- δ -lactone (GdL) and shaken gently. This was left to stand for at least 16 hours to allow for gelation to occur. The samples that were stable to vial inversion after 16 hours were tested on the rheometer to confirm gelation.

2.4.3. Rheological measurements

Dynamic rheological and viscosity measurements were performed using an Anton Paar Physica MCR301 rheometer. Strain and frequency data were collected using a vane and cup geometry (ST10-4V-8.8/97.5) so that samples could be prepared in 7 mL Sterilin vials to remove any loading issues. Viscosity data were collected using a 50 mm cone (cone angle 0.994°) geometry and temperature-controlled bottom plate. Time sweeps were collected using 50 mm sandblasted parallel plates. All measurements were collected in triplicate at 25°C.

Viscosity measurements: a 1 mL aliquot of PBI solution at the desired pH was pipetted onto the bottom plate. The top plate was lowered on top of the solution to a gap height of 0.1 mm which is determined for the cone angle on the plate. Any excess sample was trimmed using a metal spatula ensuring no gaps or bubbles along the edge of the plate. A CP50 plate geometry was used to measure the viscosity. Measurements were recorded at shear rates from 0.1 to 1000% and performed in triplicate. Errors were calculated from the standard deviation.

Strain sweeps: strain sweeps were recorded from 0.1 to 1000% strain at a set frequency of 10 rad/s with a gap height of 2 mm. Samples were prepared as described previously in 7 mL Sterilin vials. Measurements were performed in triplicate and errors were calculated from the standard deviation.

Frequency sweep: frequency sweeps were recorded from 1 rad/s to 100 rad/s under a constant strain of 0.5% with a gap height of 2 mm. This strain value was chosen as

it is within the linear viscoelastic region for the hydrogels, as determined from the strain sweeps. Samples were prepared as described previously in 7 mL Sterilin vials. Measurements were performed in triplicate and errors were calculated from the standard deviation.

Constant shear viscosity measurement: constant shear tests were measured with a constant shear of 10 s^{-1} and a viscosity measurement was taken every 30 seconds. 2 mL of gelator solution was added to a Sterilin vial containing 8 mg/mL of GdL and shaken gently. The mixture was then poured onto the middle of the bottom plate and the top plate was lowered to a gap height of 0.1 mm. Any excess sample was trimmed using a metal spatula. A CP50 plate geometry was used to measure the viscosity. The circumference of the top plate was flooded with mineral oil to prevent the gel from drying whilst gelling. Measurements typically finished in 3-4 hours.

Monitoring G' and G'' over time: measurements were carried out at an angular frequency of 10 rad/s and strain of 0.5%. 2 mL of gelator solution was added to a Sterilin vial containing 8 mg/mL of GdL and shaken gently. The mixture was then poured onto the middle of the bottom plate and the top plate was lowered to a gap height of 0.8 mm. Any excess sample was trimmed using a metal spatula. A sanded PP50 plate geometry was used to monitor G' and G'' over time. The circumference of the top plate was flooded with mineral oil to prevent the gel from drying whilst gelling. Measurements were run overnight.

2.4.4. UV-vis absorption spectroscopy

UV-vis absorption spectra were measured using an Agilent Cary 60 spectrometer. For solution spectra, stock solutions of the PBIs at the various pHs were placed in a 0.01 mm demountable cuvette and absorption was measured between 200 nm to 1100 nm on the 600 nm/min scan rate. Gel samples were prepared by adding 2 mL of 10 mg/mL PBI stock solutions to 8 mg/mL of GdL in 7 mL Sterilin vials and gently swirling until complete dissolution of the GdL. 0.5 mL of this solution was pipetted into a 0.1 mm demountable cuvette which was then sealed with Parafilm and left to stand for at least 16 hours to allow for gelation to occur. Absorption was measured between 200 nm and 1100 nm on the 600 nm/min scan rate. To form the radical anion, the samples were irradiated using a 365 nm LED (LedEngin Inc, LZ1-10U600) powered

by a custom-built 700 mA constant-current power source for 5 minutes. The power received by the sample was measured to be 21.6 mW using a ThorLabs optical power meter PM100D with a ThorLabs S120VC 200-1100 nm 50 mW diode over an area of 225 cm². The number of photons that hit the sample during 5 minutes at that power was determined to be 5.29×10^{16} photons/cm².

2.4.5. Small-angle X-ray scattering (SAXS)

Samples for scattering were prepared by making stock solutions of **PBI-L** with different cations at a concentration of 10 mg/mL, adding an equimolar amount of 0.1 M aqueous XOH (X = Li, Na, K, or Cs), and allowing to stir overnight. Aliquots of the stock solution were put into 7 mL Sterilin vials and the pH was adjusted to the desired value using either 2 M HCl or 2 M XOH (X = Li, Na, K, or Cs). A Precision Extrusion Inc, single lumen tube was filled three-quarters with the solution at desired pH and sealed with a plastic lid and Parafilm to prevent leaks or changes in pH. For the hydrogels, an aliquot of stock solution was added to a 7 mL Sterilin vial containing a pre-weighed amount of GdL and shaken gently. A capillary tube was filled three-quarters with the mixture, sealed with a plastic lid and Parafilm, and left to sit for 16 hours to allow for gelation to occur. Solutions and hydrogels were prepared before arrival on June 24th, 2021, in the lab due to the restrictions in place regarding COVID-19 and postal samples. The SAXS data for Li⁺, K⁺, and Cs⁺ at different pHs and as hydrogels were collected at the Diamond Light Source by Dr. C. J. C. Edwards-Gayle and background subtracted by Dr. R. I. Randle on July 7th, 2021. The SAXS data for Na⁺ was collected at Diamond Light Source by Dr. C. J. C. Edwards-Gayle and Dr. A. J. Smith during prior beam time (November 3rd, 2020) described in more detail in section 3.4.2.4.

Samples of **PBI-L** after irradiation and relaxation were measured at the University of Bath in collaboration with Dr. Adam Squires and 3rd year PhD student Wangli Liu. The SAXS was measured using a SAXSpoint 2.0 by Anton-Paar equipped with copper and molybdenum sources (1.542 Å and 0.7107 Å, 50 W) and a 2D EIGER R-series Hybrid Photon Counting (HPC) detector at room temperature. The samples were 576 cm away from the detector. Solutions of the PBIs were made as previously described and pH-adjusted accordingly then transferred into 1.5 mm borosilicate capillaries. The

capillaries were sealed using rubber electrical tubing that had been heated and molded into a lid. The solutions in the capillaries were irradiated using a 365 nm LED for 5 minutes using the same method as described in the UV-vis absorption spectroscopy measurements in Section 2.4.4.

The scattering length density of each **PBI-L** was determined to be $13.826 \cdot 10^{-6} \text{ \AA}^{-2}$ using the National Institute of Standards and Technology's neutron activation and scattering calculator.⁵⁴

The data were fitted to models in the Sasview software package (version 5.0.3).⁵⁵ Various models were used to fit the data. Fitting errors are provided as \pm ; the errors were obtained from the fitting software and do not consider other sources of error. These compounds are expected to form 1D fibres at low pH and they can form worm-like micelles at high pH.¹² Previous fitting of similar structures has been reported and found that cylindrical models were appropriate.¹¹ Fitting the data to different cylinder models was attempted to find the most suitable, starting with models with fewer parameters and progressing to more complex ones. A model was deemed suitable based on the reduced χ^2 : a χ^2 below 10 was deemed suitable. Generally, the model with the lowest χ^2 was chosen unless there were regions of the fit that clearly were not representative of the data set. In some cases, single models were not suitable to achieve a good fit, indicating a co-existence of structures. In these instances, models were combined using the "Easy Sum/Multi(p1, p2) editor" in the SasView software. The combined model could then be saved and used in the same manner as any other. In the results tables from the fitting shown below, a "+" sign is used to denote where two models were combined.

2.4.6. pH measurements

pH measurements were recorded using a custom-built pH/temperature logger and a HANNA pH probe (FC200) with a given error of ± 0.1 pH units. For monitoring the pH of gelation over time, 2 mL of PBI solution was added to 8 mg/mL of GdL in a 7 mL Sterilin vial which was immersed in a water bath at a set temperature of 25°C. The probe tip was then inserted into the gel with Parafilm used to seal the top of the vial/tip. The pH measurements were recorded every 30 seconds for between 14 to 18 hours until gelation was complete, and pH had stabilised.

2.4.7. Apparent pK_a titrations

pH measurements were recorded using a HANNA Edge pH logger and a HANNA pH probe (FC200) with a given error of ± 0.1 pH units. For apparent pK_a measurements, 2 mL of PBI solution was added to a 7 mL Sterilin vial which was immersed in a water bath at a set temperature of 25°C and the probe was immersed in the solution. 3 μ L – 10 μ L aliquots of HCl (0.1M) were added to the solution and the pH recorded after the reading had stabilised. The solution was gently stirred between additions of acid to avoid any gel forming and to ensure the pH was homogeneous throughout the solution. The plateaus in the data represent the apparent pK_a values.

2.4.8. Cyclic voltammetry (CV)

CVs for the solutions were collected using a three-electrode system and a PalmSens4 potentiostat with a glassy carbon working electrode, a Pt wire counter electrode and an Ag/AgCl reference electrode. The background electrolyte was 0.1 M NaCl in water. The potential was scanned from 1.0 V to -1.0 V at a scan rate of 0.05 V/s and measurements were carried out in triplicate. The clearest of the three scans was used for analysis.

Determining the experimental electron affinity (EA) / Lowest Unoccupied Molecular Orbital (LUMO) energy level vs vacuum: The reduction maximum for the first reduction potential vs Ag/AgCl was obtained from the CV data. The EA/LUMO energy in eV was then calculated by first converting to vs F_c/F_c^+ using an experimental value of +0.479 V, then to vs saturated calomel electrode (SCE) using an experimental value of +0.47 V then to vs standard hydrogen electrode (SHE) using an experimental value of -0.24 V and finally vs vacuum using a known value of 0.24 V from the literature.⁴⁶ The equation for the conversion is shown below:

$$-EA = E_{LUMO} (eV) = (Red_{max} + 0.479 V + 0.470 V - 0.24 V - 4.28 V) \quad (\text{Equation 3})$$

Determining the experimental ionisation potential (IP) / Highest Occupied Molecular Orbital (HOMO) energy level vs vacuum: Due to the limits in the solvent window of water (water oxidation) the oxidation of **PBI-L**, which is expected to occur around 1.5 V vs Ag/AgCl, could not be measured. Instead, the HOMO was approximated by subtracting the energy band gap, E_g , from the EA/LUMO energy.

The E_g , were estimated from the UV-Vis absorption spectroscopy of **PBI-L** at pH 6 with different cations, using Tauc's relationship:

$$(\alpha h\nu)^{1/n} = A(h\nu - E_g) \quad (\text{Equation 4})$$

Where A is a proportionality constant, $h\nu$ is the photon energy and α the absorption coefficient. 'n' is a constant whose value depends upon the type of transition, $n = 1/2$ for direct allowed transition.

The value for E_g was extrapolated from the tangent line to the $h\nu$ axis on the Tauc plots (Appendix 2). The equation below was then used to determine the approximate IP/HOMO energy using the following equation:

$$-IP = E_{HOMO}(eV) = E_{LUMO} - E_g \quad (\text{Equation 5})$$

2.4.9. Fabrication of **PBI-L** interlayer photovoltaic devices

Indium-doped tin oxide (ITO) coated glass slides, ($7 \Omega \text{ m}^{-1}$, 15 mm x 15 mm x 1.1 mm), were cleaned by consecutive sonication in deionised water, acetone, and isopropanol (five minutes each). The substrates were dried in a stream of compressed air then treated with O_2 plasma (Diener Electronic, Zepto model) for 10 minutes to improve wettability.⁵⁶ A zinc oxide precursor solution⁵⁷ was spin-coated onto the substrate at 2000 rpm for 60 seconds with a ramp-up of 10 seconds, in ambient conditions. The substrate was then placed on a hot plate and annealed at 120°C for 30 seconds in air. Solutions with different cations at pH 6 at a concentration of 10 mg/mL were deposited on top of the ZnO layer and spin-coated at 1000 rpm for 60 seconds, with a ramp-up of 10 seconds, in ambient conditions. The substrate was then placed on top of a hot plate and annealed at 120°C for 20 minutes in air. Two donor materials were used: P3HT and PCE10. The active layer was spin-coated at 1000 rpm for 60 seconds with a ramp of 10 seconds in a nitrogen atmosphere at room temperature. The films were then placed on a hot plate and annealed at 150°C for 20 minutes in a nitrogen atmosphere. Molybdenum trioxide (10 nm) was then deposited by thermal evaporation ($\sim 10^{-5}$ mbar) before deposition of silver electrodes (100 nm) by thermal evaporation ($\sim 10^{-5}$ mbar) using a shadow mask (electrode dimensions 1.5 mm x 3.5 mm).

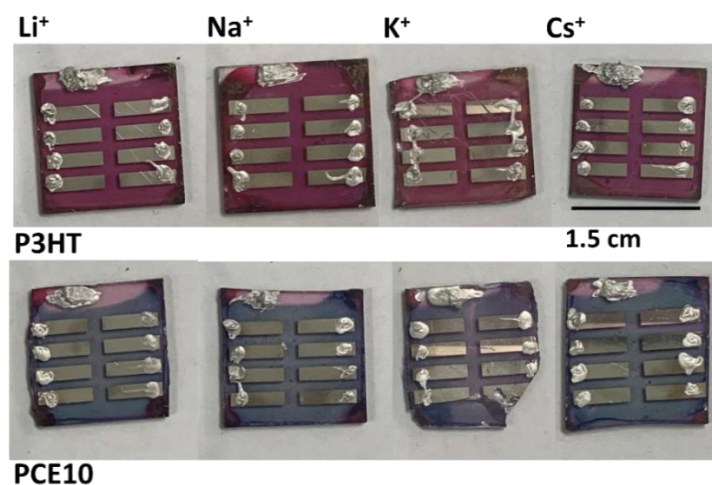


Figure 2.29. Photographs of interlayer photovoltaic devices using different donors.

2.4.10. Transmittance of **PBI-L** interlayer photovoltaic devices

Transmittance measurements were carried out using ZnO/**PBI-L** bilayer films deposited on ITO as described in Section 2.4.9 for the photovoltaic devices. The spectra were recorded using an Agilent Cary 60 spectrometer. Transmittance was measured between 200 nm and 1100 nm on a 600 nm/min scan rate and background subtracted using the transmittance of a glass slide as the background.

2.4.11 Nanoindentation of **PBI-L** interlayer photovoltaic devices

Nanoindentation measurements of the ZnO/**PBI-L** bilayer films were carried out on an Anton Paar Step X00 – Ultra Nanoindentation Tester (UNHT³) with a Berkovich indenter. A standard matrix measurement was run making three indentations along the x-axis. Parameters of this standard matrix measurement include an acquisition rate of 10 Hz, with a linear load. The maximum load was 5 mN with a loading rate of 10 mN/min and unloading rate of 10 mN/min. The step parameters include an approach distance of 7500 nm, approach speed of 5000 nm/min and retract speed of 8000 nm/min. The standard test parameters and step parameters were based on the values provided on the UNHT³ for soft materials. The ZnO/**PBI-L** bilayer films were irradiated using a 365 nm LED (LedEngin Inc, LZ1-10U600) powered by a custom-built 700 mA constant-current power source for 5 minutes, as described in the UV-vis absorption experimental section. Nanoindentation measurements on the irradiated films were carried out using the same procedure as the non-irradiated films.

2.4.12 Current–voltage characterisation of **PBI-L** interlayer photovoltaic devices

The current–voltage characterisation of the **PBI-L** interlayer photovoltaic devices with different donor materials was carried out using a Keithley 4200-SCS parameter analyser and a Newport solar simulator with a 150 W xenon arc lamp for AM1.5 illumination, which was confirmed using a calibrated solar cell. All tests were carried out in a nitrogen-filled glovebox. For K⁺ measurements for PCE10 could not be measured due to the devices being damaged (Figure 2.26) and sufficient connection to the silver electrodes was not possible. Dr. Joseph Cameron determined the information on PCE, FF, J_{sc}, and V_{oc} from the external quantum efficiency plots and emailed the summary of them to me. Ideally, there would have been multiple repeats to gain confident values with errors for the PCE, FF, J_{sc}, and V_{oc} values, however, the thermal evaporation equipment was unavailable from August 2022 until May 2023.

2.5. References

1. S. Chen, P. Slattum, C. Wang and L. Zang, *Chemical Reviews*, 2015, **115**, 11967-11998.
2. S. S. Babu, V. K. Praveen and A. Ajayaghosh, *Chemical Reviews*, 2014, **114**, 1973-2129.
3. Y. Sun, C. He, K. Sun, Y. Li, H. Dong, Z. Wang and Z. Li, *Langmuir*, 2011, **27**, 11364-11371.
4. N. Zink-Lorre, E. Font-Sanchis, Á. Sastre-Santos and F. Fernández-Lázaro, *Chemical Communications*, 2020, **56**, 3824-3838.
5. R. D. Pettipas, A. Hoff, B. S. Gelfand and G. C. Welch, *ACS Applied Materials & Interfaces*, 2022, **14**, 3103-3110.
6. A. D. Hendsbee, J.-P. Sun, W. K. Law, H. Yan, I. G. Hill, D. M. Spasyuk and G. C. Welch, *Chemistry of Materials*, 2016, **28**, 7098-7109.
7. J. Cameron, D. J. Adams, P. J. Skabara and E. R. Draper, *Journal of Materials Chemistry C*, 2022, **10**, 3944-3950.
8. E. R. Draper, L. J. Archibald, M. C. Nolan, R. Schweins, M. A. Zwijnenburg, S. Sproules and D. J. Adams, *Chemistry*, 2018, **24**, 4006-4010.
9. M. D. Segarra-Maset, V. J. Nebot, J. F. Miravet and B. Escuder, *Chemical Society Reviews*, 2013, **42**, 7086-7098.
10. E. R. Draper and D. J. Adams, *Chem*, 2017, **3**, 390-410.
11. D. McDowall, B. J. Greeves, R. Clowes, K. McAulay, A. M. Fuentes-Caparrós, L. Thomson, N. Khunti, N. Cowieson, M. C. Nolan, M. Wallace, A. I. Cooper, E. R. Draper, A. J. Cowan and D. J. Adams, *Advanced Energy Materials*, 2020, **10**.
12. M. C. Nolan, J. J. Walsh, L. L. E. Mears, E. R. Draper, M. Wallace, M. Barrow, B. Dietrich, S. M. King, A. J. Cowan and D. J. Adams, *Journal of Materials Chemistry A*, 2017, **5**, 7555-7563.
13. E. R. Draper, B. J. Greeves, M. Barrow, R. Schweins, M. A. Zwijnenburg and D. J. Adams, *Chem*, 2017, **2**, 716-731.
14. E. R. Draper, L. Wilbraham, D. J. Adams, M. Wallace, R. Schweins and M. A. Zwijnenburg, *Nanoscale*, 2019, **11**, 15917-15928.
15. M. Wallace, J. A. Iggo and D. J. Adams, *Soft Matter*, 2015, **11**, 7739-7747.
16. F. Hofmeister, *Archiv für experimentelle Pathologie und Pharmakologie* 1888, **24**, 247-260.
17. B. Kang, H. Tang, Z. Zhao and S. Song, *ACS Omega*, 2020, **5**, 6229-6239.

18. H. I. Okur, J. Hladílková, K. B. Rembert, Y. Cho, J. Heyda, J. Dzubiella, P. S. Cremer and P. Jungwirth, *The Journal of Physical Chemistry B*, 2017, **121**, 1997-2014.
19. K. Aoki, K. Shiraki and T. Hattori, *Physical Chemistry Chemical Physics*, 2016, **18**, 15060-15069.
20. S. Roy, N. Javid, J. Sefcik, P. J. Halling and R. V. Ulijn, *Langmuir*, 2012, **28**, 16664-16670.
21. L. Chen, G. Pont, K. Morris, G. Lotze, A. Squires, L. C. Serpell and D. J. Adams, *Chemical Communications*, 2011, **47**, 12071-12073.
22. E. R. Draper, H. Su, C. Brasnett, R. J. Poole, S. Rogers, H. Cui, A. Seddon and D. J. Adams, *Angewandte Chemie*, 2017, **129**, 10603-10606.
23. L. Chen, *Chemical Communications*, 2012, **48**, 9355-9357.
24. K. McAulay, P. A. Ucha, H. Wang, A. M. Fuentes-Caparrós, L. Thomson, O. Maklad, N. Khunti, N. Cowieson, M. Wallace, H. Cui, R. J. Poole, A. Seddon and D. J. Adams, *Chemical Communications*, 2020, **56**, 4094-4097.
25. M. C. Mañas-Torres, C. Gila-Vilchez, J. A. González-Vera, F. Conejero-Lara, V. Blanco, J. M. Cuerva, M. T. Lopez-Lopez, A. Orte and L. Álvarez de Cienfuegos, *Materials Chemistry Frontiers*, 2021, **5**, 5452-5462.
26. C. Backes, T. Schunk, F. Hauke and A. Hirsch, *Journal of Materials Chemistry*, 2011, **21**, 3554-3557.
27. A. Z. Cardoso, L. L. E. Mears, B. N. Cattoz, P. C. Griffiths, R. Schweins and D. J. Adams, *Soft Matter*, 2016, **12**, 3612-3621.
28. L. L. E. Mears, E. R. Draper, A. M. Castilla, H. Su, Zhuola, B. Dietrich, M. C. Nolan, G. N. Smith, J. Douth, S. Rogers, R. Akhtar, H. Cui and D. J. Adams, *Biomacromolecules*, 2017, **18**, 3531-3540.
29. D. McDowall, D. J. Adams and A. M. Seddon, *Soft Matter*, 2022, **18**, 1577-1590.
30. N. S. Murthy, *Spectroscopy*, 2017, **32**, 18-24.
31. R. A. Hule, R. P. Nagarkar, A. Altunbas, H. R. Ramay, M. C. Branco, J. P. Schneider and D. J. Pochan, *Faraday Discussions*, 2008, **139**, 251-264.
32. L. Gonzalez, C. Liu, B. Dietrich, H. Su, S. Sproules, H. Cui, D. Honecker, D. J. Adams and E. R. Draper, *Communications Chemistry*, 2018, **1**, 77.
33. E. R. Draper, R. Schweins, R. Akhtar, P. Groves, V. Chechik, M. A. Zwiijnenburg and D. J. Adams, *Chemistry of Materials*, 2016, **28**, 6336-6341.
34. G. Porod, O. Glatter and O. Kratky, *Academic Press, New York*, 1982, 17-51.
35. B. Hammouda, *Journal of Polymer Science Part B: Polymer Physics*, 2006, **44**, 3195-3199.
36. S. Ramachandran, J. Trehwella, Y. Tseng and Y. B. Yu, *Chemistry of materials*, 2006, **18**, 6157-6162.
37. E. R. Draper, J. J. Walsh, T. O. McDonald, M. A. Zwiijnenburg, P. J. Cameron, A. J. Cowan and D. J. Adams, *Journal of Materials Chemistry C*, 2014, **2**, 5570-5575.
38. R. O. Marcon and S. Brochsztain, *Langmuir*, 2007, **23**, 11972-11976.
39. D. J. Adams, M. F. Butler, W. J. Frith, M. Kirkland, L. Mullen and P. Sanderson, *Soft Matter*, 2009, **5**, 1856-1862.
40. C. L. Smith, L. L. E. Mears, B. J. Greeves, E. R. Draper, J. Douth, D. J. Adams and A. J. Cowan, *Physical Chemistry Chemical Physics*, 2019, **21**, 26466-26476.
41. E. R. Draper, O. O. Mykhaylyk and D. J. Adams, *Chemical Communications*, 2016, **52**, 6934-6937.
42. D. J. Adams, L. M. Mullen, M. Berta, L. Chen and W. J. Frith, *Soft Matter*, 2010, **6**, 1971-1980.
43. C. Tang, R. V. Ulijn and A. Saiani, *Langmuir*, 2011, **27**, 14438-14449.
44. C. Tang, A. M. Smith, R. F. Collins, R. V. Ulijn and A. Saiani, *Langmuir*, 2009, **25**, 9447-9453.
45. A. M. Fuentes-Caparrós, Z. Canales-Galarza, M. Barrow, B. Dietrich, J. Läger, M. Nemeth, E. R. Draper and D. J. Adams, *Biomacromolecules*, 2021, **22**, 1625-1638.
46. A. M. Castilla, M. Wallace, L. L. Mears, E. R. Draper, J. Douth, S. Rogers and D. J. Adams, *Soft Matter*, 2016, **12**, 7848-7854.

47. A. A. Isse and A. Gennaro, *The Journal of Physical Chemistry B*, 2010, **114**, 7894-7899.
48. S. Zhao, J. Zhang, Y. Li, H. Liu, B. Wang and M. Zhao, *Journal of Physics D: Applied Physics*, 2022, **55**, 274002.
49. C. A. Schuh, *Materials Today*, 2006, **9**, 32-40.
50. L. K. Jagadamma, M. Abdelsamie, A. El Labban, E. Aresu, G. O. Ngongang Ndjawa, D. H. Anjum, D. Cha, P. M. Beaujuge and A. Amassian, *Journal of Materials Chemistry A*, 2014, **2**, 13321-13331.
51. K. D. M. Rao, C. Hunger, R. Gupta, G. U. Kulkarni and M. Thelakkat, *Physical Chemistry Chemical Physics*, 2014, **16**, 15107-15110.
52. N. Chander, S. Singh and S. S. K. Iyer, *Solar Energy Materials and Solar Cells*, 2017, **161**, 407-415.
53. S.-H. Liao, H.-J. Jhuo, Y.-S. Cheng and S.-A. Chen, *Advanced Materials*, 2013, **25**, 4766-4771.
54. L. Zhao, S. Zhao, Z. Xu, B. Qiao, D. Huang and X. Xu, *Organic Electronics*, 2016, **34**, 188-192.
55. N. N. A. a. S. C. P. Kienzie, <https://www.ncnr.nist.gov/resources/activation/>. DOI: <https://www.ncnr.nist.gov/resources/activation/>.
56. <http://www.sasview.org/>.
57. V. Adams, J. Cameron, M. Wallace and E. R. Draper, *Chemistry – A European Journal*, 2020, **26**, 9879-9882.
58. S. Höfle, A. Schienle, M. Bruns, U. Lemmer and A. Colsmann, *Advanced Materials*, 2014, **26**, 2750-2754.

**Chapter 3: Impact of subtle change
in branched amino acid on the
assembly and properties of perylene
bisimides**

This chapter is adapted from the following publication:

“Impact of subtle change in branched amino acid on the assembly and properties of perylene bisimide hydrogels” J. G. Egan, G. Brodie, D. McDowall, A. J. Smith, C. J. C. Edwards-Gayle and E. R. Draper, *Mater. Adv.*, 2021,**2**, 5248-5253

Compounds were synthesised and characterized by J. G. Egan and G. Brodie. All experimental data were collected by J. G. Egan, with the exception of ESI-TOF MS (carried out by Uni. Of Glasgow technicians). A. J. Smith and C. J. C. Edwards-Gayle carried out the SAXS experiments. J. G. Egan, and D. McDowall fitted the SAXS data.

3.1. Introduction

The performance of PBIs in organic optoelectronic applications is impacted by the morphology of their 1D nanostructures, which in turn influences electronic performance and stability.¹⁻³ As mentioned in Chapter 1, the morphology of PBIs can be altered by changing the self-assembly using different stimuli such as pH,^{4, 5} solvent,^{6, 7} and temperature.⁸ By understanding the self-assembly and aggregation of different PBIs with different chemical structures in solution we can use molecular design and self-assembly to create PBI materials for optimal performance in optoelectronics ($PCE > 3\%$). For example, Chen *et al.* compared the difference in conductivity between two PBIs. One had been symmetrically modified (**PBI-1**) at the imide while the other was asymmetrically modified (**PBI-2**), as shown in Figure 3.1.⁹ They showed potential for solvent-dependent aggregation types of the nanomaterials.

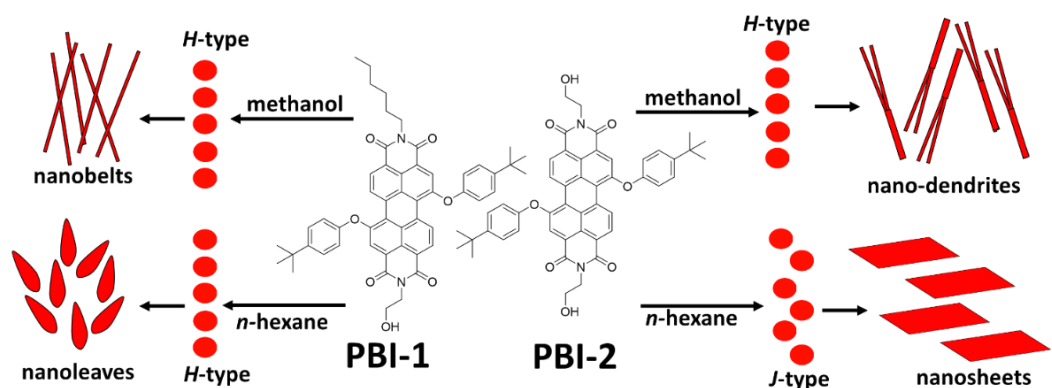


Figure 3.1. Chemical structures and cartoon of asymmetric **PBI-1** and symmetric **PBI-2** assembled into J-type or H-type aggregates and morphology of nanostructure depending on solvent choice adapted from original paper.⁹

PBI-1 was shown to only form H-type aggregates in methanol and n-hexane. These aggregates assembled into nanoleaves in hexane and nanobelts in methanol. **PBI-2** adopted H-type aggregated structures in methanol and J-type aggregated structures in n-hexane and the nanostructure of **PBI-2** consisted of nanodendrites in methanol and nanosheets in n-hexane. These PBIs saw an increase in conductivity for the nanobelts formed by **PBI-1** and dendrites formed by **PBI-2** in methanol compared to nanoleaves or nanosheets formed by the PBIs in n-hexane. This highlights the importance that aggregation and morphology have on the electronic properties.

It is expected that there will be more pronounced differences in their 1D nanostructure between PBIs with vastly different chemical structures, such as asymmetrically functionalised PBIs.^{10, 11} However, even small differences in chemical structure at the imide position have been seen to impact 1D nanostructure and resulting conductivity. Sun *et al.* synthesized PBI with *N*-Cbz-functionalised *L*-lysine at the imide position. As lysine has two amine groups, two isomers with different spatial constraints were obtained, **Cbz-PBI-K-a** and **Cbz-PBI-K-b**, Figure 3.2.¹² The two PBIs were dissolved in acetone then water was added to induce phase transfer self-assembly. **Cbz-PBI-K-b**, which had the acid group next to the imide position, had less freedom to interact with neighbouring groups which imposed a spiral constraint on its self-assembly behaviour compared to **Cbz-PBI-K-a**. At a 45% water mixture, **Cbz-PBI-K-a** formed well-defined nanobelts while **Cbz-PBI-K-b** formed only ill-defined mixtures of nanosheets and spheres. They attributed the ill-defined structures to the sterically hindered acid group hindering intermolecular bonding.¹³ As the percentage of water was increased to 55%, the length of the nanobelts decreased for **Cbz-PBI-K-a** while **Cbz-PBI-K-b** still showed a mixture of nanosheets and spheres. When the percentage of water was increased to 75%-80%, both PBIs formed spheres, which were larger in radius for **Cbz-PBI-K-a** than **Cbz-PBI-K-b**.

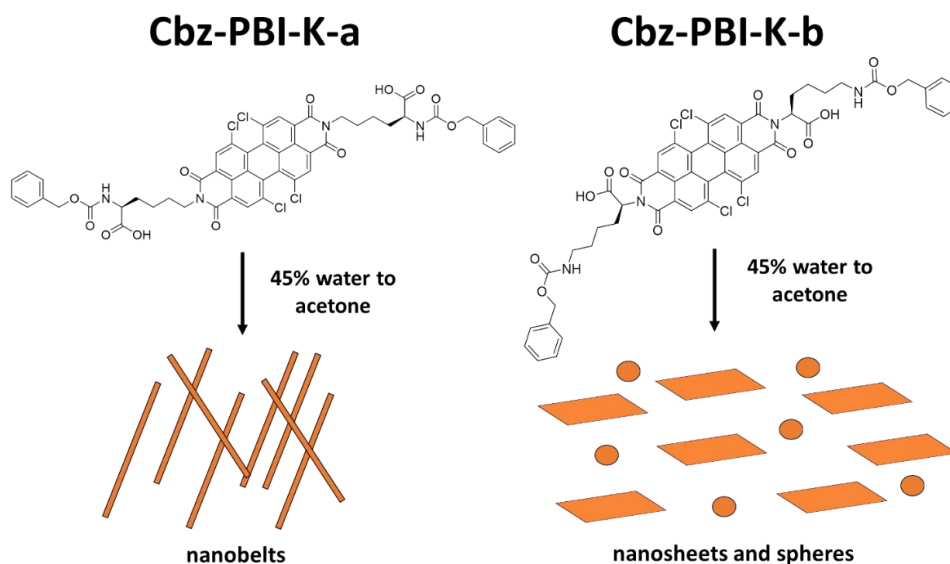


Figure 3.2. Chemical structures and cartoon of isomers **PBI-Cbz-K-a** and **PBI-Cbz-K-b** forming different nanostructured materials in 45% to 55% water in acetone mixture. Adapted from original paper.¹²

The morphology of the resulting nanostructures for **Cbz-PBI-K-a** and **Cbz-PBI-K-b** at different concentrations was also investigated. At a fixed 45% water to acetone ratio and a concentration decreased from 300 μM to 100 μM , **Cbz-PBI-K-a** was observed to form nanowires with a length of tens of μm and a diameter of about 200 nm. When the concentration was increased from 300 μM to 800 μM or 1 mM sheetlike objects formed. When these same experiments were done using **Cbz-PBI-K-b** there were still no defined nanostructures with long range ordering. The conductivity of the different nanostructured **Cbz-PBI-K-a** was measured and showed improved conductivity for the nanowires and nanobelts compared to the nanosheets. This is presumably due to the nanowires and nanobelts 3D structure improving radical anion formation due to improved packing compared to the 1D structure of nanosheets. This is to what was observed in the previous example with the asymmetric PBIs as well.

As already mentioned in Chapter 1, the ability to modify the self-assembly of PBIs using pH is an advantageous way to modify their aggregation and improve performance in electronic devices as better packing facilitates between exciton transport and improves radical formation. Sukul *et al.* synthesised PBIs substituted with *D*- or *L*-aspartic acid at the imide position with the intention of controlling the helicity of the self-assembled fibres.¹⁴ The enantiomers formed twisted rope-like fibres that had opposite helicity depending on the stereochemistry of the amino acid as the pH was lowered. Reports of these twisted fibres of PBIs in water are not abundant.¹⁵ When the pH was lowered even further it was seen that the fibres entangled and formed hydrogels with equal but opposite circular dichroism (CD) spectra. PBI materials capable of forming 3D gel networks by entangling 1D fibres through a change in pH can be used to make xerogel devices.¹⁶⁻¹⁹

Draper *et al.* investigated four different amino acid-functionalised PBIs, Figure 3.3, in solution at pH 10 and as hydrogels formed when the pH is lowered to see how amino acid side chain choice could impact self-assembled structures.²⁰ It was observed that when solutions at pH 10 of **PBI-V**, **PBI-A** and **PBI-H** were dried down they formed ordered 1D structures while **PBI-F** formed disordered structures. These four PBIs could be used to make hydrogels using a pH trigger to lower the pH. Scanning electron microscopy (SEM) of the dried xerogels showed the presence of thin entangled fibres. They showed that choice of amino acid impacted the self-

assembled structures in solution which in turn effects how they dried into xerogels. This difference in xerogel devices was linked their ability to form radical anion, with **PBI-F** showing the poorest film quality and being the least conductive.

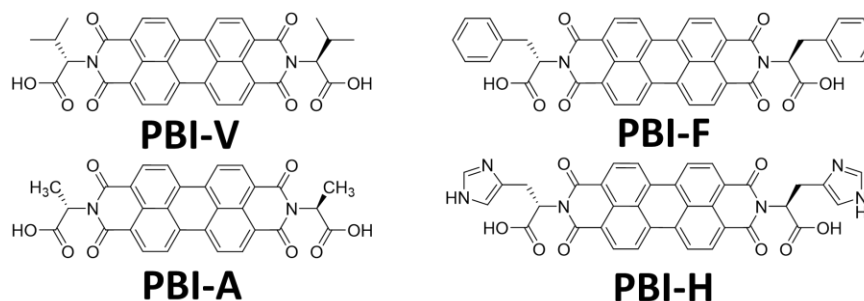


Figure 3.3. Chemical structures of four different amino acid-functionalised PBIs.²⁰

In another study by Draper *et al.* investigating the amino acid side chain choice on photoconductivity included an additional four amino acid-functionalised PBIs were investigated at pH 8.²¹ These four new PBIs had even more steric side chain groups meaning there would be a greater difference in molecular packing than in the previous study. All eight PBIs could be used to make drop-cast photoconductive films. UV-vis absorption spectroscopy showed the local molecular packing of the eight PBIs could be grouped into two groups based on the type of structures formed with **PBI-A**, **PBI-V**, **PBI-L**, **PBI-S**, and **PBI-H** in one group and **PBI-W**, **PBI-Y**, and **PBI-F** in the other. Electron paramagnetic resonance (EPR) spectroscopy of these eight PBIs showed they formed different amounts of radical anion when irradiated with a UV light source. **PBI-A**, **PBI-V**, and **PBI-S** had a high concentration of spins and formed the most radical anion. **PBI-W**, **PBI-L**, and **PBI-F** had the lowest concentration of spins and formed the least amount of radical anion. The workers attribute this difference in photoconductivity to the difference in the molecular packing in solution because of different amino acid side chains.

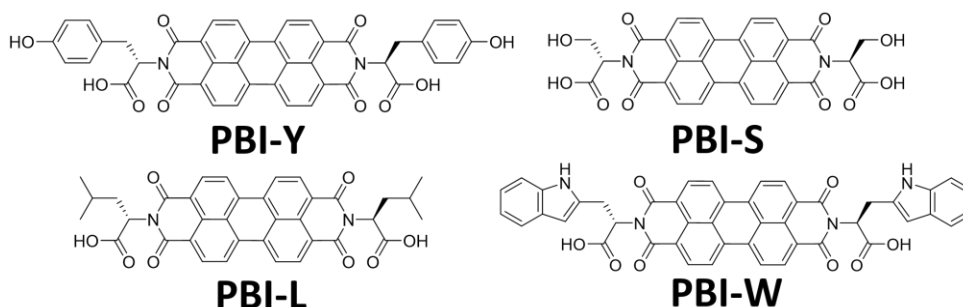


Figure 3.4. Chemical structures of additional four amino acid-functionalised PBIs.²¹

The aim of the work was to if the amino acid side chain choice could be linked to radical anion formation like before. As well, we wanted to investigate how amino acid side chain could change the gelation properties which we had not reported before. This chapter focuses further on three different amino acid-functionalised PBIs: *N,N*-di(*L*-leucine)-perylene-3,4:9,10-tetracarboxylic acid bisimide (**PBI-L**), *N,N*-di(*L*-isoleucine)-perylene-3,4:9,10-tetracarboxylic acid bisimide (**PBI-I**), and *N,N*-di(*L*-valine)-perylene-3,4:9,10-tetracarboxylic acid bisimide (**PBI-V**), shown in Figure 3.5. These three different amino acid-functionalised PBIs were chosen because they all have a hydrophobic side chain with slightly different chemical structures. While **PBI-V** and **PBI-L** have been investigated by the group before and shown to be able to form hydrogel materials. **PBI-I** had not been used by the group before and had not been used to make hydrogel materials before either. Therefore, we wanted to compare **PBI-I** to similar PBIs that were already well studied. **PBI-I** is an isomer of **PBI-L** and it would be expected to produce a similar radical anion in solution and as a hydrogel. **PBI-V** is very similar in structure to **PBI-L** but with one less carbon in the side chain making it less branched and more sterically hindered than **PBI-L** or **PBI-I**, it is expected to form the most radical anion because of the smaller side chain should improve molecular packing.

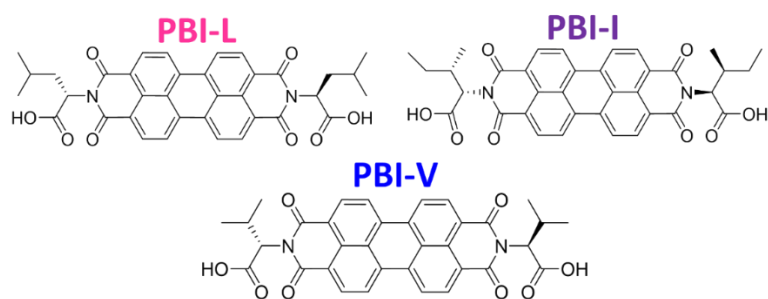


Figure 3.5. Chemical structures of **PBI-L**, **PBI-I**, and **PBI-V** used in this study.

The impact of the amino acid side chain on the molecular packing and aggregation of the three PBIs at different pHs was investigated using UV-vis absorption spectroscopy, dynamic viscosity, and small-angle X-ray scattering (SAXS). These techniques were employed to see how the different side chains on the amino acids impacted their pH-sensitive behaviour and the self-assembly of secondary structures. Electron mobility and redox potentials of the aggregates of the three PBIs at different pHs were evaluated using cyclic voltammetry (CV). The ability of the three PBIs to

form photoconductive radical anion at different pHs was then studied using UV-vis absorption spectroscopy.

PBI hydrogels were prepared using a pH trigger. The mechanical properties of the PBI hydrogels were compared to see how the different assemblies impacted the 3D hydrogel network. SAXS data of the three PBI hydrogels was collected and compared to fibre structure and morphology of the PBIs in solution at a similar pH. Finally, the kinetics of gel formation of the PBI hydrogels were monitored using $^1\text{H-NMR}$ spectroscopy, rheology, and pH to understand how the assembly of different 1D fibres into a 3D gel network can impact the bulk mechanical properties of the hydrogels. The ability of the hydrogels to form the photoconductive radical anion was again studied using UV-vis absorption spectroscopy.

3.2. Results and discussion

3.2.1 Investigation into the branched side chain structure on self assembled micellar aggregates in solution at different pHs

All PBIs were synthesised using a published method and the Draper group have previously worked with **PBI-L** and **PBI-V**,²⁰⁻²³ as have other groups.²⁴⁻²⁸ **PBI-I** has not previously been reported for use as hydrogel material. Full synthesis procedures and characterisation can be found in Section 3.4.1. Each solution of PBI was prepared in water at a concentration of 10 mg/mL with 1 equivalent of 0.1 M NaOH. The addition of base helps solubilise the PBI by bringing the pH above the apparent pK_a .²⁹ All solution work in this chapter was carried out using this method of preparation unless otherwise stated. All the PBIs formed a free-flowing deep red solution at pH 7 as shown in Figure 3.6.

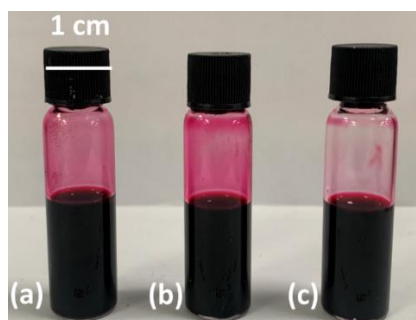


Figure 3.6. Photographs of 10 mg/mL solutions of (a) **PBI-L**, (b) **PBI-I**, and (c) **PBI-V** in 3 mL glass vials after being allowed to stir overnight.

To probe the assembly of the PBIs at the molecular level and provide information about the local molecular packing as pH is changed, the UV-vis absorption of PBI solutions at pH 5, 6, 7, 8, and 9 was measured. The absorption spectra of solutions at different pHs are shown in Figures 3.7 (a) to (c). All three PBIs at the different pHs have a weak S_0 - S_2 transition at around 380 nm and strong S_0 - S_1 transitions at 506 nm and 552 nm. The different imide functional groups are expected to have a negligible influence on the absorption and emission properties of the PBI because the nodes of the highest occupied molecular orbital (HOMO) and lowest unoccupied molecular orbital (LUMO) are at the imide nitrogen.

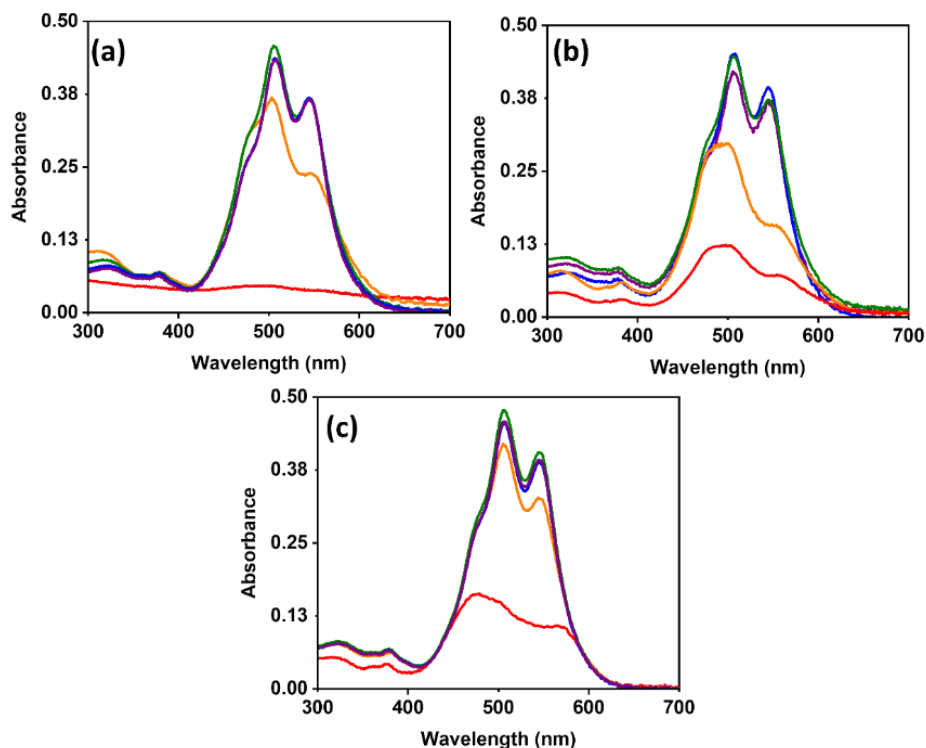


Figure 3.7. UV-vis absorption spectra of (a) **PBI-L**, (b) **PBI-I**, and (c) **PBI-V** at different pHs. pH 5 (**red**), pH 6 (**orange**), pH 7 (**green**), pH 8 (**blue**), and pH 9 (**purple**).

Each of the PBIs at a pH above 5 showed a higher absorbance intensity of the 0-1 vibronic transition of the S_0 - S_1 transition band at 506 nm compared to the 0-0 transition band at 552 nm. These spectral features have been reported to be indicative of *H*-type aggregates.³⁰ However, interpretation of packing with simple models based on classic pictures of *H*- and *J*-type packing is difficult based on the

UV-vis absorption spectrum alone due to the complexity of the PBIs' structures in water.³¹ Instead, local molecular packing can be inferred to some degree based on the UV-vis absorption spectrum. The S_0 - S_1 ratios for the three PBIs at each pH were calculated and are summarised in Table 3.1. Changes in the ratio of the S_0 - S_1 transitions suggest a change in the aggregation of PBIs as they self-assemble into larger structures (micellar aggregates or nanostructures).⁵ Upon decreasing the pH, the absorption peaks decrease in intensity indicating increased aggregation and intermolecular interaction.^{23, 32} This indicates the PBIs are self-assembling together into larger structures as pH is lowered differently depending on the amino acid side chain choice with **PBI-I** self-assembling sooner than the others.

Table 3.1. S_0 - S_1 ratios for solutions of PBIs at 10 mg/mL at different pHs determined from the absorbance at 506 nm and 552 nm.

pH	PBI-L	PBI-I	PBI-V
5	N/A	0.58	0.77
6	0.66	0.54	0.78
7	0.79	0.84	0.84
8	0.84	0.82	0.85
9	0.84	0.95	0.86

PBI-I has a lower absorbance at pH 6 and shows broadening of the S_0 - S_1 peaks. At pH 6 there is also a decrease in absorbance for both **PBI-L** and **PBI-V**, but they still have a peak wavelength like that of their S_0 - S_1 peaks at pH 7, indicating that a change in the local molecular packing of **PBI-I** happens at a higher pH than for **PBI-L** or **PBI-V**. The difference in the onset of change in the UV-vis absorption spectra between **PBI-I**, **PBI-L**, and **PBI-V** shows that **PBI-I** is packing at different pHs. At pH 5 there is an even greater decrease in absorbance for all three PBIs. This is because they begin to gel and assembled into even larger structures (micellar aggregate or nanostructures). The **PBI-L** S_0 - S_1 peaks completely decrease in absorbance into the baseline meaning at pH 5 **PBI-L** has formed structures large enough to scatter the light. Unlike **PBI-I** and **PBI-V** which still show discernible S_0 - S_1 peaks, meaning the PBIs are all self-assembling different with pH change. This shows the different PBIs can be used for pH-modified self-assembly of materials.

The UV-vis absorption spectra of the PBIs at different pHs suggest the PBIs may have different apparent pK_a values. The apparent pK_a values is expected to increase with the increase in chemical structure size. Therefore, it was expected that **PBI-L** and **PBI-I** should be the same and **PBI-V** should be lower. However, the UV-vis absorption spectra showed at pH 6 **PBI-I** begin assembling first and at pH 5 **PBI-L** has assembled into larger structure than the other two. Differences in the acid strength would explain the difference in changes of the assemblies as the pH is lowered: weaker acids would become protonated sooner and begin to assemble at higher pH values.

To investigate this further, apparent pK_a titrations were carried out on all three PBIs (data are shown in Figures 3.8 (a) to (c)). These titration data were used to determine the two apparent pK_a values for **PBI-L** ($pK_{a1} = 7.2$ and $pK_{a2} = 5.9$), **PBI-I** ($pK_{a1} = 7.1$ and $pK_{a2} = 6.6$), and **PBI-V** ($pK_{a1} = 6.7$ and $pK_{a2} = 5.9$). These values may seem high for a carboxylic acid but they have been seen before for similar systems^{17, 30, 33, 34} and they are the apparent pK_a values for the self-assembled aggregates, not the single molecules.³⁵⁻³⁷ **PBI-I** and **PBI-L** have similar apparent pK_{a1} values and **PBI-V** has a lower apparent pK_{a1} value. This means that **PBI-L** and **PBI-I** should begin undergoing a transition of nanostructures at a higher pH than **PBI-V**, which is what is seen in the absorption spectra as the pH is decreased from 7 to 6. The apparent pK_{a2} values for **PBI-L** and **PBI-V** are similar in value and now **PBI-I** has the highest apparent pK_{a2} value. The difference between the two apparent pK_a values is largest for **PBI-L** and smallest for **PBI-I**. The difference in apparent pK_a values explains the difference in the pH behaviour seen in the UV-vis absorption data and suggests that despite the similarity in chemical structure the three PBIs are forming different assemblies as the pH is changing. This has been seen previously with dipeptide gelators where the amino acid sequence was reversed and led to dramatically different behaviours for the two structures.³⁷ Knowing the apparent pK_a value is important because it gives us a guideline to what pHs our systems start assembling into long nanostructures. It is important to find an optimal pH which nanofibers have formed as the 3D structures form radical anion better because of the improve packing. However, when the pH drops too low, and the structure become too large they begin to crash out and it becomes difficult to work with them using solution processing methods.

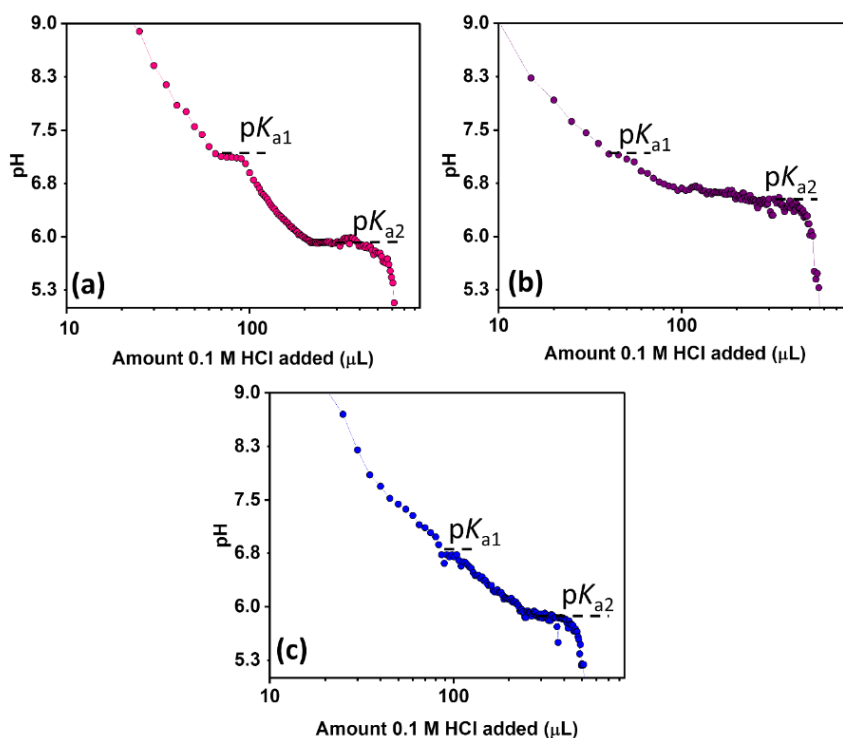


Figure 3.8. Apparent pK_a titrations of (a) **PBI-L** (pink), (b) **PBI-I** (purple) and (c) **PBI-V** (blue) using 0.1 M HCl solution.

The dynamic viscosity of the solutions at different pHs was used to probe the aggregates formed further as it is a useful technique to scan for difference in morphology before measuring the SAXS. As previously reported, when the pH is lowered, these PBIs self-assemble into worm-like micelles or fibrous-type structures and begin to gel.³⁰ This change in structures is observed as a change in the viscosity profile of the material. It has been observed previously that solutions of amino acid-functionalised PBIs at pH 7 at a concentration of 5 mg/mL mostly behave like water. When the pH is lower than the apparent pK_a values they experience shear thinning which suggests the presence of worm-like micelles, or fibrous-type structures.^{20-22, 38} The full dynamic viscosity measurements for the 10 mg/mL solutions of the three PBIs at different pH are shown in Figure 3.9 below. At pH values above the apparent pK_a values the viscosity for all three PBIs is expected to be like water. Shear thinning is clearly seen for **PBI-L** and **PBI-I** at pH 6 to 5, and **PBI-V** at pH 5 at low shear rates.

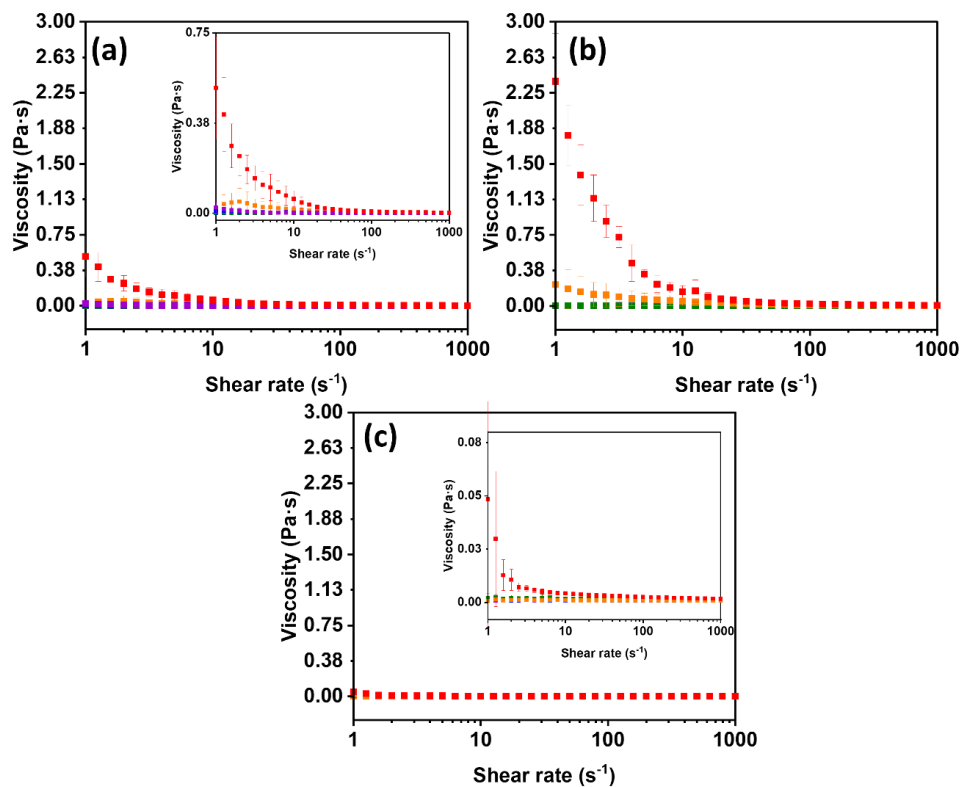


Figure 3.9. Dynamic viscosity of (a) **PBI-L**, (b) **PBI-I**, and (c) **PBI-V**. Vertical axis scaled for ease of comparison with (a) **PBI-L** and (c) **PBI-V**. Insets show expansion of vertical axis. Viscosity measurements were done at pH 5 (**red**), pH 6 (**orange**), pH 7 (**green**), pH 8 (**blue**), and pH 9 (**purple**). Measurements were performed in triplicate and errors were calculated from the standard deviation.

Figure 3.10 shows the summarised viscosity at a shear rate of 10 s^{-1} for a better visual of the viscosity values at low shear. It is at low shear we expect to see the differences in viscosity which we can relate to difference in the length, morphology or abundance of our nanostructures because they have not completely shear aligned yet. At pH 7 to 9 the viscosities for all three PBIs are similar and have values around $0.001 \text{ Pa}\cdot\text{s}$, indicating they have most likely not yet begun assembling into worm-like micelles or fibrous-type structures, or there are not enough of them to cause a change in the viscosity.

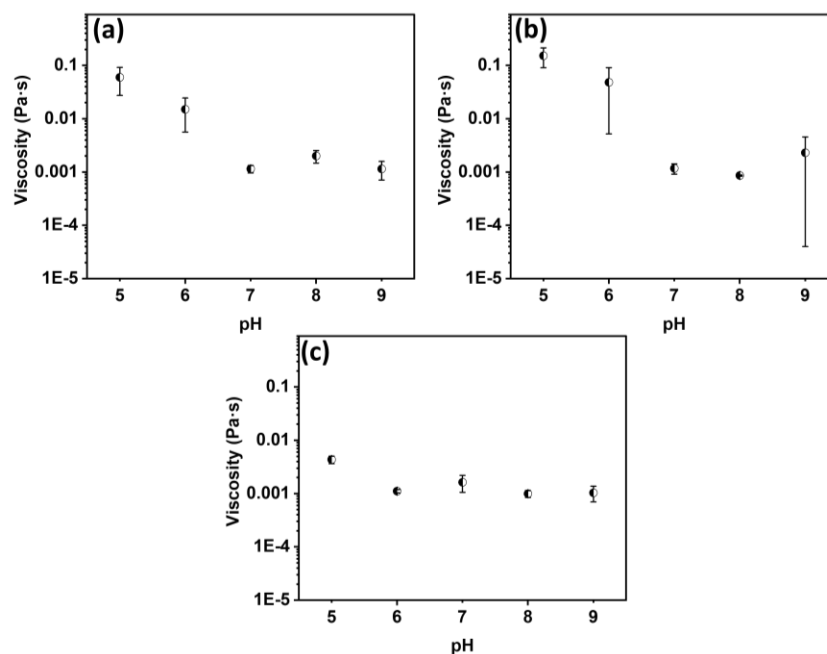


Figure 3.10. Dynamic viscosity at a shear rate of 10 s^{-1} of 10 mg/mL solutions of (a) **PBI-L** (b) **PBI-I**, and (c) **PBI-V** at different pH values. Measurements were performed in triplicate and errors were calculated from the standard deviation.

When the pH is lowered to 6, there is an increase for **PBI-I** and **PBI-L** but not for **PBI-V**. This can be explained by the different pK_a values. For **PBI-I** at pH 6 the pH is below the apparent pK_a values indicating **PBI-I** aggregates are fully protonated. At this pH the UV-vis absorption spectrum also shows a change in molecular packing. For **PBI-L** at pH 6 the pH is just below the apparent pK_{a1} and the UV-vis absorption spectrum shows changes in the absorbance intensity but no broadening as is observed for **PBI-I**. For **PBI-V** at pH 6 the pH is below the apparent pK_{a1} , however, at this pH the UV-vis absorption spectrum shows neither significant change in the absorbance intensity, nor broadening or significant viscosity increase. When the pH is reduced to 5, there is an increase in viscosity for all three PBIs, with the largest increase seen for **PBI-I**. At this point the pH is below all three PBIs' apparent pK_{a2} values and the UV-vis absorption spectra for all three PBIs show a decrease in absorbance intensity, and peak broadening. This indicates the formation of worm-like micelles, or fibrous-type structures, which may be different in morphology, length, or abundance for **PBI-I** as compared to **PBI-V** and **PBI-L**. Indicating that the pH response of the PBI may be linked to the amino acid side chain choice which we have not observed before and it is a helpful tool of hydrogel design.

In Chapter 2 we saw that the morphology was greatly impacted by the pH for **PBI-L** and different cations. Here we want to see how the morphology changed with pH for all three of the differently branched PBIs. Figure 3.11 shows the SAXS of the solutions of **PBI-L** at 10 mg/mL at different pHs as well as the fits used to model the data. Model parameters used to fit the data are summarised in Table 3.2. For **PBI-L** at pH 7 a sphere model at Q was the most suitable fit and a power law model was used to model higher Q . The need to fit the data to a power law suggests that aggregation is beginning at this pH. The sphere model is attributed to the small aggregates that have yet to assemble into larger fibre structures that are seen when the pH is lowered. **PBI-L** could be modelled at pH 6 using a correlation length model, which can be used to understand the compactness/density of fibril structures.³⁹ We attribute this to a long transition of nanostructures around their apparent pK_a values that are highly branched. At pH 5 **PBI-L** was below both apparent pK_a values and could be fitted to a flexible elliptical cylinder combined with a power law. The length of cylinders was 64.4 nm and the Kuhn length 3.94 nm. The large Kuhn length is an indication of reduced flexibility which is expected as the pH is lowered and the fibres elongate.

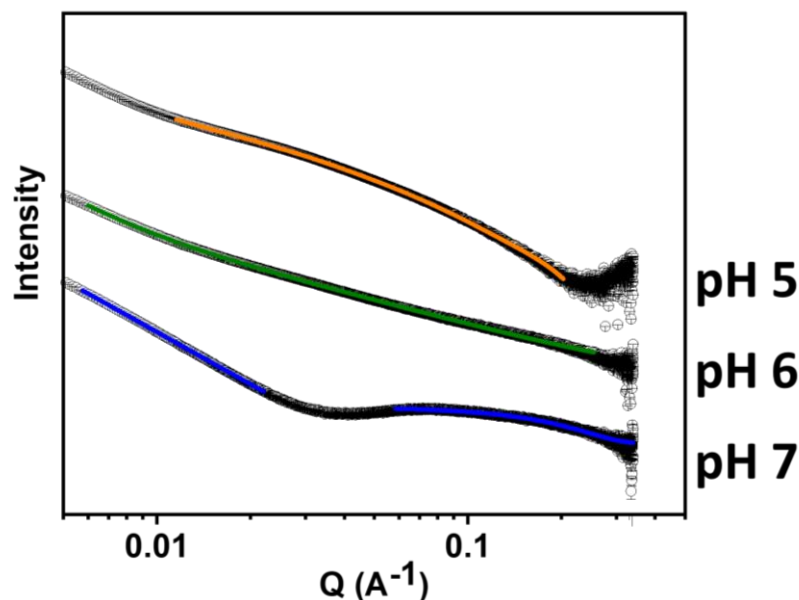


Figure 3.11. SAXS data for solutions of **PBI-L** prepared at 10 mg/mL and pH-adjusted as required with the data shown as open symbols and the fits as coloured lines indicating the pH, 5 (orange), 6 (green), and 7 (blue). Note the data are offset on the intensity scale for clarity.

Table 3.2. SAXS fit table for **PBI-L** solutions at 10 mg/mL at different pH.

pH	5	6	7	
Model	Flexible elliptical cylinder + power law	Correlation length	Sphere	Power law
Length / nm	64.4 ± 0.0519	N/A	N/A	N/A
Kuhn length (nm)	3.94 ± 0.0543	N/A	N/A	N/A
Cylinder radius (nm)	1.24 ± 0.000511	N/A	N/A	N/A
Axis Ratio	2.67 ± 0.00116	N/A	N/A	N/A
Power law	2.46 ± 0.00616	N/A	N/A	3.48 ± 0.000108
Spherical radius (nm)	N/A	N/A	1.18 ± 0.00345	N/A
Correlation length (nm)	N/A	14.8 ± 0.00527	N/A	N/A
Porod exponent	N/A	3.41 ± 0.000197	N/A	N/A
Lorentzian exponent	N/A	1.64 ± 0.000211	N/A	N/A
χ^2	6.5	4.8	1.6	4.4

Figure 3.12 shows SAXS data for solutions of **PBI-I** at different pHs as well as the fits used to model the data. Model parameters used to fit the data are summarized in Table 3.3. Unlike **PBI-L**, **PBI-I** could be modelled at pH 7 using a combined sphere and power law fit. It is expected that there are spherical micelles at this pH because the PBI is partly deprotonated. We have seen PBIs fit these spherical models at pH 7 before.²³ The sphere radius of around 1.15 nm was similar to **PBI-L**, meaning there is similar packing of molecules at this pH which isn't surprising given their similar size. At pH 6 **PBI-I** could be fitted to a flexible elliptical cylinder combined with a power law. Formation of worm-like fibre structures by **PBI-I** at this pH agrees with observations from UV-vis absorption spectroscopy, apparent pK_a values, and dynamic viscosity measurements. At pH 5, **PBI-I** could not be fitted to a flexible cylinder model anymore and was modelled using a mass fractal model instead. A fractal is a structure which appears the same regardless of length scale. Mass fractals are typically aggregates of structures that persist throughout the system instead of just the surface of the

capillary. We attribute this to a transition of nanostructures below the apparent pK_a values making it difficult to fit due to poor solubility and inconsistent nanostructures.

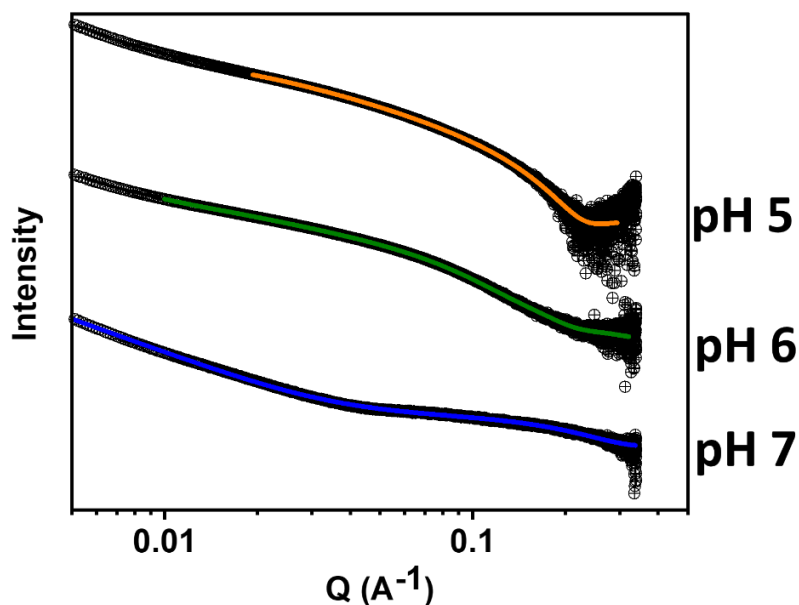


Figure 3.12. SAXS data for solutions of **PBI-I** prepared at 10 mg/mL and pH-adjusted as required with the data shown as open symbols and the fits as differently coloured lines indicating the pH, 5 (orange), 6 (green), and 7 (blue). Note the data are offset on the intensity scale for clarity.

Table 3.3. SAXS fitting results for **PBI-I** as 10 mg/mL solutions at different pH.

pH	5	6	7
Model	Mass fractal	Flexible elliptical cylinder + power law	Sphere + power law
Length (nm)	N/A	20.6 ± 0.486	N/A
Kuhn length (nm)	N/A	2.24 ± 0.381	N/A
Cylinder radius (nm)	N/A	1.52 ± 0.000518	N/A
Axis ratio	N/A	2.17 ± 0.0239	N/A
Sphere radius (nm)	N/A	N/A	1.16 ± 0.00436
Power law	N/A	2.22 ± 0.000224	2.48 ± 0.000991
Radius (nm)	1.73 ± 0.00229	N/A	N/A
Mass fractal dimension	2.00 ± 0.00239	N/A	N/A
Cut-off length (nm)	6.77 ± 0.0218	N/A	N/A
χ^2	2.7	1.7	7.1

Lastly, the SAXS data for solutions of **PBI-V** at 10 mg/mL at different pHs were fitted. Figure 3.13 shows the SAXS data as well as the fits used to model the data. Model parameters used to fit the data are summarized in Table 3.4. In contrast to the other PBIs, **PBI-V** could be fitted to a flexible cylinder model at pH 5 and 6 without issues in the high Q region. Like **PBI-I**, at pH 7 **PBI-V** could be modelled using a combined sphere and power law model. **PBI-L** and **PBI-I** have similar spherical radii, whereas the spherical radius of **PBI-V** at pH 7 is larger at 3.83 nm. Meaning it is more molecules stacked together because of the smaller amino side chain. At pH 6, **PBI-V** could be fitted to a flexible elliptical cylinder combined with a sphere. It should be noted that the lengths of the flexible elliptical cylinders for **PBI-V** at pH 6 and 5 were manually fitted to 300 nm. At pH 5, **PBI-V** was again able to be fitted to a flexible elliptical cylinder model combined with a sphere. It was fitted using similar values for the length, Kuhn length, and radius as **PBI-V** at pH 6. It is evident that the nature of the fibre structure is extremely dependent on pH as well as choice of amino acid. We can use this to our advantage for the development of hydrogels as it should impact their gelation route and their final bulk properties.

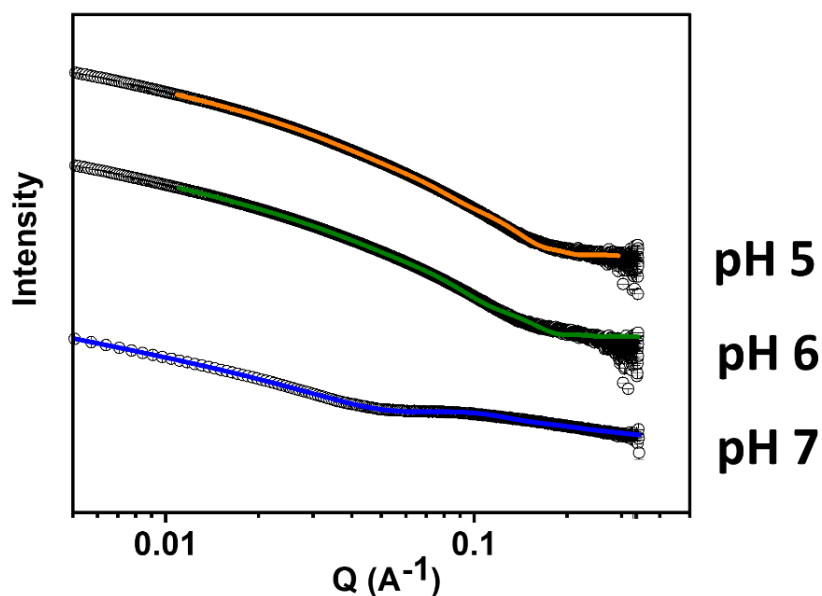


Figure 3.13. SAXS data for solutions of **PBI-V** prepared at 10 mg/mL and pH-adjusted as required with the data shown as open symbols and the fits as coloured lines indicating the pH, 5 (orange), 6 (green) and 7 (blue). Note the data are offset on the intensity scale for clarity.

Table 3.4. SAXS fitting results for **PBI-V** as 10 mg/mL solutions at different pH. *No fitting error available.

pH	5	6	7
Model	Flexible elliptical cylinder + sphere	Flexible elliptical cylinder + sphere	Sphere + power law
Length (nm)	300*	300*	N/A
Kuhn length (nm)	2.17 ± 0.000416	2.65 ± 0.00129	N/A
Cylinder radius (nm)	1.63 ± 0.000789	1.57 ± 0.00125	N/A
Axis ratio	4.09 ± 0.00346	4.55 ± 0.005	N/A
Sphere radius (nm)	4.85 ± 0.00238	4.13 ± 0.00261	3.83 ± 0.00778
Power law	N/A	N/A	1.43 ± 0.00218
χ^2	11	10	2.1

The CVs of solutions of PBIs with 0.1 M NaCl electrolyte at different pH values were collected to see if the different fibre morphologies could be linked to the reduction process for the radical anion. As the pH is lowered and the structures become larger it is expected that they should become less efficient at the electron transfer as the available surface area changes. The CVs of the PBIs at pHs 5 to 9 were measured and are shown in Figure 3.14. The reduction potentials are all around -0.6 V, which matches what was seen for amino acid-functionalised PBIs at 5 mg/mL.²¹ This is expected since the imide group does not have a great impact on HOMO and LUMO energies of PBIs.⁴⁰ However, the CVs did change shape for the different PBIs at different pH values indicating a change in electron movement and reduction process with the different self-assembled structures. At pH 7, the peak positions for the reduction potentials are similar for all three PBIs. This is not surprising as the PBIs are quite structurally similar at this pH. For **PBI-L** and **PBI-I**, the capacitance was larger for the solutions at pH 8 and 9 than pH 5, 6, and 7, whereas for **PBI-V** this trend was not observed. The changes in CV shape with a change in pH suggest that the different morphologies in solution are having an impact on the reduction process. The SAXS of **PBI-V** for pH 5 and 6 could be fitted to flexible elliptical cylinders combined to a sphere model. Compared to **PBI-L** which was modelled using a shape-independent model at pH 6 and a flexible elliptical cylinder model combined with a power law at 5. **PBI-I** could only be modelled at pH 6 using a flexible elliptical cylinder model combined with a power law. The Kuhn length for **PBI-V** at these pHs is very

low meaning their aggregates are highly flexible. This may be why **PBI-V** is seeing a difference in the reduction process compared to the other two PBIs. The reduction potentials at different pH values are compiled in Table 3.5. Again, this highlights the importance of the nature of the aggregated species present, but also gives us the opportunity to tune electron movement by changing the surface area of the PBI aggregates as they self-assemble into 3D structures.

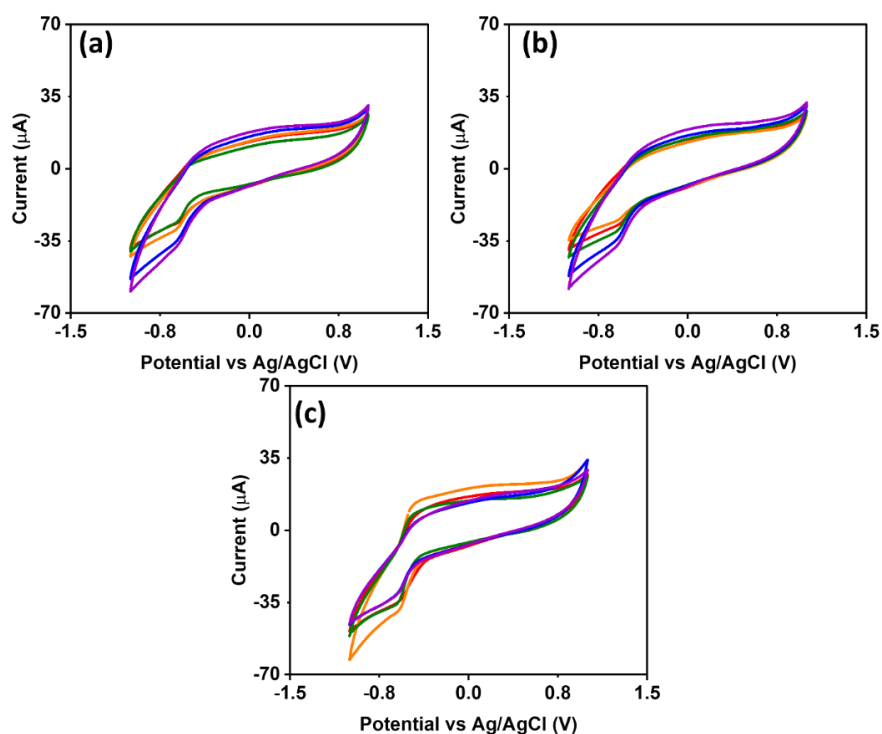


Figure 3.14. Cyclic voltammograms of (a) **PBI-L**, (b) **PBI-I**, and (c) **PBI-V** at 10 mg/mL solutions using 0.1 M NaCl electrolyte solution with a scan rate of 0.05 V/s at pH 5 (red), pH 6 (orange), pH 7 (green), pH 8 (blue), and pH 9 (purple).

Table 3.5. Reduction potentials of PBIs in solution (10 mg/mL) with 0.1 M NaCl electrolyte at different pHs and a scan rate of 0.05 V/s

	PBI-L	PBI-I	PBI-V
pH	Reduction potential (V)	Reduction potential (V)	Reduction potential (V)
5	-0.58	-0.57	-0.57
6	-0.61	-0.58	-0.58
7	-0.61	-0.56	-0.58
8	-0.62	-0.58	-0.59
9	-0.59	-0.58	-0.59

Interest in PBIs for use in optoelectronic materials relies on their ability to form photogenerated radical anion efficiently and we wanted to see if we could use pH to improve that. It has been seen for hydrogels of **PBI-V**, which form more radical than **PBI-L**, that the morphology on a larger length scale is not affected by irradiation, but the entanglement density is affected and the fibre density increased on a local packing scale.²² Meaning the radical formation is dependent on the local packing which should be higher as the local packing increases. The dynamic viscosity and SAXS showed the packing of the PBIs were highly dependent on both the pH and the amino acid side chain. With the choice of amino acid side chain changing how the PBI self-assembled as the pH was lowered. The radical anion can form by addition of a reducing agent,^{41, 42} or by irradiation using a light source.²⁰ Here we irradiated the different PBIs in solution at pHs 5 to 9 using a 365 nm LED for 5 minutes and compared the before and after UV-vis absorption spectra. To see if there is a link between the morphologies determined by SAXS at the various pH and better radical formation.

Figure 3.15 (a) shows the normalised UV-vis absorption spectra for **PBI-L**. For pH 7 to 9 there is a shift in the 0-1 vibronic transition of the S_0-S_1 band from 505 nm to 477 nm after irradiation, indicating some changes in packing resulting in the PBI absorbing at higher energy. Then for all pH values three characteristic peaks appear at 725, 815, and 980 nm after irradiation and blue shift of the peaks at 505 nm is observed. The shift is characteristic of a change in aggregate type and the new peaks are the characteristic peaks of the radical anion.⁴¹ These peaks gradually increase in absorbance intensity as the pH is decreased from 9 to 5. Figure 3.15 (b) shows the normalised UV-vis absorption spectra for **PBI-I** at different pHs. As for **PBI-L**, the three characteristic peaks for the radical anion appear after irradiation. These peaks increase in absorbance intensity for the different solutions at pH 9, 8, and 7, then for solutions at pH 6 and 5 the absorbance of the radical anion peak begin to decrease. This pH is below both apparent pK_a values and **PBI-I** is completely protonated. Also, at this pH the SAXS of **PBI-I** could again not be fitted due to what we think is a transition of nanostructures. At pHs 8 and 9 there is a shift in the 0-1 vibronic transition of the S_0-S_1 band from 505 nm to 477 nm like **PBI-L**. Lastly, Figure 3.15 (c) shows the normalised UV-vis absorption spectra for **PBI-V** at different pHs.

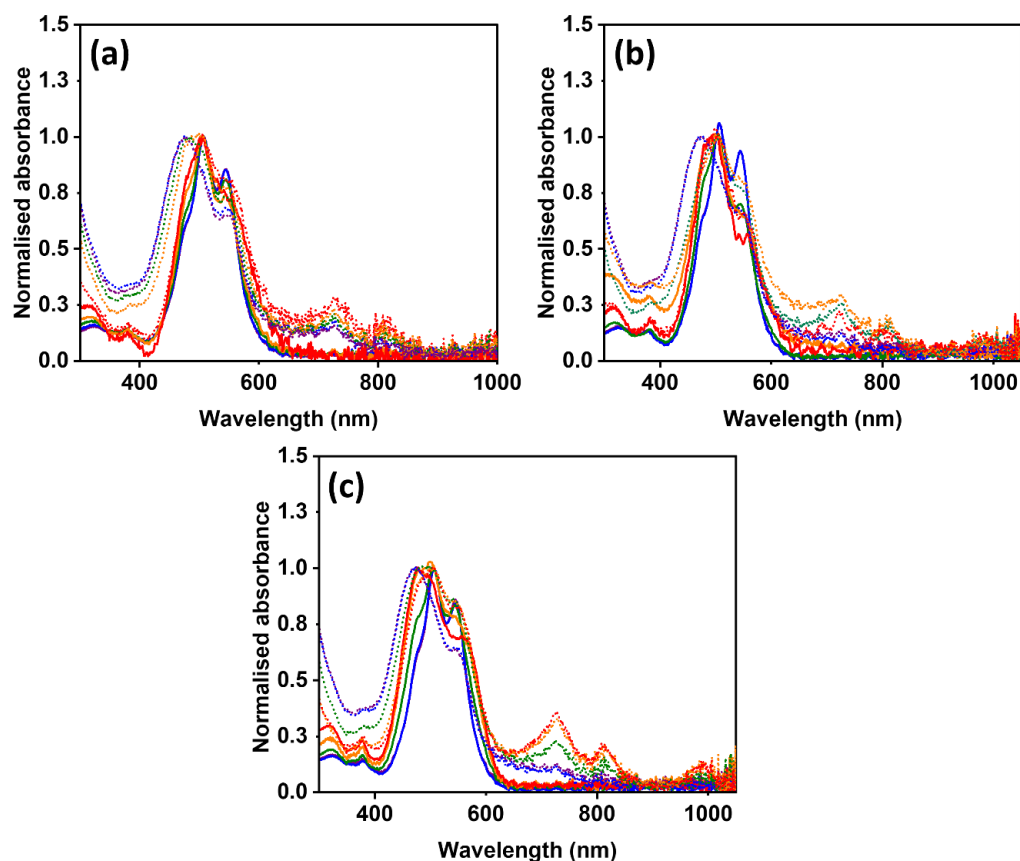


Figure 3.15. UV-vis absorption spectra of solutions at a 10 mg/mL concentration of (a) **PBI-L**, (b) **PBI-I**, and (c) **PBI-V** at pH 5 before (**solid red**) and after irradiation (**dotted red**), pH 6 before (**solid orange**) and after irradiation (**dotted orange**), pH 7 before (**solid green**) and after irradiation (**dotted green**), pH 8 before (**solid blue**) and after irradiation (**dotted blue**), and pH 9 (**solid purple**) and after irradiation (**dotted purple**).

The absorbance intensity for the radical anion is seen to be the most for the lowest pH solutions, suggesting the increased aggregation is preferential for radical anion formation and stabilisation. Like **PBI-L** and **PBI-I**, there is a shift in the 0-1 vibronic transition of the S_0 - S_1 band from 505 nm to 477 nm for pH 8 and 9. The first increase of the absorbance intensity for the radical anion is seen at pH 7 when SAXS indicates the aggregates structures fit to a spherical model and the micellar structures increase at pH 6 when the SAXS indicates the aggregate and micellar structures fit to a combined flexible elliptical and sphere model. Interestingly, for **PBI-V** at pH 5 the absorbance intensity for the radical anion peaks is the same as at pH 6, which is mirrored in the SAXS at these pHs with them both fitting to the same model. Overall,

PBI-V forms the most radical anion and **PBI-L** the least at pH 5 and 6, which we have seen previously for solutions of **PBI-V** at 5 mg/mL at pH 8.²¹ At pH 7 **PBI-I** had formed the most radical and **PBI-L** had formed the least. Finally, at pH 8 and 9 **PBI-L** had formed the most radical anion and **PBI-I** and **PBI-V** formed similar amounts. This shows the importance of pH as a tool for changing the local packing and aggregates structure to change the PBIs' optoelectronic properties.

3.2.2 Probe into the impact of amino acid choice on the hydrogel properties and gelation process

It has been shown that as the pH is lowered and the molecules pack into fibre structures the radical formation is improved, using a slow pH trigger offer more uniform self-assembled structures compare to using HCl to pH adjust. Also we wanted to investigate whether **PBI-I** could be used to prepare hydrogels with different bulk gel properties using glucono- δ -lactone (GdL), already knowing that it has a different response to pH than **PBI-L** and **PBI-V**. GdL was chosen because the hydrolysis lowers the pH below the apparent pK_a values of the PBIs where the fibres then entangle and form the gel network. The rate of gelation is determined by the kinetics of the pH decrease. Since the hydrolysis of GdL is slower than its dissolution in water, it allows for the formation of uniform gels compared to those formed from a mineral acid like HCl.⁴³ 8 mg/mL of GdL was added to each of the PBI solutions resulting in gels with a final pH of 3.7. As the pH values were all comparable, any difference in the hydrogel network is not due to final pH differences. Figure 3.16 shows photos of the PBI hydrogels inverted in Sterilin vials. Sample inversion however is only a preliminary test and does not conclusively indicate a gel. To confirm the presence of a gel bulk rheology was measured.

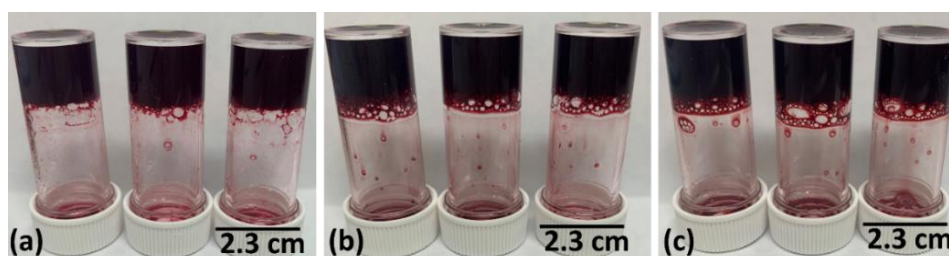


Figure 3.16. Photographs of inverted Sterilin vials containing hydrogels of (a) **PBI-L**, (b) **PBI-I**, and (c) **PBI-V**.

The bulk mechanical properties of the hydrogels were measured to see whether they would be influenced by the chemical structure and the different aggregations we have seen in the SAXS and the absorption spectroscopy seen in solution. Figure 3.17 (a) and (b) shows the average strain and frequency sweeps for each PBI. The formation of a gel can be influenced by factors such as temperature, humidity, or gelation time, so consistency is important to ensure reproducibility. The strain and frequency sweeps for each PBI were therefore measured in triplicate to obtain an average value for storage modulus (G') and loss modulus (G''). The average G' and G'' values for the linear viscoelastic regions of the hydrogels are listed in Table 3.6. The strain sweeps show that **PBI-I** has lower yield and flow points than **PBI-L** or **PBI-V**. More interestingly, there was a noticeable difference in the stiffness and $\tan\delta$ value of **PBI-I** compared to the other PBIs. All these data suggest that not only do the PBIs form different aggregates, but they also form different networks which directly impact the mechanical properties of the gel network.

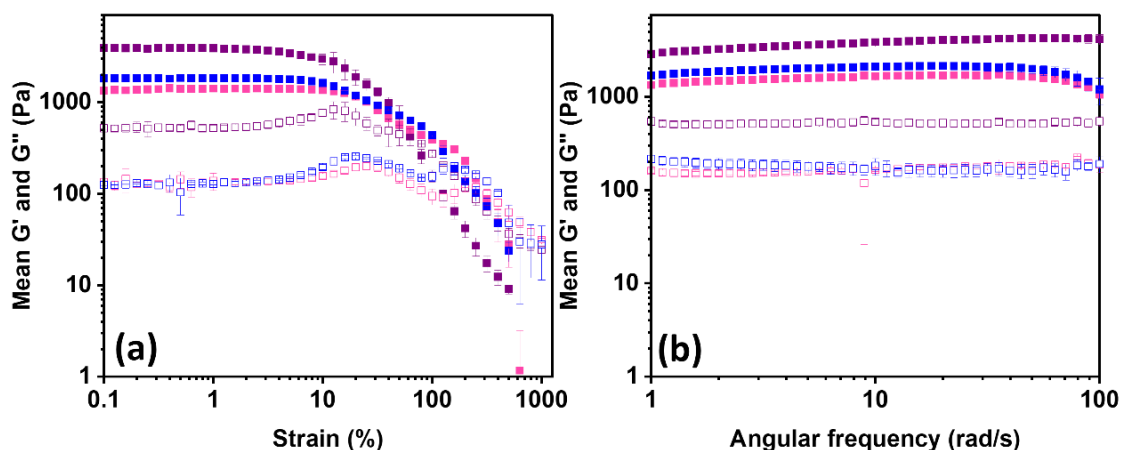


Figure 3.17. (a) Strain sweep data at 10 rad/s and (b) frequency sweep data at 0.5% strain for **PBI-L** (pink), **PBI-I** (purple), and **PBI-V** (blue). In all cases, the storage modulus (G') is represented by the closed symbols and the loss modulus (G'') is represented by open symbols. Measurements were performed in triplicate and errors were calculated from the standard deviation of 3 repeat measurements.

Table 3.6. Key bulk mechanical properties of the hydrogels with **PBI-L**, **PBI-I** and **PBI-V**. G' and G'' are taken at 10 rad/s frequency.

PBI	L	I	V
G' (Pa)	1700 ± 49	3900 ± 190	2100 ± 180
G'' (Pa)	170 ± 6.6	540 ± 36	180 ± 439
Yield point (%)	10	5	12
Flow point (%)	320	60	200
$\tan\delta$ (G''/G')	0.11	0.13	0.07

The higher-order structures of the aggregates and micellar structures of the PBI hydrogels were investigated using SAXS. Full fitting parameters for the PBIs are found in Table 3.7. All three PBI hydrogels fit flexible elliptical cylinder models. The large Kuhn length for the hydrogels is expected as the worm-like micelles start to entangle and form the network fibres, they become less flexible. Both **PBI-I** and **PBI-L** fit a flexible elliptical cylinder with a power law model, the power law allowing for a better fit to the increased scattering at low Q . **PBI-V** fit a flexible elliptical cylinder with a polydispersity of 0.3. The polydispersity allows for a size distribution of cylinder radii to be accounted for in the fit. All three PBIs had similar axis ratios and cylinder radii. The cylinders in **PBI-L** hydrogels had the longest length at 426 nm, while **PBI-I** had the smallest cylinder length at 332 nm. The Kuhn length was the largest for hydrogels of **PBI-I** (30.6 nm) compared to **PBI-V** (28.0 nm) and **PBI-L** at (15.2 nm). This decrease in flexibility may be contributing to the difference in the stiffness of the **PBI-I** hydrogels. However, it is difficult to make direct correlations between the bulk rheological properties and the SAXS because scattering only gives an image of the secondary structure and not the whole gel network.

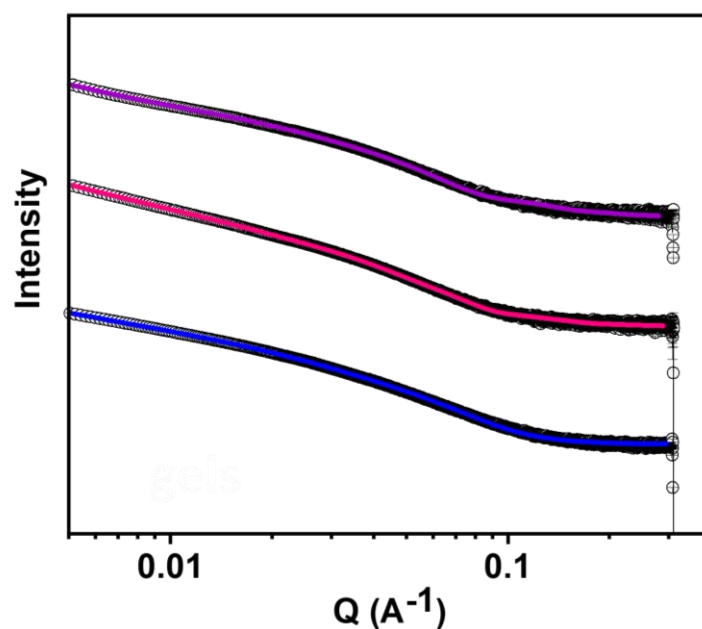


Figure 3.18. SAXS data for hydrogels of **PBI-L** (pink), **PBI-I** (purple), and **PBI-V** (blue) hydrogels with experimental data shown as open symbols and fits as a solid line. Note the data are offset on the intensity scale for clarity.

Table 3.7. SAXS fit table for **PBI-L**, **PBI-I**, and **PBI-V** hydrogels. *No fitting error available.

PBI	L	I	V
Model	Flexible elliptical cylinder + power law	Flexible elliptical cylinder + power law	Flexible elliptical cylinder polydispersity 0.3
Length (nm)	300*	332 ± 9.99	406 ± 5.99
Kuhn length (nm)	15.2 ± 0.148	30.6 ± 0.991	28.0 ± 0.0318
Cylinder radius (nm)	3.57 ± 0.0114	3.36 ± 0.00899	2.65 ± 0.00322
Axis ratio	2.23 ± 0.00121	2.38 ± 0.00993	3.51 ± 0.0108
Power law	2.76 ± 0.00458	2.31 ± 0.0117	N/A
χ^2	2.1	2.3	4.3

To understand the difference in bulk rheological properties of **PBI-I** compared to **PBI-L** and **PBI-V**, a series of kinetic studies were carried out to study the change in structure as the gel network forms over time. G' and G'' were monitored over time during gelation and the data were overlaid with pH data from GdL-triggered gelation and $^1\text{H-NMR}$ data of percentage assembly over time. Monitoring of assembly via $^1\text{H-}$

NMR is based on the detection of PBI molecules in solution and their disappearance from the NMR spectrum as they self-assemble and form longer stationary fibres.^{44, 45}

For **PBI-L** the three gelation kinetics studies were overlaid together into Figure 3.19. It is seen that for the ¹H-NMR measurement at t = 0, already 60% of the material is assembled in solution, suggesting that assembled structures are present before gelation. This is again seen in the viscosity and UV-vis absorption data and is due to the pH already being below the first apparent pK_a of **PBI-L** at 7.2 by the time the first NMR is complete. The percent assembled remains at 60% until 15 minutes into the measurements when it begins increasing rapidly. When the pH drops further to 3.6 after around one hour, we see an increase in G' which eventually plateaus as gel formation is complete and the percentage assembly reaches nearly 100%. The ¹H-NMR data for **PBI-L** show a two-stage assembly process between 20 and 30 minutes that is not seen in the rheology data, indicating that perhaps the structures in solution are elongating or thickening before starting to affect the G' value.

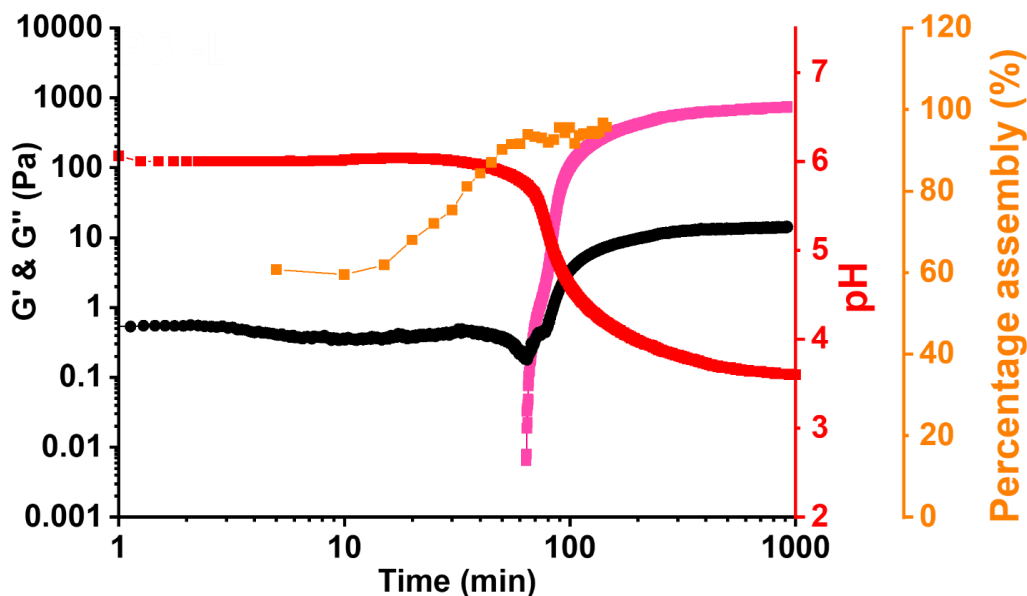


Figure 3.19. Development of G' (*pink data*) and G'' (*black data*) over time during the gelation of **PBI-L** measured at a strain of 0.5% and a frequency of 10 rad s⁻¹, compared to the change in pH (*red data*) over time and the change in percent assembly (*orange data*) of **PBI-L** over time calculated from the change in ¹H-NMR.

The three gelation kinetics studies for **PBI-I** are overlaid together in Figure 3.20: ¹H-NMR data at t = 0 suggest that the **PBI-I** solution consists of 40% assembled

structures initially. They rapidly start to assemble after 15 minutes as the pH decreases below the second apparent pK_a of 6.6. The rheological data do suggest the presence of persistent structures within the first 60 minutes of gelation. However, only after the pH drops below 3.6 does G' plateau as gel formation is complete with a final $\tan\delta$ value of 0.03. This difference between the $\tan\delta$ values of the strain sweeps between the pitot bulk measurements and the kinetic measurements above could be due to the different geometries used to carry out the measurements.⁴⁶ The $\tan\delta$ value for **PBI-I** is still larger than the value for **PBI-L** ($\tan\delta = 0.02$) observed during its kinetic measurements. **PBI-I** has pK_{a1} and pK_{a2} values for its aggregates which are closer to each other than those of the other two PBIs and therefore has different assembly kinetics resulting in different assemblies of fibrous structures and different bulk mechanical properties of the eventual hydrogels. This agrees with the different viscosity and UV-vis absorption data for **PBI-I** where **PBI-I** was assembling at higher pH values than the other two PBIs.

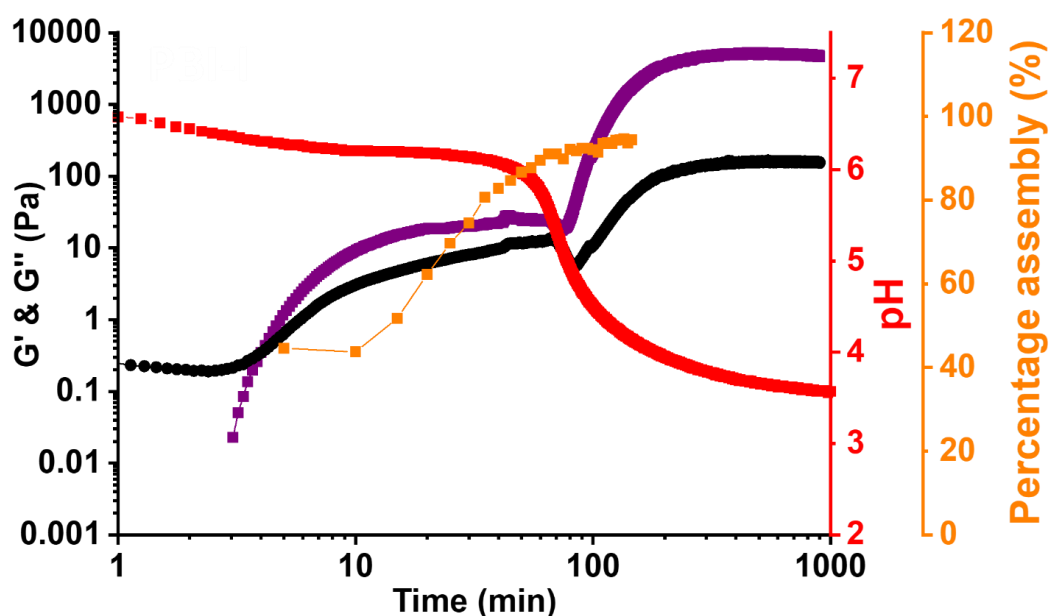


Figure 3.20. Development of G' (purple data) and G'' (black data) over time during the gelation of **PBI-I** measured at a strain of 0.5% and a frequency of 10 rad s^{-1} , compared to the change in pH (red data) over time and the change in percent assembly (orange data) of **PBI-I** over time calculated from the change in $^1\text{H-NMR}$.

For **PBI-V** the three gelation kinetics studies were overlaid together into Figure 3.21. For **PBI-V** the $^1\text{H-NMR}$ data at $t = 0$ show there are only 20% assembled structures,

which is lower than **PBI-L** and **PBI-I**. This is explained by the difference in the pK_{a1} for **PBI-V** (pH 6.7) which has not been reached yet by the time the first NMR measurement is complete. Similar to **PBI-L**, the rheological measurements for **PBI-V** do not show the presence of solid-like materials until 55 minutes into the experiment. This correlates with the pH beginning to drop. When it has dropped below both apparent pK_a values, $\tan\delta$ becomes 0.01, which is the smallest of the three PBIs. Again, differences compared to the bulk strain data may be due to the change in geometry. Like **PBI-L**, the $^1\text{H-NMR}$ data for **PBI-V** show a two-stage assembly process between 20 and 30 minutes that is not seen in the rheology data. There is an initial increase from 20% to 25% within the first 10 minutes, then at 35 minutes there is change in the rate of assembly and 20 minutes later we begin to see the presence of solid-like materials. **PBI-V** is the only PBI that is not 100% assembled when the pH begins to drop below the pK_a s. These kinetics data show that the self-assembly processes of the three PBI are all very different.

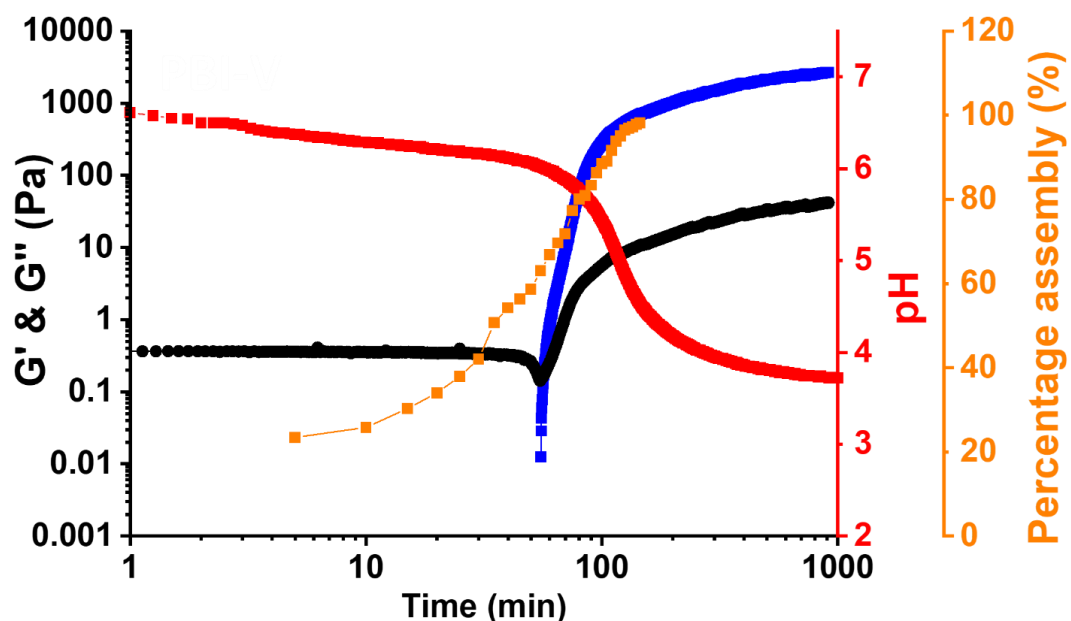


Figure 3.21. Development of G' (**blue data**) and G'' (**black data**) over time during the gelation of **PBI-V** measured at a strain of 0.5% and a frequency of 10 rad s^{-1} , compared to the change in pH (**red data**) over time and the change in percent assembly (**orange data**) of **PBI-V** over time calculated from the change in $^1\text{H-NMR}$.

Finally, to investigate how the larger nanostructures in the different gel networks affect the formation of the radical anion, the UV-vis absorption spectra of the PBI

hydrogels were measured before and after irradiation using a UV light for 5 minutes. The normalised UV-vis absorption spectra of the PBI hydrogels before and after irradiation are shown in Figure 3.22. The S_0-S_1 peaks at 510 nm and 545 nm in solution have shifted to 475 nm and 570 nm for **PBI-V** as a hydrogel, which is expected when aggregation has occurred. The S_0-S_1 peak ratios for **PBI-L** and **PBI-I** hydrogels are similar to one another at 0.55 but the **PBI-V** hydrogel has a much larger ratio of 0.67. This indicates that the **PBI-V** gel network is aggregated in a different way compared to **PBI-L** and **PBI-I**. After irradiation there is an appearance of peaks at 730, 813, and 990 nm corresponding to the radical anion in all the gels.⁴¹ As a hydrogel, **PBI-V** forms the most of the conductive radical anion while **PBI-L** produces the least. Again, this difference in radical formation has been seen in previous work, indicating that both the molecular packing and the networks formed through gelation are impacting the ability to form the radical anion.²⁰

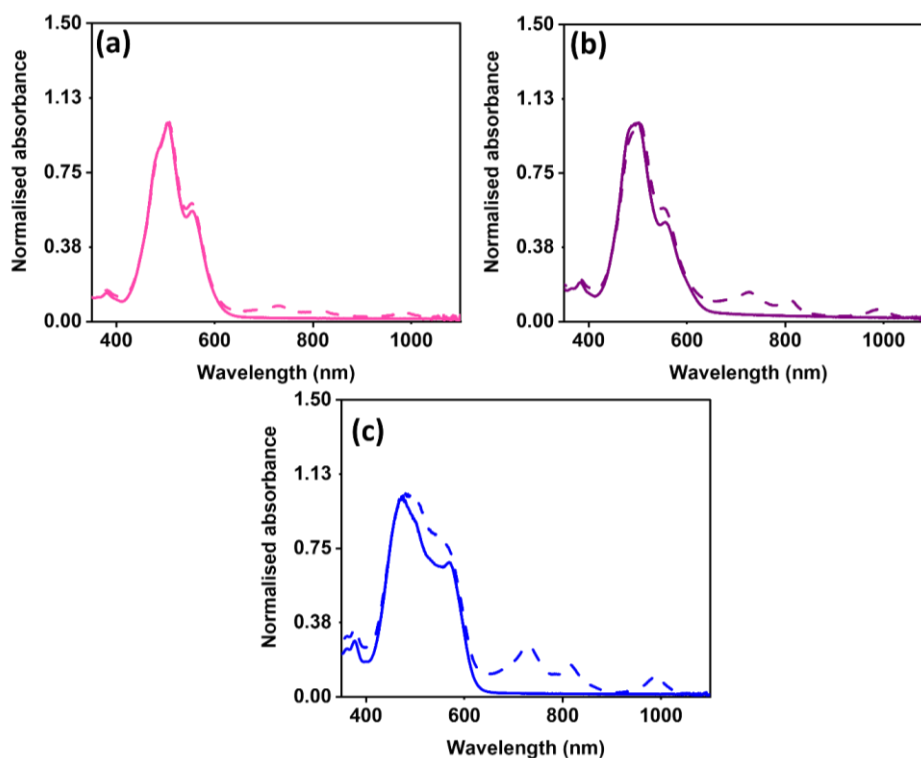


Figure 3.22. UV-vis absorption spectra of hydrogels made using (a) **PBI-L** before (solid pink) and after (dashed pink) irradiation, (b) **PBI-I** before (solid purple) and after (dashed purple) irradiation, (c) **PBI-V** before (solid blue) and after (dashed blue) irradiation.

3.3. Conclusions

This work exemplifies how slight changes in the chemical structure of PBIs can have a major impact on the larger assemblies. Already we had seen that the amino acid side chain choice could impact the radical anion formation, with smaller side chain groups forming more radical anion. However, we had not investigated how the side chain choice could be used to tune pH dependent self-assembly and the hydrogel properties. The differences in behaviour were evident when the pH of the solutions was changed. The UV-vis absorption and viscosity data of the solutions showed that, as the pH was lowered, **PBI-I** was assembling into different micellar structures compared to **PBI-V** and **PBI-L**. This difference may be due to the asymmetric side chain in the amino acid affecting the self-assembled aggregates and packing. SAXS showed that the nature of the micellar and nanostructure for the PBIs is extremely dependent on pH and amino acid side chain choice. UV-vis absorption spectroscopy of the solutions at different pHs showed that as the pH is lowered the amount of radical formed increases. **PBI-V** formed the largest amount of conductive radical anion in solution while **PBI-L** formed the least. From these results it could be said that the smaller hydrophobic the side chain of the amino acid the more efficient the packing of the PBIs, which in term yields better radical anion formation.

Bulk rheology showed that the hydrogels made using **PBI-I** were distinctly stiffer than those made using **PBI-L** and **PBI-V**. SAXS of the hydrogels with **PBI-I** being the least flexible and shortest in length which may explain the difference in the gel stiffness. Gelation kinetics studies of the gels during formation showed a completely different behaviour for **PBI-I** compared to **PBI-V** and **PBI-L**, supporting the theory that the side chain choice could also be used to change gel properties. UV-vis absorption spectroscopy of the hydrogels showed that **PBI-V** formed the largest amount of conductive radical anion and **PBI-L** forming the least, which follows the trend previously seen whereas the amino aside chain increase in size it forms less radical. In the future these results could be used as guidelines in chemical structure design to help tailor the efficiency of the radical anion formation or the hydrogel's stiffness and strength.

3.4. Experimental

3.4.1 Materials and Synthetic procedures

All chemicals were purchased from Merck Life Science or Alfa Aesar and used without further purification. Deionised water was used throughout. All PBIs were synthesised using a published method.^{20-28, 47}

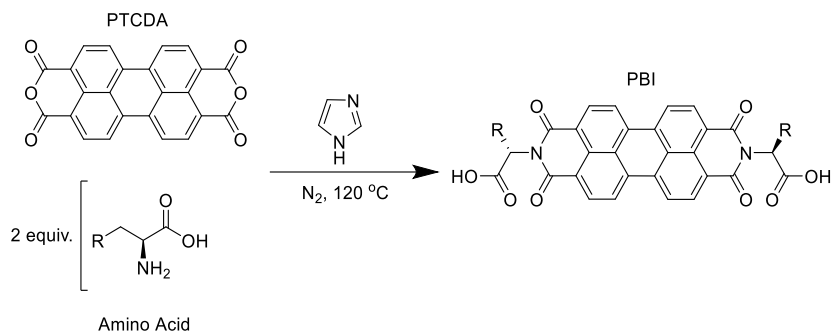


Figure 3.23. General reaction scheme for an imide substitution for an amino acid-substituted PBI.

In a 100 mL Schlenk flask, 1 equiv. of 3,4:9,10-perylenetetracarboxylic acid dianhydride (PTCDA), 2 equiv. of amino acid (*L*-isoleucine, *L*-leucine, or *L*-valine) and 10 equivs. of imidazole were combined. The flask was placed under an atmosphere of nitrogen and allowed to stir for 5 h at 130°C. Then the reaction was cooled down to 90°C and diluted with deionised water (approx. 5 mL/mmol PTCDA) via syringe and needle. The reaction was then stirred for 1 hour and gravity filtered while warm into a 250 mL round bottom flask to remove unreacted PTCDA. Next, 2 M HCl (approx. 1 mL/mmol PTCDA) was added to the 250 mL flask to lower the pH and precipitate the product. This was vacuum filtered to isolate the product as a gel-cake in the filter. The cake was allowed to air-dry overnight, before being resuspended in 2 M HCl and boiled for 5 hours to remove residual imidazole. The suspension was then filtered, and the solid in the filter was freeze-dried.

N, N'-Di(*L*-leucine)-perylene-3,4:9,10-tetracarboxylic acid bisimide (**PBI-L**)

Yield (1.41 g, 45%) ¹H-NMR (400 MHz, DMSO-*d*₆, 25°C) δ (ppm) = 8.6 (dd, 4H, J = 8.9 Hz, J = 21 Hz); 8.4 (dd, 4H, J = 8.9 Hz, J = 21 Hz); 5.6 (d, 2H, J = 5.6); 2.1 (m, 4H); 1.63 (m, 2H); 1.0 (d, 6H, J = 6.4 Hz); 0.9 (d, 6H, J = 6.3 Hz).

^{13}C -NMR (100 MHz, DMSO- d_6 , 25°C) δ (ppm) = 171.6 (COOH); 162.9 (C=O); 134.5, 128.9, 124.6, 122.5 (perylene core); 52.0 (CH); 38.2 (CH); 25.5 (CH $_2$); 23.5 (CH $_3$); 22.5 (CH $_3$).

FT-IR: ν/cm^{-1} 3115b (O-H), 1692s (C=O), 1589s (C=O), 1341s (C-O), 1174s (C-O), 799s (aromatic C-H), 741 (aromatic C-H).

HR-ESI-TOF MS: calculated 641.1899 Da for $[\text{C}_{36}\text{H}_{30}\text{N}_2\text{NaO}_8]^+$, found 641.1865 Da.

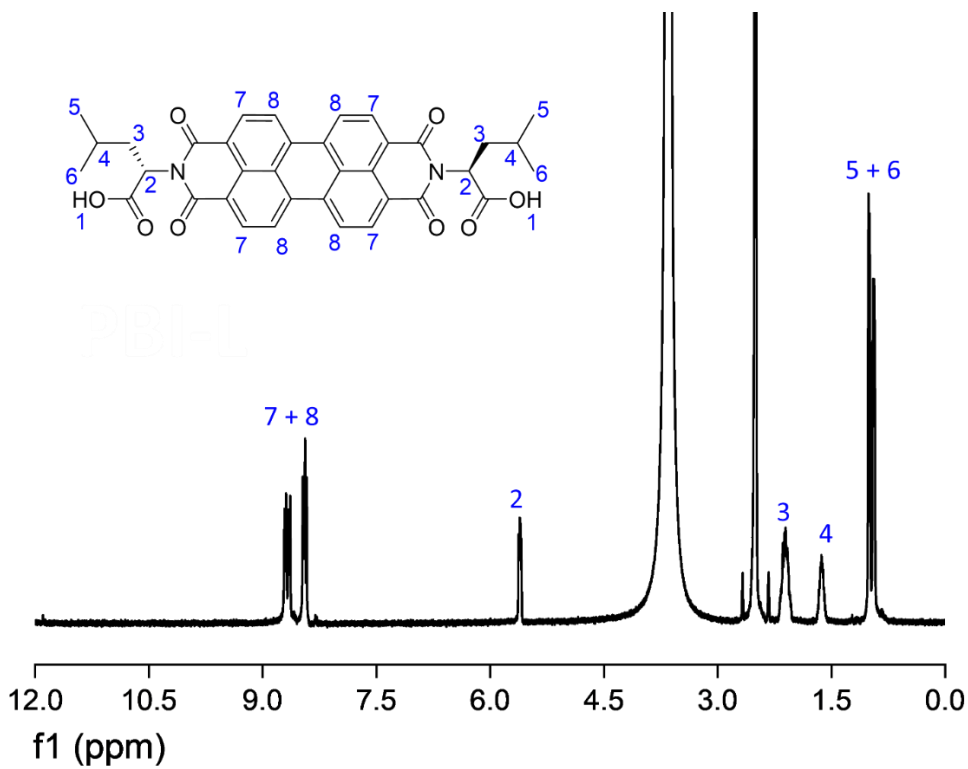


Figure 3.24. ^1H -NMR spectrum of **PBI-L** in DMSO- d_6 at 25°C.

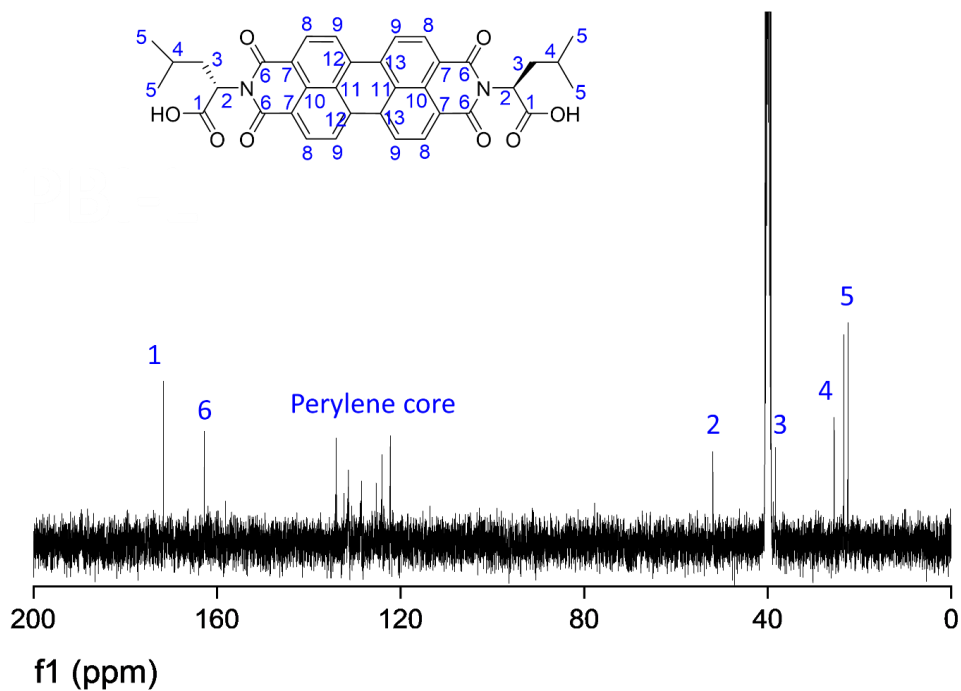


Figure 3.25. ^{13}C -NMR spectrum of **PBI-L** in DMSO-d_6 at 25°C .

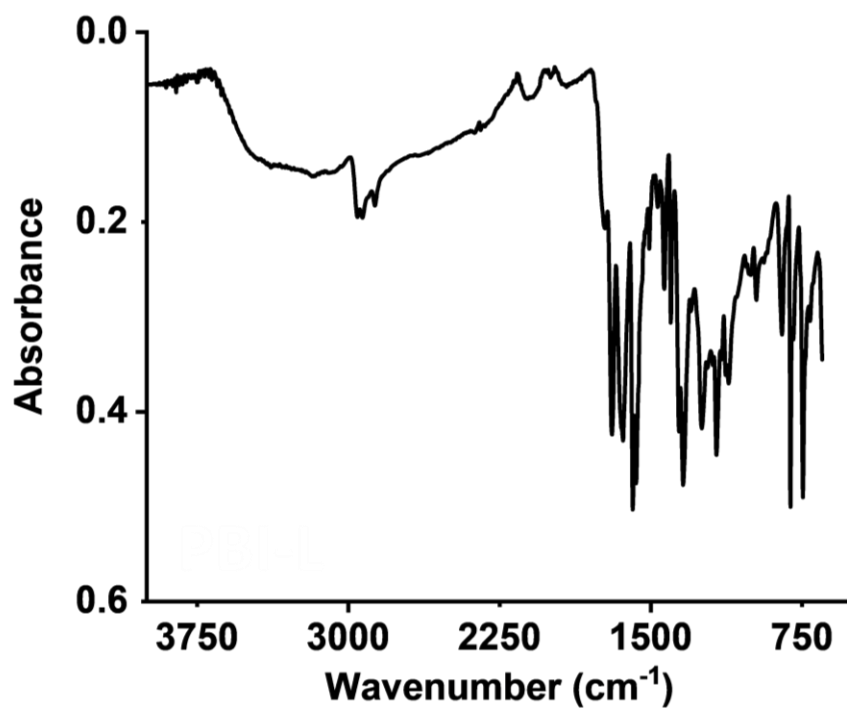
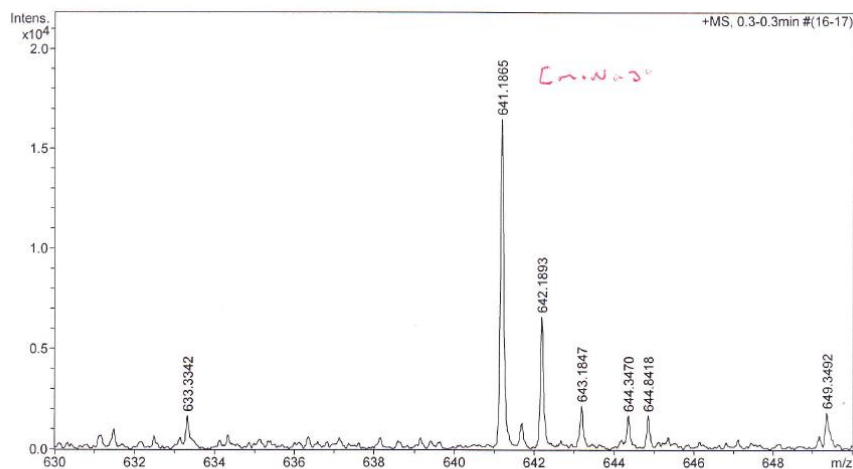


Figure 3.26. Powder FTIR spectrum of **PBI-L**.

Analysis Info
 Analysis Name D:\Data\Mass Spectrometry Service\74451-000001.d
 Method LM MS 50 to 1100 KIM 071215.m
 Sample Name Dietrich-JE03-001
 Comment
 Acquisition Date 11/13/2019 9:08:16 AM
 Operator user
 Instrument / Ser# micrOTOF-Q 74

Acquisition Parameter
 Source Type ESI Ion Polarity Positive
 Scan Begin 50 m/z
 Scan End 1100 m/z



Formula	z	m/z	Meas. m/z	err [ppm]	err [mDa]
C ₃₆ H ₃₀ N ₂ NaO ₈	1+	641.1894	641.1865	4.6	2.9

Figure 3.27. Mass spectrum of **PBI-L** in DMSO.

N, N'-Di(L-isoleucine)-perylene-3,4:9,10-tetracarboxylic acid bisimide (**PBI-I**)

Yield (4.24 g, 86%) ¹H-NMR (400 MHz, DMSO-*d*₆, 25°C) δ (ppm) = 8.24 – 7.92 (m, 8H), 5.26 (dd, J = 9.0, 2.2 Hz, 2H), 1.97 (m, 1H), 1.33 (m, 2H), 1.24 (d, J = 6.4 Hz, 3H), 1.02 (t, J = 7.4 Hz, 3H), 0.84 (t, J = 7.3 Hz, 3H), 0.77 (d, J = 6.9 Hz, 3H).

¹³C-NMR (100 MHz, DMSO-*d*₆, 25°C) δ (ppm) = 170.7 (COOH); 162.3 (C=O); 133.4, 131.0, 128.0, 124.8, 123.3, 121.5 (perylene core); 57.6 (CH), 56.3 (CH), 33.2 (CH), 33.1 (CH), 27.9 (CH₂); 24.9 (CH₂); 18.1 (CH₃); 14.8 (CH₃); 11.2 (CH₃); 11.0 (CH₃).

FT-IR: ν/cm⁻¹ 3171b (O-H), 1698s (C=O), 1595s (C=O), 1331s (C-O), 1179s (C-O), 805s (aromatic C-H), 745 (aromatic C-H).

HR-ESI-TOF MS: calculated 641.1899 Da for [C₃₆H₃₀N₂NaO₈]⁺, found 641.1889 Da.

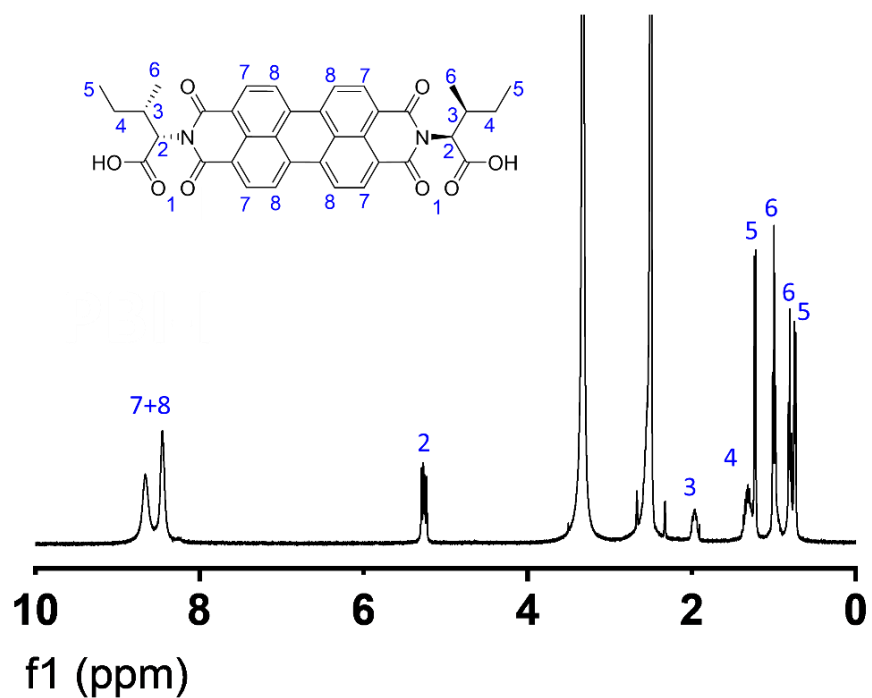


Figure 3.28. $^1\text{H-NMR}$ spectrum of **PBI-I** in DMSO-d_6 at 25°C .

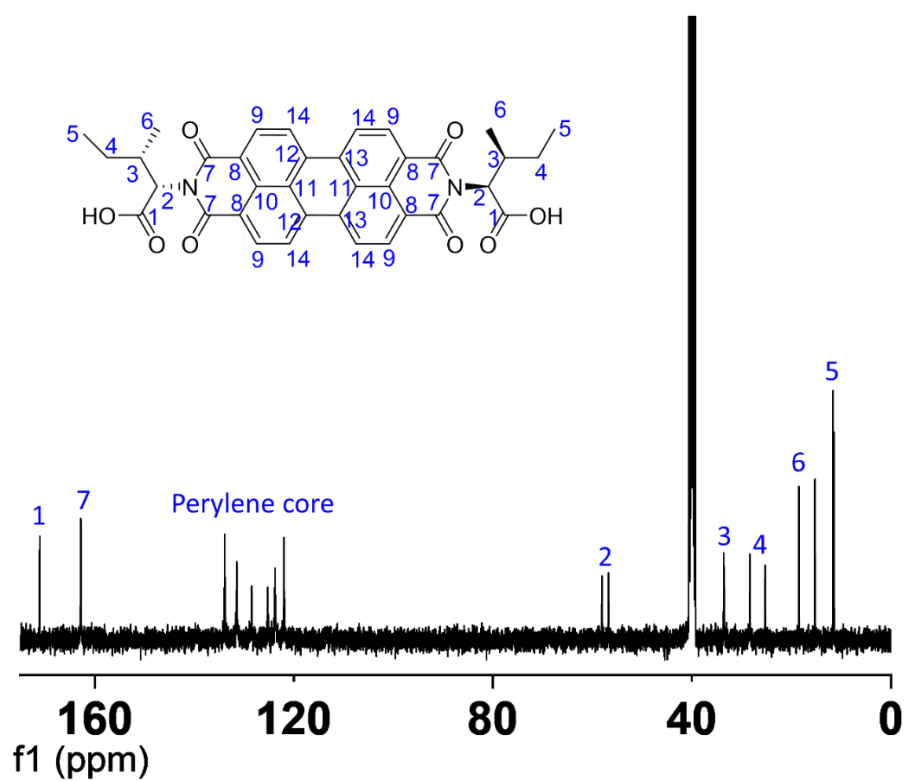


Figure 3.29. $^{13}\text{C-NMR}$ spectrum of **PBI-I** in DMSO-d_6 at 25°C .

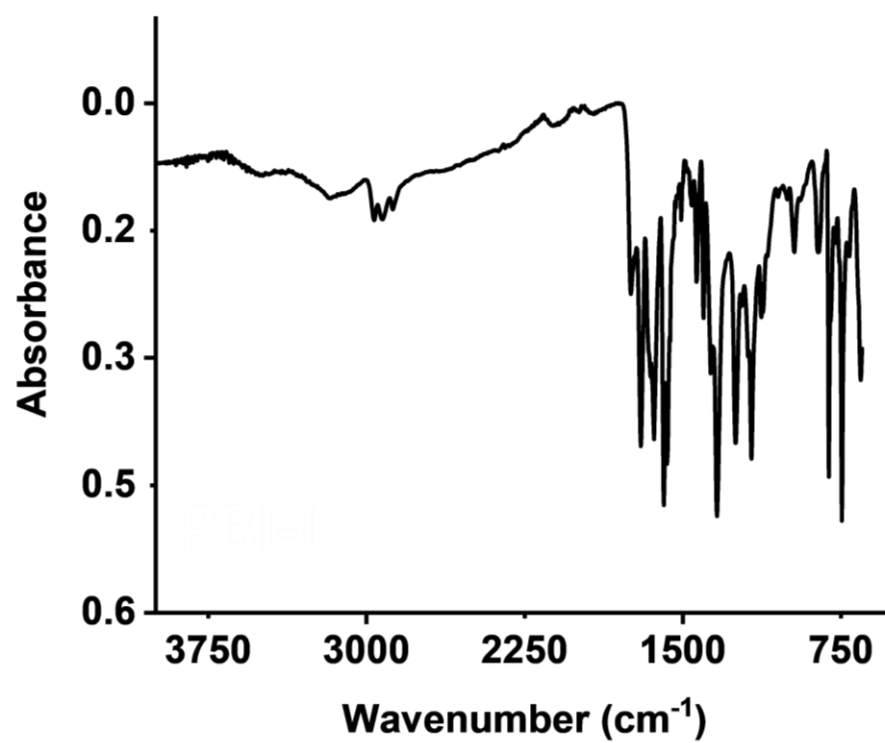
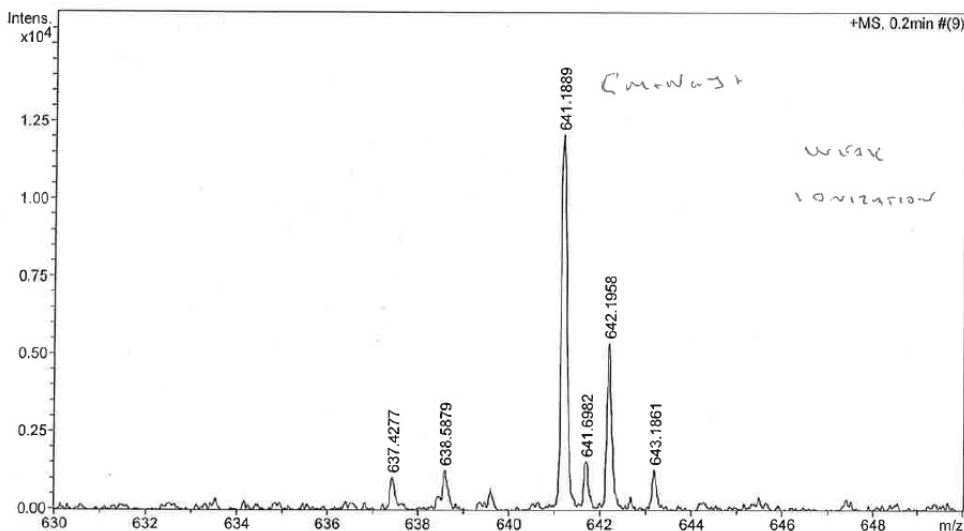


Figure 3.30. Powder FTIR spectrum of PBI-I.

Analysis Info		Acquisition Date	9/22/2020 8:40:55 AM
Analysis Name	D:\Data\Mass Spectrometry Service\76146-000001.d	Operator	user
Method	LM MS 50 to 1100 KIM 071215.m	Instrument / Ser#	micrOTOF-Q 74
Sample Name	Dietrich-GB-PBI-I		
Comment			

Acquisition Parameter			
Source Type	ESI	Ion Polarity	Positive
Scan Begin	50 m/z		
Scan End	1100 m/z		



Formula	z	m/z	Meas. m/z	err [ppm]	err [mDa]
C ₃₆ H ₃₀ N ₂ NaO ₈	1+	641.1894	641.1889	0.9	0.6

Figure 3.31. Mass spectrum of **PBI-I** in ethanol.

N, N'-Di(L-valine)-perylene-3,4,9,10-tetracarboxylic acid bisimide (**PBI-V**)

Yield (1.97 g, 65%) ¹H-NMR (400 MHz, DMSO-*d*₆, 25°C) δ (ppm) = 8.6 (d, 4H, J = 7.6 Hz); 8.4 (d, 4H, J = 7.6 Hz); 5.2 (d, 2H, J = 9.2 Hz); 2.7 (q, 2H, J = 6.3 Hz); 1.2 (d, 6H, J = 6.3 Hz); 0.8 (d, 6H, J = 6.7 Hz).

¹³C-NMR (100 MHz, DMSO-*d*₆, 25°C) δ (ppm) = 170.9 (COOH); 163.1 (C=O); 134.6, 131.9, 128.9, 124.5, 122.3 (perylene core); 58.6 (CH); 27.5 (CH₂), 22.6 (CH₃), 19.5 (CH₃).

FT-IR: ν/cm⁻¹ 2953b (O-H), 1694s (C=O), 1580s (C=O), 1332s (C-O), 1164s (O-H), 803s (aromatic C-H), 714s (aromatic C-H).

HR-ESI-TOF MS: calculated 613.1586 Da for [C₃₄H₂₆N₂NaO₈]⁺, found 613.1562 Da.

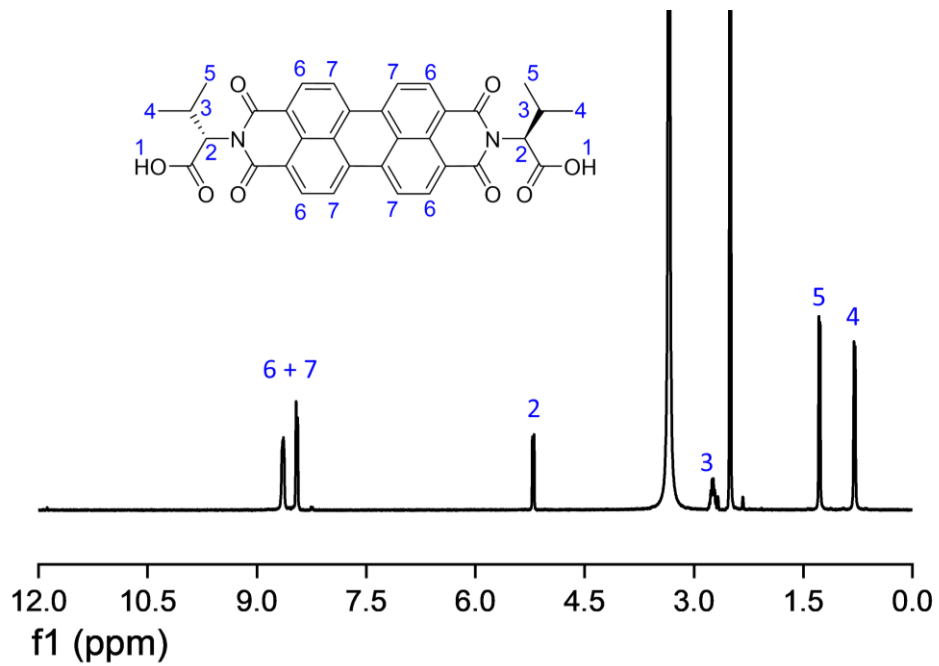


Figure 3.32. $^1\text{H-NMR}$ spectrum of **PBI-V** in $\text{DMSO-}d_6$ at 25°C .

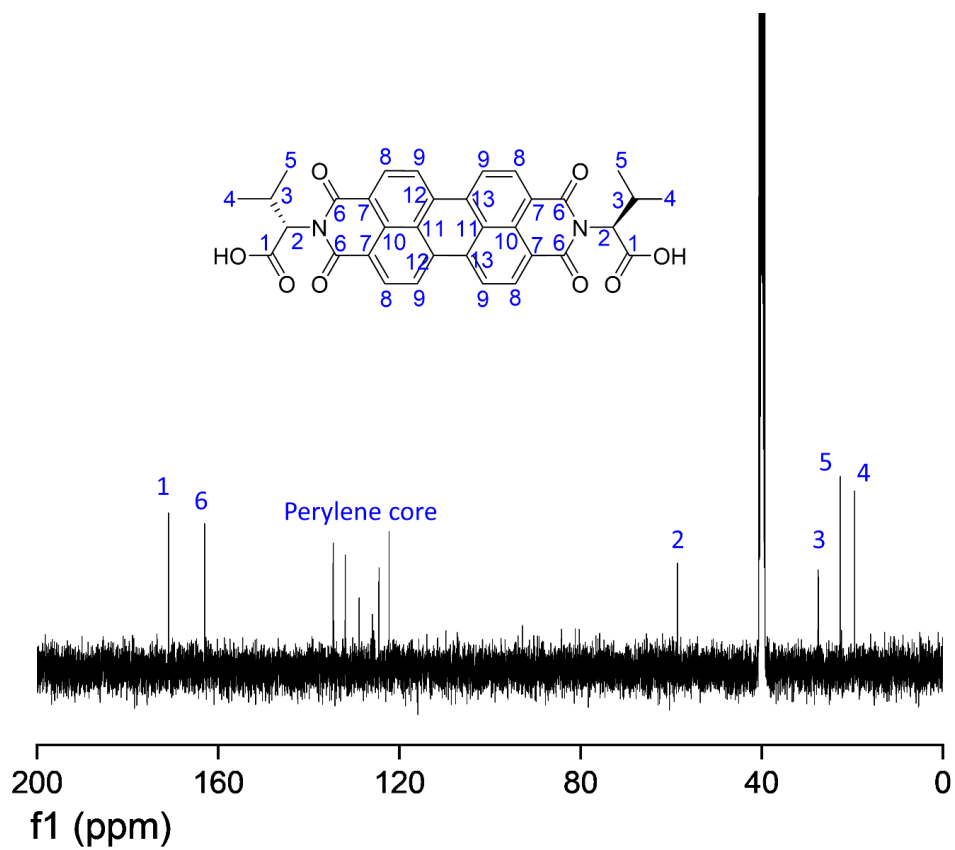


Figure 3.33. $^{13}\text{C-NMR}$ spectrum of **PBI-V** in $\text{DMSO-}d_6$ at 25°C .

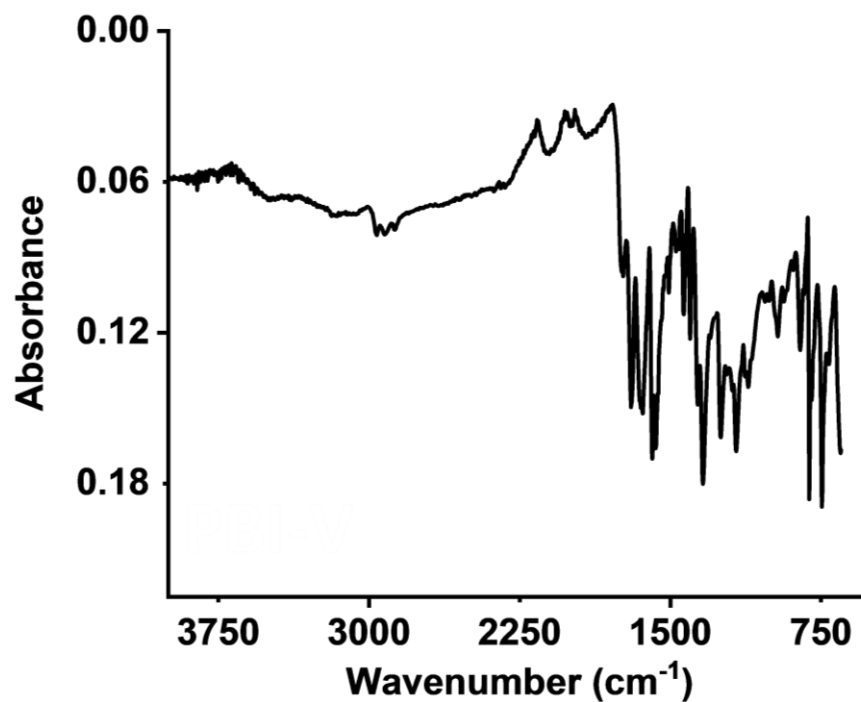
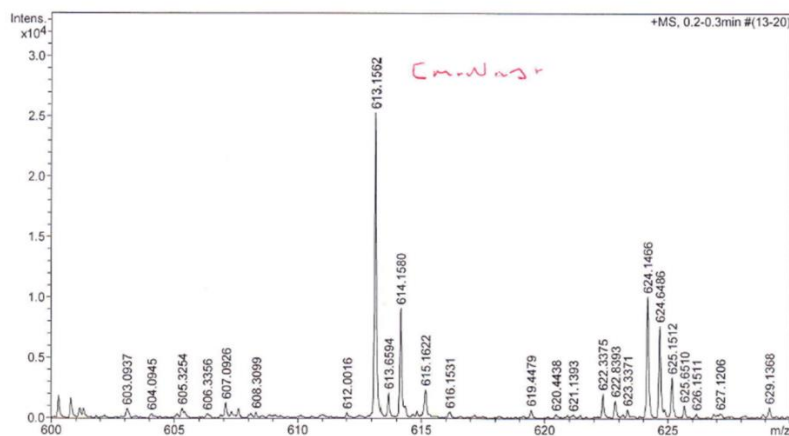


Figure 3.34. Powder FTIR spectrum of **PBI-V**.

Analysis Info			Acquisition Date
Analysis Name	D:\Data\Mass Spectrometry Service\74452-000001.d		11/13/2019 8:31:13 AM
Method	LM MS 50 to 1100 KIM 071215.m		Operator user
Sample Name	Dietrich-JE02-001		Instrument / Ser# micrOTOF-Q 74
Comment			
Acquisition Parameter			
Source Type	ESI	Ion Polarity	Positive
Scan Begin	50 m/z		
Scan End	1100 m/z		



Formula	z	m/z	Meas. m/z	err [ppm]	err [mDa]
C 34 H 26 N 2 Na O 8	1+	613.1581	613.1562	3.2	2.0

Figure 3.35. Mass spectrum of **PBI-V** in DMSO.

3.4.2 Methods

3.4.2.1 Characterisation of PBIs

All nuclear magnetic resonance (NMR) spectra were measured using a Bruker DPX-400 spectrometer operating at 400 MHz for ^1H -NMR and 100 MHz for ^{13}C -NMR in d_6 -DMSO. Infrared (IR) spectra were collected using a Thermo Nicolet Is5 (Diamond ATR attachment). The spectra were recorded at 64 scans and a resolution of 4 cm^{-1} . The background was of the empty ATR crystal and spectra were recorded of the PBIs as solid powders. Mass spectrometry was performed using a Bruker MicroTOF mass spectrometer using electrospray ionization (MS-ESI).

3.4.2.2 Preparation of PBI solutions

Solutions were prepared at a concentration of 10 mg/mL of PBI. For the preparation of 5 mL of solution, 50 mg of PBI was weighed into a vial. One molar equivalent of sodium hydroxide (0.1 M, aqueous) was added to the PBI and the volume was made up to 5 mL with deionised water. The solution was stirred for at least 16 hours to allow all the PBI to dissolve. A large stock solution of each PBI was prepared to ensure that the solutions were the same for each experiment. The pH of each vial was adjusted as necessary using 2 M HCl or 2 M NaOH to obtain the desired pH. Preparation of all samples was carried out at room temperature (around 25°C in the daytime).

3.4.2.3 Preparation of hydrogels

Hydrogels were formed using a pH switch from a solution at 10 mg/mL gelator concentration, as described above. 2 mL of the gelator solution was transferred to a 7 mL Sterilin vial which contained 8 mg/mL of glucono- δ -lactone (GdL) and shaken gently. This was left to stand for at least 16 hours to allow for gelation to occur. The samples that were stable to vial inversion after 16 hours were rheologically tested to confirm gelation.

3.4.2.4 Small-angle X-ray scattering (SAXS) data

For solution samples, aliquots of PBI stock solution were transferred into 7 mL Sterilin vials and the pH was adjusted to the desired value using either 2 M HCl or 2 M

NaOH. A Precision Extrusion Inc, single lumen tube was filled three-quarters with the solution and sealed with a plastic lid and parafilm to prevent leaks or change in the pH.

For hydrogel samples, aliquots of stock solution were added to 7 mL Sterilin vials that contained 8 mg/mL of GdL and shaken gently until all the GdL dissolved. A capillary tube was filled three-quarters with the gelling solution, sealed with a plastic lid and parafilm, and left to sit for 16 hours to allow for gelation to occur.

Scattering data were collected at I22, under experiment number SM27906-1, using a beam energy of 12.4 keV and a sample-to-detector distance of 5.647m calibrated using a standard sample of silver behenate. Data were collected as a single frame of 1 s duration and reduced to a 1D dataset using the DAWN software package and standard pipelines.^{48, 49} The scattering length density of each material was calculated using the National Institute of Standards and Technology neutron activation and scattering calculator.⁵⁰

Table 3.8. Calculated scattering length density for different PBIs used.

PBI	X-ray scattering length density (\AA^{-2})
-L	$13.826 \cdot 10^{-6}$
-I	$13.826 \cdot 10^{-6}$
-V	$13.769 \cdot 10^{-6}$

The data were fitted to models in the SasView software package (version 5.0.3).⁵¹ Various models were used to fit the data. Fitting errors are provided as \pm ; the errors were obtained from the fitting software and do not consider other sources of error. These compounds are expected to form 1D fibres at low pH and can form worm-like or spherical micelle structures at high pH.^{20, 30} Fitting the data to different cylinder models was attempted to find the most suitable, starting from models with the fewest parameters, and progressing to more complex ones. The polydispersity allows for the size distribution of the cylinder radii to be accounted for in the fit. A power law fit was used to capture an increase in scattering at low Q. At pH 7 this is due to aggregates

beginning to form and as the pH is lowered the increased scattering at low Q may be due to scattering off the fibre network.^{23, 52}

A model was deemed suitable based on the reduced χ^2 , with a χ^2 value below 10 being deemed suitable. Generally, the model with the lowest χ^2 was chosen unless there were regions of the fit that clearly were not representative of the data set. In some cases, single models were not suitable to achieve a good fit, indicating a co-existence of structures or a structure that could not be represented by the models in the software. In these instances, models were combined using the “Easy Sum/Multi(p1, p2) editor” in the SasView software. The combined model could then be saved and used in the same manner as any other. In the fit tables a “+” sign is used to denote where two models were combined.

3.2.4.5 Rheological measurements

Dynamic rheological and viscosity measurements were performed using an Anton Paar Physica MCR101 rheometer. Strain and frequency data were collected using a vane and cup geometry (ST10-4V-8.8/97.5) so that samples could be prepared in 7 mL Sterilin vials to remove any loading issues. Viscosity data were collected using a 50 mm cone (cone angle 0.994°) geometry and temperature-controlled bottom plate. Monitoring of G' and G'' over time was collected using 50 mm diameter sandblasted parallel plates. All measurements were collected in triplicate at 25°C.

Viscosity measurements: a 1 mL aliquot of PBI solution at the desired pH was pipetted onto the bottom plate. The top plate was lowered on top of the solution to a gap height of 0.1 mm which is determined for the cone angle on the plate. Any excess sample was trimmed using a metal spatula ensuring no gaps or bubbles along the edge of the plate. A CP50 plate geometry was used to measure the viscosity. Measurements were recorded at a shear rate from 1-1000 s⁻¹ and performed in triplicate. Errors were calculated from the standard deviation.

Strain sweeps: strain sweeps were recorded from 0.1-1000% strain at a set frequency of 10 rad/s with a gap height of 2 mm. Samples were prepared as described previously in 7 mL Sterilin vials. Measurements were performed in triplicate and errors were calculated from the standard deviation.

Frequency sweep: frequency scans were recorded from 1-100 rad/s under a constant strain of 0.5% with a gap height of 2 mm. The strain was chosen because it is in the linear viscoelastic region for the hydrogels. Samples were prepared as described previously in 7 mL Sterilin vial. Measurements were performed in triplicate and errors were calculated from the standard deviation.

Monitoring G' and G'' over time: measurements were done at an angular frequency of 10 rad/s and strain of 0.5%. 2 mL of PBI solution was added to a Sterilin vial containing 8 mg/mL of GdL and shaken gently. The mixture was then poured onto the middle of the bottom plate and the top plate was lowered to a gap height of 0.8 mm. Any excess sample was trimmed using a metal spatula. A sanded PP50 plate geometry was used to monitor G' and G'' over time. The circumference of the top plate was flooded with mineral oil to prevent the gel from drying whilst gelling. Measurements were run overnight.

3.4.2.6 UV-vis absorption spectroscopy

UV-vis absorption spectra were measured using an Agilent Cary 60 spectrometer. For solution spectra, stock solutions of the PBIs at the various pHs were placed in a 0.01 mm demountable cuvette and absorption was measured between 200 nm to 1100 nm on the 600 nm/min scan rate. Gel samples were prepared by adding 2 mL of 10 mg/mL PBI stock solutions to 8 mg/mL of GdL in 7 mL Sterilin vials and gently swirling until complete dissolution of the GdL. 0.5 mL of this solution was pipetted into a 0.1 mm demountable cuvette which was then parafilm and left to stand for at least 16 hours to allow for gelation to occur. Absorption was measured between 200 nm and 1100 nm on the 600 nm/min scan rate. To form the radical anion, the samples were irradiated using a 365 nm LED (LedEngin Inc, LZ1-10U600) powered by a constant-current power source for 5 minutes. The power hitting the sample was measured to be 21.6 mW using a ThorLabs optical power meter PM100D with a ThorLabs S120VC 200-1100 nm 50 mW diode over an area of 225 cm². The number of photons that hit the sample during 5 minutes at that power was determined to be 5.29×10^{16} photons/cm².

3.4.2.7 pH measurements

pH measurements were recorded using a custom-built pH/temperature logger and a HANNA pH probe (FC200) with a given error of ± 0.1 . For monitoring the pH of gelation over time, 2 mL of PBI solution was added to GdL in a 7 mL Sterilin vial which was immersed in a water bath at a temperature of 25°C. The probe tip was then inserted into the gel with Parafilm used to seal the top of the vial/tip. The pH measurements were recorded every 30 seconds for between 14 to 18 hours until gelation was complete and pH had stabilised.

3.4.2.8 Apparent pK_a titrations

pH measurements were recorded using a HANNA edge pH logger and a HANNA pH probe (FC200) with a given error of ± 0.1 . For apparent pK_a measurements, 2 mL of PBI solution was added to a 7 mL Sterilin vial which was immersed in a water bath at a temperature of 25°C and the probe was immersed in the solution. 3 μ L – 10 μ L aliquots of HCl (0.1M) were added to the solution and the pH recorded after the reading had stabilised. The solution was gently stirred between additions of acid to avoid any gel forming and to ensure the pH was homogeneous throughout the solution. The plateaus in the data represent the apparent pK_a values.

3.4.2.9 Cyclic voltammetry (CV)

CVs for the solutions were collected using a three-electrode system and a PalmSens4 potentiostat with a glassy carbon working electrode, a Pt wire counter electrode and an Ag/AgCl reference electrode. The background electrolyte was 0.1 M NaCl in water. The potential was scanned from 1.0 V to -1.0 V at a scan rate of 0.05 V/s and measurements were carried out in triplicate. The clearest of the three scans was used for analysis.

3.4.2.10 $^1\text{H-NMR}$ spectroscopy kinetics

$^1\text{H-NMR}$ spectra were measured using a Bruker DPX-400 spectrometer operating at 400 MHz with the temperature internally controlled. Samples were run in $\text{D}_2\text{O}/\text{NaOD}$ with a capillary tube containing 0.1% polydimethylsiloxane (PDMS) in tetrachloroethylene solution as a standard. A spectrum of 1 mL PBI stock solution including the standard capillary and 2 μ L of ethanol was recorded prior to the addition

of GdL: this is the time zero measurement ($t = 0$). As some of the PBI is expected to already be assembled the ethanol was used to determine the percent unassembled at $t = 0$. This was done by determining the ratio of the known amount of ethanol and PBI in solution. From this the theoretical integral ratio of the ethanol methylene group and a methyl group of the PBI was calculated. This calculated theoretical integral ratio for the 100% unassembled system was compared to the observed integral ratio to determine the percent already assembled. This ranged from 20% to 60% depending on the PBI. Next, 8 mg/mL of GdL was added to another 1 mL aliquot of PBI stock solution, transferred into an NMR tube containing the standard capillary, and inserted into the spectrometer. Due to experimental limitations, there was a 5-10 minutes' delay between the insertion of the sample into the instrument and the first measurement. Spectra were recorded every 5 minutes until the proton peaks were no longer detectable. This took 4-5 hours depending on the sample. Example spectra recorded over time are shown in Appendix 2 to 4. The PDMS reference proton environment was integrated and set to the same value in all spectra. The protons for the PBI were then integrated and compared to the integral for the same PBI's peaks at $t = 0$. From this the percentage assembled was calculated and a trend was plotted against time.

3.5 References

1. S. Chen, P. Slattum, C. Wang and L. Zang, *Chemical Reviews*, 2015, **115**, 11967-11998.
2. J. Cameron, D. J. Adams, P. J. Skabara and E. R. Draper, *Journal of Materials Chemistry C*, 2022, **10**, 3944-3950.
3. R. Khurana, J. Mohanty, N. Padma, N. Barooah and A. C. Bhasikuttan, *Chemistry – A European Journal*, 2019, **25**, 13939-13944.
4. J. Zhang, S. You, S. Yan, K. Müllen, W. Yang and M. Yin, *Chemical Communications*, 2014, **50**, 7511-7513.
5. A. Datar, K. Balakrishnan and L. Zang, *Chemical Communications*, 2013, **49**, 6894-6896.
6. S. Bai, S. Debnath, N. Javid, P. W. J. M. Frederix, S. Fleming, C. Pappas and R. V. Ulijn, *Langmuir*, 2014, **30**, 7576-7584.
7. D. Görl and F. Würthner, *Angewandte Chemie International Edition*, 2016, **55**, 12094-12098.
8. V. Grande, B. Soberats, S. Herbst, V. Stepanenko and F. Würthner, *Chemical Science*, 2018, **9**, 6904-6911.
9. Y. Chen, Y. Feng, J. Gao and M. Bouvet, *Journal of Colloid and Interface Science*, 2012, **368**, 387-394.
10. L. Fan, W. Zhu, J. Li and H. Tian, *Synthetic Metals*, 2004, **145**, 203-210.
11. C. D. Schmidt, C. Böttcher and A. Hirsch, *European Journal of Organic Chemistry*, 2007, **2007**, 5497-5505.
12. Y. Sun, C. He, K. Sun, Y. Li, H. Dong, Z. Wang and Z. Li, *Langmuir*, 2011, **27**, 11364-11371.

13. A. L. Briseno, S. C. B. Mannsfeld, C. Reese, J. M. Hancock, Y. Xiong, S. A. Jenekhe, Z. Bao and Y. Xia, *Nano Letters*, 2007, **7**, 2847-2853.
14. P. K. Sukul, P. K. Singh, S. K. Maji and S. Malik, *Journal of Materials Chemistry B*, 2013, **1**, 153-156.
15. Y. Huang, J. Hu, W. Kuang, Z. Wei and C. F. J. Faul, *Chemical Communications*, 2011, **47**, 5554-5556.
16. X. Li, Y. Li, G. Feng, T. Wang, J. Ren and X. Yu, *ChemistrySelect*, 2020, **5**, 4389-4392.
17. E. R. Draper, J. R. Lee, M. Wallace, F. Jäckel, A. J. Cowan and D. J. Adams, *Chemical Science*, 2016, **7**, 6499-6505.
18. S. Roy, D. Kumar Maiti, S. Panigrahi, D. Basak and A. Banerjee, *RSC Advances*, 2012, **2**, 11053-11060.
19. S. Roy, D. K. Maiti, S. Panigrahi, D. Basak and A. Banerjee, *Physical Chemistry Chemical Physics*, 2014, **16**, 6041-6049.
20. E. R. Draper, J. J. Walsh, T. O. McDonald, M. A. Zwijnenburg, P. J. Cameron, A. J. Cowan and D. J. Adams, *Journal of Materials Chemistry C*, 2014, **2**, 5570-5575.
21. E. R. Draper, L. J. Archibald, M. C. Nolan, R. Schweins, M. A. Zwijnenburg, S. Sproules and D. J. Adams, *Chemistry*, 2018, **24**, 4006-4010.
22. E. R. Draper, R. Schweins, R. Akhtar, P. Groves, V. Chechik, M. A. Zwijnenburg and D. J. Adams, *Chemistry of Materials*, 2016, **28**, 6336-6341.
23. D. McDowall, B. J. Greeves, R. Clowes, K. McAulay, A. M. Fuentes-Caparrós, L. Thomson, N. Khunti, N. Cowieson, M. C. Nolan, M. Wallace, A. I. Cooper, E. R. Draper, A. J. Cowan and D. J. Adams, *Advanced Energy Materials*, 2020, **10**.
24. N. B. Bowden, K. A. Willets, W. E. Moerner and R. M. Waymouth, *Macromolecules*, 2002, **35**, 8122-8125.
25. Y. Xu, S. Leng, C. Xue, R. Sun, J. Pan, J. Ford and S. Jin, *Angew Chem International Edition*, 2007, **46**, 3896-3899.
26. M. J. Farooqi, M. A. Penick, J. Burch, G. R. Negrete and L. Brancalion, *Spectrochimica Acta Part A: Molecular and Biomolecular Spectroscopy*, 2016, **153**, 124-131.
27. S. A. Boer, C. S. Hawes and D. R. Turner, *Chemical Communications*, 2014, **50**, 1125-1127.
28. R. F. Araújo, C. J. R. Silva, M. C. Paiva, M. M. Franco and M. F. Proença, *RSC Advances*, 2013, **3**.
29. J. Raeburn, A. Zamith Cardoso and D. J. Adams, *Chemical Society Reviews*, 2013, **42**, 5143-5156.
30. Z. Chen, V. Stepanenko, V. Dehm, P. Prins, L. D. A. Siebbeles, J. Seibt, P. Marquetand, V. Engel and F. Würthner, *Chemistry – A European Journal*, 2007, **13**, 436-449.
31. E. R. Draper, L. Wilbraham, D. J. Adams, M. Wallace, R. Schweins and M. A. Zwijnenburg, *Nanoscale*, 2019, **11**, 15917-15928.
32. M. C. Nolan, J. J. Walsh, L. L. E. Mears, E. R. Draper, M. Wallace, M. Barrow, B. Dietrich, S. M. King, A. J. Cowan and D. J. Adams, *Journal of Materials Chemistry A*, 2017, **5**, 7555-7563.
33. E. R. Draper, B. J. Greeves, M. Barrow, R. Schweins, M. A. Zwijnenburg and D. J. Adams, *Chem*, 2017, **2**, 716-731.
34. A. M. Castilla, E. R. Draper, M. C. Nolan, C. Brasnett, A. Seddon, L. L. E. Mears, N. Cowieson and D. J. Adams, *Scientific Reports*, 2017, **7**, 8380.
35. C. Tang, A. M. Smith, R. F. Collins, R. V. Ulijn and A. Saiani, *Langmuir*, 2009, **25**, 9447-9453.
36. C. Tang, R. V. Ulijn and A. Saiani, *The European Physical Journal E*, 2013, **36**, 111.
37. L. Chen, S. Revel, K. Morris, L. C. Serpell and D. J. Adams, *Langmuir*, 2010, **26**, 13466-13471.
38. J. J. Walsh, J. R. Lee, E. R. Draper, S. M. King, F. Jäckel, M. A. Zwijnenburg, D. J. Adams and A. J. Cowan, *The Journal of Physical Chemistry C*, 2016, **120**, 18479-18486.
39. R. A. Hule, R. P. Nagarkar, A. Altunbas, H. R. Ramay, M. C. Branco, J. P. Schneider and D. J. Pochan, *Faraday Discussions*, 2008, **139**, 251-264.

40. F. Würthner, C. R. Saha-Moller, B. Fimmel, S. Ogi, P. Leowanawat and D. Schmidt, *Chemical Reviews*, 2016, **116**, 962-1052.
41. R. O. Marcon and S. Brochsztain, *The Journal of Physical Chemistry A*, 2009, **113**, 1747-1752.
42. S. Seifert, D. Schmidt and F. Würthner, *Chemical Science*, 2015, **6**, 1663-1667.
43. D. J. Adams, M. F. Butler, W. J. Frith, M. Kirkland, L. Mullen and P. Sanderson, *Soft Matter*, 2009, **5**, 1856-1862.
44. E. R. Cross, S. Sproules, R. Schweins, E. R. Draper and D. J. Adams, *Journal of the American Chemical Society*, 2018, **140**, 8667-8670.
45. B. Escuder, M. Llusar and J. F. Miravet, *The Journal of Organic Chemistry*, 2006, **71**, 7747-7752.
46. A. M. Fuentes-Caparrós, Z. Canales-Galarza, M. Barrow, B. Dietrich, J. Läger, M. Nemeth, E. R. Draper and D. J. Adams, *Biomacromolecules*, 2021, **22**, 1625-1638.
47. L. Xue, H. Wu, Y. Shi, H. Liu, Y. Chen and X. Li, *Soft Matter*, 2011, **7**, 6213-6221.
48. J. Filik, A. W. Ashton, P. C. Y. Chang, P. A. Chater, S. J. Day, M. Drakopoulos, M. W. Gerring, M. L. Hart, O. V. Magdysyuk, S. Michalik, A. Smith, C. C. Tang, N. J. Terrill, M. T. Wharmby and H. Wilhelm, *Journal of Applied Crystallography*, 2017, **50**, 959-966.
49. B. R. Pauw, A. J. Smith, T. Snow, N. J. Terrill and A. F. Thunemann, *Journal of Applied Crystallography*, 2017, **50**, 1800-1811.
50. P. Kienzle, *NIST Neutron Activation and Scattering Calculator*, , DOI: <https://www.ncnr.nist.gov/resources/activation/>.
51. <http://www.sasview.org/>.
52. D. McDowall, D. J. Adams and A. M. Seddon, *Soft Matter*, 2022, **18**, 1577-1590.

Chapter 4: Photogenerating behaviour of a pyrrolidine bay- substituted perylene bisimide at different pH values

4.1. Introduction

The use of light as a stimulus is an attractive method for hydrogel based smart materials in commercial applications such as drug delivery, catalysts, or photochromic devices. This attractiveness is due to the speed of the response, the scope for changing the response through wavelength choice, and the non-invasive nature of this method. There are numerous reports of the chemical structure of low molecular weight gelators (LMWGs) being modified through irradiation with light post gelation. Typically for LMWGs, the change in the chemical structure's flexibility, bulkiness, or charge upon irradiation leads to the change in the fibres' morphology which leads to sol-gel transitions.¹⁻³ For perylene bisimide (PBI) LMWGs, Draper *et al.* reported a PBI hydrogel where the formation of the radical anion through irradiation with UV light resulted in a change in the packing in the self-assembled aggregates.⁴ This led to a change in fibrous network and an increase in the stiffness and strength of the gel, which is not often observed. Changing of fibre morphology through the formation of PBI radicals in solution has not been investigated extensively either. Liu *et al.* did report the changing the PBI supramolecular morphology in a D₂O solution through the formation of radical anion.⁵ However, in this investigation the radical anion was formed through the addition of a chemical reducing agent (Na₂S₂O₄), thus highlighting the need to investigate the formation of PBI radicals through irradiation for the modifying of self-assembled structures in solution further.

PBIs are typically used as electron acceptor materials, therefore their ability to form radical anion and dianion has been heavily explored.⁶⁻⁹ However, there is a gap in the literature about the formation of the PBI radical cation and dications, with only a few reports where these radicals were investigated.¹⁰⁻¹³ This is because the oxidation of PBIs can be challenging due to the stabilisation of the highest occupied molecular orbital (HOMO) by the electron withdrawing imide groups. The oxidation potential of a PBI can be lowered by modifying the chemical structure at the core.^{14, 15} PBIs that can be more easily oxidised have been shown to be promising donor materials for applications in light harvesting,^{16, 17} photovoltaic,^{18, 19} and photochromic devices.²⁰

Reports where the radical cations or dications could be generated often involve a PBI that has an aliphatic amine group substituted at the bay position. This is because the

amine group adds electron density to the core which shifts the redox potentials of the oxidation. This is due to the HOMO and the lowest unoccupied molecular orbital (LUMO) now both being located on the PBI core.^{19, 21} This also results in the PBIs absorbing at shorter wavelengths and presenting as blue or green materials. Ahrens *et al.* reported the synthesis of PBIs with *n*-octylamino groups substituted onto the core at the 1,6- and 1,7-positions.¹¹ They investigated the different optical and electronic properties of these regioisomers and their ability to form radical cations. Spectroelectrochemical oxidation of the PBIs showed they were able to form radical cations resulting in a change in the UV-vis absorption spectrum. They also measured the electron paramagnetic resonance (EPR) spectroscopy after the two PBIs were treated with the oxidiser NOSbF_6 to confirm the formation of radical cations. The radical cationic amines were stable, with a 50-80% decrease in the cation bands' signal intensity after sitting in a sealed tube for several days.

The various synthetic routes for core substitution at the bay position for PBIs were discussed in more detail in Chapter 1. This section expands on the nucleophilic substitution with aliphatic cyclic amines, which are better nucleophiles than alkyl amines and therefore the reactions typically have higher yields. The addition of cyclic amines onto the core commonly involves the addition of a halogen such as bromine onto the bay position, then the nucleophilic substitution with the cyclic amine, as shown in Figure 4.1.^{14, 19, 21-23}

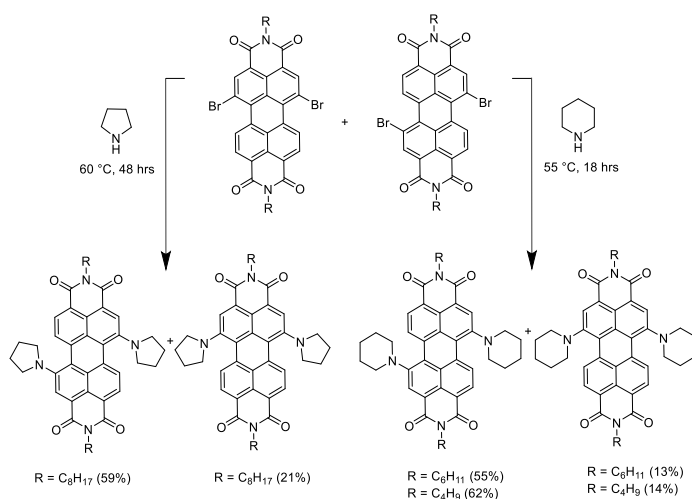


Figure 4.1. Synthesis of 1,7- and 1,6-diamino-PBIs from the regioisomeric mixture of dibromo-PBIs.^{14, 21-23}

There is variation in the yields, with some of the highest values reported being 55-62% for those substituted with pyrrolidine. However, in all these synthetic routes there is a challenge to purify the amine-substituted product. The substitution with aliphatic amines leads to regioisomeric mixtures of 1,7- and 1,6-substituted diamino-PBIs due to the starting material typically being a regioisomeric mixture of di-brominated PBI. Separation of these mixtures can be difficult due to the isomers having similar hydrophilicities and polarities which leads to low yields due to repetitive crystallizations and column chromatography.^{22, 23}

Separation of the regioisomers is important because the position of these aliphatic amine groups can have a major impact on the electronic and optical properties of the PBI. Dubey *et al.* compared the optical and electronic properties of 1,6- and 1,7-substituted PBIs (**1,6-PBI** and **1,7-PBI**) in organic solvents, Figure 4.2 (a), to see how the position of the pyrrolidine impacted the materials.²³ They reported that the **1,7-PBI** was a green-coloured material while **1,6-PBI** was a deep blue-coloured material. This difference in colour was reflected in the UV-vis absorption, Figure 4.2 (b): **1,7-PBI** had absorption peaks corresponding to S_0-S_1 transitions between 650 nm and 700 nm. These absorptions for **1,6-PBI** were significantly weaker and blue-shifted by 15 nm. The **1,6-PBI** absorbed in more of the visible region making it of interest for applications where larger absorption cross-section in the visible region is needed such as photovoltaics.

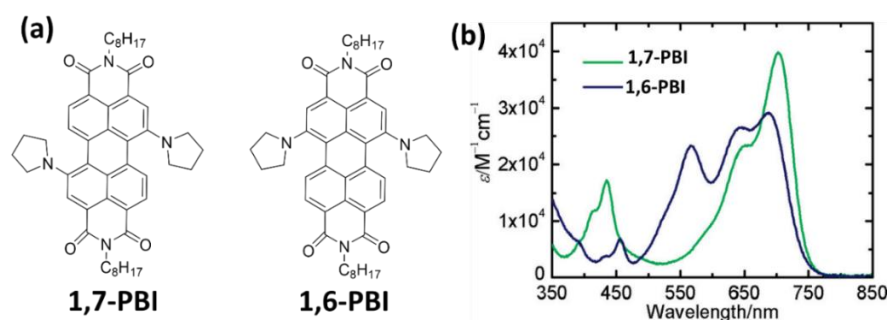


Figure 4.2. (a) Chemical structures of **1,7-PBI** and **1,6-PBI**. (b) Steady-state absorption of **1,7-PBI** and **1,6-PBI** in chloroform. Adapted from original paper.²³

Differential pulse voltammetry (DPV) in benzonitrile showed that both materials had two reversible reduction potentials. The **1,7-PBI** also had two reversible oxidation potentials while the **1,6-PBI** had one reversible and one irreversible oxidation

process. The oxidation potentials for the **1,6-PBI** also occurred at slightly higher potentials, indicating the easier removal of electrons for **1,7-PBI**. This increase in oxidation potentials for a 1,6-amine-substituted PBI was previously observed.¹¹ The workers explained the trend based on the HOMOs and LUMOs calculated by density functional theory (DFT), which showed that 1,6-PBI had a larger HOMO-LUMO gap. The choice between 1,7- and 1,6-position does have a major impact on the optical and electronic properties, therefore the ideal synthetic route used for adding an aliphatic amine to the core of a PBI should be selective.

In 2014, Raunch *et al.* reported a synthetic route that was able to directly substitute aliphatic amines onto core-unsubstituted PBIs using mild reaction conditions.²⁴ The synthesis was selective for mono-substituted or 1,6-di-substituted products with moderate to good yields for several different secondary cyclic amine nucleophiles. The new synthetic route for the amination of core-unsubstituted PBIs also used an inexpensive copper salt as a catalyst that was not air- or moisture-sensitive. For PBIs with a long alkane chain at the imide position the use of pyrrolidine resulted in selectivity for the 1,6-di-substituted product, shown in Figure 4.3.

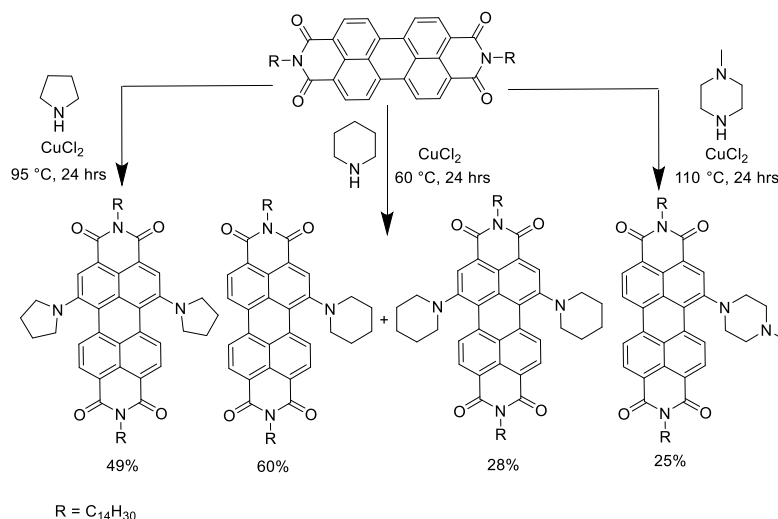


Figure 4.3. Direct amination of core-unsubstituted PBIs with cyclic amines using mild conditions and a copper(II) catalyst.²⁴

The use of piperidine with the same core-unsubstituted PBI resulted in a mixture of mono-substituted and 1,6-di-substituted products. The use of 1-methylpiperazine with the same core-unsubstituted PBI led to mono-substituted product selectivity but in low

yields. The workers compared reaction selectivity for core-unsubstituted PBIs with increasingly bulky groups at the imide position. Bulkier substituents at the imide position seem to favour the formation of the 1,6-di-substituted products with pyrrolidine and piperidine.

Previous reports have shown a focus on absorption and electronic properties of 1,6-di-substituted PBIs, however, aggregation or self-assembled structures across various length scales of these materials are often overlooked. This chapter focuses on the absorption and electronic properties as well as the aggregation and self-assembled structures for three amino acid-functionalised PBIs that have been directly core substituted at the 1,6-bay position with pyrrolidine groups. The amino acids chosen are *L*-alanine (**PBI-A-1**), *L*-valine (**PBI-V-1**), and *L*-leucine (**PBI-L-1**), Figure 4.4. These PBIs were chosen for substitution with pyrrolidine as they have been studied previously by the group as hydrogels and photoconductive devices.^{4, 8, 9, 25} These reports have shown that as the amino acid side chain decreases in size the amount of radical capable of forming increases due to an improvement in π - π stacking. We were interested in seeing if this difference in radical formation was still present with radical cation or dication formation for the core-substituted PBIs or if this is no longer true because the core substituted core has disrupted the π - π stacking too much.

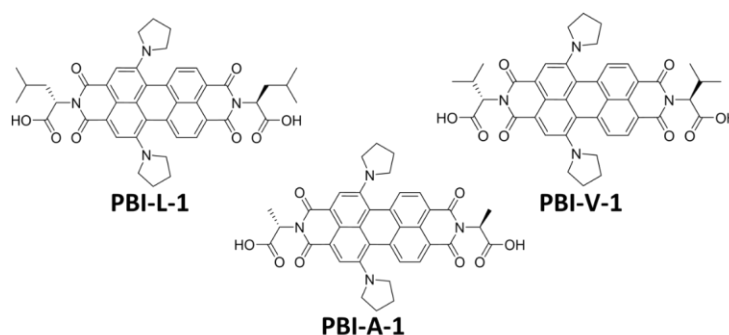


Figure 4.4. Chemical structures of **PBI-L-1**, **PBI-A-1**, and **PBI-V-1** used in this study.

The synthesis was carried out under mild conditions at room temperature using copper(II) chloride catalysis. Unlike previously reported 1,6-pyrrolidine-substituted PBIs, these PBIs could be solubilised in water when the pH was raised above their apparent pK_a values. UV-vis absorption spectroscopy and square wave voltammetry (SWV) measurements were carried out to study the optical and electronic properties

of the newly synthesised materials in solution. This was also done to see how these properties can be impacted by the differences in self-assembled structure due to amino acid choice.

To investigate the ability of these materials to form radical, the PBIs were irradiated using different wavelengths of light to see if they could form a radical cation or dication. EPR spectroscopy and spectroelectrochemistry were carried out to confirm radical cation formation. The dynamic viscosity of the solutions was measured after being irradiated for different time periods to see if the self-assembled nanostructures were altered upon formation of radical cation and dication. How the irradiation impacts the self-assembly of secondary structures in solution was investigated using small-angle X-ray scattering (SAXS).

As we have reported, changing pH is a simple way the environment which results in a change the self-assembled structures of amino acid-functionalised PBIs in water.^{8, 26} Therefore we wanted to investigate this for their core-substituted versions too. To see if the fibre length, morphology, and abundance of the PBIs in solution changed when the pH is lowered, the dynamic viscosity was initially measured as it is a useful way to scan for these differences. Apparent pK_a titrations were carried out to see how the increased hydrophobicity at the core impacts the apparent pK_a values. How pH impacts the nanostructures of the PBIs was investigated using SAXS. Next, the impact of pH on the ability of the PBIs to form the radical cation and dication after irradiation was investigated. Finally, a pH trigger was added to solutions of the core substituted PBIs over several concentrations to see if they could form hydrogels. These materials have not been reported before and therefore their ability to gel in is unknown. This is interesting because they could then be used in xerogel devices which could be used to measure conductivity. Again, a pH trigger was used because it can induce more uniform self-assembly as the pH is lowered. Bulk rheology and SAXS were investigated to see how the different amino acids impacted the bulk mechanical properties and fibre structures to see if there was an observable difference in these properties as the side chain size was increased. The ability of these hydrogels to form radical when irradiated with UV light was then probed to see if they responded the same as when in solution.

4.2. Results and discussion

4.2.1 Synthesis, Optical and Electronic properties of novel core substituted PBIs

The direct amination of the core of the PBIs with pyrrolidine was accomplished by stirring the corresponding PBI with pyrrolidine as the nucleophile and the solvent, the CuCl_2 salt as the catalyst, and O_2 in the air as an oxidant. In the proposed mechanism by Ruach *et al.* CuCl_2 coordinates to the pyrrolidine solvent and oxidises it to form an ammonium radical.^{24, 27} The radical is then deprotonated by excess pyrrolidine and bonds to the PBI core at the bay position.^{28, 29} There is a proton-coupled electron transfer (PCET) and the mono-substituted product is formed.³⁰ The CuCl_2 is regenerated by air-oxidation.

The reaction mixture containing PBI, pyrrolidine, and CuCl_2 was initially a red colour. After around 2 hours it had turned a purple colour. This is likely due to there being a mixture of product and starting material. The reaction was considered complete when the reaction mixture was completely blue in colour. The reactions were carried out on 2 g scale and produced yields of 55% for **PBI-A-1**, 61% for **PBI-V-1**, and 65% for **PBI-L-1**. This reaction was considered more favourable over other methods because pyrrolidine was a reactant and a solvent. Pyrrolidine is a strong base and helped solubilise the initial amino acid-functionalised PBIs better than organic solvents such as chloroform or toluene. Once the reaction was complete, acid was slowly added to convert excess pyrrolidine to a salt which was washed out with an excess of water. The product was recrystallised from methanol to remove any unreacted PBIs.

Full experimental procedures and characterisation of the pyrrolidine-appended PBIs are provided in the experimental methods part of this chapter. It is reported that the di-substituted product was substituted at the 1,6 positions instead of the 1,7 due to differences in the reactivity when the core is initially substituted.²⁴ The position of the substitution on the core can be determined by looking at the proton pattern in the aromatic regions of the $^1\text{H-NMR}$ spectra. The aromatic region of the $^1\text{H-NMR}$ spectra for the three PBIs in chloroform-*d* is shown in Figure 4.5. These spectra support the idea that the 1,6-di-substituted product was formed over the 1,7-di-substituted product. As they have the doublet-single-doublet pattern previously reported for the

1,6-product instead of the single-doublet-doublet pattern reported for the 1,7-product.²³

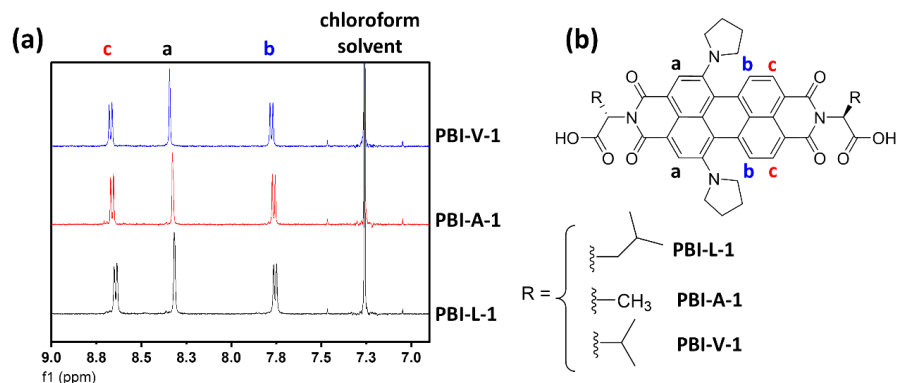


Figure 4.5. (a) $^1\text{H-NMR}$ spectra of **PBI-L-1** (black), **PBI-A-1** (red), and (c) **PBI-V-1** (blue) in chloroform- d focused on the aromatic region. (b) Chemical structure of substituted PBIs with relevant protons labelled a to c.

All three of the core-substituted PBIs were a blue colour in solution at pH 7, shown below in Figure 4.6, which is characteristic of the 1,6-system and due to the addition of electron density to the core impacting the HOMO-LUMO band gap.^{11, 15, 23} The PBIs were solubilised in water at a concentration of 10 mg/mL by adding 1 equivalent of 0.1 M NaOH as it is believed this will bring the pH above an apparent pK_a value.³¹ Prior to this work there are only two other reports of a pyrrolidine-substituted PBI material which could be solubilised in water, but these reports dealt with 1,7-systems.^{32, 33}

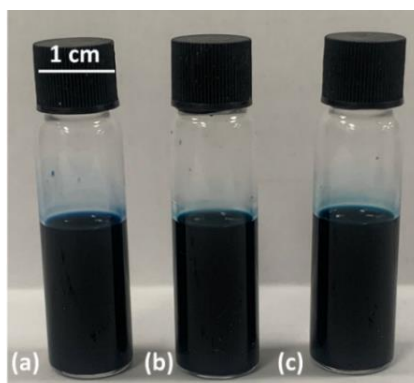


Figure 4.6. Photograph of (a) **PBI-L-1**, (b) **PBI-A-1**, and (c) **PBI-V-1** in water solubilised with 1 equivalent of 0.1 M NaOH at a concentration of 10 mg/mL.

The optical properties of the core-substituted PBIs at ground state were then investigated using UV-vis absorption spectroscopy, as shown in Figure 4.7. The lowest-energy band corresponding to the S_0 - S_1 transition is highly red-shifted with respect to the core-unsubstituted PBIs.⁸ The width of the absorbance region between 500 nm and 800 nm for the S_0 - S_1 transition peaks is another good indicator that the 1,6-di-substituted product was formed over the 1,7-di-substituted product. The 1,7-substituted product is reported to absorb in a much narrower region of 600 nm to 750 nm.^{22, 23} While all three PBIs absorbed between 500 and 800 nm, the intensity and position of their absorptions were different for each PBI. This difference in intensity and position agrees with what has previously been reported,⁸ and work seen in previous chapters. The choice of amino acid at the imide position has an impact on the molecular packing resulting in differences in the peak ratios for the S_0 - S_1 transitions.

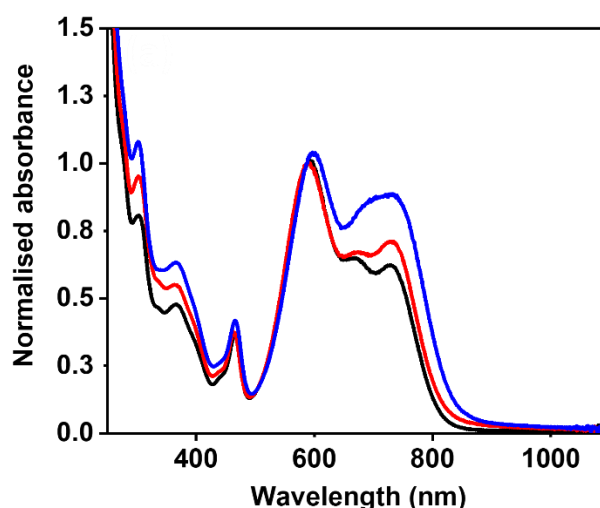


Figure 4.7. UV-vis absorption spectrum for (a) **PBI-L-1** (red), (b) **PBI-A-1** (black), and (c) **PBI-V-1** (blue) at pH 7 at a concentration of 10 mg/mL.

As discussed in Chapter 1, by substituting the core, the HOMO and LUMO band gap will be greatly impacted.^{15, 34} The impact of the pyrrolidine groups on the redox properties was investigated by measuring the SWVs of the three core-substituted PBIs in solution in a three-electrode setup to determine the potential for the redox processes. SWV was used instead of cyclic voltammetry (CV) to gain better resolution of the closely spaced reduction and oxidization peaks. The SWV data are shown in Figure 4.8 (a) to (c). As these are new materials, a background was

measured to confirm that there were no reduction or oxidation events due to the electrolyte. All three PBIs have four peaks in the SWV, two reductions and two oxidations, which relate to the formation of radical anion, dianion, cation, and dication. Similar PBI systems with cyclic amines substituted to the core have been reported to exhibit multiple oxidations.^{23, 35} The oxidation peaks appear to be irreversible showing that the electron transfer of the radical cation and dication is limited, most likely due to irreversible decomposition of the cation radicals. The reduction peaks on the other hand, which represent the formation of radical anion and dianion, appear to be quasi-reversible indicating electron transfer is quite irreversible or reversible.

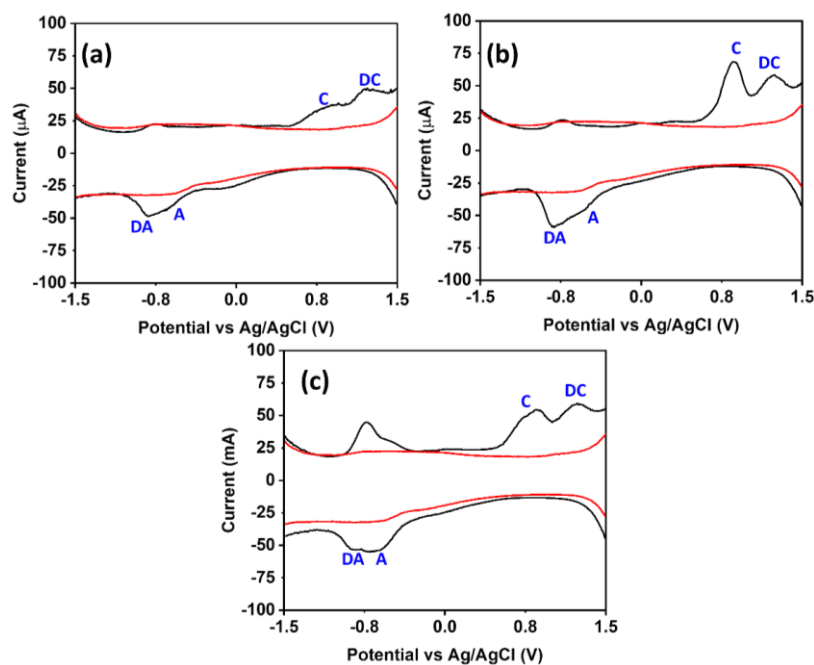


Figure 4.8. SWV of (a) **PBI-L-1 (black)**, (b) **PBI-A-1 (black)**, and (c) **PBI-V-1 (black)** and 0.1 M NaCl electrolyte background (**red**) at a frequency of 20 Hz. With the peaks corresponding to the radical anion (**A**), dianion (**DA**), cation (**C**) and dication (**DC**) labelled.

The reduction and oxidation potentials are summarised in Table 4.1 and are similar for all three PBIs regardless of the amino acid group. This is expected since the functional group at the imide position does not have a great impact on the reduction and oxidation potentials of PBIs compared to bay/ortho substitution.³⁶ However, the imide functionalisation can impact the redox reaction efficiencies as it can impact the molecular packing and assembled fibres. The UV-vis absorption spectra of the

ground-state core-substituted PBIs did show differences in the molecular packing based on the peak ratios for the S_0 - S_1 transitions. For **PBI-L-1** and **PBI-A-1** the peak heights at -0.7 V were smaller compared to **PBI-V-1** indicating they are less efficient at the formation of radical anion whereas **PBI-A-1** has the largest peak height for 0.68 V indicating a great efficiency in forming the radical cation. This illustrates the impact that imide functionalisation can have on the redox reaction efficiencies.

Table 4.1. Oxidation and reduction potentials for pyrrolidine-substituted PBIs with different amino acids groups.

PBI	E_{red1} (V)	E_{red2} (V)	E_{ox1} (V)	E_{ox2} (V)
L-1	-0.74	-0.51	0.68	1.2
A-1	-0.73	-0.51	0.68	1.2
V-1	-0.73	-0.55	0.66	1.2

From SWV the experimental ionisation potentials (IP) and electron affinities (EA) of the PBIs could be calculated. These values are related to the HOMO-LUMO and are listed in Table 4.2. The band gap energies were determined from a Tauc plot calculated from the UV-vis absorption spectra of the PBIs and are comparable to other systems with amine-substituted cores.³⁵ Here we observed that **PBI-V-1** had the lowest-lying HOMO/LUMO value, this demonstrates that small adjustments in the HOMO/LUMO energy levels can be accomplished through change in the amino acid chemical structure due to changes in the packing.

Table 4.2. Experimental ionisation potential (HOMO) and electron affinity (LUMO) values for PBIs at pH 7. Calculated according to literature procedure using the experimentally determined redox potentials ($E_{HOMO} = - [E_{ox1 \text{ vs } Fc/Fc^+} + 5.15 \text{ eV}]$ and $E_{LUMO} = - [E_{red2 \text{ vs } Fc/Fc^+} + 5.15 \text{ eV}]$) using the F_c/F_c^+ vs. vacuum = 5.15 eV.^{37, 38} The E_{gap} was determined from a Tauc plot; calculations are described in section 4.4.2.6.

PBI	E_{LUMO} (eV vs vacuum)	E_{HOMO} (eV vs vacuum)	ΔE_{gap}
L-1	-5.07	-6.26	1.57
A-1	-5.07	-6.26	1.57
V-1	-5.03	-6.24	1.52

4.2.2 Investigation to the photoexcitation properties of the core substituted PBIs

To investigate the photogenerated behaviour of the core-substituted PBIs, the solutions were irradiated using wavelengths where they absorbed in the ground state spectrum. Initially the PBIs were irradiated using $\lambda = 365$ nm, 490 nm, 590 nm, and 740 nm as these were wavelengths at which the ground state spectra showed the core-substituted PBIs to be strongly absorbing, all shown in Appendix 8. Only after being irradiated with 365 nm light for 15 minutes, was there a decrease in the absorbance for the peak at 730 nm and an increase in the absorbances at 655 nm and 505 nm. This same change is not observed in the spectra of the core-substituted PBIs with any of the wavelengths in the lower-energy visible light range.

As this looked to be a slow process, The core-substituted PBIs were irradiated with a 365 nm LED for a longer period, Figure 4.9. After irradiation for 30 minutes, there was a decrease in the absorbance for the peak at 730 nm and an increase in the absorbances at 505 nm and 655 nm. Upon increasing the irradiation time to 60 minutes, this change in absorbance at 505 nm, 655 nm, and 730 nm continued. It is believed that the observed changes for the core-substituted PBIs are due to the formation of radical cation or dication. However, it is difficult to assign the peaks to either the cation or dication due to the differences in peak assignment throughout the literature.^{11, 40, 41} These differences in assignment are often justified by the differences in the chemical structure and placement of the secondary amine group on the core. As there are no clear isosbestic points indicating one neutral species and either radical cation or dication, it is likely there is a mixture of the two occurring. The spectra for the three core-substituted PBIs were also remeasured after being allowed to sit at room temperature under normal atmosphere to gauge the radical cations' stability. After being left overnight the UV-vis absorption spectra for **PBI-L-1** and **PBI-V-1** showed that the absorbances at 600 nm had reverted close to their original values, while **PBI-A-1** showed the peaks at 505 nm and 730 nm had decreased slightly indicating some reversibility in the molecular packing as well.

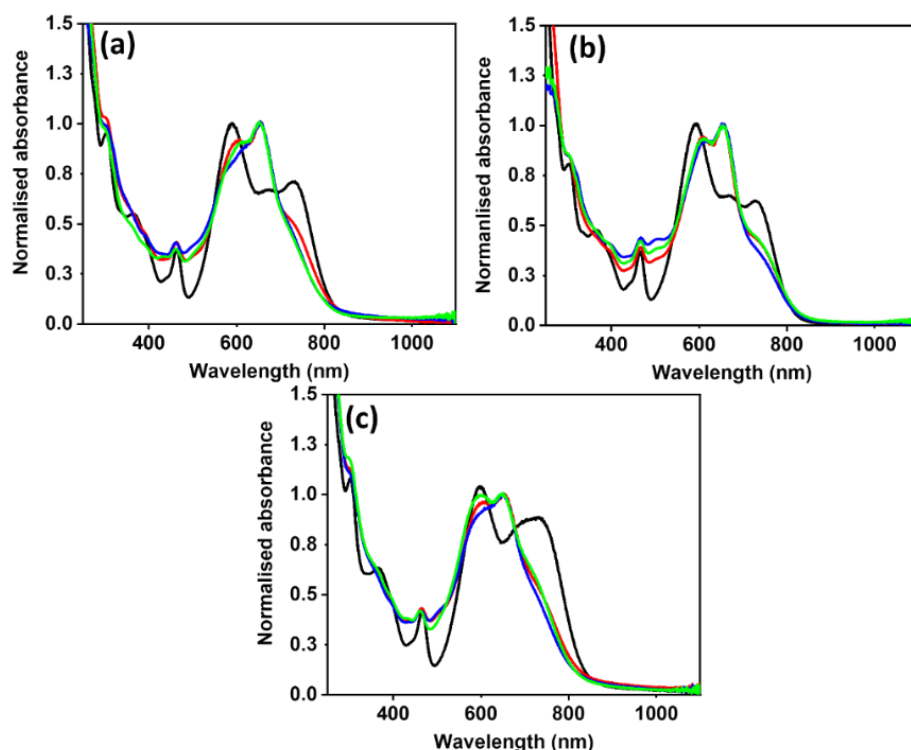


Figure 4.9. UV-vis absorption spectra for (a) **PBI-L-1**, (b) **PBI-A-1**, and (c) **PBI-V-1** pre-irradiation (**black**), after being irradiated for 30 minutes (**red**), after being irradiated for 60 minutes (**blue**), and after being allowed to relax overnight (**green**).

Along with a change in the UV-vis absorption spectra there is also a visible colour change in the core-substituted PBIs after irradiation. Figure 4.10 shows photographs of the PBIs before and after irradiation with UV light for 60 minutes, where after irradiation they are a visibly darker colour.

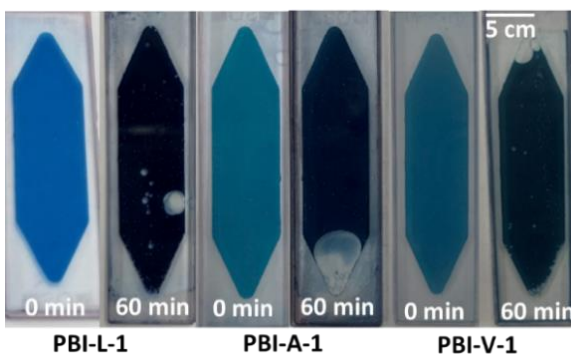


Figure 4.10. Photographs of the three core-substituted PBIs in solution at pH 7 in 0.1 mm cuvettes before and after being irradiated with 365 nm light for 60 minutes.

The radical cation for PBIs is EPR-active while the dication is EPR-silent.⁴¹ To get a better understanding of which cation is formed upon irradiation and to confirm if a radical is generated, the EPR spectra were collected, Figure 4.11 (a) to (c). The EPR spectrum of **PBI-L-1** shows a very small signal that does not change significantly after a longer irradiation period. There is possibly a preference for **PBI-L-1** to form radical dication over the radical cation. **PBI-A-1** does show an increase in signal for the radical cation after irradiation and forms the most radical cation of the three PBIs. There looks to be a shoulder only for **PBI-A-1** in the signal around 343.5 mT, which could suggest that there are two differently aggregated species in solution forming the radical cation. **PBI-V-1** shows an increase in the signal for radical cation after irradiation. This signal is stronger than that for **PBI-L-1** but weaker than that for **PBI-A-1**. It was seen previously for core-unsubstituted PBIs that the side chain group has a major impact on the amount of radical formed: as the branching in the side chain increased there was a decrease in the radical anion signal.⁸ The same trend is observed here for the core-substituted PBIs.

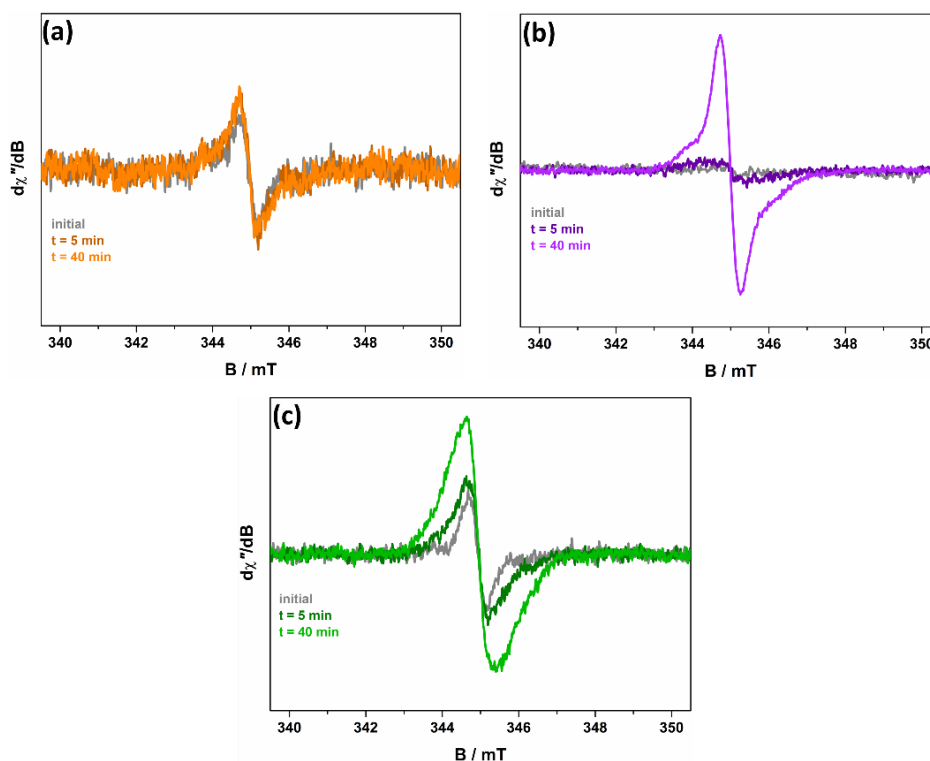


Figure 4.11. EPR signal measured for solutions before irradiation and after being irradiated for 5 minutes and 40 minutes with a 365 nm LED. (a) **PBI-L-1** (orange), (b) **PBI-A-1** (purple), and (c) **PBI-V-1** (green). Data collected by Dr Stephen Sproules.

The spectroelectrochemistry was measured to attempt to link changes in the UV-vis absorption spectra when irradiated to the different oxidising processes. It should be noted that to measure the spectroelectrochemistry, the solutions had to be diluted to 0.5 mg/mL to get absorbance values below 1 because of the larger cuvette size. As concentration can impact the aggregation and self-assembled structures in solution a concentration series was investigated to check (Appendix 9).⁴² It was observed that for **PBI-A-1** and **PBI-L-1** the ratio between the peaks at 590 nm and 675 nm to 730 nm increases as the concentration decreased, indicating that there is a change in the molecular packing at the different concentrations. The normalised spectra of **PBI-V-1** at 0.5 mg/mL shows there is the appearance of a new peak at 675 nm, indicating the molecular packing does change at this concentration. The SWV also revealed the redox properties of the core-substituted PBIs at lower concentrations in the spectroelectrochemistry setup had changed (Appendix 10). There is a shift in the redox potentials for the anion and cation radicals as well, which is likely due to the changes in the reference and working electrode material.⁴³ Lastly, in this setup at this concentration there are no longer two clear and distinct oxidation peaks. Therefore, spectroelectrochemistry could only be used to investigate this single irreversible oxidation, presumably corresponding to the formation of radical cation.

Knowing these differences, the spectroelectrochemistry was still used to link changes in the UV-vis absorption to the formation of radical cation. For **PBI-L-1**, 0.7 V vs Pt was applied for 30 minutes, and the absorbance spectra were collected after every 5 minutes, Figure 4.12 (a). After the first 5 minutes of 0.7 V being applied, a new peak at 505 nm appeared and the absorbance at 730 nm decreased. For **PBI-A-1** and **PBI-V-1**, Figure 4.12 (b) and (c), after 5 minutes of this potential being applied, there was the same appearance of a peak at 505 nm and a decrease in the absorbance at 730 nm. This increase at 505 nm is similar to what was observed in the UV-vis spectra for the core-substituted PBIs when they were irradiated with UV light and supports the idea that a radical cation is formed. Unlike the UV-vis absorption spectra of the core-substituted PBIs when the system is irradiated, however, there is no increase in the absorbance at 655 nm when the single oxidation potential is applied. An increase in absorbance in this region has been linked to the formation of radical dication for 1,7-systems,^{40, 41} which would explain why it is not occurring at this single oxidation

potential. However, it is difficult to make a direct comparison with our system since the core substitution position has a major impact on the radical formation properties. Another method would use a chemical oxidate to compare; however, the common oxidiser (NOSbF_6) is highly air sensitive.

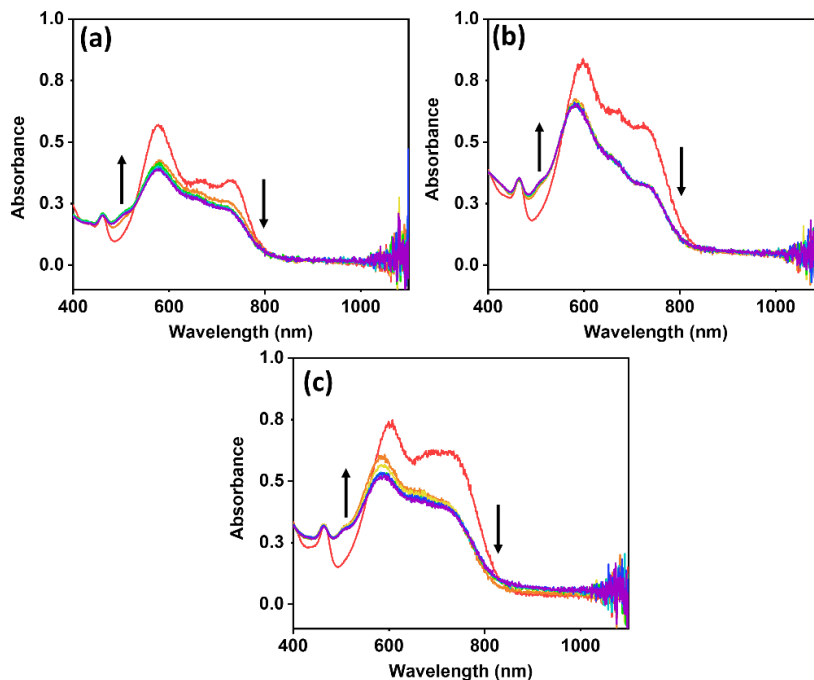


Figure 4.12. UV-vis absorption spectra of (a) **PBI-L-1**, (b) **PBI-A-1**, and (c) **PBI-V-1** measured at $t = 0$ minutes (red) when no potential was applied and after 0.7 V vs Pt was applied. Spectra were measured at 5-minute intervals up to 30 minutes, $t = 5$ minutes (orange), $t = 10$ minutes (yellow), $t = 15$ minutes (green), $t = 20$ minutes (teal), $t = 25$ minutes (blue), and $t = 30$ minutes (purple).

As discussed in the introduction of this chapter, the change in nanostructures after forming any radical is often overlooked. Here we decided to probe this by scanning the change in self-assembled structures after irradiation using dynamic viscosity, Figure 4.13 (a) to (c). This was done by irradiating a bulk solution and then transferring it to the rheometer for measurement. To rule out the possibility that the viscosity is increasing due to heat emanating from the 365 nm LED, a control test was done where the core substituted PBIs were heated at 40°C for 60 minutes and the viscosity was measured. This showed there was either no change in the viscosity or the viscosity decreased due to the increase in solubility of the core substituted PBI aggregates, Appendix 11.

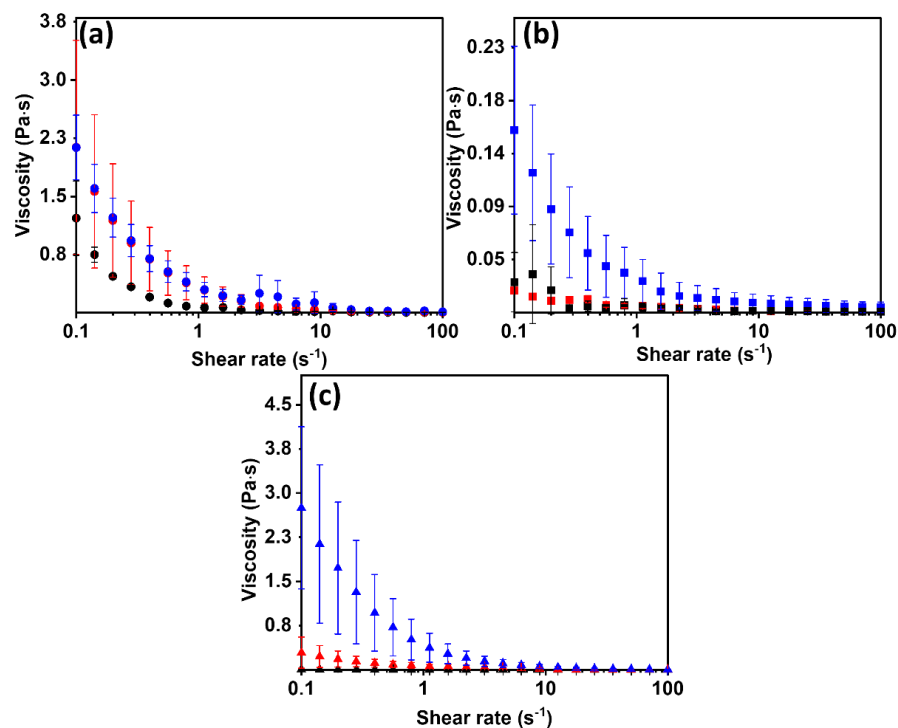


Figure 4.13. Dynamic viscosities of (a) **PBI-L-1**, (b) **PBI-A-1**, and (c) **PBI-V-1** at pH 7. Viscosity measurements were done pre-irradiation (**black**), after being irradiated for 30 minutes (**red**), and after being irradiated for 60 minutes (**blue**). Measurements were performed in triplicate and errors were calculated from the standard deviations.

Shear thinning is observed in all cases for all three core-substituted PBIs which indicates the presence of assembled micelles in solution and expected for amino acids functionalized PBIs.⁴⁴ For **PBI-L-1**, Figure 4.13 (a), after irradiation for 30 minutes there was an increase in viscosity at low shear, however, there was large variation between the repeated viscosity measurements. Therefore, there was no statistically significant change in the viscosity at this point. After 60 minutes, there was an increase in viscosity from 0.06 Pa·s at 1 s⁻¹ for the initial solution to 0.3 Pa·s. For **PBI-A-1**, Figure 4.13 (b), the initial solution at the same shear rate was 0.005 Pa·s which was much lower than **PBI-L-1**, indicating a difference between the two PBIs in terms of their fibre length, morphology, or abundance of fibres. After 30 minutes the viscosity of **PBI-A-1** at the same shear rate was 0.005 Pa·s and after 60 minutes the viscosity had increased to 0.03 Pa·s. It should be noted that there was a larger variation between measurements for this sample, especially at lower and higher shear rates, indicating some irreproducibility. Lastly, for **PBI-V-1**, Figure 4.13

(c), the initial solution at a shear rate of 1 s^{-1} had viscosity of $0.0012 \text{ Pa}\cdot\text{s}$ making it the least viscous all three initial solutions. It saw the most significant increase in viscosity to $0.06 \text{ Pa}\cdot\text{s}$ after being irradiated for 30 minutes. After 60 minutes the viscosity had increased further to $0.4 \text{ Pa}\cdot\text{s}$, with some variation between measurements at low and high shear. This is supported by the UV-vis absorption spectra of **PBI-V-1** which showed the largest decrease in absorbance at 730 nm after 60 minutes of irradiation. This change in viscosity upon irradiation could be due to either the presence of the radical cation or dication changing the structures present, or how the structures interact with each other in solution.

To investigate the change in the micellar and nanostructures of the PBIs as they are irradiated with UV light in greater detail compared to viscosity, SAXS data were collected before irradiation, after being irradiated for 60 minutes and after being allowed to relax overnight. As seen in Chapter 2, the SAXS data were fitted to correlation models when possible. The SAXS data and respective fits for **PBI-L-1** are shown in Figure 4.14, with the fit parameters detailed in Table 4.3. The correlation length is expected to increase when there is a change in the solubility and an increase in the fibre mesh size.⁴⁵ The correlation length increased upon irradiation indicating there is an increase in the weighted-average interdistance between crosslinks possibly due to the changes in the charge of the aggregates as the cations are formed. The Porod exponent increased upon irradiation which means there is a change in the clusters on the larger nanostructure and microstructure length scale.⁴⁶ The Lorentz exponent also increased upon irradiation, which is an indication of a change in the nanofibre–solvent interactions on a local scale. A Lorentzian exponent below 2 indicates that the fibres are behaving as if they are in a good solvent. When this exponent is greater than 2, it indicates reduced fibre-solvent interactions.⁴⁷ After being allowed to relax overnight there was a negligible increase in the correlation length and a slight increase in the Lorentz exponent indicating the fibre–solvent interactions had become less favourable. The Porod exponent had decreased which showed some reversibility in the cluster structures. Though there is not a direct correlation between the molecular packing and the nanostructures, this agrees with UV-vis absorption data which showed changes in the packing after being allowed to sit overnight.

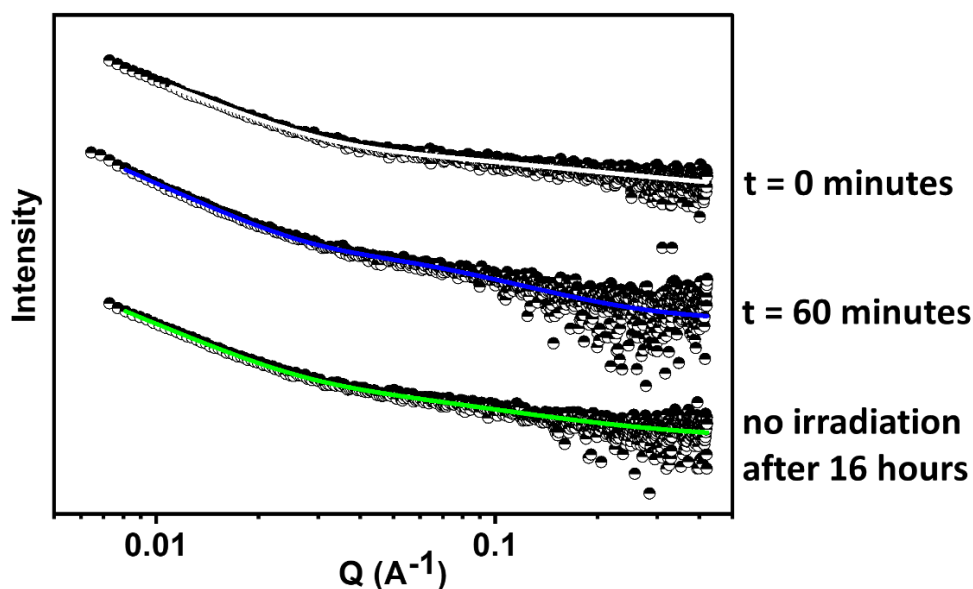


Figure 4.14. SAXS for solutions of **PBI-L-1** irradiated with a 365 nm LED for different amounts of time and then allowed to relax overnight. Scattering data are shown as half-open points and the fits as coloured lines. The initial solution fit is **white**, after being irradiated for 60 minutes is **blue**, and after being allowed to sit overnight is **green**. Note the data are offset on the intensity scale for clarity.

Table 4.3. SAXS fit table for solutions of **PBI-L-1** irradiated with a 365 nm LED for different amounts of time. *No fitting error available.

Irradiation period (minutes)	0	60	Allowed to relax overnight
<i>Model</i>	<i>Correlation length</i>	<i>Correlation length</i>	<i>Correlation length</i>
<i>Correlation length (nm)</i>	1.47 ± 0.0101	2.82 ± 0.0337	2.85 ± 0.00972
<i>Porod exponent</i>	3.62 ± 0.00299	4.21 ± 0.00461	3.86 ± 0.00237
<i>Lorentzian exponent</i>	1.34 ± 0.0117	2.12 ± 0.0438	2.28 ± 0.0849
χ^2	2.0	3.4	3.7

SAXS was again used to see if the micellar structures followed a similar trend to what was observed in the viscosity and UV-vis absorption measurements for **PBI-A-1**. The SAXS data and respective fits for **PBI-A-1** are shown in Figure 4.15, with the fit parameters detailed in Table 4.4. All the data for **PBI-A-1** were fit to a sphere combined with a power law instead of a correlation length model even though the viscosity showed shear thinning. This model suggests that there is a co-existence of free molecules and a very small fraction of weakly scattering worm-like micelles.^{48, 49}

The presence of two differently-assembled species in solution would support the shoulder signal observed in the EPR. The power law used to fit the scattering at low Q accounts for the larger fibre structures beginning to form at this pH.⁵⁰ The spherical radius for the initial solution was 1.32 ± 0.01 nm. After 60 minutes, the spherical radius was reduced, indicating there was a change in the nanostructures packing during irradiation. This is supported by the increase in the power law which implies an increase in segregation within the system and more densely packed structures. This also agrees with the viscosity of **PBI-A-1** which showed an increase after irradiation. After being allowed to sit overnight the spherical radius in solution increased back closer to its original value but the power increased further. UV-vis absorption spectroscopy of **PBI-A-1** did show that after being allowed to sit overnight the peaks at 505 nm and 730 nm decreased back slightly indicating some reversibility in the packing. Interestingly, **PBI-A-1** had formed the most radical cation even though it has formed spherical micelles instead of fibres; this is opposite to what was seen in previous chapters where fibres were more favourable when form radical anion for the core substituted PBIs.

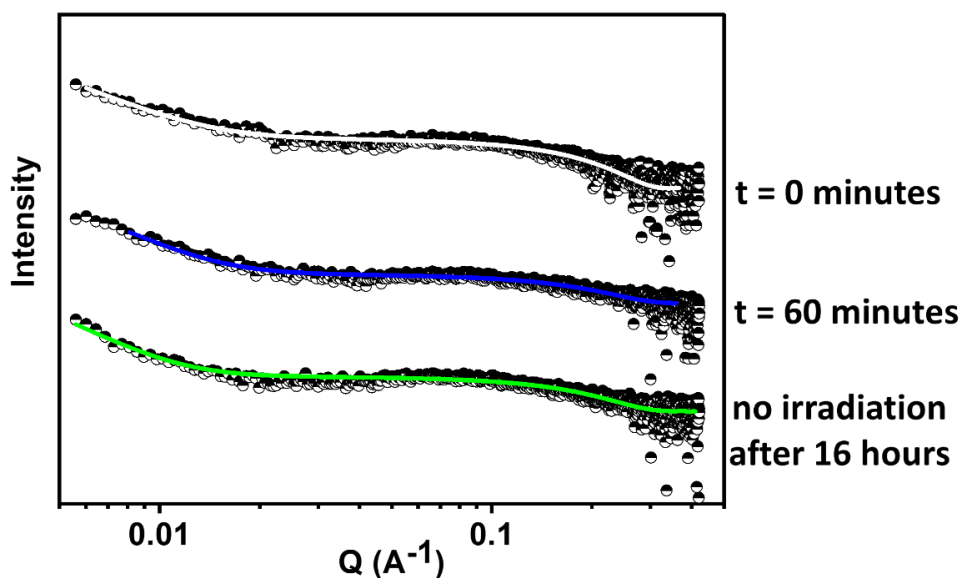


Figure 4.15. SAXS for solutions of **PBI-A-1** irradiated with a 365 nm LED for different amounts of time and then allowed to relax overnight. Scattering data are shown as half-open points and the fits as coloured lines. The initial solution fit is **white**, after being irradiated for 60 minutes is **blue**, and after being allowed to relax overnight is **green**. Note the data are offset on the intensity scale for clarity.

Table 4.4. SAXS fit table for solutions of **PBI-A-1** irradiated with a 365 nm LED for different amounts of time.

Irradiation period (minutes)	0	60	Allowed to relax overnight
Model	Sphere + power law	Sphere + power law	Sphere + power law
Sphere radius (nm)	1.32 ± 0.0101	1.22 ± 0.0101	1.27 ± 0.00503
Power law	3.36 ± 0.0139	3.73 ± 0.101	4.00 ± 0.00427
χ^2	2.3	1.9	4.8

Lastly, the SAXS was collected for **PBI-V-1** in solution. Figure 4.16 shows the SAXS data and respective fits for **PBI-V-1** after being irradiated for 60 minutes and allowed to relax. Full fitting parameters for the respective fits for **PBI-V-1** can be found in Table 4.5. Like **PBI-L-1**, the data for **PBI-V-1** after irradiation and after being allowed to relax overnight were fitted using a correlation length model. The changes in aggregation for **PBI-V-1** after irradiation are having a greater impact on the local scale of the fibres compared to **PBI-L-1**. This is supported by the viscosity and by the UV-vis absorption spectra which showed **PBI-V-1** had the largest change in molecular packing and morphology after irradiation. There was also a slight increase in the Porod exponent which indicates a change in the longer length scale which would be attributed to the change in viscosity. After **PBI-V-1** was allowed to sit overnight there was another increase in the correlation length. However, the Lorentz exponent did not change significantly and the Porod exponent decreased back toward the initial value. The UV-vis absorption for **PBI-V-1** showed that the absorbance at 600 nm reverted closest to the initial solution absorbance.

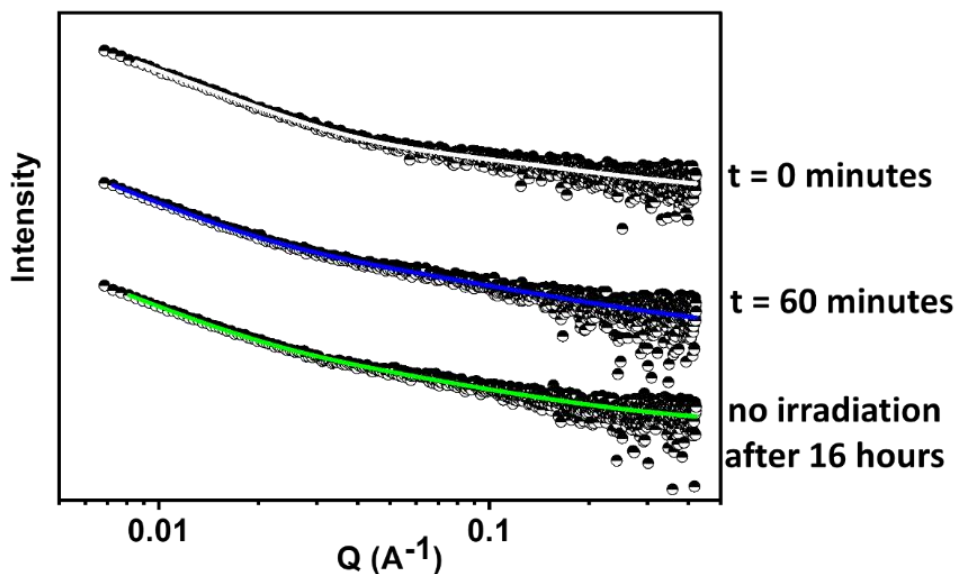


Figure 4.16. SAXS for solutions of **PBI-V-1** irradiated with a 365 nm LED for different amounts of time and then allowed to relax overnight. Scattering data are shown as half-open points and the fits as coloured lines. The initial solution fit is **white**, after being irradiated for 60 minutes is **blue**, and after being allowed to relax overnight is **green**. Note the data are offset on the intensity scale for clarity.

Table 4.5. SAXS fit table for solutions of **PBI-V-1** irradiated with a 365 nm LED for different amounts of time. *No fitting error available.

Irradiation period (minutes)	0	60	Allowed to relax overnight
<i>Model</i>	<i>Correlation length</i>	<i>Correlation length</i>	<i>Correlation length</i>
<i>Correlation length (nm)</i>	1.06 ± 0.0127	3.76 ± 0.0186	3.99 ± 0.0206
<i>Porod exponent</i>	3.22 ± 0.00201	3.44 ± 0.00348	3.33 ± 0.00325
<i>Lorentzian exponent</i>	1.76 ± 0.0211	1.61 ± 0.0137	1.63 ± 0.0138
χ^2	2.5	2.7	3.2

4.2.3 Probe into the impact of pH on the packing and self assembled aggregates of the core substituted PBIs

Core-unsubstituted PBIs self-assemble into fibrous-type structures and can begin to gel when the pH is lowered if the conditions are suitable, as seen in previous reports.⁵¹ It is the ability to modify their self-assembly using pH that makes them

useful for conductive hydrogel applications.^{4, 52} It is also advantageous method for changing the structures because it is reversible and the water is not diluted with more toxic solvent. To see if the core-substituted PBIs behaved similarly to the core-unsubstituted PBIs, pH-dependence of aggregation was screened. It should be noted that these viscosity measurements were measured on a different rheometer to the solutions before and after irradiation. The two rheometers have different sensitivity at low shear rates meaning the viscosity trends may be comparable but the absolute viscosity values cannot be compared.

The dynamic viscosity of **PBI-L-1**, Figure 4.17 (a), showed shear thinning for solutions regardless of pH. The viscosity at a shear rate of 1 s^{-1} was larger for pH 9 (1.5 Pa·s) and 6 (3.8 Pa·s) compared to the other pHs values, however, due to the variability between the viscosity measurements this difference is not statistically significant. The dynamic viscosity of **PBI-A-1**, Figure 4.17 (b), showed an increase in viscosity at low shear for solutions at low pH, which has been seen for PBIs in Chapter 3. For **PBI-A-1** at pH 8 and 9, the viscosities at a shear rate of 1 s^{-1} were 0.0021 Pa·s and 0.0017 Pa·s, respectively, which is similar to the viscosity of water. At pH 6 and 7 there was an increase in viscosity at the same shear rate to 0.41 Pa·s and 0.13 Pa·s, respectively, suggesting fibres had begun to form at these pHs.

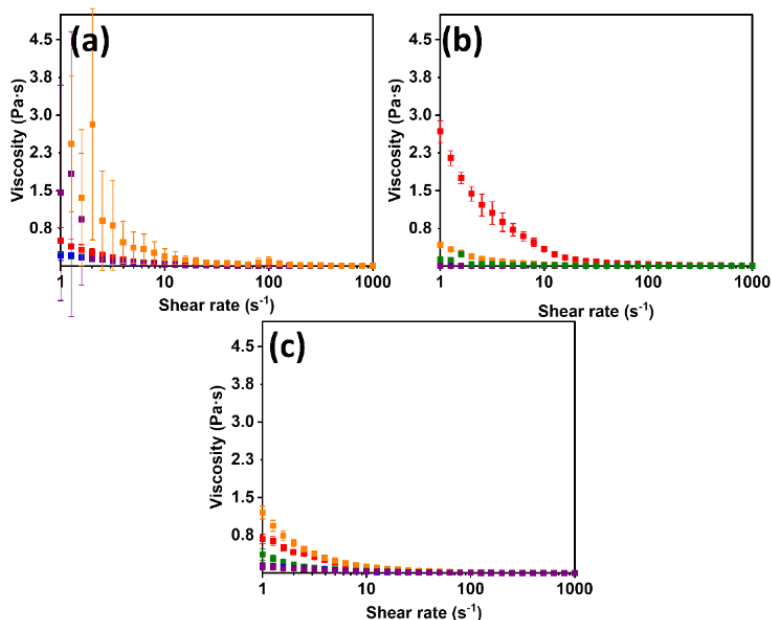


Figure 4.17. Dynamic viscosity of (a) **PBI-L-1**, (b) **PBI-A-1**, and (c) **PBI-V-1**. Viscosity measurements were collected at pH 5 (red), pH 6 (orange), pH 7 (green), pH 8

(blue), and pH 9 (purple). Measurements were performed in triplicate and errors were calculated from the standard deviation.

At pH 5 the viscosity at 1 s^{-1} shear rate was $2.6 \text{ Pa}\cdot\text{s}$, the largest in the series, suggesting there is a great deal of aggregates self-assembled into elongated fibrous structures at this pH. The dynamic viscosity of **PBI-V-1**, Figure 4.17 (c), showed shear thinning for solutions at pH 7, 6, and 5. At a shear rate of 1 s^{-1} there is an increase in viscosity at pH 5 ($0.67 \text{ Pa}\cdot\text{s}$) and 6 ($1.2 \text{ Pa}\cdot\text{s}$) compared to pH 7 ($0.23 \text{ Pa}\cdot\text{s}$).

This increase in viscosity at low shear between solutions at pH 7 and 6 which suggests an apparent pK_a of the molecule in this area causing self-assembly between these two pHs. As seen throughout this work the pH-sensitive properties of the core-substituted PBI are different depending on the amino acid chemical structure and this can be used as a parameter for their gelation process. The viscosity data at different pHs suggests the changes in self-assembled structures are different for the core-substituted PBIs. To see if the apparent pK_a values could explain these differences in self-assembly, pK_a titrations were done, Figures 4.18 (a-c), and the two apparent pK_a values for each PBI are listed in Table 4.6. The higher apparent pK_{a1} values for **PBI-L-1** (7.4) and **PBI-V-1** (7.0) explain the differences in the models used to fit the SAXS data collected for the solutions at pH 7 compared to **PBI-A-1** (6.4) discussed earlier in this Chapter. At this pH, **PBI-L-1** and **PBI-V-1** aggregates have begun self-assembling. The pH difference between the apparent pK_a values for **PBI-L-1** is the smallest and the largest is for **PBI-A-1**. This difference in apparent pK_{a1} and pK_{a2} values indicates a longer transition period for self-assembled structures and may favour changes in morphology differently. It is supported by what is observed in the dynamic viscosity, where **PBI-A-1** showed significant difference in the fibre length, morphology, or abundance at the different pHs, while **PBI-L-1** showed a less significant change in the viscosity regardless of pH due to the shorter transition period between apparent pK_a s.^{53, 54}

Table 4.6. Summarised apparent pK_a values for the different PBIs at 10 mg/mL.

PBI	pK_{a1}	pK_{a2}
A-1	6.4	5.5
V-1	7.0	6.3
L-1	7.4	6.9

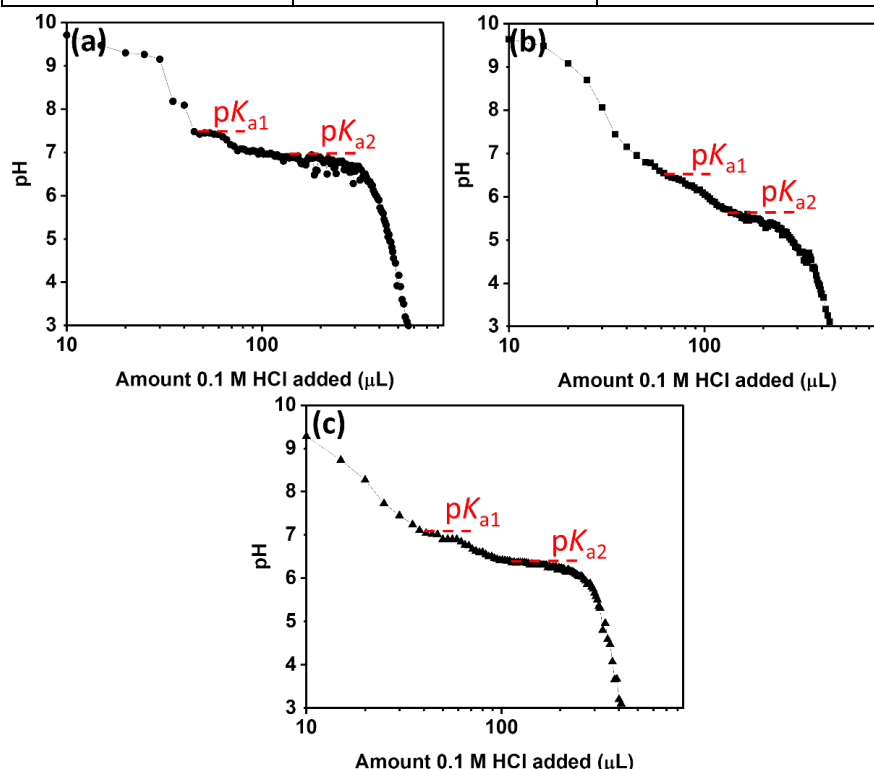


Figure 4.18. Apparent pK_a titrations of (a) **PBI-L-1**, (b) **PBI-A-1**, and (c) **PBI-V-1** using 0.1 M HCl solution.

The SAXS data of the core-substituted PBIs were collected to get a more detailed look at the nanostructures at different pHs across the apparent pK_a value compared to the viscosity scans. The SAXS data and respective fits for **PBI-L-1** at pH 5, 6, and 7 are shown in Figure 4.19. These pHs were chosen because they are all around the apparent pK_a values of the three core-substituted PBIs. The parameters for the fits are detailed in Table 4.7. The viscosity at low shear rates did not show statistically significant changes between the solutions at pH 7, 6, or 5. The pK_a titrations also revealed there were only small intervals between the apparent pK_a values. Therefore, it is not expected for there to be a major change in the morphology of the aggregates

across these pH values. As discussed earlier in this chapter, the model used for **PBI-L-1** at pH 7 was a correlation length model which is indicative of a branched fibre system.⁵⁵ This pH is below the first apparent pK_a of **PBI-L-1** and close to the second apparent pK_a value. **PBI-L-1** at pH 6 could also be fit using a correlation length model. The correlation length at this pH was larger than the value seen at pH 7. This increase in correlation length indicated a larger distance between crosslinks which would indicate a less dense fibre system and a larger fibre mesh size. The Lorentzian exponent is higher for pH 6 compared to pH 7. This indicates there is a change in the local scale of the fibres possibly due to a change in charge and solubility. The Porod exponent describing the fibre clusters for pH 7 was larger than that for pH 6 indicating a change in the clustering and swelling of the fibre system. **PBI-L-1** at pH 5 could still be fit using a correlation length model, and a similar trend as before was observed. The Lorentzian exponent increased further and the Porod exponent decreased. As aggregates of **PBI-L-1** become protonated there is a change in the hydrophobicity which is having an impact on the clustering and fibre density on the local and longer length scales but not causing a change in morphology.

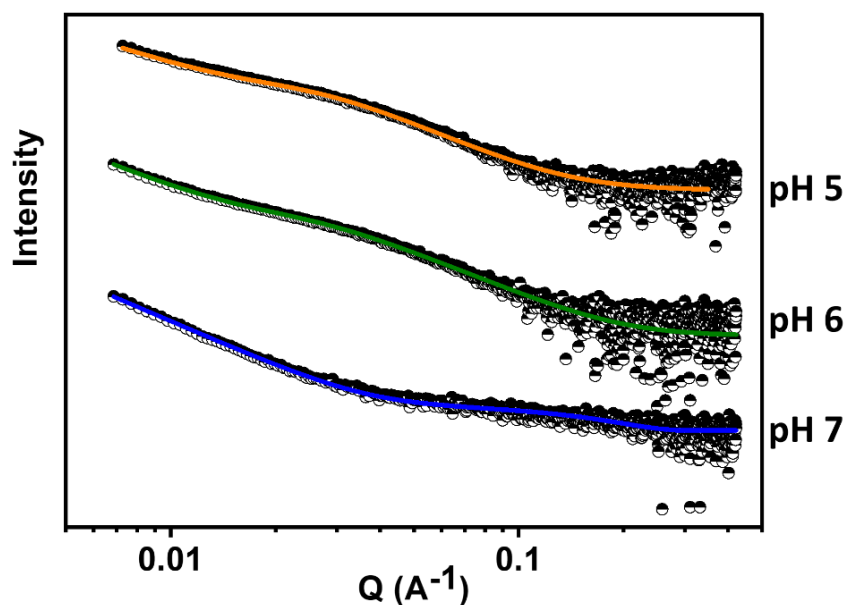


Figure 4.19. SAXS data for solutions of **PBI-L-1** prepared at 10 mg/mL and pH-adjusted as required with the data shown as open symbols and the fits as coloured lines indicating the pH: 5 (orange), 6 (green), and 7 (blue). Note the data are offset on the intensity scale for clarity.

Table 4.7. SAXS fitting results for **PBI-L-1** as 10 mg/mL solutions at different pH. *No fitting error available.

pH	7	6	5
Model	Correlation length	Correlation length	Correlation length
Correlation length (nm)	1.47 ± 0.0128	3.82 ± 0.0505	3.46 ± 0.0492
Porod exponent	3.62 ± 0.00306	3.42 ± 0.0312	2.75 ± 0.0415
Lorentzian exponent	1.34 ± 0.0138	3.41 ± 0.0312	3.71 ± 0.0527
χ^2	2.0	2.0	4.5

The SAXS data from **PBI-A-1** at different pHs with overlaid fits is shown in Figure 4.20, with the fit parameters detailed in Table 4.8. At pH 7, **PBI-A-1** was fitted to a sphere combined with a power law to account for spherical micelles with weakly scattering worm-like micelles. This pH is above both apparent pK_a values but showed a viscosity at low shear rates larger than that of solutions at pH 8 or 9. This indicates there is some self-assembly of aggregates into larger structures beginning at this pH. At pH 6, which is below the first apparent pK_a value, the viscosity showed an increase at low shear rates and the morphology, length, or abundance of the self-assembled structures is expected to change. This is supported by the SAXS which could be fitted using a flexible elliptical cylinder model at this pH. At pH 5, below the apparent pK_a values, the viscosity showed an even larger increase at low shear rates. This means there should be another change in the morphology, length, or abundance of the self-assembled fibre structures. While **PBI-A-1** was still modelled using a flexible elliptical cylinder model, there was a change in the fitting parameters such as fibre length, Kuhn length, and axis ratio. All these parameters were larger for **PBI-A-1** at pH 5 than those at pH 6. The Kuhn length increase indicates the fibres are becoming less flexible as they become more hydrophobic through further assembly. The increase in the axis ratio indicates compression of the fibres. These data suggest the fibre structures of **PBI-A-1** are self-assembling and elongating further at the lower pHs as seen for similar systems.^{26, 56}

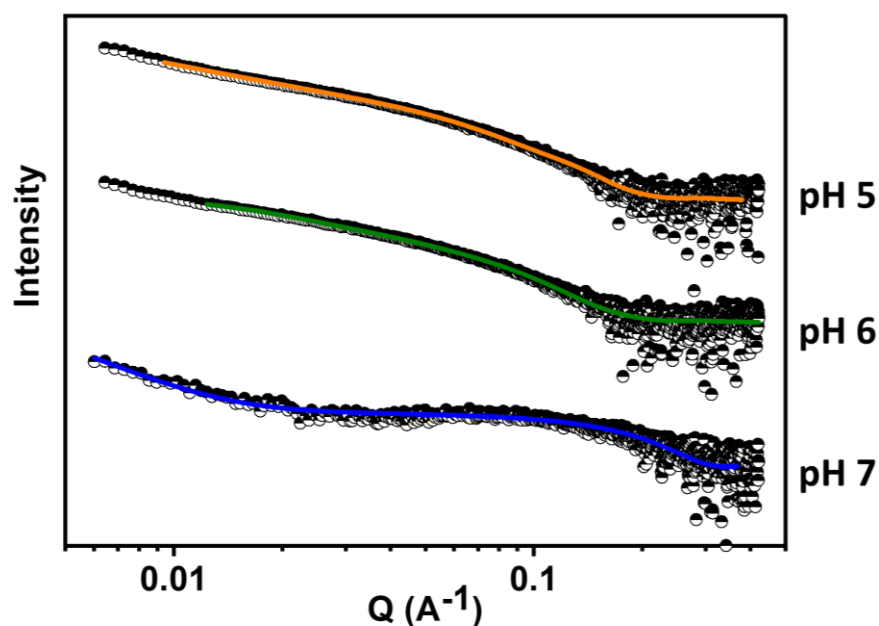


Figure 4.20. SAXS data for solutions of **PBI-A-1** prepared at 10 mg/mL and pH-adjusted as required with the data shown as open symbols and the fits as coloured lines indicating the pH: 5 (orange), 6 (green), and 7 (blue). Note the data are offset on the intensity scale for clarity.

Table 4.8. SAXS fitting results for **PBI-A-1** as 10 mg/mL solutions at different pH. *No fitting error available.

pH	7	6	5
Model	Sphere + power law	Flexible elliptical cylinder	Flexible elliptical cylinder
Sphere radius (nm)	1.32 ± 0.0108	N/A	N/A
Power law	3.36 ± 0.0819	N/A	N/A
Length (nm)	N/A	79.5 ± 2.01	300 ± 9.99
Kuhn length (nm)	N/A	7.95 ± 0.000399	17.8 ± 0.202
Cylinder radius (nm)	N/A	1.56 ± 0.0114	1.51 ± 0.0624
Axis ratio	N/A	1.89 ± 0.0206	2.82 ± 0.0217
χ^2	2.3	3.8	3.5

The SAXS data of **PBI-V-1** at different pHs with overlaid fits are shown in Figure 4.21, with the fit parameters detailed in Table 4.9. The data for **PBI-V-1** at pH 7 was fitted to the correlation length model. The viscosity did show some shear thinning at this pH. Also, this pH was below the apparent pK_{a1} value indicating some self-assembled

structures should be present. The viscosity at low shear rates showed an increase in viscosity between pH 7 and pH 6 and it was observed that the apparent pK_{a2} value was between these pHs. Therefore, it is expected for there to be some change in the morphology, abundance, or length of the aggregates between these pH values. **PBI-V-1** at pH 6 could still be fitted to a correlation length model, however, the correlation length at pH 6 was much larger than at pH 7. This indicates a change in the fibre density and increase in mesh size as the aggregate charge has changed similarly to what was observed for **PBI-L-1**. The Lorentzian exponent for high- Q scattering was manually fitted to 4 as the maximum limit. This is expected since as the fibres become more hydrophobic, they are also becoming more insoluble in water. At pH 5 the Lorentzian exponent was still manually fitted to 4, indicating the fibre–solvent interactions have not changed greatly compared to pH 6 as they are both below the apparent pK_a values. There was a slight increase in the Porod exponent at the different pHs indicating the change in the aggregate charge is not changing the clusters on a large scale.

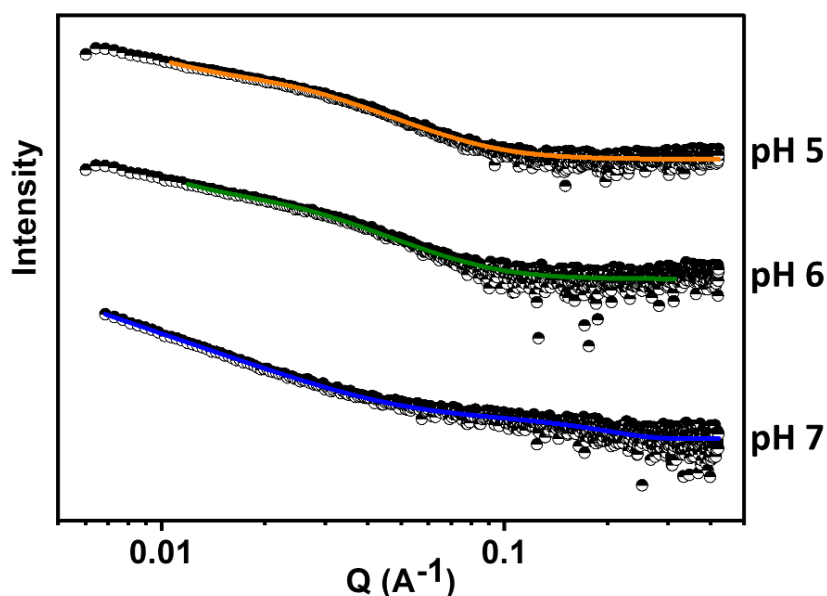


Figure 4.21. SAXS data for solutions of **PBI-V-1** prepared at 10 mg/mL and pH-adjusted as required with the data shown as open symbols and the fits as coloured lines indicating the pH: 5 (orange), 6 (green), and 7 (blue). Note the data are offset on the intensity scale for clarity.

Table 4.9. SAXS fitting results for **PBI-V-1** as 10 mg/mL solutions at different pH. *No fitting error available.

pH	7	6	5
<i>Model</i>	<i>Correlation length</i>	<i>Correlation length</i>	<i>Correlation length</i>
<i>Correlation length (nm)</i>	1.06 ± 0.0113	3.93 ± 0.00598	3.71 ± 0.00867
<i>Porod exponent</i>	3.22 ± 0.00199	3.29 ± 0.00138	3.38 ± 0.0448
<i>Lorentzian exponent</i>	1.76 ± 0.0204	4*	4*
χ^2	2.5	5.3	9.4

Lastly, the impact of pH on the core-substituted PBIs' ability to form radical cation or dication was investigated, Figure 4.22 (a) to (c). The initial solutions showed that the absorbance region between 500 nm and 800 nm for the S₀-S₁ transition peaks did not show broadening as the pH was lowered. All three core-substituted PBIs at pH 7, 8, and 9 showed the same trend as before, where, upon irradiation with UV light, there was an increase in absorbance at 505 nm and 655 nm and a decrease at 730 nm. For **PBI-L-1** at pH 5 and 6 there still appears to be an increase in absorbance at 655 nm, however, the appearance of a new peak at 505 nm and absorbance decrease at 730 nm after irradiation becomes less clear. For **PBI-V-1** at pH 6, the increase in absorbance at 505 nm and 655 nm and decrease at 730 nm is still observed. At pH 5 there is no longer an observable difference in the spectrum before or after irradiation. As the pH is lowered there is an increase in the concentration of electron acceptors available to help facilitate the formation of the radical cation and dication. Therefore, it would be expected for the formation of radical cation and dication to improve as pH is lowered. Instead, what is observed is that once the pH is below the apparent pK_a values the decrease in solubility and changes in the self-assembled structures becomes the overriding factor impacting the radical formation. The viscosity did not show much change in the morphology, length, or abundance of fibres for **PBI-V-1** and **PBI-L-1** between these pHs. However, SAXS measurements showed that the solvent-fibre interactions became less favourable at these pHs, possibly owing to a decrease in solubility.

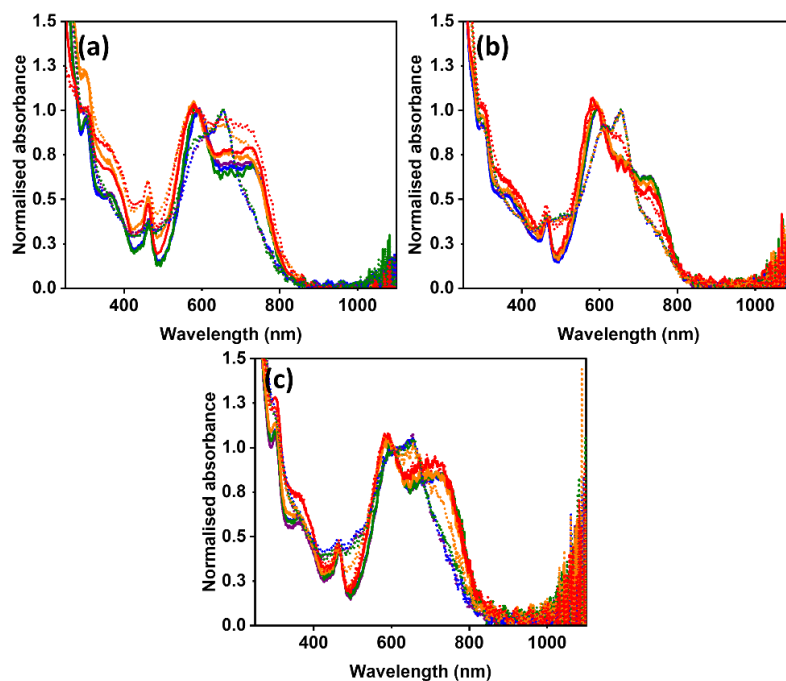


Figure 4.22. UV-vis absorption spectra of solutions at a 10 mg/mL concentration of (a) **PBI-L-1**, (b) **PBI-A-1**, and (c) **PBI-V-1** at pH 5 before (**solid red**) and after irradiation (**dotted red**), pH 6 before (**solid orange**) and after irradiation (**dotted orange**), pH 7 before (**solid green**) and after irradiation (**dotted green**), pH 8 before (**solid blue**) and after irradiation (**dotted blue**), and pH 9 (**solid purple**) and after irradiation (**dotted purple**).

The UV-vis absorption spectra for **PBI-A-1** at pH 6 and pH 5 still showed the same trend as before, however, for pH 5 there was not as great of an increase at 655 nm or a decrease at 730 nm. The SAXS of **PBI-A-1** showed that, unlike the other two core-substituted PBIs, it had formed flexible cylinders at pH 6 and 5, with larger size parameters for the cylinders at pH 5. In Chapter 3, it was seen that as the pH is increased and the core-unsubstituted PBIs begin to self-assemble into fibrous structures, their ability to form radical anion is improved. The opposite trend was observed for the three core-substituted PBIs, showing that pH is having a major influence on the radical cation and dication formation.

4.2.4 Development of pH triggered hydrogel materials using core substituted PBIs

As the core-unsubstituted PBIs were shown to be effective gelators, we were interested in investigating if the core-substituted PBIs could form hydrogels upon lowering the pH and potentially be used in xerogel devices. Unlike the core

unsubstituted PBIs discuss in the previous chapters of this thesis these materials have never been reported to form hydrogels, therefore, the minimum gelation concentrations (mgc) needed to be determined for all three. This is also an initial scan before running rheology. Figure 4.23 shows **PBI-L-1** prepared at different concentrations triggered with an appropriate amount of glucono- δ -lactone (GdL), 3 mg/mL to 8 mg/mL, to get a final pH of 3.4. Gelation was achieved above 1 mg/mL of gelator, although syneresis was observed at all **PBI-L-1** concentrations up to 10 mg/mL, at which point syneresis had less of an impact. Syneresis is the phenomenon in which a gel undergoes macroscopic contractions and expels some solvent that was initially immobilised in the gel network. This has been observed with other hydrogel systems made using dipeptide gelators triggered with GdL.⁵⁷ To minimise the impact of syneresis, the Sterilin vial inner walls were sanded to increase surface roughness as this should increase the surface tension between hydrogel and vial.

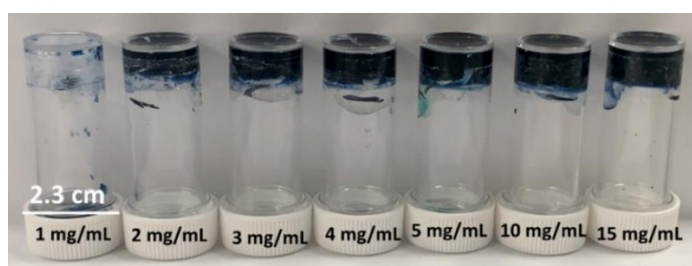


Figure 4.23. Determining the mgc from photographs of samples prepared using different concentrations of **PBI-L-1** on the addition of GdL.

Figure 4.24 shows the mgc determination for **PBI-A-1**. As before, the inner vial walls had been sanded. The lowest concentration for **PBI-A-1** that could form an invertible sample was 3 mg/mL. Unlike **PBI-L-1**, there was no major syneresis observed for the lower concentrations.

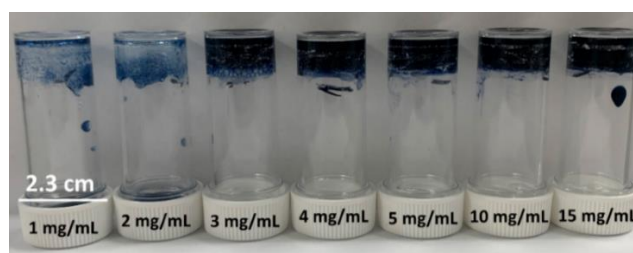


Figure 4.24. Determining the mgc from photographs of samples prepared using different concentrations of **PBI-A-1** on the addition of GdL.

Lastly, Figure 4.25 shows the mgc determination of **PBI-V-1**. **PBI-V-1** behaved differently to the other PBIs. At the lower concentrations of 1-4 mg/mL, **PBI-V-1** did not form invertible samples and there were no precipitates along the walls to indicate that aggregates had formed. It was not until the concentration was 5 mg/mL that the solution looked to have formed some type of precipitate in solution. However, these were incapable of immobilising the water. The only concentration at which **PBI-V-1** produced an invertible sample was 15 mg/mL, meaning there is a difference in the self-assembly route for **PBI-V-1** when pH is lowered compared to the other PBIs.

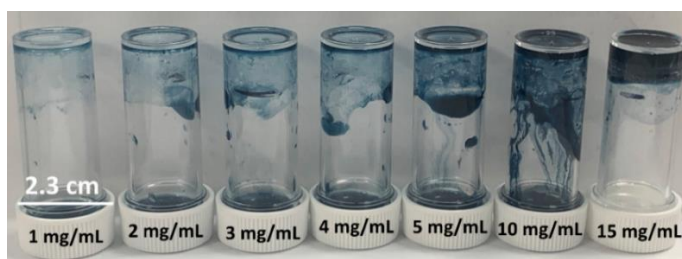


Figure 4.25. Determining the mgc from photographs of samples prepared using different concentrations of **PBI-V-1** on the addition of GdL.

Since it was observed that all of the core-substituted PBIs could form invertible samples when the solutions were at a concentration of 15 mg/mL with 8 mg/mL of GdL, this concentration was used for further gelation studies. This concentration also showed the smallest amount of syneresis compared to the other concentrations. For rheological measurements, the vial inner walls were again sanded. Figure 4.26 shows photographs of the GdL-triggered hydrogels of the three PBIs in sanded vials.

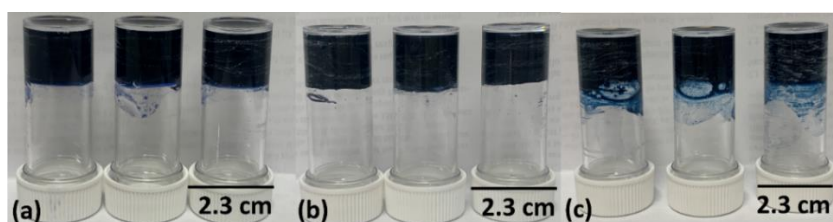


Figure 4.26. Photographs of inverted 7 mL Sterilin vials with sanded inner walls containing GdL-triggered hydrogels of (a) **PBI-L-1**, (b) **PBI-A-1**, and (c) **PBI-V-1** made using solutions at 15 mg/mL with a final pH of 3.4.

The bulk mechanical properties of the hydrogels were determined by measuring the strain and frequency sweeps which are shown in Figure 4.27 (a) and (b). The results

from these measurements are summarised in Table 4.10. For the core-substituted gels, **PBI-A-1** is stiffer than **PBI-L-1**, which is in turn stiffer than **PBI-V-1**. The trend is seen clearly in the strain and frequency sweeps. This trend is not surprising as the **PBI-V-1** hydrogels are just at their mgc compared to the other core-substituted PBIs which are above their mgcs.

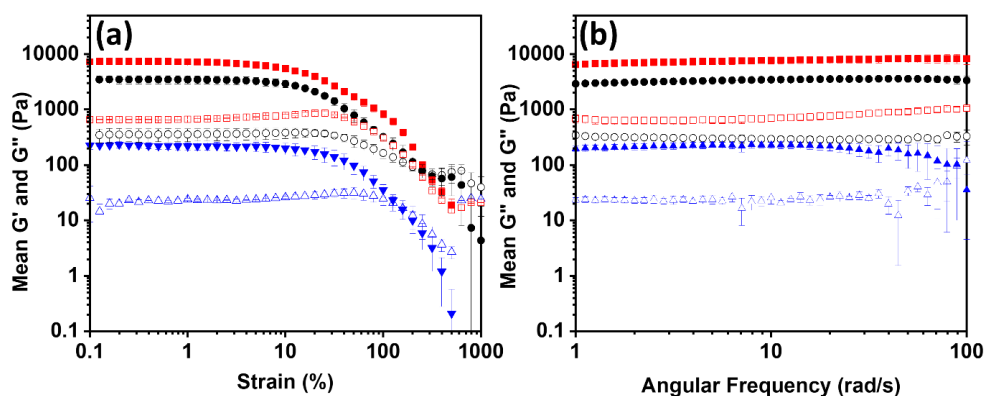


Figure 4.27. (a) Strain sweep data at 10 rad/s and (b) frequency sweep data at 0.5% strain for **PBI-L-1** (black), **PBI-A-1** (red), and **PBI-V-1** (blue). In all cases, the storage modulus (G') is represented by the closed symbols and the loss modulus (G'') is represented by open symbols. Measurements were performed in triplicate and errors were calculated from the standard deviation.

All the core-substituted PBIs show frequency-independent behaviour, suggesting these are ‘true’ gels. The strain sweeps show that the strongest hydrogels are **PBI-L-1** (7.9%), then **PBI-V-1** (6.3%), and finally **PBI-A-1** (5.0%), these strengths are low for LMWGs. The flow points (the point at which the sample begins to flow) follow the same trend as the stiffness of the hydrogels with **PBI-A-1** having the highest flow point and **PBI-V-1** the lowest.

Table 4.10. Key bulk mechanical properties of the hydrogels with **PBI-L-1**, **PBI-A-1**, and **PBI-V-1**. G' and G'' are taken at 10 rad/s frequency.

PBI	L-1	A-1	V-1
G' (Pa)	3400 ± 210	7700 ± 1100	230 ± 28
G'' (Pa)	290 ± 27	690 ± 95	25 ± 5.9
Yield point (%)	7.9	5.0	6.3
Flow point (%)	320	490	160
$\tan \delta$ (G''/G')	0.085	0.089	0.11

SAXS was used to further look at the micellar structures of the different core-substituted PBI hydrogels. Figure 4.28 shows the data for the hydrogels and the fitted models with details of the models summarised in Table 4.11. The hydrogels of **PBI-L-1** and **PBI-V-1** at 15 mg/mL could be fitted using a flexible elliptical cylinder model combined with a power law. The addition of the power law for **PBI-L-1** and **PBI-V-1** is characteristic of the increased impact of syneresis as the power law component implies an increase in segregation within the network as water is expelled.⁵⁷ Hydrogels of **PBI-A-1** at this concentration could be fitted to a flexible elliptical cylinder, like the solutions at 10 mg/mL at pH 5. **PBI-V-1** was modelled with a polydispersity on the radius to achieve the best fit. Polydispersity is applied to fit systems that do not have monodisperse structures. SAXS also showed that the size parameters of the cylinder structures for **PBI-V-1** were vastly different than those of the other two core-substituted PBIs, with **PBI-V-1** having the largest Kuhn length, cylinder radius, and axis ratio. These differences may explain the bulk rheological properties. However, it is difficult to make a direct correlation between the SAXS and rheology because the SAXS only looks at the fibre structures and not the network as a whole.

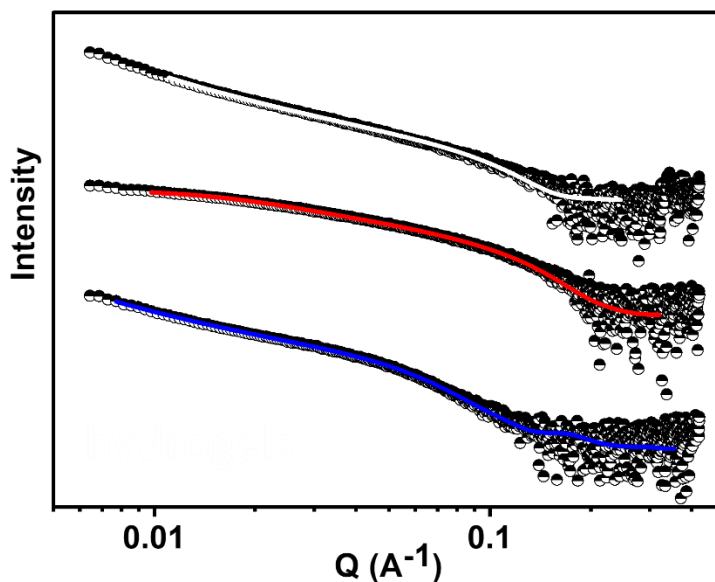


Figure 4.28. SAXS data for hydrogels of **PBI-L-1** (white), **PBI-A-1** (red), and **PBI-V-1** (blue) made using solutions at 15 mg/mL with a final pH of 3.4, with experimental data shown as open symbols and fits as solid lines. Note the data are offset on the intensity scale for clarity.

Table 4.11. SAXS fit table for **PBI-L-1**, **PBI-A-1**, and **PBI-V-1** hydrogels. *No fitting error available.

PBI	L-1	A-1	V-1
<i>Model</i>	<i>Flexible elliptical cylinder + power law</i>	<i>Flexible elliptical cylinder</i>	<i>Flexible elliptical cylinder + power law polydispersity 0.3</i>
<i>Length (nm)</i>	109 ± 1.96	70.0 ± 0.547	300*
<i>Kuhn length (nm)</i>	5.55 ± 0.0827	6.32 ± 0.101	21.8 ± 1.99
<i>Cylinder radius (nm)</i>	1.81 ± 0.00417	1.43 ± 0.00433	2.77 ± 0.0169
<i>Axis ratio</i>	1.59 ± 0.00747	1.70 ± 0.0411	1.85 ± 0.0236
<i>Power law</i>	3.77 ± 0.00115	N/A	3.39 ± 0.0471
χ^2	4.7	3.6	4.6

As there was a difference in the gel structures formed by the core-substituted PBIs, their ability to produce the radical cation was investigated. The hydrogels were photographed before and after being irradiated for 60 minutes with a 365 nm LED and are shown in Figure 4.29. As the concentration of the hydrogels is 15 mg/mL, they are a very dark blue colour to begin with, making it more difficult to see any colour change. However, for **PBI-L-1**, the photographs show that there is an initial crack in the hydrogel due to syneresis while gelling. After being irradiated, this crack became larger due to the gel syneresing further. This could either be due to a further change in pH or due to a change in temperature caused by irradiation.

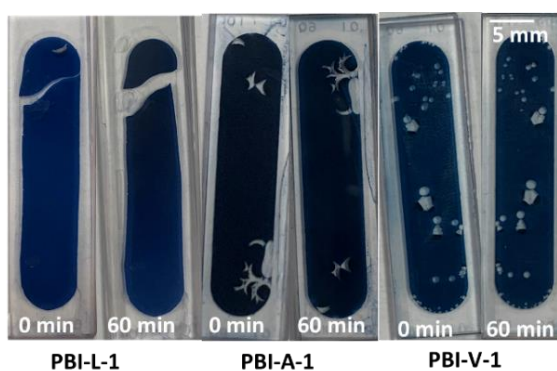


Figure 4.29. Photographs of the three core-substituted PBIs as hydrogels in 0.1 mm cuvettes before and after being irradiated using a 365 nm LED for 60 minutes.

As the colour change was difficult to observe by eye, the UV-vis absorption spectra of the hydrogels were collected before and after irradiation. Figure 4.30 (a) to (c) shows

the UV-vis absorption spectra for the core-substituted PBIs as hydrogels. The pre-irradiation spectra of the hydrogels are similar in shape to those of the solutions at pH 7 and there are no changes in the ratio of the main 595 nm and 730 nm peaks. This agrees with UV-vis absorption spectroscopy and SAXS which showed there are some already self-assembled structures in solution. Upon irradiation, the UV-vis absorption spectra of the core-substituted PBIs do not appear to change. There is no decrease in the absorbance at 730 nm or increase in the absorbances at 505 nm and 655 nm, as was seen in solution. Only for **PBI-L-1**, Figure 4.30 (a), after being irradiated for 60 minutes, does the absorbance spectrum show any changes as the peak at 655 nm appears to increase. However, this could be due to the gel shrinking and the network shifting. UV-vis absorption spectroscopy suggests that the core-substituted PBIs cannot photochemically form the radical cation or dication. This can be explained by the increased concentration used to form hydrogels as well as a reduced ability of the PBIs to form radical cation when the pH is lowered due to the change in aggregation and increased packing causing a self-quenching, which links to pervious reports.^{49, 58,}

59

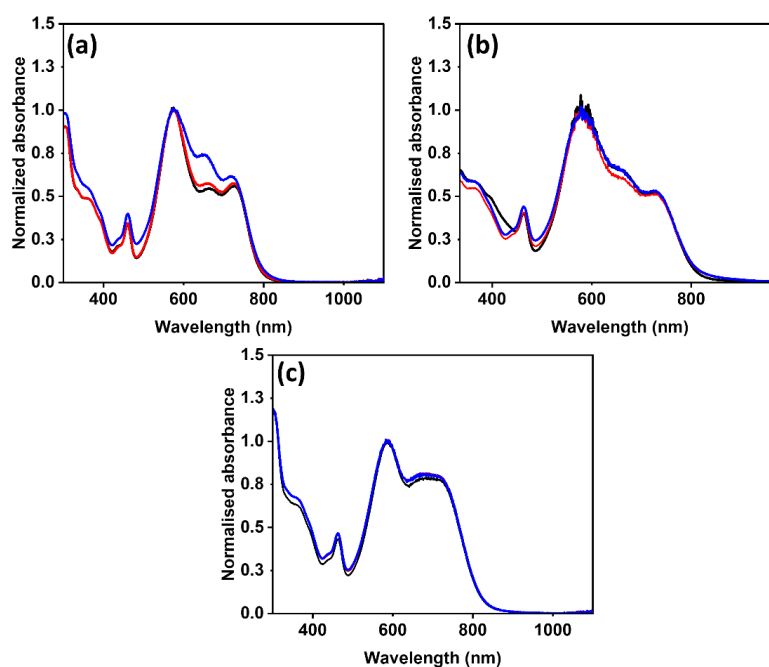


Figure 4.30. UV-vis absorption spectra for (a) **PBI-L-1**, (b) **PBI-A-1**, and (c) **PBI-V-1** hydrogels pre-irradiation (**black**), after being irradiated for 30 minutes (**red**), and after being irradiated for 60 minutes (**blue**) with a 365 nm LED.

The impact of aggregation of the hydrogel at a low pH on the formation of radical cation is further confirmed by EPR spectroscopy, Figure 4.31 (a) to (c). Here it was observed for all three core-substituted PBIs as hydrogels that upon irradiation there is no significant change in EPR signal for the radical cation. The dication is EPR-silent and it may be thought that the hydrogels prefer to form the dication instead of cation when in a gel state. However, since there are also no changes in the UV-vis spectra for any of the core-substituted PBIs after irradiation, it is more likely that neither radical cation nor dication are formed. This highlights the impact that changes in the self-assembled structures have on the radical formation properties of PBIs. The impact on the hydrogel's network on the ability of the PBIs to form radical cation / dication could be investigated further by growing a hydrogel in the spectroelectrochemical kit and oxidizing it electrochemically.

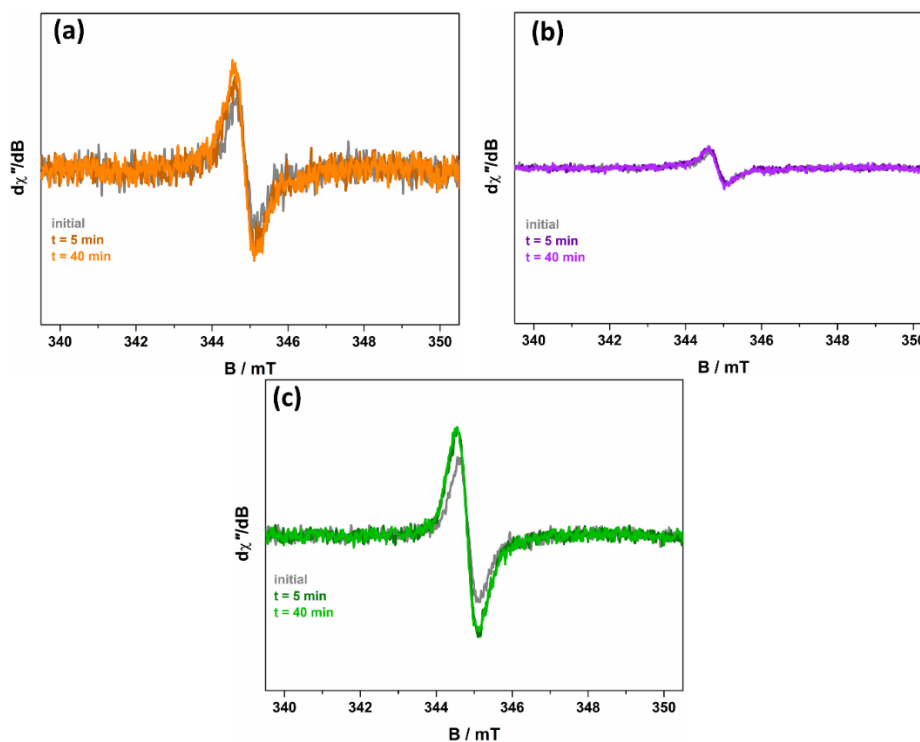


Figure 4.31. EPR signal measured for hydrogels before irradiation, and after irradiation for 5 minutes and 40 minutes with a 365 nm LED. (a) **PBI-L-1** (orange), (b) **PBI-A-1** (purple), and (c) **PBI-V-1** (green). Data collected by Dr Stephen Sproules.

4.3. Conclusions

In conclusion, three new core-substituted PBIs with different amino acid groups at the imide position were synthesised. These new materials could be solubilised in aqueous media by the addition of base which has never been reported for these systems before. Again, opening up the door for new PBI materials that can be incorporated into photovoltaic devices using greener solution processing methods which are favourable for commercialisation. The added electron density from the pyrrolidine groups resulted in absorption over a wide range of the red region of the visible spectrum resulting in a blue colour. This also led to a shift in the oxidation potentials and smaller band gap energies.

There are very limited reports of the radical cations and dications of PBIs and this work attempted to explore them in more detail both in terms of their optical properties and their impact on packing. Upon irradiation with UV light there was a change UV-vis absorbance spectra which was believed to be due to the formation of a mixture of radical cation and dication in solution. The spectroelectrochemistry showed that the changes are likely due to the formation of radical cation. EPR spectroscopy showed a difference in radical cation formation for the different core-substituted PBIs like a trend previously reported for the radical anion seen in this thesis. As the amino acid side chain decreased in size the radical formation increases presumably due to differences in packing of the structure across the various length scales. The packing in the self-assembled nanostructures as the radical cation and dication is formed were investigated as well to see if there was a link between radical formation and more favourable radical formation as was done in previous chapters. The SAXS showed **PBI-A-1** which formed the most radical cation had a spherical morphology whereas **PBI-L-1** and **PBI-V-1** which were assembled into larger fibrous structures formed less.

The choice of amino acid functional group for the core substituted PBIs can be used to change how the self-assembled structures were influenced by pH as well as radical formation. This agrees with what was seen in the previous chapter for the core unsubstituted PBIs. Showing a trend that can be used to set new chemical structure parameters for PBIs to impact their radical formation and their hydrogel properties. The PBIs were used to make hydrogels using a pH trigger for the first time, however,

the hydrogels were prone to syneresis. The hydrogels were irradiated but did not show the same changes in the UV-vis absorbance spectra as the solutions. This could be due to a higher concentration used as well as the pH needed to make the hydrogels.

4.4. Experimental

4.4.1 Materials and synthetic procedures

All chemicals were purchased from Merck Life Science or Alfa Aesar and used without further purification. Deionised water was used throughout.

To the best of our knowledge, all the core-substituted PBI-amino acid compounds that were synthesised have not been previously reported. The synthesis was based on a procedure that has been published for similar systems.^{24, 60}

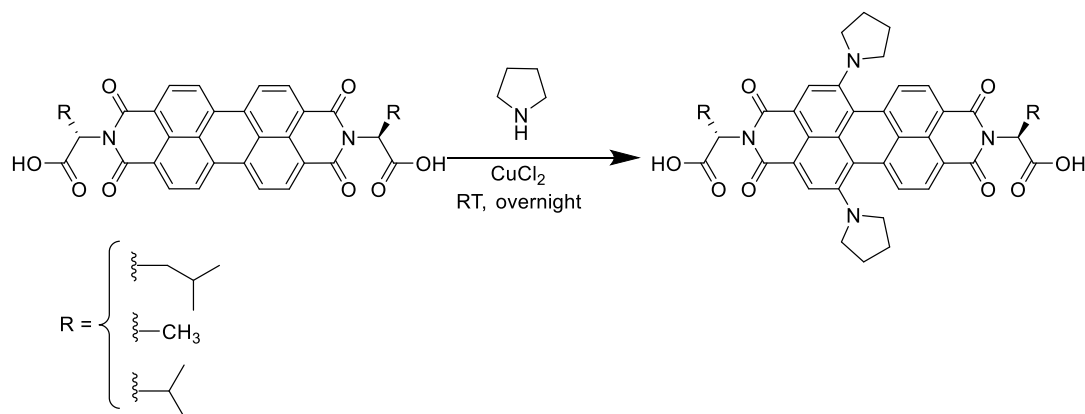


Figure 4.35. General reaction scheme for bay substitution of amino acid-substituted PBIs.

In a 250 mL round-bottom flask, 1 equiv. of copper(II) chloride was added to 200 equiv. of pyrrolidine followed by 1 equiv. of the desired amino acid-substituted PBI. The reaction was allowed to stir overnight at room temperature under air and was considered complete when the red colour had changed to blue. The reaction was quenched by immersing the flask in an ice bath and slowly adding 2 M HCl (approx. 0.75 mL/mmol pyrrolidine). The mixture was then boiled for several hours to help remove residual pyrrolidine. The suspension was gravity-filtered and allowed to air-dry overnight. Once dry, it was put into a 50 mL flask with 15 mL of methanol and sonicated for 15 minutes then filtered to remove any mono-substituted material. The

methanol wash was repeated once more, then the product was allowed to dry in air overnight. The NMRs were measured by dissolving 2 mg of sample in 1 mL of DMSO-*d*₆ and 2 μL of trifluoroacetic acid (TFA). The TFA was added to improve the solubility by acting as an ion pairing agent to help disrupt the π-π stacking. For the ¹³C-NMR there is very poor resolution of the perylene core due to aggregation and the sample was heated to 80°C to improve solubility further.

N, N'-Di(L-leucine)-13-di-1-pyrrolidinylanthra[2,1,9-def:6,5,10-d'ef']-perylene-3,4:9,10-tetracarboxylic acid bisimide (**PBI-L-1**)

Yield (0.966 g, 65%) ¹H-NMR (500 MHz, DMSO-*d*₆, 25°C) δ (ppm) = 8.44 (s, 2H), 8.09 (s, 2H), 7.37 (s, 2H), 5.66 (m, 2H), 2.12 (m, 4H), 1.87 (s, 4H), 1.51 (m, 2H), 0.97 (t, J = 4.0 Hz, 6H), 0.89 (t, J = 4.0 Hz, 6H).

¹³C-NMR (125 MHz, DMSO-*d*₆, 80°C) δ (ppm) = 171.85 (COOH); 158.8 (C=O); 150.2 (C-N); 135.8, 130.8, 123.4, 117.9, 116.8 (perylene core); 52.3 (CH₂); 51.7 (CH); 38.4 (CH₂); 25.6 (CH₂); 23.4 (CH); 22.4 (CH₃).

FT-IR: ν/cm⁻¹ 3488b (O-H), 1677m (tertiary amine), 1572s (C=O), 1339s (C-O), 1110m (C-O), 795m (aromatic C-H), 743m (aromatic C-H).

HR-ESI-TOF MS: calculated 757.3238 Da for [C₄₄H₄₅N₄O₈]⁺, found 757.3239 Da

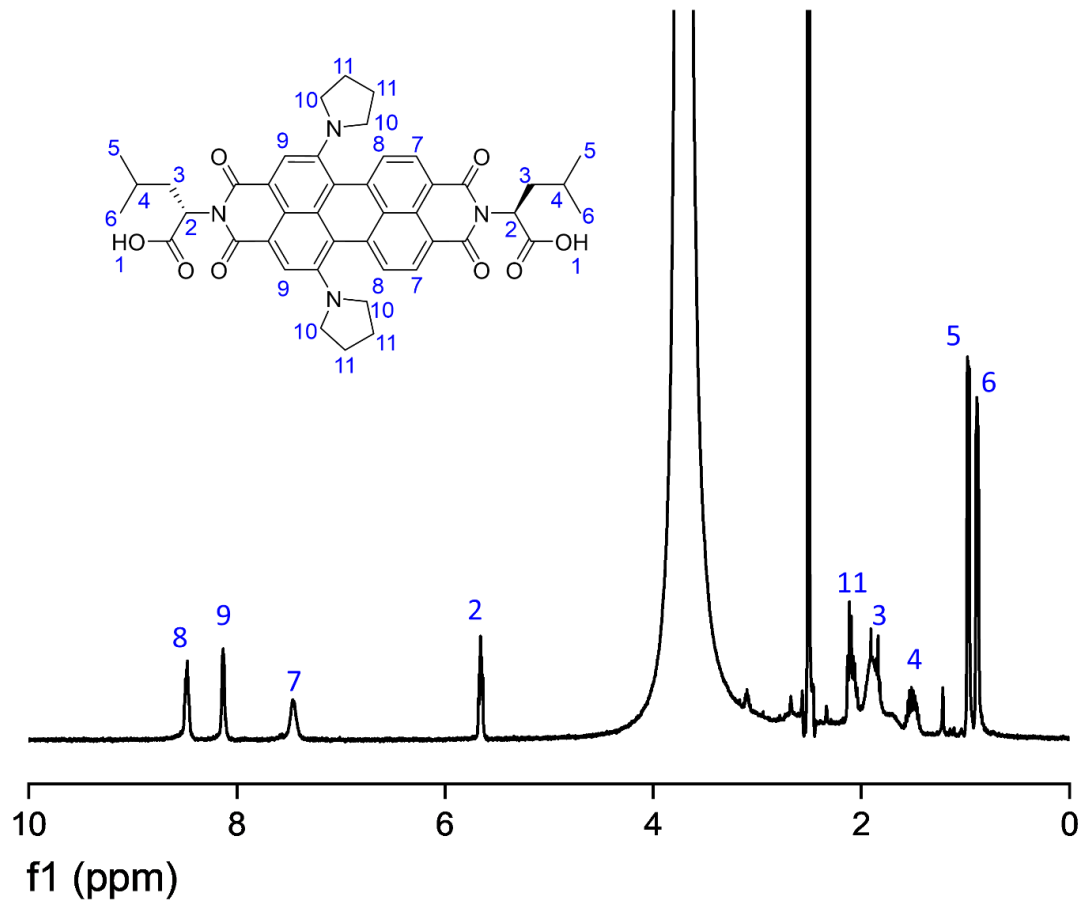


Figure 4.36. ¹H-NMR spectrum of **PBI-L-1** in DMSO-d₆+TFA at 25°C.

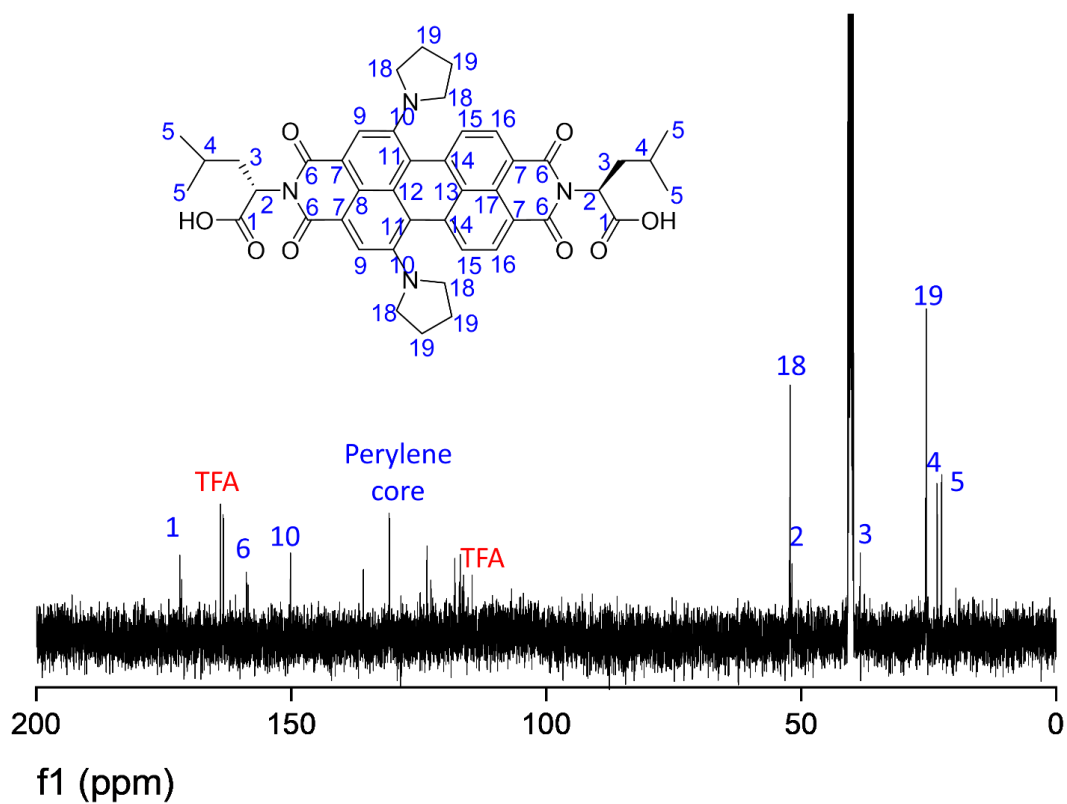


Figure 4.37. ^{13}C -NMR spectrum of **PBI-L-1** in $\text{DMSO-}d_6$ +TFA at 80°C .

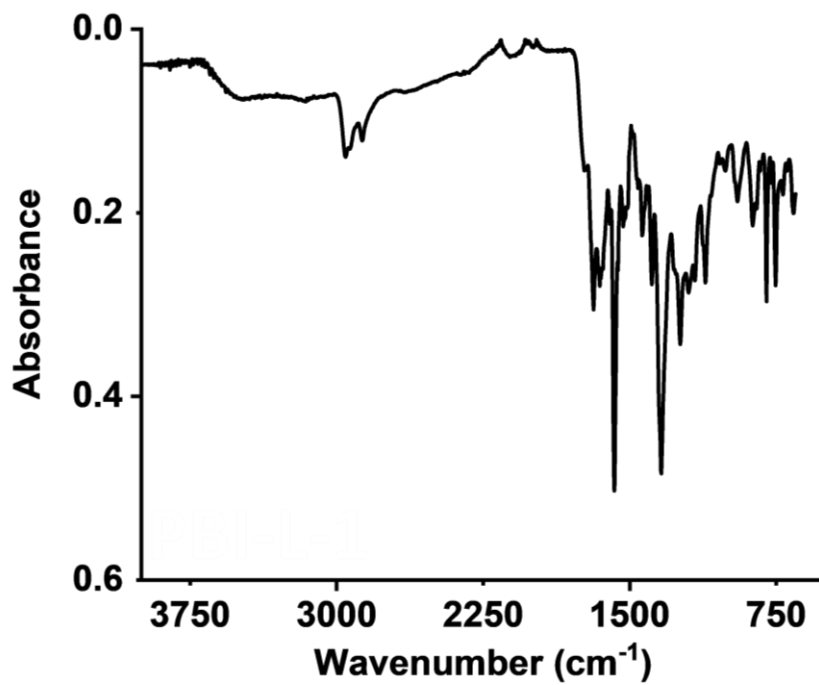


Figure 4.38. Powder FTIR spectrum of **PBI-L-1**.

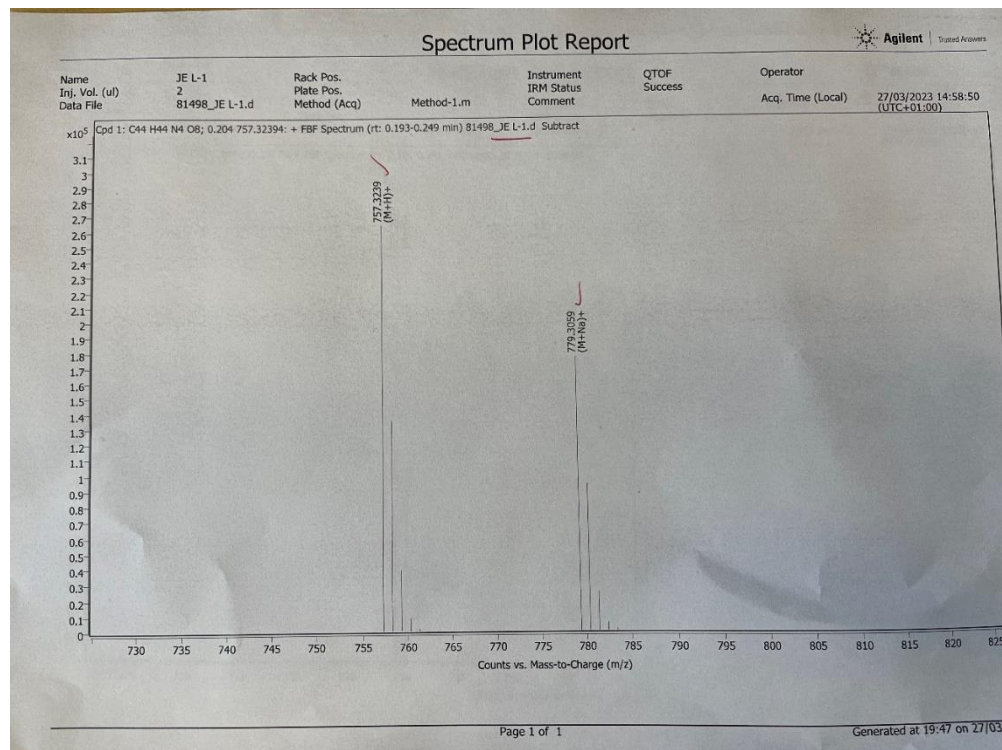


Figure 4.39. Mass spectrum of **PBI-L-1** in chloroform.

N, N'-Di(L-alanine)-13-di-1-pyrrolidinylanthra[2,1,9-def:6,5,10-d'e'f']-perylene-3,4:9,10-tetracarboxylic acid bisimide (**PBI-A-1**)

Yield (1.12 g, 55%) $^1\text{H-NMR}$ (500 MHz, $\text{DMSO-}d_6$, 25°C) δ (ppm) = 8.44 (s, 2H), 8.08 (s, 2H), 7.38 (s, 2H), 5.66 (m, 2H), 1.91 (s, 8H), 1.62 (d, $J = 4.0$ Hz, 3H), 1.55 (d, $J = 4.0$ Hz, 3H).

$^{13}\text{C-NMR}$ (125 MHz, $\text{DMSO-}d_6$, 80°C) δ (ppm) = 171.8 (COOH); 163.5 (C=O); 158.7 (C-N); 135.8, 130.6, 122.8, 117.8, 116.7, 114.5 (perylene core); 52.1 (CH_2); 48.9 (CH); 25.4 (CH_2); 15.0 (CH_3).

FT-IR: ν/cm^{-1} 3436b (O-H), 1669m (tertiary amine), 1574m (C=O), 1312m (C-O), 969w (C-O), 805w (aromatic C-H), 745w (aromatic C-H).

HR-ESI-TOF MS: calculated 673.2279 Da for $[\text{C}_{38}\text{H}_{33}\text{N}_4\text{O}_8]^+$, found 673.2299 Da

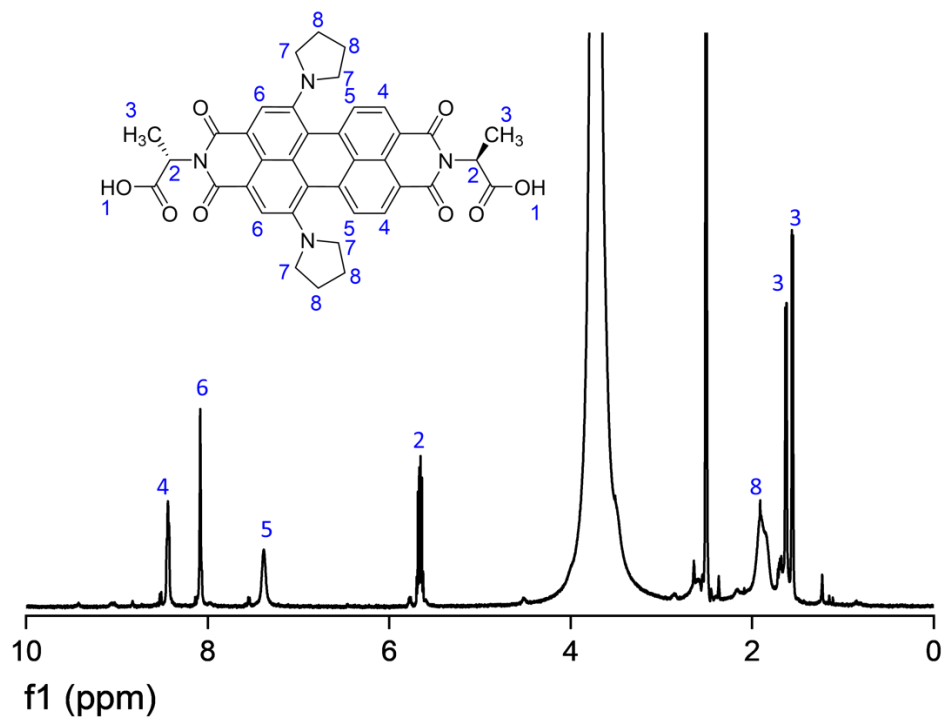


Figure 4.40. ¹H-NMR spectrum of **PBI-A-1** in DMSO-*d*₆+TFA at 25°C.

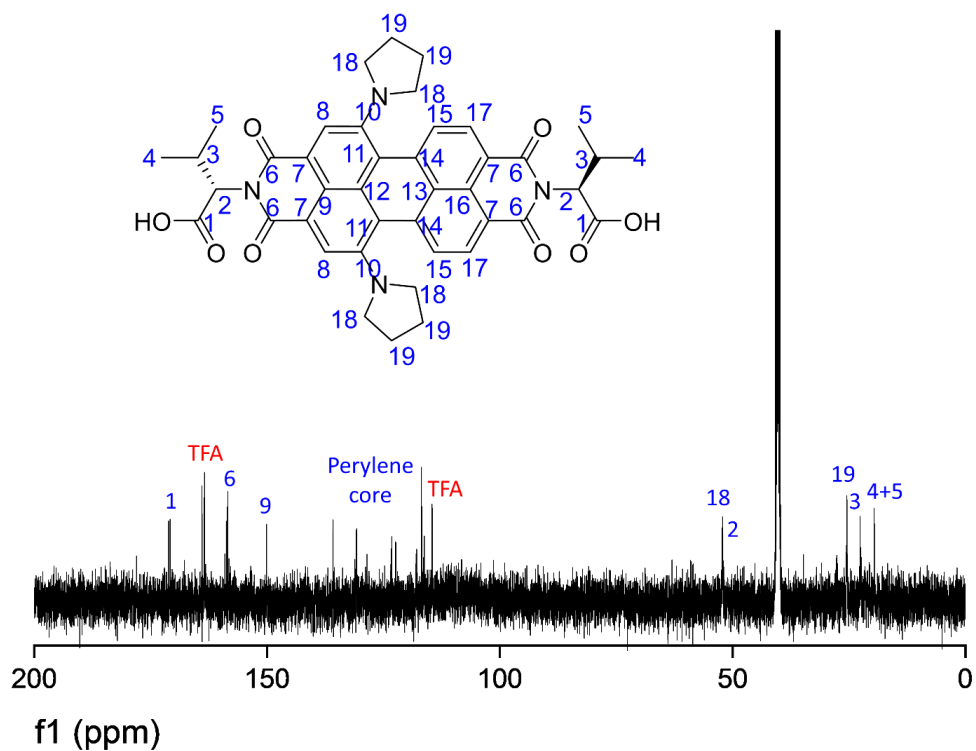


Figure 4.41. ¹³C-NMR spectrum of **PBI-A-1** in DMSO-*d*₆+TFA at 80°C.

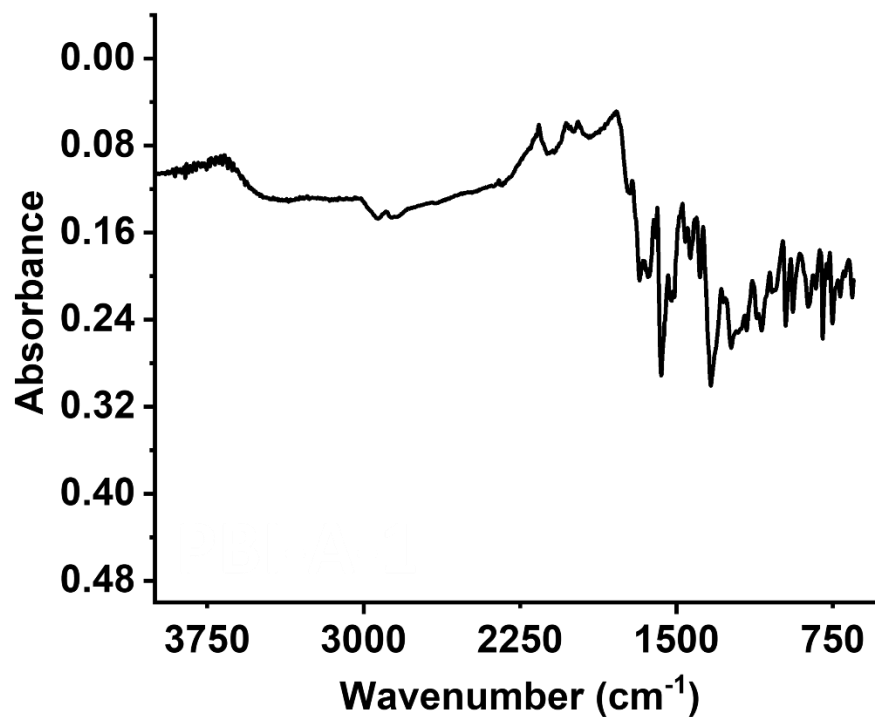


Figure 4.42. Powder FTIR spectrum of **PBI-A-1**.

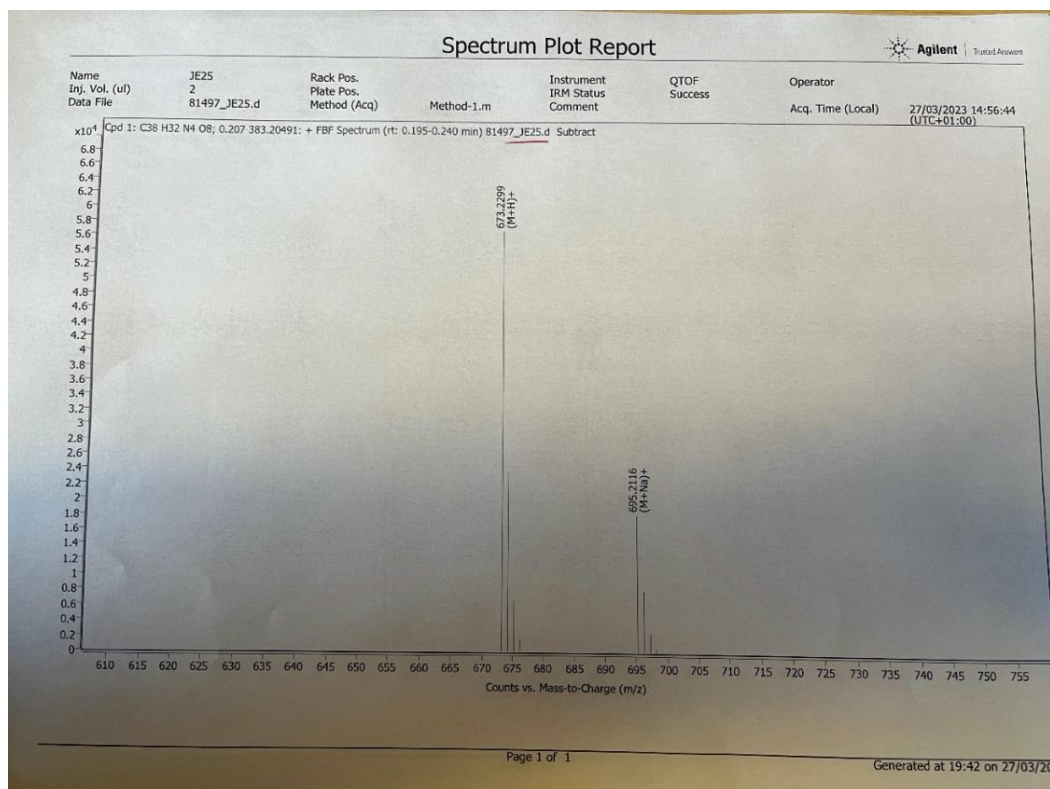


Figure 4.43. High resolution mass spectrum of **PBI-A-1** in chloroform.

N, N'-Di(*L*-valine)-13-di-1-pyrrolidinylanthra[2,1,9-def:6,5,10-d'e'f']-perylene-3,4:9,10-tetracarboxylic acid bisimide (**PBI-V-1**)

Yield (0.983 g, 61%) $^1\text{H-NMR}$ (500 MHz, $\text{DMSO-}d_6$ + TFA, 25°C) δ (ppm) = 8.51 (s, 2H), 8.17 (s, 2H), 7.52 (s, 2H), 5.22 (td, $J = 4.0, 8.0$ Hz, 2H), 2.74 (m, 2H), 1.95 (m, 8H), 1.26 (dd, $J = 4.0, 8.0$ Hz, 6H), 0.73 (dd, $J = 8.0, 16.0$ Hz, 6H).

$^{13}\text{C-NMR}$ (125 MHz, $\text{DMSO-}d_6$ + TFA, 80°C) δ (ppm) = 171.2 (COOH); 164.0 (C=O); 158.5 (C-N); 150.1(C); 135.8, 130.7, 123.2, 122.3, 116.2, 116.0, 114.5 (perylene core); 52.2 (CH₂); 25.5 (CH₂); 22.6 (CH); 19.5 (CH₃).

FT-IR: ν/cm^{-1} 3470b (O-H), 1686m (tertiary amine), 1589s (C=O), 1347s (C-O), 941m (C-O), 808m (aromatic C-H), 747m (aromatic C-H).

HR-ESI-TOF MS: calculated 729.2825 Da for $[\text{C}_{42}\text{H}_{41}\text{N}_4\text{O}_8]^+$, found 729.2927 Da.

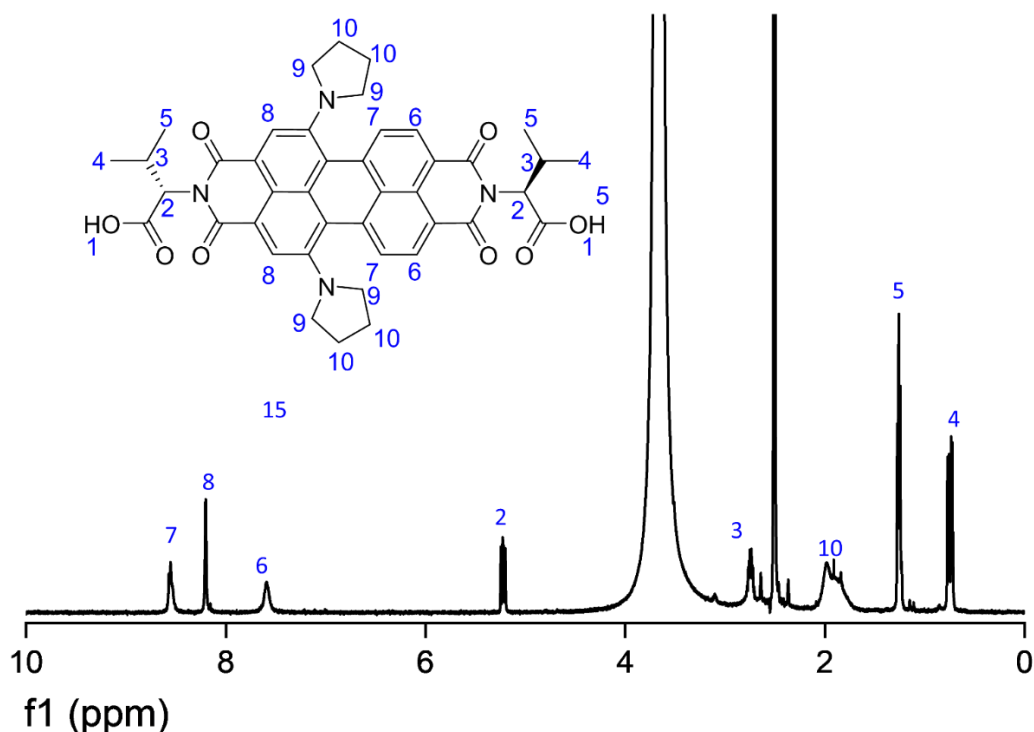


Figure 4.44. $^1\text{H-NMR}$ spectrum of **PBI-V-1** in $\text{DMSO-}d_6$ +TFA at 25°C .

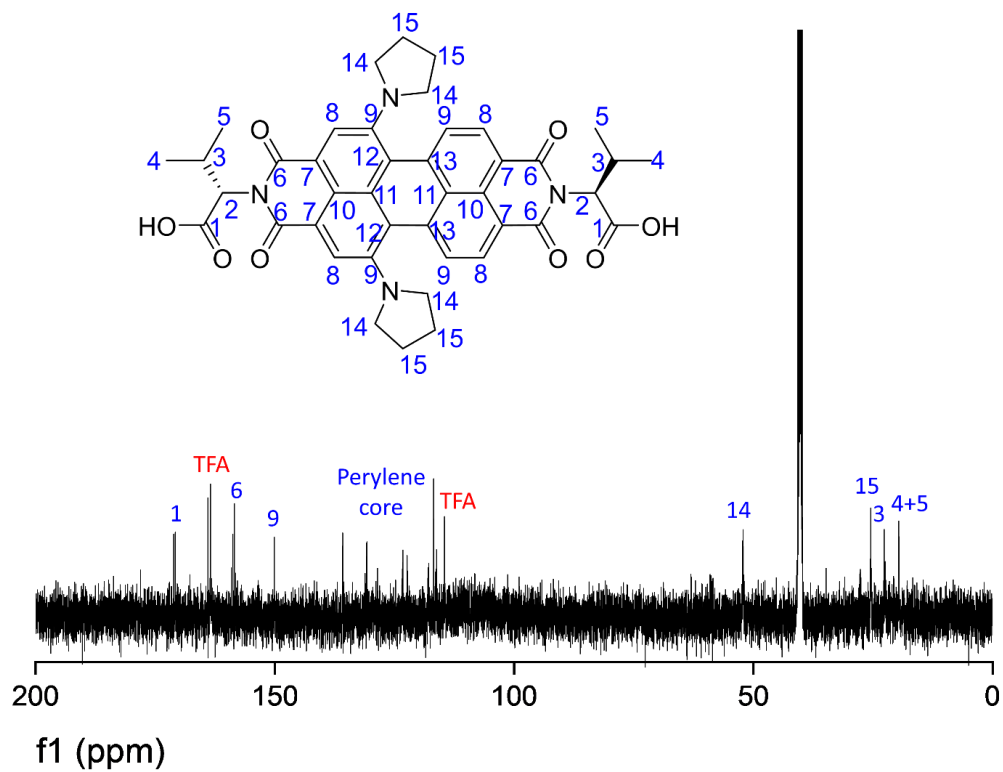


Figure 4.45. ^{13}C -NMR spectrum of **PBI-V-1** in $\text{DMSO-}d_6$ +TFA at 80°C .

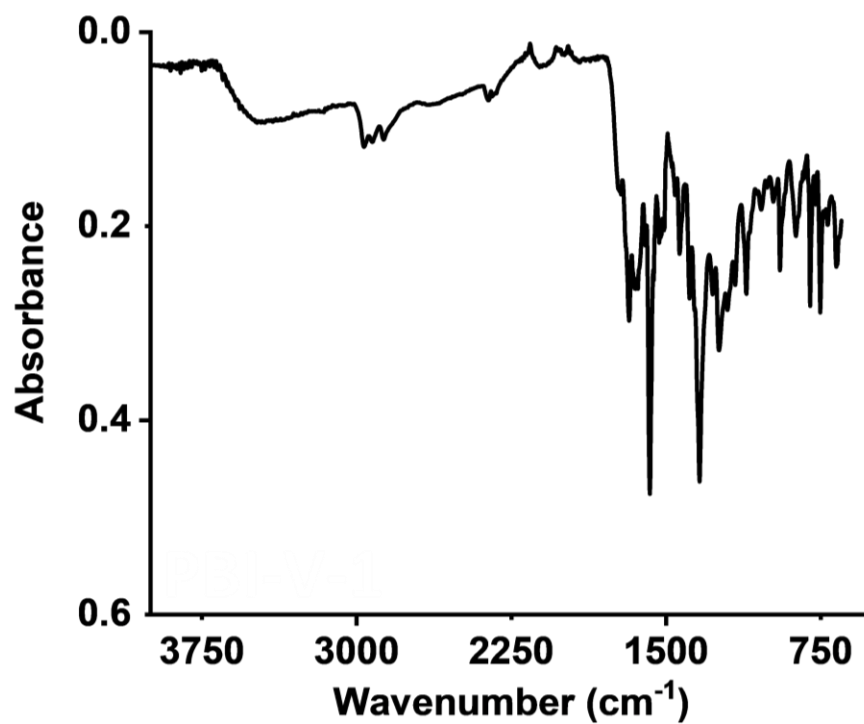


Figure 4.46. Powder FTIR spectrum of **PBI-V-1**.

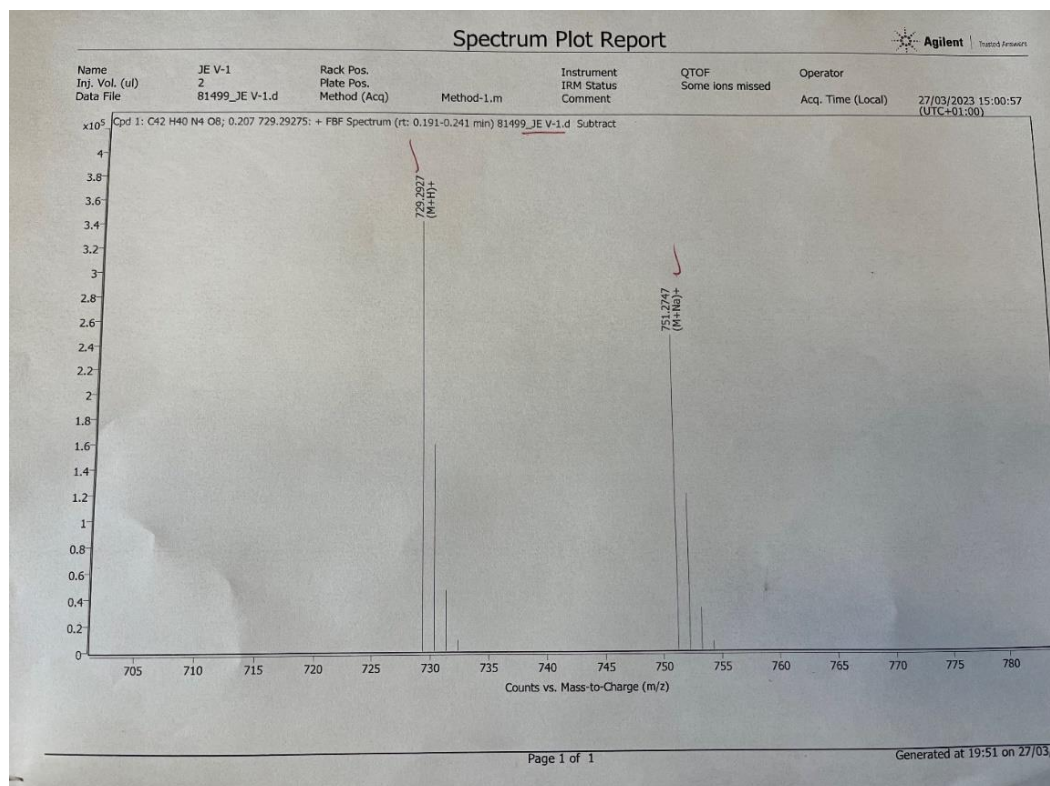


Figure 4.47. Mass spectrum of **PBI-V-1** in chloroform.

4.4.2. Methods

4.4.2.1 Characterisation of PBIs

All the nuclear magnetic resonance (NMR) spectra were collected using a Bruker DPX-500 spectrometer operating at 500 MHz for ^1H -NMR and 125 MHz for ^{13}C -NMR in d_6 -DMSO with 2 μL of TFA. Infrared (IR) spectra were collected using a Thermo Nicolet Is5 (Diamond ATR attachment). The spectra were recorded at 64 scans and a resolution of 4 cm^{-1} . The background was of the empty ATR crystal and spectra were recorded of the PBIs as solid powders. Mass spectrometry was performed using a Bruker MicroTOF mass spectrometer using electrospray ionisation (MS-ESI).

4.4.2.2 Preparation of PBI solutions

Solutions were prepared at a concentration of 10 mg/mL of PBI unless otherwise stated. For the preparation of 5 mL of solution, 50 mg of PBI was weighed into a vial. One molar equivalent of sodium hydroxide (0.1 M, aqueous) was added to the PBI,

and the solution was made up to 5 mL with deionised water. The solution was stirred for at least 16 hours to allow all the PBI to dissolve. A large stock solution of each PBI was prepared to ensure that the solutions were the same for each experiment. The pH of each vial was adjusted as necessary using 2 M HCl or 2 M NaOH to obtain the desired pH. Preparation of all samples was carried out at room temperature (around 25°C in the daytime).

4.4.2.3 Preparation of PBI hydrogels

For mgc determination, hydrogels were formed using a pH switch from solutions at concentrations ranging from 1 mg/mL to 15 mg/mL. Solutions at these concentrations were prepared using the procedure described above. To minimise the impact of syneresis, the inner walls of the 7 mL Sterilin vials were sanded from vial bottom to a height of 0.75 cm using a DiiDa multifunctional polishing tool with a small cylindrical bit on the lowest speed. An appropriate amount of glucono- δ -lactone (GdL), 3 mg/mL to 8 mg/mL, was added to the sanded vials and 1 mL of solution at the desired concentration was transferred to it and the vial was shaken gently. This was left to stand for at least 16 hours to allow for gelation to occur.

Hydrogels for bulk rheological measurements were formed using a pH switch from a solution at 15 mg/mL gelator concentration. The inner walls of 7 mL Sterilin vials were sanded from vial bottom to a height of 1.5 cm as described above. 8 mg/mL of GdL and 2 mL of gelator solution were then transferred into the vials and shaken gently. The vials were left to stand for at least 16 hours to allow for gelation to occur. The samples that were stable to vial inversion after 16 hours were rheologically tested to confirm gelation.

4.4.2.4 UV-vis absorption spectroscopy measurements

All UV-vis absorption spectra were measured using an Agilent Cary 60 spectrometer. For the initial spectra of the PBIs in solution, the samples were made by taking a stock solution of the PBIs with a concentration of 10 mg/mL at pH 7, placing them in a 0.01 mm cuvette, and measuring between 200 nm and 1100 nm on the 600 nm/min scan rate.

For irradiation studies, the following LEDs were chosen, all powered by the same 700 mA constant-current power source: 365 nm, 490 nm, 590 nm, and 740 nm (LedEngin Inc). These wavelengths were chosen based on the PBIs' pre-irradiation UV-vis absorption bands. The power hitting the sample over an area of 225 cm² was measured using a ThorLabs PM100D optical power meter with a ThorLabs S120VC 200-1100 nm 50 mW photodiode detector. The details of the LED used, power hitting the sample, and the number of photons hitting the sample are summarised below in Table 4.12.

Table 4.12. *Summary of irradiation studies.*

Wavelength (nm)	Power hitting the sample	Number of photons hitting the sample after 30 minutes / area
365	21.6 mW	3.17×10 ¹⁷ photons/cm ²
490	4.91 mW	9.69×10 ¹⁶ photons/cm ²
590	4.28 mW	1.03×10 ¹⁷ photons/cm ²
740	3.38 mW	1.00×10 ¹⁷ photons/cm ²

The UV-vis absorption spectra of the PBIs at different pHs were measured by taking a stock solution of PBI with a concentration of 10 mg/mL and distributing aliquots to five 7 mL Sterilin vials. The pH of each vial was adjusted as necessary using 2 M HCl or 2 M NaOH.

For UV-vis absorption spectroscopy of hydrogels, the samples were prepared by adding 2 mL of 15 mg/mL PBI stock solutions to 8 mg/mL of GdL in 7 mL Sterilin vials and gently swirling until complete dissolution of the GdL. 0.5 mL of these solutions was pipetted into 0.1 mm demountable cuvettes which were then parafilm and left to stand for at least 16 hours to allow for gelation to occur. Absorption was measured between 200 nm and 1100 nm on the 600 nm/min scan rate.

4.4.2.5 Rheological measurements of the irradiated samples

Dynamic viscosity measurements after being irradiated were performed using an Anton Paar Physica MCR302 rheometer with a 365 nm LED held in place under the quartz bottom plate using a bespoke 3D-printed holder. Figure 4.48 shows the setup of the MCR302 with the 365 nm LED in place.

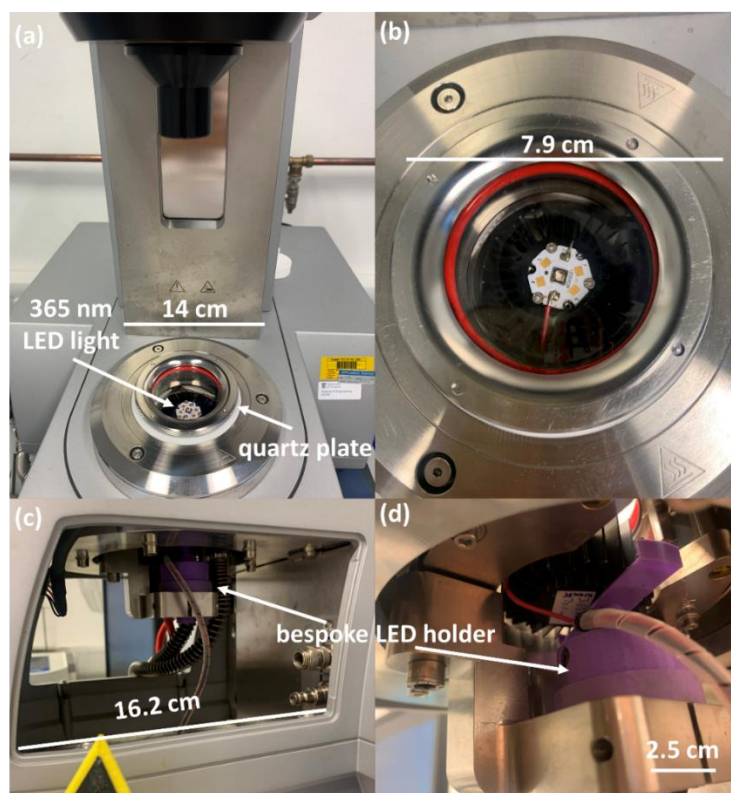


Figure 4.48. (a) and (b) Anton Paar Physica MCR302 rheometer set up with a 365 nm LED powered by a constant-current power source. (c) and (d) bespoke 3D-printed LED holder placed inside of Anton Paar Physica MCR302 rheometer with a 365 nm LED.

Viscosity data were collected using a 50 mm cone (cone angle 0.994°) geometry and temperature-controlled bottom plate. The samples were irradiated using the method described for the UV-vis absorption spectroscopy measurements.

Dynamic viscosity measurements after irradiation: a 1 mL aliquot of PBI solution was pipetted onto the quartz bottom plate. The top plate was lowered on top of the solution to a gap height of 0.1 mm which is determined for the cone angle on the plate. Any excess sample was trimmed away with a small edge of a paper towel ensuring no gaps or bubbles along the edge of the plate. A CP50 plate geometry was used to measure the viscosity. Measurements were recorded at a shear rate from 0.1 to 100% and performed in triplicate. Errors were calculated from the standard deviation.

After viscosity measurement of the initial solution, the 365 nm LED was switched on for 30 minutes. After 30 minutes the light was switched off and another viscosity measurement was run. This procedure was repeated for another 30 minutes for a total irradiation time of 60 minutes.

4.4.2.6 Square wave voltammetry measurements (SWV)

SWVs for the solutions were collected using a three-electrode system and a PalmSens4 potentiostat with a glassy carbon working electrode, a Pt wire counter electrode and an Ag/AgCl reference electrode. The background electrolyte was 0.1 M NaCl in water. The potential was scanned from 1.5 V to -1.5 V at a frequency of 20 Hz.

Determining the experimental electron affinity (EA) / Lowest Unoccupied Molecular Orbital (LUMO) energy level vs vacuum: The reduction maximum for the first reduction potential vs Ag/AgCl was obtained from the CV data. Then the reduction was converted to vs Fc/Fc^+ using an experimental value of +0.479 V. Next the EA/LUMO energy in eV with respect to vacuum was determined using the following equation from the literature:⁶¹

$$-EA = E_{LUMO} (eV) = -[E_{red2} + 5.15eV] \quad (\text{Equation 6})$$

Determining the experimental ionisation potential (IP) / Highest Occupied Molecular Orbital (HOMO) energy level vs vacuum: The oxidation maximum for the first reduction potential vs Ag/AgCl was obtained from the CV data. The oxidation potential was converted to vs Fc/Fc^+ using an experimental value of +0.479 V. Next the IP/HOMO energy in eV with respect to vacuum was determined using the following equation from the literature:⁶¹

$$-IP = E_{HOMO} (eV) = -[E_{ox1} + 5.15eV] \quad (\text{Equation 7})$$

Calculating the E_{gap} from Tauc Plots: The E_g , were estimated from the UV-Vis absorption spectra at pH 7 using Tauc's relationship:

$$(\alpha h\nu)^{1/n} = A(h\nu - E_g) \quad (\text{Equation 8})$$

Where A is a proportionality constant, $h\nu$ is the photon energy and α the absorption coefficient. 'n' is a constant whose value depends upon the type of transition, $n = 1/2$

for direct allowed transition. The value for E_g was extrapolated from the tangent line to the $h\nu$ axis on the Tauc plots (Appendix 7).

4.4.2.7 Spectroelectrochemistry measurements

The spectroelectrochemistry was measured on an aliquot of 0.25 mL of PBI solution at 10 mg/mL diluted to 0.5 mg/mL using 2 mL of 0.1 NaCl electrolyte and 2.75 mL of DI water. This solution was transferred into a LabOmak UF spectroelectrochemical cell with a Pt gauze working electrode, a Pt gauze counter electrode, and a Pt wire reference electrode. A PalmSens4 potentiostat was connected to the spectroelectrochemical cell kit and an initial cyclic voltammogram was recorded to check connections. A UV-vis absorption spectrum was then collected for $t = 0$. The chronoamperometry experiment was then run at the desired potential over a period of 30 minutes. UV-vis absorption was measured on a cycle between 400 nm to 1100 nm on a 800 nm/min scan rate every 5 minutes for 30 minutes.

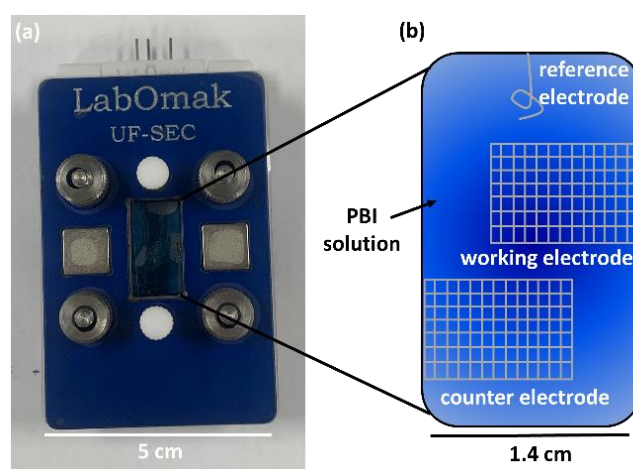


Figure 4.49. (a) Photograph of LabOmak UF-spectroelectrochemical cell with **PBI-A-1** solution after a voltage of 1 V had been applied for 30 minutes. (b) Diagram of the cell window with the different electrodes labelled.

4.4.2.8 pH measurements

pH measurements were recorded using a custom-built pH/temperature logger and a HANNA pH probe (FC200) designed specifically for gels with a given error of ± 0.1 pH units.

4.4.2.9 Apparent pK_a titrations

2 mL of PBI solution was added to a 7 mL Sterilin vial which was immersed in a water bath at a set temperature of 25°C and the probe was immersed in the solution. 5 μ L – 10 μ L aliquots of HCl (0.1M) were added to the solution and the pH recorded after the reading had stabilised. The solution was gently stirred between additions of acid to avoid any gel forming and to ensure the pH was homogeneous throughout the solution. The plateaus in the data represent the apparent pK_a values.

4.4.2.10 Rheological measurements of the solutions at different pHs and as pH-triggered hydrogels

Dynamic viscosity measurements of solutions and strain and frequency sweeps of the hydrogels were performed using an Anton Paar Physica MCR101 rheometer. Strain and frequency data were collected using a vane and cup geometry (ST10-4V-8.8/97.5) so that samples could be prepared in 7 mL Sterilin vials to remove any loading issues. Viscosity data were collected using a 50 mm cone (cone angle 0.994°) geometry and temperature-controlled bottom plate. All measurements were collected in triplicate at 25°C.

Dynamic viscosity measurements at different pHs: a 1 mL aliquot of PBI solution at the desired pH was pipetted onto the bottom plate. The top plate was lowered on top of the solution to a gap height of 0.1 mm which is determined for the cone angle of the plate. Any excess sample was trimmed using a metal spatula ensuring no gaps or bubbles along the edge of the plate. A CP50 plate geometry was used to measure the viscosity. Measurements were recorded at a shear rate from 1-1000% and performed in triplicate. Errors were calculated from the standard deviation.

Strain sweeps: strain sweeps were recorded from 0.1-1000% strain at a set frequency of 10 rad/s with a gap height of 2 mm. Samples were prepared as described previously in 7 mL Sterilin vials. Measurements were performed in triplicate and errors were calculated from the standard deviation.

Frequency sweeps: frequency scans were recorded from 1 rad/s to 100 rad/s under a constant strain of 0.5% with a gap height of 2 mm. The strain was chosen because it is in the linear viscoelastic region for the hydrogels. Samples were prepared as

described previously in 7 mL Sterilin vials. Measurements were performed in triplicate and errors were calculated from the standard deviation.

4.4.2.11 Small-angle X-ray scattering (SAXS)

Samples were measured at the University of Bath in collaboration with Dr. Adam Squires and 3rd year PhD student Wangli Liu. The SAXS was measured using a SAXSpoint 2.0 by Anton-Paar equipped with copper and molybdenum sources (1.542 Å and 0.7107 Å, 50 W) and a 2D EIGER R-series Hybrid Photon Counting (HPC) detector at room temperature. The samples were 576 cm away from the detector. The solutions in the capillaries were measured before irradiation, then the same capillary was irradiated using a 365 nm LED for up to 60 minutes using the same method described in Section 4.4.2.5. SAXS data were collected after 60 minutes of irradiation then the capillaries were left to sit overnight and SAXS was collected again. Solutions of the PBIs were made as previously described and pH-adjusted accordingly then transferred into 1.5 mm borosilicate capillaries. The capillaries were sealed using rubber electrical tubing that had been heated and molded into a lid. Hydrogels were prepared using the method described in the preparation of core-substituted PBI hydrogels in Sterilin vials then quickly transferred to the capillaries to allow them to gel overnight. SAXS was collected after the hydrogels had been allowed to sit and gelation had occurred.

The scattering length density of each material was calculated using the National Institute of Standards and Technology neutron activation and scattering calculator.⁶²

Table 4.13. Calculated scattering length density for different PBIs used.

PBI	X-ray scattering length density (\AA^{-2})
-L-1	$9.042 \cdot 10^{-6}$
-A-1	$8.912 \cdot 10^{-6}$
-V-1	$8.973 \cdot 10^{-6}$

The data were fitted to models in the SasView software package (version 5.0.3).⁶³ Various models were used to fit the data. Fitting errors are provided as \pm ; the errors were obtained from the fitting software and reported to the 0.001 nm value as any

lower was not deemed particularly accurate. Fitting the data to different spherical, shape-independent, and cylinder models was attempted to find the most suitable, starting from models with the fewest parameters, and progressing to more complex ones. A power law fit was used to capture an increase in scattering at low Q.

A model was deemed suitable based on the reduced χ^2 , with a χ^2 value below 10 being deemed suitable. Generally, the model with the lowest χ^2 was chosen unless there were regions of the fit that clearly were not representative of the data set. In some cases, single models were not suitable to achieve a good fit, indicating a co-existence of structures or a structure that could not be represented by the models in the software. In these instances, models were combined using the “Easy Sum/Multi(p1, p2) editor” in the SasView software. The combined model could then be saved and used in the same manner as any other. In the fit tables a “+” sign is used to denote where two models were combined.

4.4.2.12 Electron resonance spectroscopy (EPR)

All EPR data were recorded at X-band frequency (9.67 GHz) on a Bruker ELEXSYS E500 spectrometer equipped with an ER 4102ST-O optical transmission resonator. All measurements were collected using either 10 mg/mL solutions or 15 mg/mL hydrogels prepared as described in Section 4.4.2.5. Solutions were transferred directly into soda glass capillary tubes. Hydrogels were prepared using the method described in the preparation of PBI hydrogels in Sterilin vials with GdL then quickly transferred to the capillaries to allow to gel overnight. Capillary tubes were filled to 20 mm and sealed at one end. EPR measurements were performed by Dr Stephen Sproules.

4.5 References

1. E. R. Draper and D. J. Adams, *Chemical Communications*, 2016, **52**, 8196-8206.
2. S. Panja and D. J. Adams, *Chemical Society Reviews*, 2021, **50**, 5165-5200.
3. X. Yang, G. Zhang and D. Zhang, *Journal of Materials Chemistry*, 2012, **22**, 38-50.
4. E. R. Draper, R. Schweins, R. Akhtar, P. Groves, V. Chechik, M. A. Zwijnenburg and D. J. Adams, *Chemistry of Materials*, 2016, **28**, 6336-6341.
5. K. Liu, A. Levy, C. Liu and J.-H. Olivier, *Chemistry of Materials*, 2018, **30**, 2143-2150.
6. R. O. Marcon and S. Brochsztain, *The Journal of Physical Chemistry A*, 2009, **113**, 1747-1752.
7. L. Zhong, F. Xing, W. Shi, L. Yan, L. Xie and S. Zhu, *ACS Applied Materials & Interfaces*, 2013, **5**, 3401-3407.
8. E. R. Draper, L. J. Archibald, M. C. Nolan, R. Schweins, M. A. Zwijnenburg, S. Sproules and D. J. Adams, *Chemistry*, 2018, **24**, 4006-4010.

9. E. R. Draper, J. J. Walsh, T. O. McDonald, M. A. Zwijnenburg, P. J. Cameron, A. J. Cowan and D. J. Adams, *Journal of Materials Chemistry C*, 2014, **2**, 5570-5575.
10. S. Pluczyk, P. Zassowski, R. Rybakiewicz, R. Wielgosz, M. Zagorska, M. Lapkowski and A. Pron, *RSC Advances*, 2015, **5**, 7401-7412.
11. M. J. Ahrens, M. J. Tauber and M. R. Wasielewski, *The Journal of Organic Chemistry*, 2006, **71**, 2107-2114.
12. U. Rohr, C. Kohl, K. Müllen, A. van de Craats and J. Warman, *Journal of Materials Chemistry*, 2001, **11**, 1789-1799.
13. F. Würthner, V. Stepanenko, Z. Chen, C. R. Saha-Möller, N. Kocher and D. Stalke, *The Journal of Organic Chemistry*, 2004, **69**, 7933-7939.
14. A. Nowak-Król and F. Würthner, *Organic Chemistry Frontiers*, 2019, **6**, 1272-1318.
15. L. Rocard, A. Goujon and P. Hudhomme, *Molecules*, 2020, **25**.
16. A. Perez-Velasco, V. Gorteau and S. Matile, *Angewandte Chemie International Edition*, 2008, **47**, 921-923.
17. B. Rybtchinski, L. E. Sinks and M. R. Wasielewski, *Journal of the American Chemical Society*, 2004, **126**, 12268-12269.
18. Y. Shibano, T. Umeyama, Y. Matano, N. V. Tkachenko, H. Lemmetyinen and H. Imahori, *Organic Letters*, 2006, **8**, 4425-4428.
19. Y. Shibano, T. Umeyama, Y. Matano and H. Imahori, *Organic Letters*, 2007, **9**, 1971-1974.
20. M. Berberich, A.-M. Krause, M. Orlandi, F. Scandola and F. Würthner, *Angewandte Chemie International Edition*, 2008, **47**, 6616-6619.
21. Y. Zhao and M. R. Wasielewski, *Tetrahedron Letters*, 1999, **40**, 7047-7050.
22. L. Fan, Y. Xu and H. Tian, *Tetrahedron Letters*, 2005, **46**, 4443-4447.
23. R. K. Dubey, A. Efimov and H. Lemmetyinen, *Chemistry of Materials*, 2011, **23**, 778-788.
24. G. Rauch and S. Hoger, *Chem Commun (Camb)*, 2014, **50**, 5659-5661.
25. E. R. Draper, J. R. Lee, M. Wallace, F. Jäckel, A. J. Cowan and D. J. Adams, *Chemical Science*, 2016, **7**, 6499-6505.
26. D. McDowall, B. J. Greeves, R. Clowes, K. McAulay, A. M. Fuentes-Caparrós, L. Thomson, N. Khunti, N. Cowieson, M. C. Nolan, M. Wallace, A. I. Cooper, E. R. Draper, A. J. Cowan and D. J. Adams, *Advanced Energy Materials*, 2020, **10**.
27. J. R. Clifton and J. T. Yoke III, *Inorganic Chemistry*, 1968, **7**, 39-46.
28. D. Mackay and W. A. Waters, *Journal of the Chemical Society C: Organic*, 1966, 813-816.
29. P. Neta, P. Maruthamuthu, P. Carton and R. Fessenden, *The Journal of Physical Chemistry*, 1978, **82**, 1875-1878.
30. J. M. Mayer, *Accounts of Chemical Research*, 2011, **44**, 36-46.
31. J. Raeburn, A. Zamith Cardoso and D. J. Adams, *Chemical Society Reviews*, 2013, **42**, 5143-5156.
32. P. K. Sukul, A. Datta and S. Malik, *Chemistry – A European Journal*, 2014, **20**, 3019-3022.
33. F. Menacher and H.-A. Wagenknecht, *European Journal of Organic Chemistry*, 2011, **2011**, 4564-4570.
34. F. Würthner, C. R. Saha-Möller, B. Fimmel, S. Ogi, P. Leowanawat and D. Schmidt, *Chemical Reviews*, 2016, **116**, 962-1052.
35. D. Gutiérrez-Moreno, Á. Sastre-Santos and F. Fernández-Lázaro, *Organic Chemistry Frontiers*, 2018, **5**, 1830-1834.
36. F. Würthner, *Chemical Communications*, 2004, 1564-1579.
37. R. Renner, M. Stolte, J. Heitmüller, T. Brixner, C. Lambert and F. Würthner, *Materials Horizons*, 2022, **9**, 350-359.
38. A. Nowak-Król, K. Shoyama, M. Stolte and F. Würthner, *Chemical Communications*, 2018, **54**, 13763-13772.

39. R. O. Marcon, J. G. dos Santos, K. M. Figueiredo and S. Brochsztain, *Langmuir*, 2006, **22**, 1680-1687.
40. A. S. Lukas, Y. Zhao, S. E. Miller and M. R. Wasielewski, *The Journal of Physical Chemistry B*, 2002, **106**, 1299-1306.
41. G. Goretzki, E. S. Davies, S. P. Argent, W. Z. Alsindi, A. J. Blake, J. E. Warren, J. McMaster and N. R. Champness, *The Journal of Organic Chemistry*, 2008, **73**, 8808-8814.
42. F. D'Anna, S. Marullo, G. Lazzara, P. Vitale and R. Noto, *Chemistry – A European Journal*, 2015, **21**, 14780-14790.
43. N. Elgrishi, K. J. Rountree, B. D. McCarthy, E. S. Rountree, T. T. Eisenhart and J. L. Dempsey, *Journal of Chemical Education*, 2018, **95**, 197-206.
44. E. R. Draper, H. Su, C. Brasnett, R. J. Poole, S. Rogers, H. Cui, A. Seddon and D. J. Adams, *Angewandte Chemie*, 2017, **129**, 10603-10606.
45. B. Hammouda and D. L. Ho, *Journal of Polymer Science Part B: Polymer Physics*, 2007, **45**, 2196-2200.
46. S. Ramachandran, J. Trehwella, Y. Tseng and Y. B. Yu, *Chemistry of Materials*, 2006, **18**, 6157-6162.
47. M. J. Majcher, S. Himbert, F. Vito, M. A. Campea, R. Dave, G. Vetergaard Jensen, M. C. Rheinstadter, N. M. B. Smeets and T. Hoare, *Macromolecules*, 2022, **55**, 7303-7317.
48. A. M. Castilla, E. R. Draper, M. C. Nolan, C. Brasnett, A. Seddon, L. L. E. Mears, N. Cowieson and D. J. Adams, *Scientific Reports*, 2017, **7**, 8380.
49. E. R. Draper, B. Dietrich, C. Brasnett, S. Sproules, T. O. McDonald, A. M. Seddon and D. J. Adams, *Macromolecular Rapid Communications*, 2018, **39**, 1700746.
50. D. McDowall, D. J. Adams and A. M. Seddon, *Soft Matter*, 2022, **18**, 1577-1590.
51. E. R. Draper, L. Wilbraham, D. J. Adams, M. Wallace, R. Schweins and M. A. Zwijnenburg, *Nanoscale*, 2019, **11**, 15917-15928.
52. E. R. Draper, B. J. Greeves, M. Barrow, R. Schweins, M. A. Zwijnenburg and D. J. Adams, *Chem*, 2017, **2**, 716-731.
53. D. J. Adams, L. M. Mullen, M. Berta, L. Chen and W. J. Frith, *Soft Matter*, 2010, **6**, 1971-1980.
54. C. Tang, A. M. Smith, R. F. Collins, R. V. Ulijn and A. Saiani, *Langmuir*, 2009, **25**, 9447-9453.
55. R. A. Hule, R. P. Nagarkar, A. Altunbas, H. R. Ramay, M. C. Branco, J. P. Schneider and D. J. Pochan, *Faraday Discussions*, 2008, **139**, 251-264.
56. M. C. Nolan, J. J. Walsh, L. L. E. Mears, E. R. Draper, M. Wallace, M. Barrow, B. Dietrich, S. M. King, A. J. Cowan and D. J. Adams, *Journal of Materials Chemistry A*, 2017, **5**, 7555-7563.
57. A. M. Castilla, M. Wallace, L. L. Mears, E. R. Draper, J. Dutch, S. Rogers and D. J. Adams, *Soft Matter*, 2016, **12**, 7848-7854.
58. L. L. Miller and K. R. Mann, *Accounts of Chemical Research*, 1996, **29**, 417-423.
59. P. Li, D. Zhang, Y. Zhang, W. Lu, J. Zhang, W. Wang, Q. He, P. Théato and T. Chen, *ACS Macro Letters*, 2019, **8**, 937-942.
60. M. Kremer, M. Kersten and S. Höger, *Organic Chemistry Frontiers*, 2018, **5**, 1825-1829.
61. C. C. L. W. K. AE and S. D. B. G. E. Considerations, *Adv. Mater*, 2011, **23**, 2367-2371.
62. P. Kienzle, *NIST Neutron Activation and Scattering Calculator*, , DOI: <https://www.ncnr.nist.gov/resources/activation/>.
63. <http://www.sasview.org/>.

Chapter 5: Summary, conclusions and future work

5.1 Conclusions

There is a push to develop and design water-soluble materials for greener solvent processing methods in organic photovoltaic devices (OPVs). Perylene bisimides (PBIs) are materials often used in OPVs because they are highly absorbent and *n*-type semiconductors. Throughout the literature there are examples of altering the PBIs' chemical structure to improve their solubility in water. Typically, the water solubility is improved through the addition of an ionic group such as an amine, phosphonic acid, or carboxylic acid. However, the role of pH of water and how this can be used to change the self-assembled nano- and micro-structures is often overlooked. More research on this topic is needed to offer parameters which allow for better design of OPVs. Making more direct links to how structure can impact the pH response of these water soluble PBIs is needed. As well as determining which pHs form nanostructures that are not only better at forming radical but are still workable for solution process.

This work looked at how the packing of aggregates for amino acid-functionalised PBIs could be changed to influence their pH sensitivity. The pH sensitivity was linked to the apparent pK_a values of the aggregates formed in solution. This value could help act as a pH guide for where fibres would be formed before they crash out of solution and become difficult to work with. The structural differences in the micellar aggregates led to differences in the self-assembled nano- and microstructures which had an impact on their radical anion or cation formation properties.

For **PBI-L**, the counterion size in the basic solution used to alter the pH was changed to tailor the aggregates in solution in hope of improving its radical anion formation properties. This method offered an easier route to changing structures compared to synthesis as it was less time-consuming. It is expected that counterion choice would affect the solubility of the aggregates formed in solution as larger counterions should stabilise larger aggregates. Small-angle X-ray scattering (SAXS) showed that the nanostructure's morphology was highly dependent on the counterions size at the pH decreased. The UV-vis absorption spectroscopy larger aggregates formed by Cs^+ showed the most radical formed after irradiation with UV-light as pH was lowered. Hydrogels were made using with the different solutions as a pH trigger as it offered a

more uniform way to lower the pH and cause the aggregate to self-assemble into larger structures. The different aggregates had an impact on the gelation kinetics and differences in bulk rheological properties hydrogels. With the strength of the hydrogels increasing with counterion size, Cs⁺ was the strongest. Hydrogels made with Cs⁺ and K⁺ formed the most radical supporting the idea that larger nanostructure favoured radical formation. Since it was shown that the counterion choice had improve radical formation in solution and as hydrogels the solutions at pH 6 were then used to make multilayer OPVs. The devices made with Li⁺ showed the most promising power conversion efficiency (PCE). This may be due to these devices having a slightly lower λ_{\max} , however, more tests are required to confirm this result.

Next, three PBIs with small variations in the amino acid side chain were investigated in both solution and as hydrogels. It was seen that the functional group at the imide position played an important role in molecular packing which, in turn, impacted the radical formation. Smaller amino acid side chains were able to pack better and resulted in more radical anion being formed. We had seen this before, but we have not seen a report where their amino side chain could also be used to impact the pH response. These aggregates of the different PBIs had different apparent pK_a values. **PBI-I** had the highest pK_{a2} of 6.6 while **PBI-L** and **PBI-V** had the same pK_{a2} of 5.9. These different apparent pK_a values caused them to self-assemble differently at the same pH. SAXS data was collected and showed how the amino acid side chain impacted the nanostructures over a range of pHs near the apparent pK_a values. UV-vis absorption spectroscopy showed that the amount of radical anion formed upon irradiation increased as pH was lowered, with **PBI-V** forming more radical anion at pH 5 and 6 than the other PBIs. Indicating that larger structures favoured radical anion formation. The difference in pH response also resulted in a change of the bulk rheological properties for the pH triggered hydrogels. These differences in pH sensitivity had a huge impact on the PBIs' gelation kinetics as well. This led to differences in the bulk of the hydrogels formed with a pH trigger, with **PBI-I** hydrogels being nearly twice as stiff as the other two PBI hydrogels.

Finally, the properties of three PBIs with small variations in the amino acid side chain were dramatically changed through a core substitution with pyrrolidine. These materials had not been reported before and show promise for more environmentally

friendly options for OPV devices. The addition of electron density to the core enabled the formation of radical cation and dication with both UV light and electrochemically. These radicals are rarely discussed in the literature and this work helps fill the gap in knowledge. The increase in hydrophobicity in the chemical structure also caused an increase in the apparent pK_a values. SAXS data showed that spherical micelles were present at pH 7 for **PBI-A-1**. This is because it was the only PBI with a pK_{a1} value below 7. On the other hand, shape-independent fibres had already formed at pH 7 for **PBI-L-1** and **PBI-V-1** which was due to their higher pK_{a1} values. EPR showed that the spherical micelles form radical cation than the shape independent fibres. We believe showed that the fibres with larger mesh sizes were not able to form cation and dication as efficiently possibly due to the increased mesh size causing a self-quenching. The pH-triggered hydrogels of the three PBIs were reported for the first time and showed differences in the bulk rheological properties, showing how amino acid side chain can be used to change the bulk gel properties. However, the hydrogels could no longer form radical cation upon irradiation due to the increased concentration and self-assembly of aggregates at the lower pH impacting the hydrogel network's ability to absorb UV light.

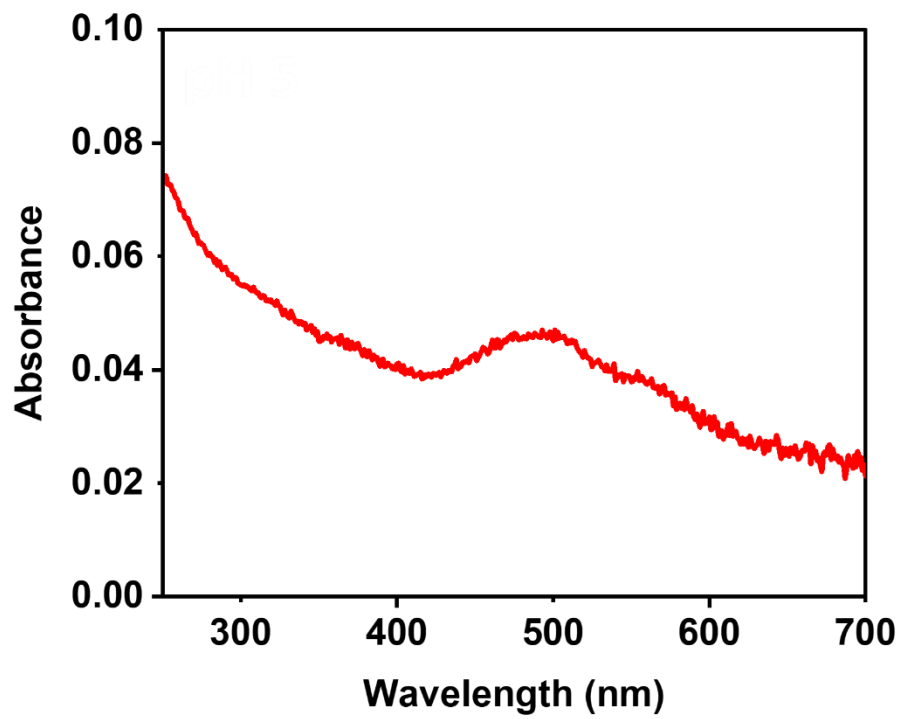
In conclusion, it was observed that pH is a useful way to modify PBI self-assembled structures across multiple length scales. As it does not change the solvent composition and the self-assembly can be reversed when pH change. It is important to investigate these materials through a series of techniques to gain insight into the self-assembly across various length scales as it is often difficult to link the changes in the aggregate nanostructure to the bulk rheological and conductive properties just based on a chemical structure change. It was observed that the different chemical structures of the amino acid side chain had a major impact on the pH sensitivity, while core substitution impacted the optical and redox properties. The optimal pH for favourable self-assembled structures was when there was a balance between the elongated fibre structures and good solubility. For PBIs in solution this was observed at pHs around their apparent pK_a values as they began to self-assemble from spherical micelles into fibre structures. By knowing these pK_a we were able to gauge what pH the structures there is a balance between the elongated fibre structures and good solubility. Radical anion or cation formation was very dependent on the self-

assembled structures formed at these different pHs with flexible elliptical cylinders better at forming radical anion, cation, or dication than shape-independent fibres or spherical micelles. When the pH was lowered too far below the pK_{a2} value for any of these PBIs, they began to precipitate out of solution making it challenging to process them into OPV devices. This could be overcome by using a pH trigger which allowed for slower decrease in pH resulting in more uniform elongation of fibres into hydrogels. However, the hydrogel networks are randomly organised which can still be an obstacle to electron transfer efficiency and radical formation. Overall, pH is a powerful tool for changing the radical formation properties of PBIs by change their self-assembled structures into elongated nanofibers which had improved packing.

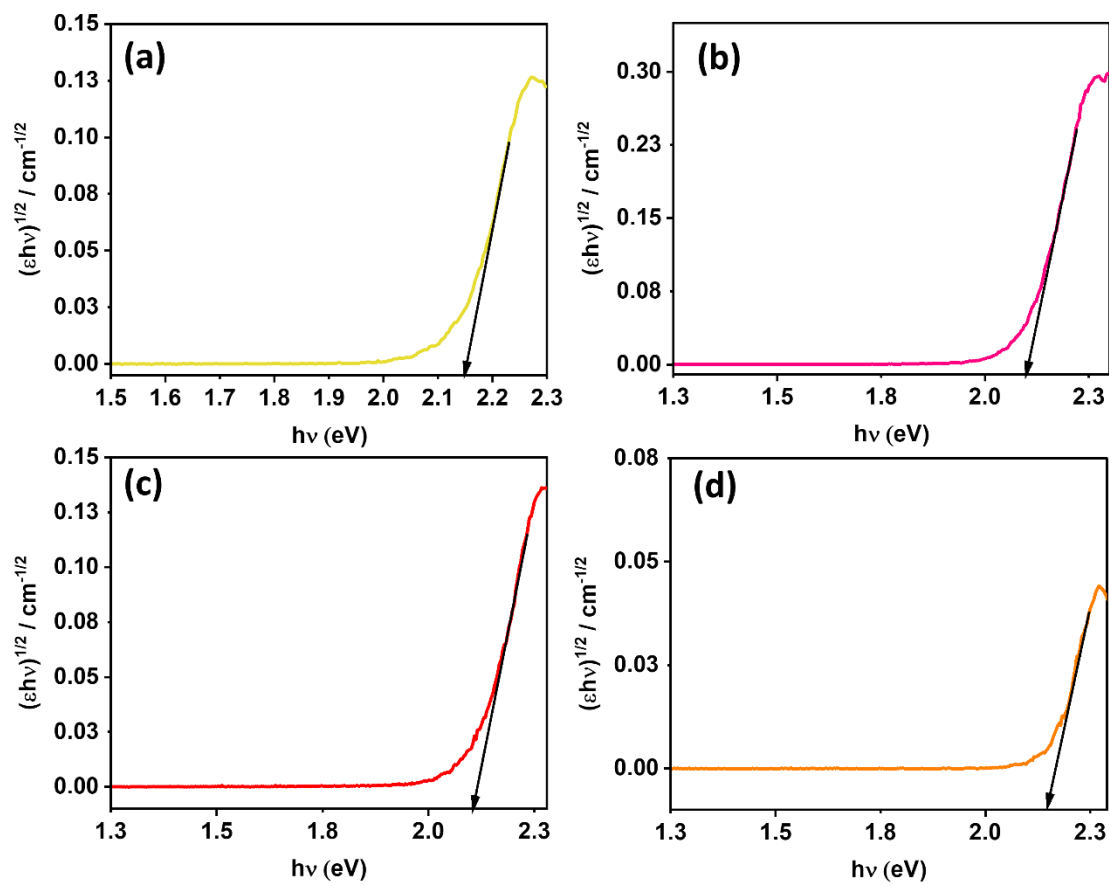
As device fabrication is critical for OPVs, future work would involve further investigation of these water-soluble PBIs as transport interlayers at different pHs to optimise the PCE. The core-substituted PBIs have a small band gap energy meaning they could be useful as electron-donating layers in OPVs. However, it was seen that lowering the pH reduced their ability to form radical cation. Instead, future work could look at using solutions of these core-substituted PBIs at higher pHs to develop electron-donating materials.

Another direction would be to monosubstitute the PBIs at their core with a primary or secondary amine group. The monosubstituted products would result in a green PBI material which absorbs in the red region. Materials that absorb in that region are favourable for OPVs as they mimic the absorption window of plants. In addition, monosubstitution at the PBI core would not cause as much twisting compared to polysubstitution, thus limiting the interference that the new functional group would have on the π - π stacking. The primary and secondary amines would donate electron density to the core lowering the energy band gap. These amines could also be protonated or deprotonated by adjusting the pH which could in turn be used to tailor the self-assembled nanostructures in solution further.

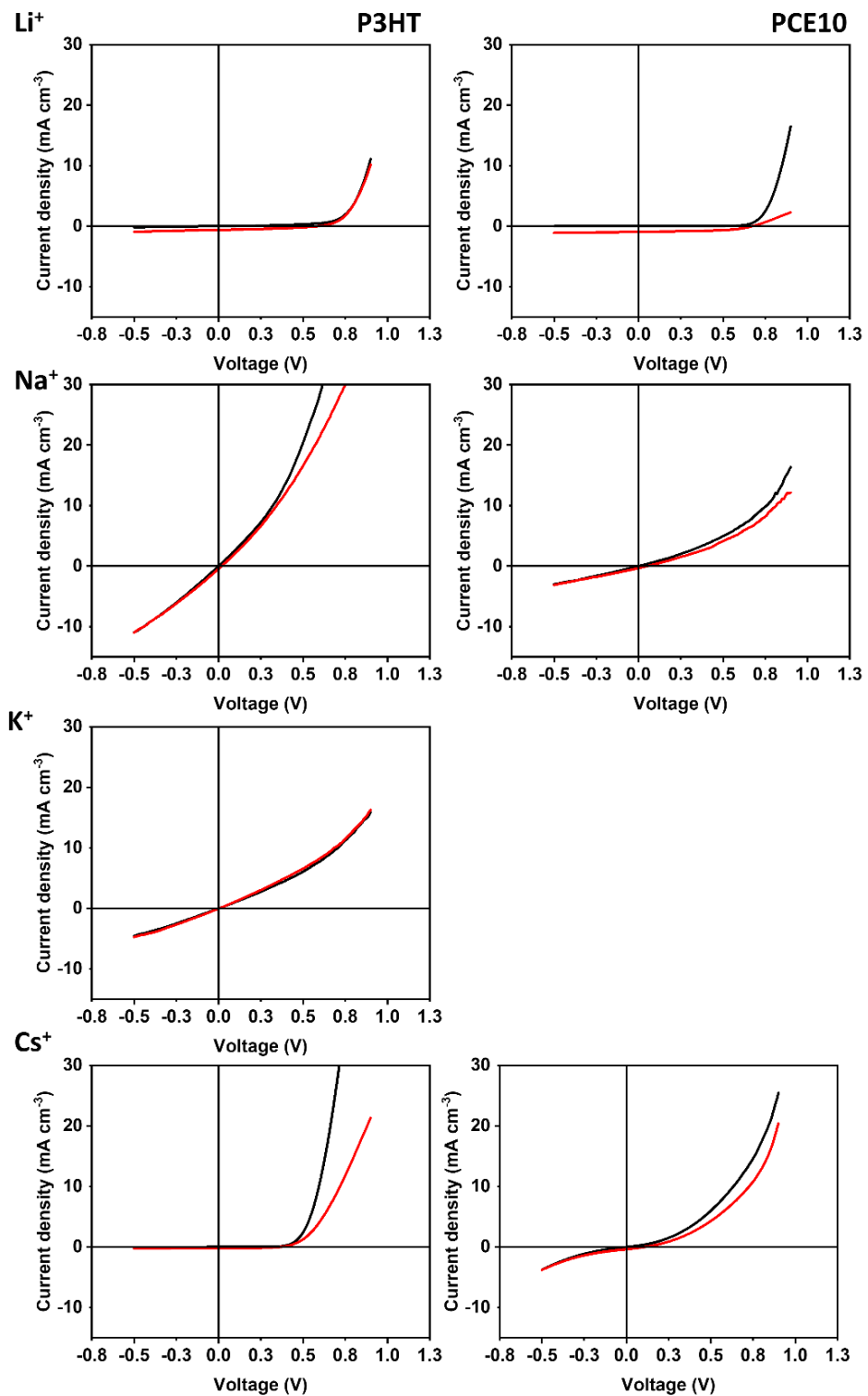
Chapter 6: Appendix



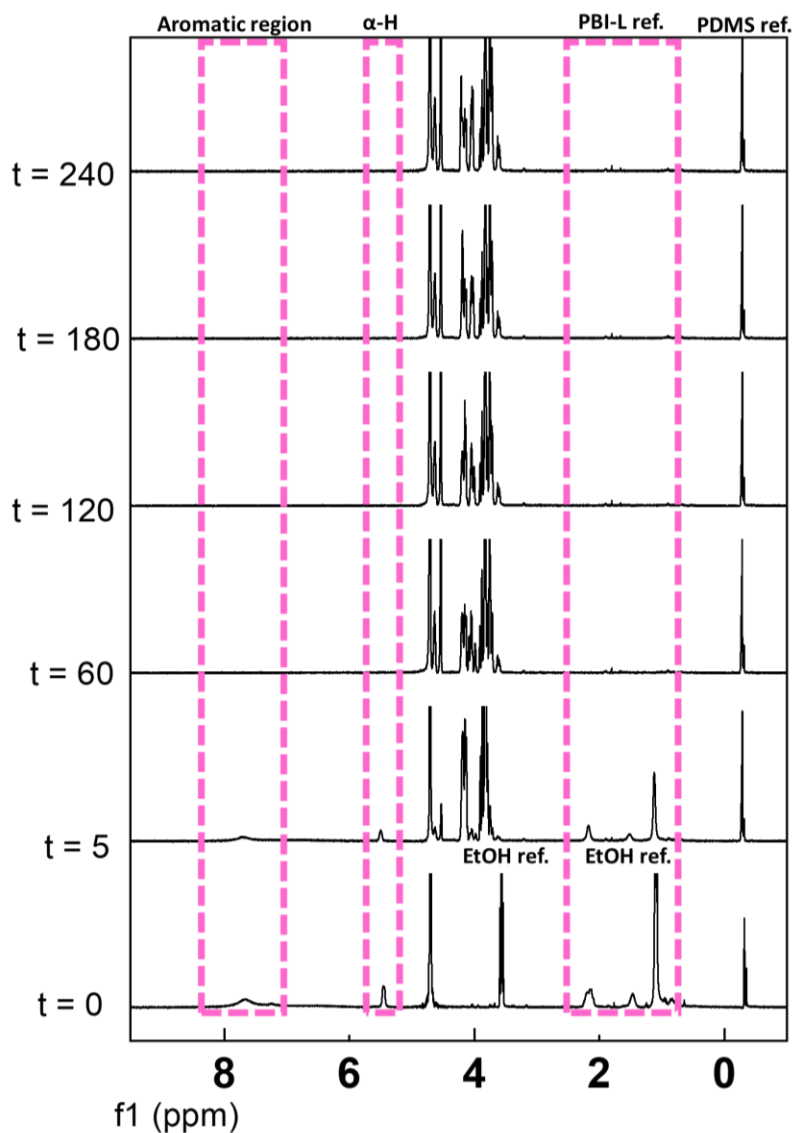
Appendix 1. UV-vis absorption spectrum of **PBI-L** at pH 5 with Na⁺ scaled up on the y-axis.



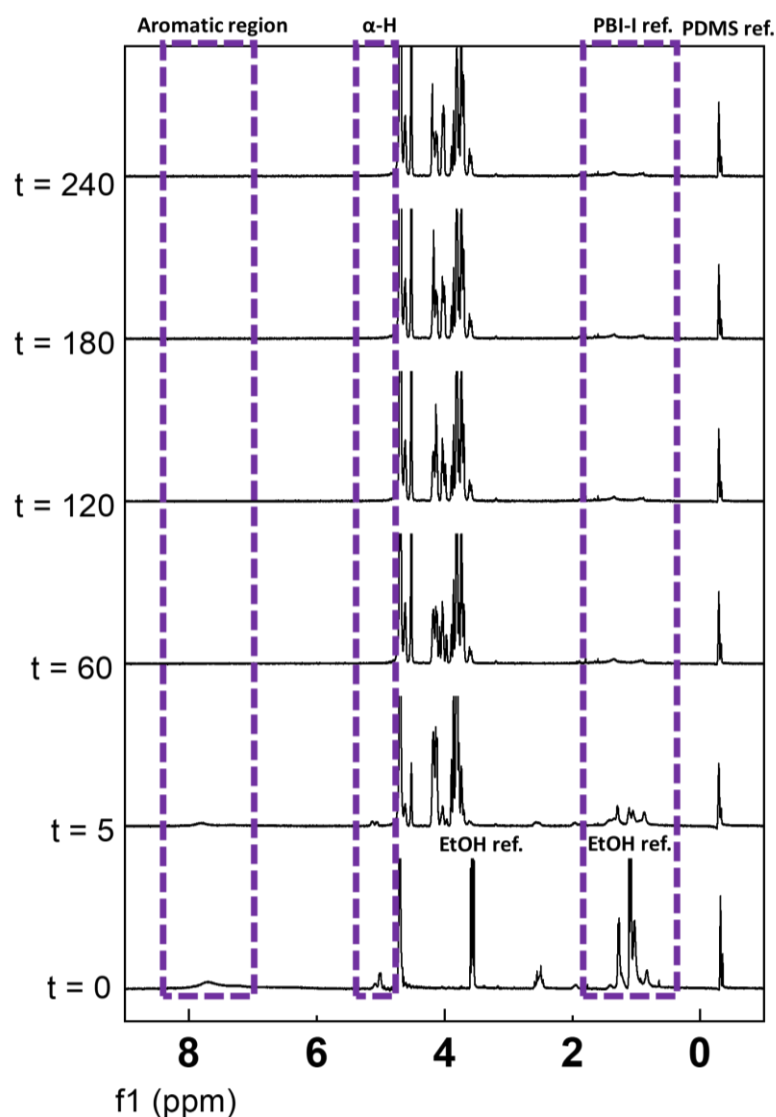
Appendix 2. Tauc plots including linear fit (**black**) from the UV-vis absorption spectrum of (a) Li^+ (**yellow**), (b) Na^+ (**pink**), (c) K^+ (**red**), and (d) Cs^+ (**orange**) at pH 6.



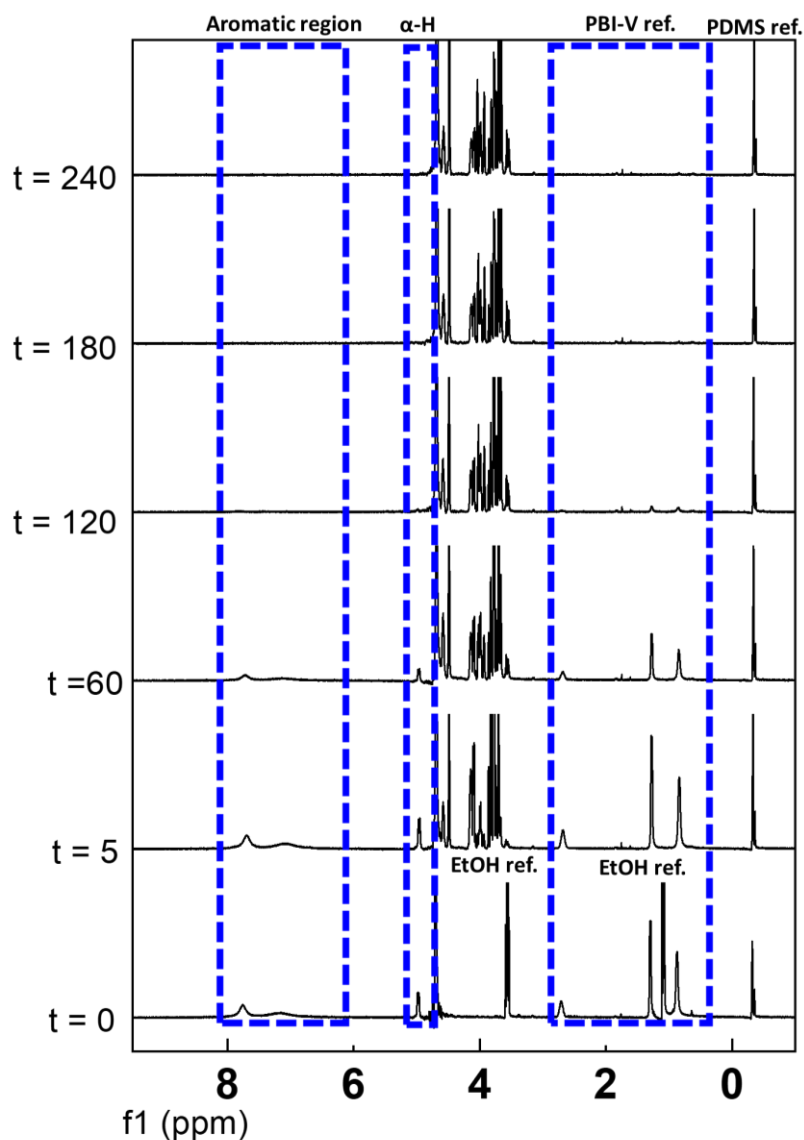
Appendix 3. Representative example *J-V* characteristics of OPV devices with structure ITO/ZnO/**PBI-L**/P3HT /MoO₃/Ag (left) or ITO/ZnO/**PBI-L**/PCE10 /MoO₃/Ag (right) with different cations before irradiation (**black**) and after irradiation (**red**) using a Newport solar simulator with 150 W Xe lamp for AM1.5 irradiation.



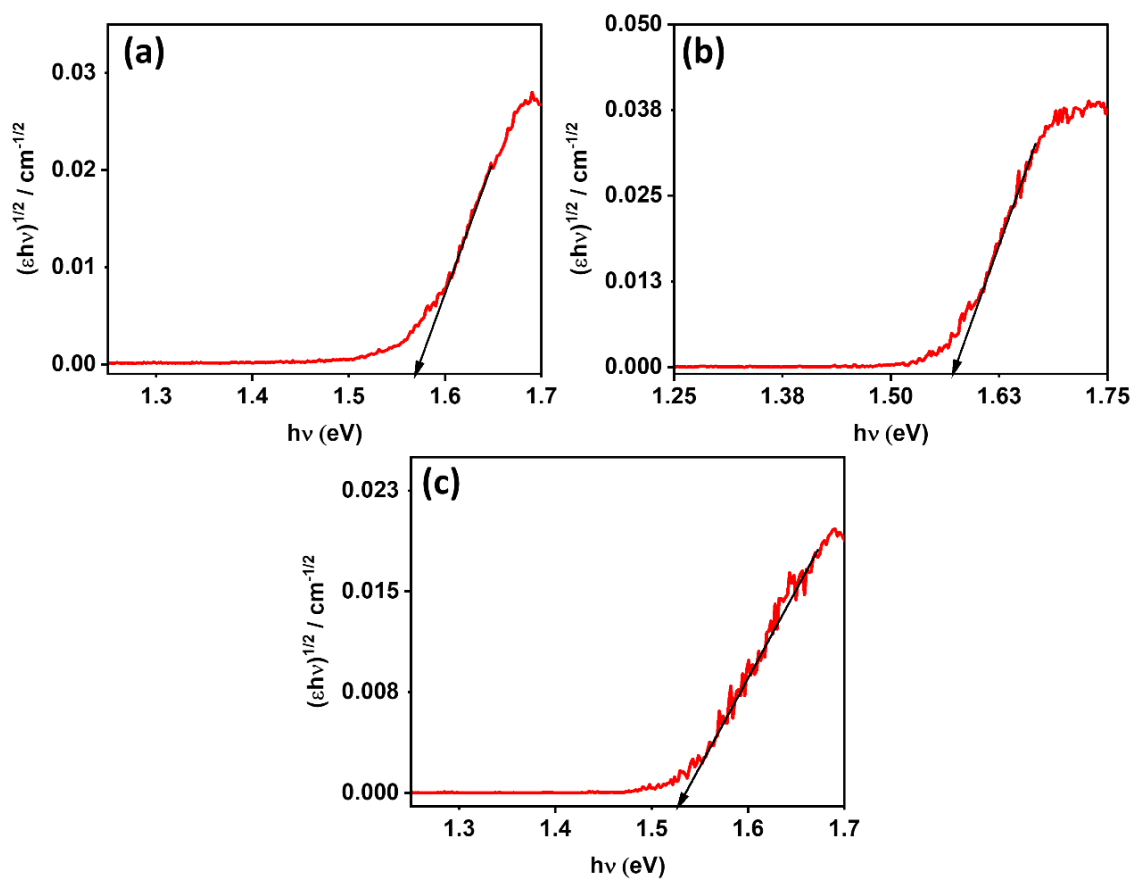
Appendix 4. ^1H NMR spectra recorded over time after the addition of GdL to a solution of **PBI-L** in $\text{D}_2\text{O}/\text{NaOD}$. The time (in minutes) at which the data were collected is shown on the left, with the peaks corresponding to **PBI-L** highlighted in pink. The peaks between around 3.5 and 4.3 ppm are from GdL and its hydrolysis products (mainly gluconic acid). The peak at 4.8 ppm is from the solvent. At $t = 0$, 2 μL of ethanol was added and the peak at 3.5 ppm for the methylene group was integrated to determine the initial percent assembled in solution. The methyl groups from the $[\text{SiO}(\text{CH}_3)_2]$ chain units and $(-\text{Si}(\text{CH}_3)_2\text{OH})$ terminal groups of the PDMS standard against which the peaks of **PBI-L** are integrated are at -0.5 ppm. The proton environment labelled **PBI-L ref.** was used to determine percentage assembly over time.



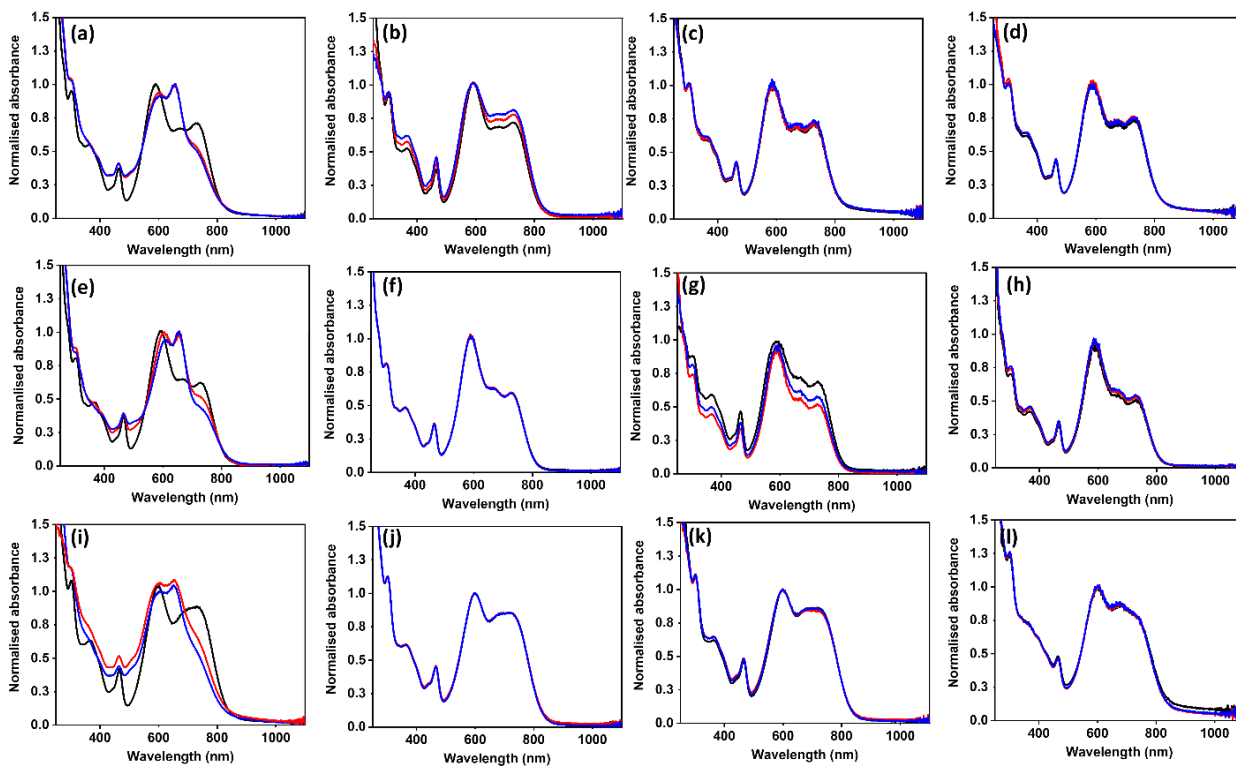
Appendix 5. ^1H NMR spectra recorded over time after the addition of GdL to a solution of **PBI-I** in $\text{D}_2\text{O}/\text{NaOD}$. The time (in minutes) at which the data were collected is shown on the left, with the peaks corresponding to **PBI-I** highlighted in purple. The peaks between around 3.5 and 4.3 ppm are from GdL and its hydrolysis products (mainly gluconic acid). The peak at 4.8 ppm is from the solvent. At $t = 0$, 2 μL of ethanol was added and the peak at 3.5 ppm for the methylene group was integrated to determine the initial percent assembled in solution. The methyl groups from the $[\text{SiO}(\text{CH}_3)_2]$ chain units and $(-\text{Si}(\text{CH}_3)_2\text{OH})$ terminal groups of the PDMS standard against which the peaks of **PBI-I** are integrated are at -0.5 ppm. The proton environment labelled **PBI-I** ref. was used to determine the percentage assembly over time.



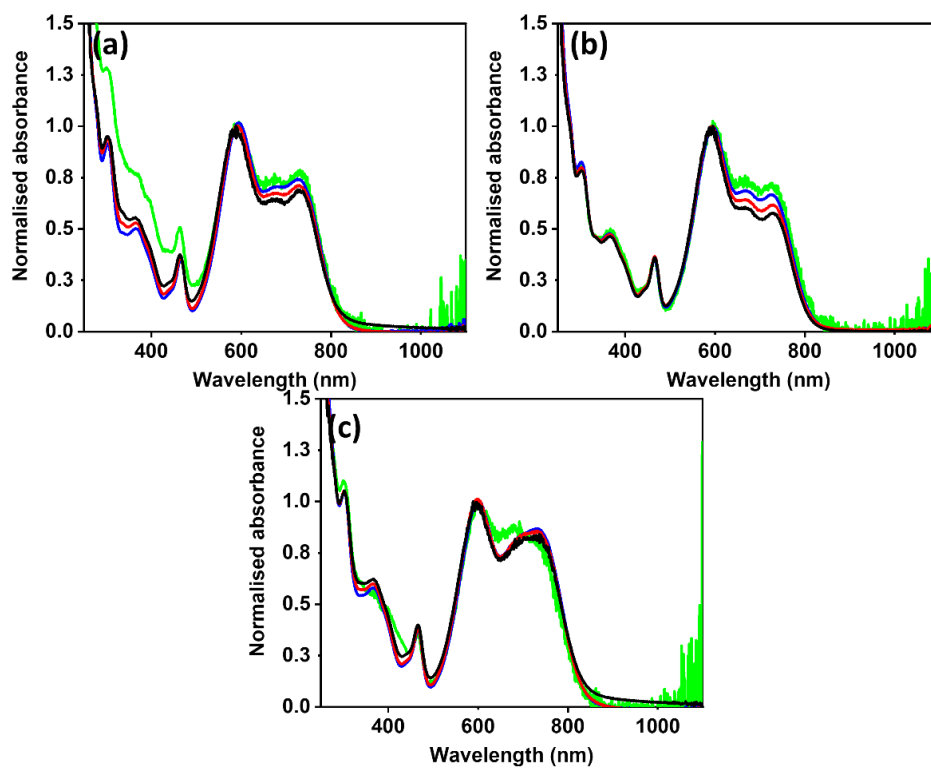
Appendix 6. ¹H NMR spectra recorded over time after the addition of GdL to a solution of **PBI-V** in D₂O/NaOD. The time (in minutes) at which the data were collected is shown on the left, with the peaks corresponding to **PBI-V** highlighted in blue. The peaks between around 3.5 and 4.3 ppm are from GdL and its hydrolysis products (mainly gluconic acid). The peak at 4.8 ppm is from the solvent. At t = 0, 2 μL of ethanol was added and the peak at 3.5 ppm for the methylene group was integrated to determine the initial percent assembled in solution. The methyl groups from the [SiO(CH₃)₂] chain units and (-Si(CH₃)₂OH) terminal groups of the PDMS standard against which the peaks of **PBI-V** are integrated are at -0.5 ppm. The proton environment labelled **PBI-V ref.** was used to determine the percentage assembly over time.



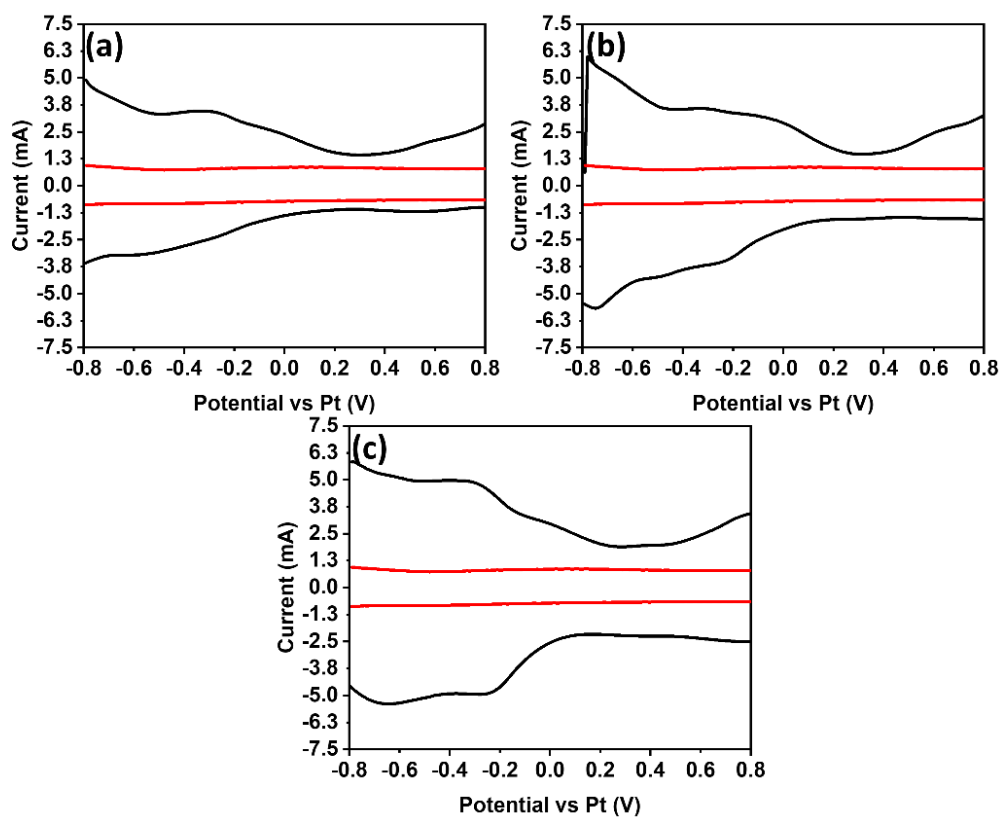
Appendix 7. Tauc plots (red) including linear fit (black) from the UV-vis absorption spectrum of (a) **PBI-L-1**, (b) **PBI-A-1**, and (d) **PBI-V-1** at pH 7.



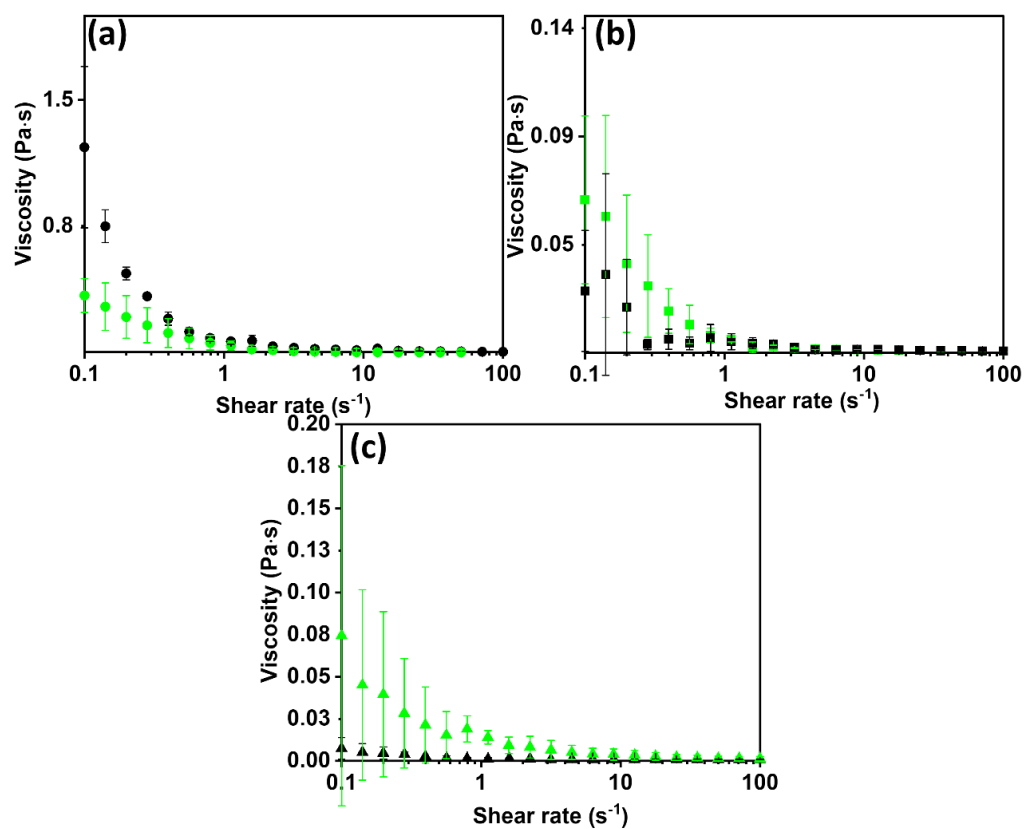
Appendix 8. UV-vis absorption spectra for (a-d) **PBI-L-1**, (e-h) **PBI-A-1**, and (i-l) **PBI-V-1** pre-irradiation (**black**), after being irradiated for 15 minutes (**red**), and 30 minutes (**blue**) with a (a,e,i) 365 nm LED, (b,f,j) 490 nm LED, (c,g,k) 590 nm LED, and (d,h,l) 740 nm LED.



Appendix 9. UV-vis absorption spectra for (a) **PBI-L-1**, (b) **PBI-A-1**, and (c) **PBI-V-1** at 15 mg/mL (**black**), 10 mg/mL (**red**), 5 mg/mL (**blue**), and 0.5 mg/mL (**green**) at pH 7 normalised to allow for comparison of peak intensities.



Appendix 10. SWV of (a) **PBI-L-1 (black)**, (b) **PBI-A-1 (black)**, and (c) **PBI-V-1 (black)**, and 0.1 M NaCl electrolyte background (**red**) at a frequency of 40 Hz.



Appendix 11. Dynamic viscosities of (a) **PBI-L-1**, (b) **PBI-A-1**, and (c) **PBI-V-1** at pH 7. Viscosity measurements were done pre-irradiation (**black**), and after being heated at 40°C for 60 minutes (**green**). Measurements were performed in triplicate and errors were calculated from the standard deviations.

Appendix Table 1. SAXS fit table for solutions prepared at pH 7 with Li⁺, Na⁺, K⁺, and Cs⁺.

Cation	Li ⁺	Na ⁺	K ⁺	Cs ⁺
Model	Sphere	Sphere	Sphere	Sphere
Sphere scale	0.000717 ± 4×10 ⁻⁶	0.000871 ± 9×10 ⁻⁶	0.000607 ± 3×10 ⁻⁶	0.000561 ± 2×10 ⁻⁶
Background (cm ⁻¹)	0.00362 ± 2×10 ⁻⁵	0.00262 ± 3×10 ⁻⁵	0.00269 ± 2×10 ⁻⁵	0.00454 ± 1×10 ⁻⁵
Sphere radius (nm)	1.29 ± 0.002	1.18 ± 0.003	1.32 ± 0.002	1.44 ± 0.02
χ ²	1.9	1.6	2.4	2.2
Model	Power law	Power law	Power law	Power law
Power law scale	2.47×10 ⁻⁸ ± 9×10 ⁻¹⁰	4.64×10 ⁻⁸ ± 3×10 ⁻¹⁰	3.02×10 ⁻⁹ ± 5×10 ⁻¹⁰	7.02×10 ⁻⁹ ± 5×10 ⁻¹⁰
Background (cm ⁻¹)	0.0123 ± 0.0002	0.000202 ± 7×10 ⁻⁵	0.0124 ± 0.0002	0.0182 ± 0.002
Power law	3.46 ± 0.0001	3.48 ± 0.0001	3.59 ± 0.004	3.56 ± 0.02
χ ²	1.9	4.4	1.6	2.9

Appendix Table 2. SAXS fit table for solutions prepared at pH 6 with Li⁺, Na⁺, K⁺, and Cs⁺.

Cation	Li ⁺	Na ⁺	K ⁺	Cs ⁺
Model	Correlation length	Correlation length	Correlation length	Correlation length
Correlation length scale	0.442 ± 0.001	0.969 ± 0.0002	1 ± 0.0001	0.0649 ± 2×10 ⁻⁶
Background (cm ⁻¹)	0.00185 ± 0.0001	0.000875 ± 0.00001	0.0001 ± 0.00001	0.000679 ± 5×10 ⁻⁶

Lorentzian scaling factor	0.0374 ± 0.003	1.01 ± 0.001	0.0197 ± 0.0001	0.378 ± 0.0004
Porod scaling factor	$3.53 \times 10^{-6} \pm 3 \times 10^{-9}$	$6.59 \times 10^{-8} \pm 4 \times 10^{-11}$	$2.38 \times 10^{-7} \pm 4 \times 10^{-9}$	$1.89 \times 10^{-5} \pm 2 \times 10^{-8}$
Correlation length (nm)	0.638 ± 0.001	14.8 ± 0.005	0.748 ± 0.002	0.857 ± 0.001
Porod exponent	2.63 ± 0.002	3.41 ± 0.0001	2.84 ± 0.003	2.60 ± 0.003
Lorentzian exponent	3.19 ± 0.02	1.64 ± 0.0002	2.26 ± 0.016	2.35 ± 0.004
χ^2	5.0	4.8	4.5	3.0

Appendix Table 3. SAXS fit table for solutions prepared at pH 5 with Li⁺, Na⁺, K⁺ and Cs⁺.

Cation	Li ⁺	Na ⁺	K ⁺	Cs ⁺
Model	Flexible elliptical cylinder + power law	Flexible elliptical cylinder + power law	Mass fractal	Flexible elliptical cylinder + power law
Flexible elliptical cylinder scale	$0.000419 \pm 1 \times 10^{-5}$	$0.000122 \pm 2 \times 10^{-6}$	N/A	$0.000264 \pm 7 \times 10^{-7}$
Power law scale	$5.09 \times 10^{-7} \pm 5 \times 10^{-9}$	$2.15 \times 10^{-5} \pm 2 \times 10^{-8}$	N/A	$4.17 \times 10^{-7} \pm 4 \times 10^{-8}$
Mass fractal scale	N/A	N/A	$0.000186 \pm 6 \times 10^{-7}$	N/A
Background (cm ⁻¹)	$0.000424 \pm 1 \times 10^{-5}$	$2.11 \times 10^{-6} \pm 4 \times 10^{-10}$	$0.000266 \pm 2 \times 10^{-5}$	$0.00245 \pm 9 \times 10^{-6}$
Length (nm)	34.5 ± 0.00003	64.4 ± 0.05	N/A	34.2 ± 0.003
Kuhn length (nm)	8.64 ± 0.02	3.94 ± 0.06	N/A	8.57 ± 0.03
Cylinder radius (nm)	1.14 ± 0.001	1.24 ± 0.0005	N/A	1.31 ± 0.001

Axis ratio	3.15 ± 0.005	2.67 ± 0.001	N/A	2.88 ± 0.006
Power law	3.23 ± 0.002	2.46 ± 0.006	N/A	3.51 ± 0.008
Radius (nm)	N/A	N/A	1.06 ± 0.004	N/A
Mass fractal dimension	N/A	N/A	2.44 ± 0.001	N/A
Cut-off length (nm)	N/A	N/A	4.08 ± 0.004	N/A
χ^2	7.2	6.5	9.7	4.0

Appendix Table 4. SAXS fitting results for solutions with Li^+ , Na^+ , K^+ , and Cs^+ , counter ions as hydrogels. *No fitting error available.

Cation	Li^+	Na^+	K^+	Cs^+
Model	Flexible elliptical cylinder + power law	Flexible elliptical cylinder + power law	Flexible elliptical cylinder + power law	Mass fractal
Flexible elliptical cylinder scale	$0.000254 \pm 2 \times 10^{-7}$	$1.58 \times 10^7 \pm 2 \times 10^4$	$0.00021 \pm 9 \times 10^{-7}$	N/A
Power law scale	$9.76 \times 10^{-9} \pm 3 \times 10^{-10}$	$7.58 \times 10^5 \pm 1 \times 10^4$	$2.91 \times 10^{-7} \pm 4 \times 10^{-9}$	N/A
Mass fractal scale	N/A	N/A	N/A	$0.000172 \pm 2 \times 10^{-7}$
Background (cm^{-1})	$0.00369 \pm 6 \times 10^{-6}$	$3.58 \times 10^8 \pm 1 \times 10^{-6}$	$0.00368 \pm 7 \times 10^{-6}$	$0.00447 \pm 7 \times 10^{-6}$
Length (nm)	103 ± 0.0006	300*	275 ± 3.00	N/A
Kuhn length (nm)	10.3 ± 0.05	15.2 ± 0.1	4.01 ± 0.05	N/A
Cylinder radius (nm)	1.61 ± 0.002	3.57 ± 0.01	1.41 ± 0.005	N/A
Axis ratio	2.52 ± 0.005	2.23 ± 0.001	2.13 ± 0.07	N/A
Power law	4.21 ± 0.007	2.76 ± 0.004	3.47 ± 0.003	N/A
Radius (nm)	N/A	N/A	N/A	1.72 ± 0.002
Mass fractal dimension	N/A	N/A	N/A	2.25 ± 0.001

Cut-off length (nm)	N/A	N/A	N/A	90.5 ± 10.0
χ^2	2.4	2.1	1.7	1.2

Appendix Table 5. SAXS fit table for solutions prepared at pH 6 with Li⁺, Na⁺, K⁺, and Cs⁺ after being irradiated for 5 minutes. *No fitting error available.

Cation	Li ⁺	Na ⁺	K ⁺	Cs ⁺
Model	Correlation length	Correlation length	Correlation length	Correlation length
Correlation length scale	1*	1*	1*	1*
Background / (cm ⁻¹)	0.00181 ± 0.0007	0.000267 ± 0.00002	0.00203 ± 0.002	0.0147 ± 0.004
Lorentzian scaling factor	18.9 ± 0.02	5.83 ± 0.03	14.9 ± 0.003	6.15 ± 0.7
Porod scaling factor	5.98×10 ⁻⁵ ± 7×10 ⁻⁸	9.53×10 ⁻⁵ ± 2×10 ⁻⁷	5.17×10 ⁻⁶ ± 2×10 ⁻⁸	5.66×10 ⁻⁴ ± 4×10 ⁻⁶
Correlation length (nm)	3.49 ± 0.003	3.21 ± 0.04	3.33 ± 0.005	3.02 ± 0.07
Porod exponent	3.08 ± 0.001	2.79 ± 0.04	3.21 ± 0.0005	2.62 ± 0.05
Lorentzian exponent	3.84 ± 0.006	3.83 ± 0.05	4*	4*
χ^2	5.3	5.0	8.7	2.8

Appendix Table 6. SAXS fit table for **PBI-L** solutions at 10 mg/mL at pH 5.

pH	5	6	7	
Model	Flexible elliptical cylinder + power law	Correlation length	Sphere	Power law
Flexible elliptical cylinder scale	0.000122 ± 2×10 ⁻⁶	N/A	N/A	N/A
Correlation	N/A	0.969 ± 0.0002	N/A	N/A

length scale				
Sphere scale	N/A	N/A	0.000871 ± 9×10 ⁻⁶	N/A
Power law scale	2.15×10 ⁻⁵ ± 2×10 ⁻⁸	N/A	N/A	4.64×10 ⁻⁸ ± 3×10 ⁻¹⁰
Background (cm ⁻¹)	2.11×10 ⁻⁶ ± 4×10 ⁻¹⁰	0.000875 ± 0.00001	0.00262 ± 3×10 ⁻⁵	0.000202 ± 7×10 ⁻⁵
Length / nm	64.4 ± 0.05	N/A	N/A	N/A
Kuhn length (nm)	3.94 ± 0.0563	N/A	N/A	N/A
Cylinder radius (nm)	1.24 ± 0.0005	N/A	N/A	N/A
Axis Ratio	2.67 ± 0.001	N/A	N/A	N/A
Power law	2.46 ± 0.006	N/A	N/A	3.48 ± 0.0001
Spherical radius (nm)	N/A	N/A	1.18 ± 0.003	N/A
Lorentzian scaling factor	N/A	1.01 ± 0.001	N/A	N/A
Porod scaling factor	N/A	6.59 × 10 ⁻⁸ ± 4 × 10 ⁻¹¹	N/A	N/A
Correlation length (nm)	N/A	14.8 ± 0.005	N/A	N/A
Porod exponent	N/A	3.41 ± 0.0001	N/A	N/A
Lorentzian exponent	N/A	1.64 ± 0.0002	N/A	N/A
χ ²	6.5	4.8	1.6	4.4

Appendix Table 7. SAXS fitting results for **PBI-I** as 10 mg/mL solutions at different pH.

pH	5	6	7
Model	Mass fractal	Flexible elliptical cylinder + power law	Sphere + power law
Mass fractal scale	0.000379 ± 2×10 ⁻⁶	N/A	N/A
Flexible elliptical	N/A	0.000203 ± 5×10 ⁻⁸	N/A

<i>cylinder scale</i>			
<i>Sphere scale</i>	N/A	N/A	$0.000273 \pm 5 \times 10^{-7}$
<i>Power law scale</i>	N/A	$2.45 \times 10^{-5} \pm 2 \times 10^{-6}$	$3.01 \times 10^{-6} \pm 2 \times 10^{-9}$
<i>Background (cm⁻¹)</i>	$0.000317 \pm 6 \times 10^{-6}$	$0.000537 \pm 6 \times 10^{-6}$	$0.00416 \pm 7 \times 10^{-6}$
<i>Length (nm)</i>	N/A	20.6 ± 0.5	N/A
<i>Kuhn length (nm)</i>	N/A	2.24 ± 0.4	N/A
<i>Cylinder radius (nm)</i>	N/A	1.52 ± 0.0005	N/A
<i>Axis ratio</i>	N/A	2.17 ± 0.02	N/A
<i>Sphere radius (nm)</i>	N/A	N/A	1.16 ± 0.004
<i>Power law</i>	N/A	2.22 ± 0.0002	2.48 ± 0.001
<i>Radius (nm)</i>	1.73 ± 0.002	N/A	N/A
<i>Mass fractal dimension</i>	2.00 ± 0.002	N/A	N/A
<i>Cut-off length (nm)</i>	6.77 ± 0.02	N/A	N/A
χ^2	2.7	1.7	7.1

Appendix Table 8. SAXS fitting results for **PBI-V** as 10 mg/mL solutions at different pH. *No fitting error available.

<i>pH</i>	5	6	7
<i>Model</i>	<i>Flexible elliptical cylinder + sphere</i>	<i>Flexible elliptical cylinder + sphere</i>	<i>Sphere + power law</i>
<i>Flexible elliptical cylinder scale</i>	$0.000221 \pm 6 \times 10^{-7}$	$0.000149 \pm 5 \times 10^{-7}$	N/A
<i>Sphere scale</i>	$5.01 \times 10^{-5} \pm 1 \times 10^{-7}$	$4.08 \times 10^{-5} \pm 2 \times 10^{-7}$	$0.000171 \pm 1 \times 10^{-6}$
<i>Power law scale</i>	N/A	N/A	$0.000836 \pm 9 \times 10^{-6}$
<i>Background (cm⁻¹)</i>	$0.00208 \pm 7 \times 10^{-6}$	$0.00258 \pm 7 \times 10^{-6}$	$0.00361 \pm 6 \times 10^{-5}$
<i>Length (nm)</i>	300*	300*	N/A

<i>Kuhn length (nm)</i>	2.17 ± 0.0004	2.65 ± 0.001	N/A
<i>Cylinder radius (nm)</i>	1.63 ± 0.0008	1.57 ± 0.001	N/A
<i>Axis ratio</i>	4.09 ± 0.003	4.55 ± 0.005	N/A
<i>Sphere radius (nm)</i>	4.85 ± 0.003	4.13 ± 0.003	3.83 ± 0.008
<i>Power law</i>	N/A	N/A	1.43 ± 0.002
χ^2	11	10	2.1

Appendix Table 9. SAXS fit table for **PBI-L**, **PBI-I**, and **PBI-V** hydrogels. *No fitting error available.

PBI	L	I	V
<i>Model</i>	<i>Flexible elliptical</i> <i>cylinder + power law</i>	<i>Flexible elliptical</i> <i>cylinder + power law</i>	<i>Flexible elliptical</i> <i>cylinder polydispersity</i> 0.3
<i>Flexible elliptical</i> <i>cylinder scale</i>	$1.58 \times 10^7 \pm 2 \times 10^4$	$1.86 \times 10^7 \pm 3 \times 10^4$	0.00146 ± 0.0004
<i>Power law scale</i>	$7.58 \times 10^5 \pm 1 \times 10^4$	$2.23 \times 10^6 \pm 1 \times 10^4$	N/A
<i>Background (cm⁻¹)</i>	$3.58 \times 10^8 \pm 1.53 \times 10^6$	$3.56 \times 10^8 \pm 2 \times 10^6$	0.0257 ± 0.001
<i>Length (nm)</i>	300*	332 ± 10.0	406 ± 6.00
<i>Kuhn length (nm)</i>	15.2 ± 0.1	30.6 ± 1.00	28.0 ± 0.03
<i>Cylinder radius (nm)</i>	3.57 ± 0.01	3.36 ± 0.009	2.65 ± 0.003
<i>Axis ratio</i>	2.23 ± 0.001	2.38 ± 0.01	3.51 ± 0.01
<i>Power law</i>	2.76 ± 0.004	2.31 ± 0.01	N/A
χ^2	2.1	2.3	4.3

Appendix Table 10. SAXS fit table for solutions of **PBI-L-1** irradiated with a 365 nm LED for different amounts of time. *No fitting error available.

<i>Irradiation period (minutes)</i>	0	60	Allowed to relax overnight
<i>Model</i>	<i>Correlation length</i>	<i>Correlation length</i>	<i>Correlation length</i>
<i>Correlation length scale</i>	1*	1*	1*
<i>Background (cm⁻¹)</i>	0.0194 ± 0.001	0.0101 ± 0.0007	0.0511 ± 0.0006
<i>Lorentzian scaling factor</i>	0.435 ± 0.01	0.199 ± 0.002	0.688 ± 0.001
<i>Porod scaling factor</i>	1.42×10 ⁻⁷ ± 3×10 ⁻⁹	1.15×10 ⁻⁷ ± 1×10 ⁻⁹	7.46×10 ⁻⁷ ± 1×10 ⁻⁹
<i>Correlation length (nm)</i>	1.47 ± 0.01	2.82 ± 0.03	2.85 ± 0.1
<i>Porod exponent</i>	3.62 ± 0.003	4.21 ± 0.005	3.86 ± 0.002
<i>Lorentzian exponent</i>	1.34 ± 0.01	2.12 ± 0.04	2.28 ± 0.08
χ^2	2.0	3.4	3.7

Appendix Table 11. SAXS fit table for solutions of **PBI-A-1** irradiated with a 365 nm LED for different amounts of time.

<i>Irradiation period (minutes)</i>	0	60	Allowed to relax overnight
<i>Model</i>	<i>Sphere + power law</i>	<i>Sphere + power law</i>	<i>Sphere + power law</i>
<i>Sphere scale</i>	0.0157 ± 0.0003	0.0177 ± 0.0005	0.0208 ± 0.0002
<i>Power law scale</i>	2.61×10 ⁻⁷ ± 9×10 ⁻⁸	7.31×10 ⁻⁸ ± 2×10 ⁻⁹	1.03×10 ⁻⁸ ± 2×10 ⁻¹⁰
<i>Background (cm⁻¹)</i>	0.0022 ± 0.001	0.0785 ± 0.002	0.0697 ± 0.001

Sphere radius (nm)	1.32 ± 0.01	1.22 ± 0.01	1.27 ± 0.005
Power law	3.36 ± 0.01	3.73 ± 0.10	4.00 ± 0.004
χ^2	2.3	1.9	4.8

Appendix Table 12. SAXS fit table for solutions of **PBI-V-1** irradiated with a 365 nm LED for different amounts of time. *No fitting error available.

Irradiation period (minutes)	0	60	Allowed to relax overnight
Model	Correlation length	Correlation length	Correlation length
Correlation length scale	1*	1*	1*
Background (cm^{-1})	0.0211 ± 0.001	0.00966 ± 0.0001	0.0251 ± 0.001
Lorentzian scaling factor	0.251 ± 0.001	1.55 ± 0.01	1.97 ± 0.01
Porod scaling factor	$1.06 \times 10^{-5} \pm 6 \times 10^{-7}$	$3.58 \times 10^{-6} \pm 1 \times 10^{-8}$	$3.02 \times 10^{-6} \pm 1 \times 10^{-8}$
Correlation length (nm)	1.06 ± 0.01	3.76 ± 0.02	3.99 ± 0.02
Porod exponent	3.22 ± 0.002	3.44 ± 0.003	3.33 ± 0.003
Lorentzian exponent	1.76 ± 0.02	1.61 ± 0.01	1.63 ± 0.01
χ^2	2.5	2.7	3.2

Appendix Table 13. SAXS fitting results for **PBI-L-1** as 10 mg/mL solutions at different pH. *No fitting error available.

pH	7	6	5
Model	Correlation length	Correlation length	Correlation length
Correlation length	1*	1*	1*

<i>scale</i>			
<i>Background (cm⁻¹)</i>	0.0194 ± 0.001	0.0124 ± 0.0007	0.0457 ± 0.0007
<i>Lorentzian scaling factor</i>	0.435 ± 0.01	12.2 ± 0.5	12.4 ± 0.5
<i>Porod scaling factor</i>	1.42×10 ⁻⁷ ± 3×10 ⁻⁹	7.38×10 ⁻⁶ ± 3×10 ⁻⁹	1.56×10 ⁻⁴ ± 4×10 ⁻⁷
<i>Correlation length (nm)</i>	1.47 ± 0.01	3.82 ± 0.05	3.46 ± 0.05
<i>Porod exponent</i>	3.62 ± 0.003	3.42 ± 0.03	2.75 ± 0.04
<i>Lorentzian exponent</i>	1.34 ± 0.01	3.41 ± 0.03	3.71 ± 0.05
χ^2	2.0	2.0	4.5

Appendix Table 14. SAXS fitting results for **PBI-A-1** as 10 mg/mL solutions at different pH. *No fitting error available.

pH	7	6	5
<i>Model</i>	<i>Sphere + power law</i>	<i>Flexible elliptical cylinder</i>	<i>Flexible elliptical cylinder</i>
<i>Correlation length scale</i>	1*	0.00877	0.00879 ± 0.0002
<i>Background (cm⁻¹)</i>	0.0211 ± 0.001	0.0547	0.0447 ± 0.001
<i>Sphere radius (nm)</i>	1.32 ± 0.01	N/A	N/A
<i>Power law</i>	3.36 ± 0.08	N/A	N/A
<i>Length (nm)</i>	N/A	79.5 ± 2.0	300 ± 10
<i>Kuhn length (nm)</i>	N/A	7.95 ± 0.0004	17.8 ± 0.2
<i>Cylinder radius (nm)</i>	N/A	1.56 ± 0.01	1.51 ± 0.06
<i>Axis ratio</i>	N/A	1.89 ± 0.02	2.82 ± 0.02
χ^2	2.3	3.8	3.5

Appendix Table 15. SAXS fitting results for **PBI-V-1** as 10 mg/mL solutions at different pH. *No fitting error available.

pH	7	6	5
Model	Correlation length	Correlation length	Correlation length
Correlation length scale	1*	1*	1*
Background (cm ⁻¹)	0.0211 ± 0.001	0.0842 ± 0.0006	0.149 ± 0.0005
Lorentzian scaling factor	0.251 ± 0.001	9.55 ± 0.2	15.8 ± 0.2
Porod scaling factor	1.06×10 ⁻⁵ ± 6×10 ⁻⁷	8.53×10 ⁻⁶ ± 5×10 ⁻⁸	8.91×10 ⁻⁶ ± 6×10 ⁻⁸
Correlation length (nm)	1.06 ± 0.01	3.93 ± 0.006	3.71 ± 0.009
Porod exponent	3.22 ± 0.002	3.29 ± 0.001	3.38 ± 0.04
Lorentzian exponent	1.76 ± 0.02	4*	4*
χ ²	2.5	5.3	9.4

Appendix Table 16. SAXS fit table for **PBI-L-1**, **PBI-A-1**, and **PBI-V-1** hydrogels. *No fitting error available.

PBI	L-1	A-1	V-1
Model	Flexible elliptical cylinder + power law	Flexible elliptical cylinder	Flexible elliptical cylinder + power law polydispersity 0.3
Flexible elliptical cylinder scale	0.00644 ± 2×10 ⁻⁵	0.0166 ± 2×10 ⁻⁵	0.00732 ± 1×10 ⁻⁵
Power law scale	3.12×10 ⁻⁶ ± 1×10 ⁻⁸	N/A	1.29×10 ⁻⁵ ± 6×10 ⁻⁸
Background (cm ⁻¹)	0.0271 ± 0.001	0.00647 ± 0.0006	0.0141 ± 0.0006
Length (nm)	109 ± 1.96	70.0 ± 0.5	300*
Kuhn length (nm)	5.55 ± 0.08	6.32 ± 0.10	21.8 ± 2

<i>Cylinder radius (nm)</i>	1.81 ± 0.004	1.43 ± 0.004	2.77 ± 0.02
<i>Axis ratio</i>	1.59 ± 0.007	1.70 ± 0.041	1.85 ± 0.02
<i>Power law</i>	3.77 ± 0.001	N/A	3.39 ± 0.05
χ^2	4.7	3.6	4.6